

## ABSTRACT

TABOR, JORDAN ASHLEY. Textile-based Soft Sensors for Prosthetic Environment Monitoring (Under the direction of Dr. Tushar K. Ghosh).

Amputees often experience discomfort when wearing their prosthetic devices and as the amputee population grows,<sup>[1]</sup> this becomes a more prevalent and pressing issue. New prosthetic technologies are necessary to construct comfortable, well-fitted liners and sockets<sup>[2-5]</sup> but an established issue in the development of new prosthetic technology is the lack of practical, accurate, inner socket sensors to monitor the inner socket environment (ISE), or the region between the residual limb and the socket. While rigid sensors do provide insight into the ISE, they do not possess required compliance for use at the residual limb/socket interface.<sup>[6]</sup> Textile-based sensors provide promising potential for sensing within the ISE because they are flexible and comfortable while also providing opportunities to create large, dense sensor arrays. Here, I propose two approaches to fabricating textile-based pressure sensors for ISE monitoring. The first is a capacitive sensor structure fabricated through a simple, and scalable sewing process using commercially available conductive yarns. The second sensor approach is a uniquely shaped fiber produced through a process commonly employed in the textile industry, melt extrusion. Additionally, I propose two custom set-ups which can be used to evaluate textile-based sensors in simulated prosthetic environments. These efforts serve as a promising first step toward creating flexible sensors for seamlessly monitoring the ISE.

© Copyright 2021 by Jordan Ashley Tabor

All Rights Reserved

Textile-based Soft Sensors for Prosthetic Environment Monitoring

by  
Jordan Ashley Tabor

A dissertation submitted to the Graduate Faculty of  
North Carolina State University  
in partial fulfillment of the  
requirements for the degree of  
Doctor of Philosophy

Fiber and Polymer Science

Raleigh, North Carolina  
2021

APPROVED BY:

---

Dr. Tushar K. Ghosh  
Committee Chair

---

Dr. Alper Bozkurt

---

Dr. Helen (He) Huang

---

Dr. Martin King

## **DEDICATION**

I dedicate this work to those that have supported me throughout my research journey including: my parents, James and Donna Tabor, my brothers, Justin, Jared, and Joshua Tabor, as well as my partner, Paul Zavattieri.

## **BIOGRAPHY**

Jordan Tabor is a Chapel Hill, North Carolina native and received her B.S. degree in Textile Technology, Summa Cum Laude, from NC State University in 2015. Upon completion of her undergraduate, she began her M.S. in Textile Engineering at NC State University. Her master's thesis studied the structure-property relationships of nonwoven fabrics and was funded by The Nonwovens Institute. Upon completion of her master's, Jordan began her PhD in Fiber and Polymer Science in 2017. During her PhD, Jordan's research was funded by the National Science Foundation and focused on creating flexible sensors for biomedical applications. Over the course of her PhD, Jordan also completed a minor in Electrical and Computer Engineering as well as a Nonwovens Certificate. During her graduate career, Jordan received several research honors and fellowships including First Place Presentation at NC State's Graduate Research symposium, the Sigma Xi Graduate Research Award, as well as the Pulcra Chemical Graduate Fellowship. In addition to her research accomplishments, Jordan served as a teaching assistant for three different courses and instructed a Textile Engineering course. During her PhD, Jordan also completed an internship with BASF's Leadership Development Program and served as an officer for the organization, Graduate Women in Science.

## ACKNOWLEDGMENTS

Thank you to my adviser, Dr. Tushar K. Ghosh, for his mentorship and support during both my undergraduate and graduate career. I also want to thank Dr. Alper Bozkurt, Dr. Helen (He) Huang, and Dr. Martin King for serving on my committee and providing guidance throughout my PhD. I am also grateful for my research group-mates and lab-mates: Kony Chatterjee, Shuzhen Wei, and Ashish Kapoor who were great colleagues, friends, and support systems throughout this process.

I also want to thank all those that collaborated with me and made my research possible. From NC State's Electrical and Computer Engineering department, I thank: Talha Agcayazi, Brendan Thompson, and Michael McKnight for their assistance with the electrical aspects of this project. I would like to thank my collaborators from UNC Chapel Hill/NC State's Biomedical Engineering department: Aaron Fleming, and Dr. Ming Liu for their assistance with the biomedical aspects of this project. Thank you to, Dr. Michael Lee, Brandon Barham, Derek Frankena, and Stephen Harper for assisting with the prosthetics aspects of this project. Finally, thank you to Eric Lawrence and Stephen Sharp for sharing their expertise and time to facilitate the production of the tricomponent melt-extruded fibers.

## TABLE OF CONTENTS

LIST OF TABLES .....	viii
LIST OF FIGURES .....	ix
1 Introduction.....	1
2 Review of Literature .....	2
2.1 Prosthetic Components.....	4
2.1.1 Liner-liner .....	5
2.1.2 Liner .....	5
2.1.3 Socks .....	6
2.1.4 Socket.....	7
2.2 The Inner Socket Environment .....	7
2.3 Sensors for the Inner Socket Environment Monitoring .....	8
2.3.1 Stress Sensing Mechanisms .....	9
2.3.2 Monitoring Stress within the Inner Socket Environment .....	12
2.4 Potential Application of Textile-based Sensing for Inner Socket Environment Monitoring .....	21
2.4.1 Materials .....	21
2.4.2 Fabrication .....	28
2.4.3 Modes of Sensing.....	32
2.4.4 Performance Parameters .....	33
2.4.5 Stress Sensing .....	34
2.4.6 Moisture Sensing .....	46
2.5 Summary and Outlook .....	54
3 Textile-based Soft Sensors for Prosthetic Environment Monitoring Introduction .....	55
4 Fully-Textile Seam-Line Sensors for Facile Textile Integration and Tunable Multi-Modal Sensing of Pressure, Humidity, and Wetness .....	57
4.1 Abstract .....	58
4.2 Introduction .....	58
4.3 Sensing Architecture .....	61
4.4 Results and Discussion.....	62
4.4.1 Characterization of Materials.....	63
4.4.2 Mechanical Properties of the Sensor Assembly.....	64
4.4.3 Electromechanical Characterization of Seam-line Sensors .....	69
4.4.4 Relative Humidity and Wetness Sensing.....	77

4.5	Proof of Concept Demonstration.....	81
4.5.1	Pressure Mat.....	82
4.5.2	Wearable Human-Machine Interface.....	85
4.6	Conclusions.....	86
4.7	Experimental Section.....	87
4.8	Acknowledgment.....	91
4.9	Supplementary Information.....	91
5	Textile-Based Pressure Sensors for Monitoring Prosthetic-Socket Interfaces.....	94
5.1	Abstract.....	95
5.2	Introduction.....	95
5.3	System Design.....	98
5.3.1	Sensor Array.....	100
5.3.2	Analog to Digital Conversion Printed Circuit Board.....	101
5.3.3	Data Collection Printed Circuit Board.....	102
5.3.4	Real-time Data Visualization.....	103
5.4	Seam-line Sensor Evaluation in Simulated Inner Socket Environment.....	103
5.4.1	Artificial Limb Testing.....	104
5.4.2	Able-Bodied Testing with Bent-Knee Adapter.....	107
5.5	Amputee Testing.....	111
5.6	Conclusion.....	116
5.7	Acknowledgement.....	117
6	Tricomponent Melt Extrusion of Fiber Sensors for Electronic Textiles.....	117
6.1	Abstract.....	118
6.2	Introduction.....	118
6.3	Fiber Shape and Sensor Geometry.....	120
6.4	Materials.....	122
6.4.1	Polymer Selection.....	122
6.4.2	Polymer Characterization.....	123
6.5	Fiber Formation: Tricomponent Extrusion and Drawing.....	126
6.5.1	Optimization of the Extrusion Process Parameters.....	127
6.5.2	Tricomponent Extrusion Trials.....	128
6.5.3	Drawing.....	130
6.6	Fiber Characterization.....	131
6.6.1	Optical Microscopy and Dimensional Analysis.....	131

6.6.2	Mechanical Behavior of Fibers .....	133
6.6.3	Fiber Sensory Behavior.....	135
6.7	Conclusion.....	139
6.8	Acknowledgement.....	139
6.9	Supplementary Information.....	140
7	Melt-Extruded Fibers Sensors for Electronic Textiles.....	146
7.1	Abstract .....	146
7.2	Introduction .....	147
7.3	Fiber Shape and Sensor Architecture .....	149
7.4	Mechanical Characterization.....	151
7.5	Characterization of Sensory Behavior.....	153
7.6	Proof of Concept Demonstration – Pressure Sensing Fabric .....	159
7.7	Conclusion.....	162
7.8	Experimental Section .....	163
7.9	Acknowledgement.....	165
8	Summary and Future Work.....	165

## LIST OF TABLES

Table 1:	Summary of samples and corresponding nomenclature Reprinted with permission from <sup>[20]</sup> ©2020 WILEY-VCH Verlag GmbH & Co. KGaA, Weinheim.....	61
Table 2:	Mechanical properties of SLSs. Reprinted with permission from <sup>[20]</sup> ©2020 WILEY-VCH Verlag GmbH & Co. KGaA, Weinheim. ....	91
Table 3:	Electromechanical properties of SLS. Reprinted with permission from <sup>[20]</sup> ©2020 WILEY-VCH Verlag GmbH & Co. KGaA, Weinheim. ....	92
Table 4:	Summary of advantages/disadvantages and example applications of different materials used. Reprinted with permission from <sup>[20]</sup> ©2020 WILEY-VCH Verlag GmbH & Co. KGaA, Weinheim. ....	92
Table 5:	Parameters of the tricomponent line's extruders .....	140
Table 6:	Pump speeds used in the TME experiments .....	141
Table 7:	Temperature profiles used in the TME experiments (please note that Extruder C has a fourth heating zone not present in Extruder A and B) .....	142
Table 8:	Process settings for drawing 50:40:10 fibers.....	142

## LIST OF FIGURES

Figure 1:	Prosthetic components (a) Socket, pylon and foot <sup>[94]</sup> (b) Cross-sectional view of layers worn beneath the socket..... 5	5
Figure 2:	Sensor schematics (a) Resistive sensing modality (b) Parallel-plate capacitor..... 10	10
Figure 3:	Commercial sensors used to measure LL prosthetic stress distributions (a) SGs mounted to prosthetic socket. Reprinted with permission from <sup>[44]</sup> © 2004 Elsevier Ltd. All rights reserved. (b) Load cell instrumented onto socket. Reprinted with permission from <sup>[119]</sup> © 2019 IPPEM. Published by Elsevier Ltd. All rights reserved. (c) F-socket by Tekscan attached to residual limb. Reprinted with permission from <sup>[23]</sup> © 2012 Elsevier Ltd. All rights reserved.) (d) Pliance by Novel attached to residual limb (Reprinted with permission from <sup>[127]</sup> © 2009 Elsevier Ltd. All rights reserved.) ..... 14	14
Figure 4:	Normal and shear stresses reported within the ISE (a) Normal pressure ranges reported in literature (Paper 1, <sup>[39]</sup> Paper 2, <sup>[121]</sup> Paper 3, <sup>[40]</sup> Paper 4, <sup>[11]</sup> Paper 5, <sup>[41]</sup> Paper 6, <sup>[120]</sup> Paper 7, <sup>[42]</sup> Paper 8, <sup>[43]</sup> Paper 9, <sup>[44]</sup> Paper 10, <sup>[119]</sup> Paper 11, <sup>[22]</sup> Paper 12, <sup>[106]</sup> Paper 13, <sup>[118]</sup> Paper 14, <sup>[117]</sup> Paper 15, <sup>[23]</sup> Paper 16, <sup>[116]</sup> Paper 17, <sup>[115]</sup> Paper 18, <sup>[26]</sup> Paper 19, <sup>[114]</sup> Paper 20, <sup>[113]</sup> Paper 21, <sup>[112]</sup> Paper 22, <sup>[12]</sup> Paper 23 <sup>[111]</sup> ) (b) Shear stress ranges reported in literature (Paper 1, <sup>[39]</sup> Paper 2, <sup>[40]</sup> Paper 3, <sup>[17]</sup> Paper 4, <sup>[43]</sup> Paper 5, <sup>[44]</sup> Paper 6, <sup>[119]</sup> Paper 7 <sup>[12]</sup> )..... 16	16
Figure 5:	Sensors proposed for measuring stresses within the ISE (a) Transducers mounted to the socket. Reprinted with permission from <sup>[122]</sup> © 1998 IPPEM. Published by Elsevier Ltd. All rights reserved. (b) MEMS-based pressure sensor for ISE monitoring. Reprinted with permission from <sup>[146]</sup> © 2011, IEEE. (c) Custom-prosthetic socket insert with incorporated FSRs. Reprinted with permission from <sup>[142]</sup> © 2017 IPPEM. Published by Elsevier Ltd. All rights reserved. (d) Capacitive sensor structure created via 3D printing and lithography. Reprinted with permission from <sup>[6]</sup> © 2016 Published by Elsevier Ltd on behalf of IPPEM. (e) CNT/PVDF piezoresistive film sensor attached to residual limb. Reprinted with permission from <sup>[33]</sup> Copyright © 2017, IEEE. (f) Shear sensor for monitoring knee-bending. Reprinted with permission from <sup>[38]</sup> © 2017 MDPI. .... 18	18
Figure 6:	Textile-based resistive stress sensor fabrication and structure (a) Fabrication of a double-twisted conductive smart thread. Reprinted with permission from <sup>[63]</sup> © 2016 WILEY-VCH Verlag GmbH & Co. KGaA, Weinheim. (b) Fabrication of a stretchable electronic fabric capable of pressure sensing. Reprinted with permission from <sup>[66]</sup> © 2015 WILEY-VCH Verlag GmbH & Co. KGaA, Weinheim. (c) Fabrication of a stretchable conductive core-shell fiber with wrinkled microstructure including twisting of the fibers into a yarn-like structure and wrapping the yarn around a human figure to indicate flexibility. Reprinted with permission from <sup>[59]</sup> © 2016 WILEY-VCH Verlag GmbH & Co. KGaA, Weinheim. (d) Construction of sewn fabric sensor consisting of four fabric layers. Reprinted with permission from <sup>[61]</sup> © 2014 The Authors. Published by Elsevier B.V. (e) Elastomeric tubes injected with metallic alloy to create microfiber sensor which can be incorporated into	

	a fabric gloves. Reprinted with permission from <sup>[230]</sup> © 2018, American Chemical Society. ....	36
Figure 7:	Responses of textile-based resistive sensors (a) Resistance versus applied load for a double-twisted conductive smart thread. Reprinted with permission from <sup>[63]</sup> © 2016 WILEY-VCH Verlag GmbH & Co. KGaA, Weinheim. (b) Relative resistance change with load of a stretchable electronic fabric. Reprinted with permission from <sup>[66]</sup> © 2015 WILEY-VCH Verlag GmbH & Co. KGaA, Weinheim. (c) Relative resistance change with pressure for stretchable conductive core-shell fiber with wrinkled microstructure and change of resistance with two stacked fibers (inlet image). Reprinted with permission from <sup>[59]</sup> © 2016 WILEY-VCH Verlag GmbH & Co. KGaA, Weinheim. (d) Layered fabric sensor performance when exposed to cyclic loads of 35N. Reprinted with permission from <sup>[61]</sup> © 2014 The Authors. Published by Elsevier B.V. (e) Pressure sensing and reliability performance of microfiber sensor consisting of elastomeric tubes injected with metallic alloy. Reprinted with permission from <sup>[230]</sup> © 2018, American Chemical Society.....	39
Figure 8:	Capacitive textile-based stress sensors structure and sensing mechanisms (a) View of a fiber-based capacitive sensors. Reprinted with permission from <sup>[57]</sup> © 2016 Springer Nature. (b) PA/PEDOT:PSS/Cytop fiber-based sensor structure and schematic of sensing mechanism. Reprinted with permission from <sup>[48]</sup> © 2012 Elsevier B.V. All rights reserved. (c) Ag fibers/cotton wrapper fiber/PU yarn-based sensor structure and capacitor formation at crossover points in fabric structure. Reprinted with permission from <sup>[54]</sup> © 2019 WILEY-VCH Verlag GmbH & Co. KGaA, Weinheim. (d) Pressure sensing array consisting of microstructured PDMS/CNT fibers. Reprinted with permission from <sup>[49]</sup> © 2019 Elsevier B.V. All rights reserved. (e) Sensor structure and working mechanism of flexible sensor consisting of microstructured PDMS layer and fabric electrodes. Reprinted with permission from <sup>[50]</sup> © 2017 WILEY-VCH Verlag GmbH & Co. KGaA, Weinheim.....	43
Figure 9:	Capacitive textile-based stress sensor responses (a) Cotton/Pt fiber-based sensor response to loads of 0.1, 0.5 and 1 N. Reprinted with permission from <sup>[57]</sup> © 2016 Springer Nature. (b) PA/PEDOT:PSS/Cytop fiber-based sensor response to 4.9 N/cm <sup>2</sup> pressure. Reprinted with permission from <sup>[48]</sup> © 2012 Elsevier B.V. All rights reserved. (c) Relative change in capacitance and applied pressure of the array of Ag fibers/cotton wrapper fiber/PU yarn-based sensor. Reprinted with permission from <sup>[54]</sup> © 2019 WILEY-VCH Verlag GmbH & Co. KGaA, Weinheim. (d) Response of microstructured/CNT fibers to pressure. Reprinted with permission from <sup>[49]</sup> © 2019 Elsevier B.V. All rights reserved. (e) Relative change in capacitance of flexible sensor consisting of microstructured PDMS layer and knit or woven electrodes. Reprinted with permission from <sup>[50]</sup> © 2017 WILEY-VCH Verlag GmbH & Co. KGaA, Weinheim.....	45
Figure 10:	Schematics of common RH sensing mechanisms (a) Resistive RH sensing. Higher RH in environment results in more water captured by the hygroscopic material, increasing the distance between conductive particles and hence	

	increasing the resistance. Reprinted with permission from <sup>[76]</sup> © 2017 Springer Nature. (b) Capacitive RH sensing. Higher RH in environment, more water captured by hygroscopic dielectric material (yellow layer), capacitance increases due to increase in dielectric constant. Reprinted with permission from <sup>[83]</sup> © 2017 American Chemical Society. Figure plate printed with permission from <sup>[233]</sup> © 2020 WILEY-VCH Verlag GmbH & Co. KGaA, Weinheim. ....	47
Figure 11:	Fiber-based RH sensors and RH sensing results (a) RSF fiber coated in MWCNTs/Ca <sup>2+</sup> /silk coating to provide RH response. Reprinted with permission from <sup>[76]</sup> © 2017 Springer Nature. (b) PET fiber coated in PVA sensing layer and Cu sputtered electrodes and corresponding response to RH. Reprinted with permission from <sup>[91]</sup> © 2017 Elsevier B.V. All rights reserved. (c) MWCNT yarn and graphical representation of resistance change with RH. Reprinted with permission from <sup>[92]</sup> © 2016 Elsevier B.V. All rights reserved. Figure plate printed with permission from <sup>[233]</sup> © 2020 WILEY-VCH Verlag GmbH & Co. KGaA, Weinheim. ....	51
Figure 12:	Sensor architecture and components (a) fabric-based distributed sensor network (b) schematic of fabric/thread-based parallel plate capacitor (c) silver threads at 40x magnification (d) SS threads at 40x magnification (e) SLS network produced with silver threads (f) SLS network produced with SS threads. Reprinted with permission from <sup>[20]</sup> ©2020 WILEY-VCH Verlag GmbH & Co. KGaA, Weinheim. ....	59
Figure 13.	Dielectric properties of the textile mediums and mechanical properties of the seam-line sensors (a) change in dielectric constant of a textile dielectric layer under strain (b) stress/strain behavior of the cotton-silver sample (c) stress/strain behavior and moduli of samples produced with SS yarns (d) stress/strain behavior and moduli of samples produced with silver yarns (e) moduli and mechanical hysteresis values calculated for each sample (shaded regions group fabric dielectrics to aid in sample comparison) (f) mechanical hysteresis of a representative sensor. Reprinted with permission from <sup>[20]</sup> ©2020 WILEY-VCH Verlag GmbH & Co. KGaA, Weinheim. ....	66
Figure 14.	Sensor properties (a) electromechanical response of the cotton-silver sample (b) electromechanical responses and sensitivities of samples produced with SS yarns (c) electromechanical responses and sensitivities of samples produced with silver polyamide yarns (d) hysteresis of a single representative pixel (e) sensitivity and electrical hysteresis values calculated for each sample (shaded regions group fabric dielectrics to aid in sample comparison). Reprinted with permission from <sup>[20]</sup> ©2020 WILEY-VCH Verlag GmbH & Co. KGaA, Weinheim. ....	71
Figure 15.	Dynamic response and response/relax time of seam-line sensors (a) dynamic response of cotton-silver samples (b) dynamic response of PET-silver samples (c) dynamic response of cotton Kraton-silver samples. (d) Response and (e) relaxation time of the cotton-silver sample for loading and unloading of ~50kPa (f) graphical representation of average response/relax times of each sample. Reprinted with permission from <sup>[20]</sup> ©2020 WILEY-VCH Verlag GmbH & Co. KGaA, Weinheim. ....	76

Figure 16.	Relative humidity sensing (a) RH test set up (b) capacitive pressure responses of cotton-silver samples at various humidity levels (c) capacitive pressure responses of PET-silver samples at various humidity levels (d) capacitive pressure responses of Kraton-silver samples at various humidity levels. Reprinted with permission from <sup>[20]</sup> ©2020 WILEY-VCH Verlag GmbH & Co. KGaA, Weinheim. ....	79
Figure 17.	Wetness sensing performance of the various samples tested. Sample pictures ~1m after DI water application is given as insets. Average absorption time is found at the lowest impedance response of the top and bottom yarn in the sample (N=3). (a) cotton-Silver (b) PET-Silver (c) Kraton-Silver (d) cotton-SS (e) PET-SS (f) Kraton-SS. Reprinted with permission from <sup>[20]</sup> ©2020 WILEY-VCH Verlag GmbH & Co. KGaA, Weinheim. ....	81
Figure 18.	Proof of concept demonstrations (a) pressure application on pressure sensing mat - row 5, column 2 (b) pressure application on pressure sensing mat - row 4, column 3 (c) pressure application on pressure sensing mat - row 3, column 4 (d) pressure application on pressure sensing mat - row 2, column 5 (e) pressure application on pressure sensing mat - row 1, column 6 (f-j) demonstration of drone being operated by a wearable sensor interface. Reprinted with permission from <sup>[20]</sup> ©2020 WILEY-VCH Verlag GmbH & Co. KGaA, Weinheim. ....	84
Figure 19:	Dissipation factor of the textile dielectrics under compressive straining. Reprinted with permission from <sup>[20]</sup> ©2020 WILEY-VCH Verlag GmbH & Co. KGaA, Weinheim. ....	93
Figure 20:	Stability of pressure sensing in 1,000-cycle tests. Silver thread samples with cotton (a) PET (b) and Kraton (c) dielectric materials. Stainless-steel thread samples with cotton (d) PET (e) and Kraton (f) dielectric materials. Capacitance differences are shown to highlight the response range changes. Reprinted with permission from <sup>[20]</sup> ©2020 WILEY-VCH Verlag GmbH & Co. KGaA, Weinheim. ....	93
Figure 21:	Stability of pressure sensing in 1,000-cycle tests. Silver thread samples with cotton (a) PET (b) and Kraton (c) dielectric materials. Stainless-steel thread samples with cotton (d) PET (e) and Kraton (f) dielectric materials. Capacitance is shown without baseline removal to highlight the baseline drift. Reprinted with permission from <sup>[20]</sup> ©2020 WILEY-VCH Verlag GmbH & Co. KGaA, Weinheim. ....	94
Figure 22:	Sensor architecture, system design, and integration (a) Schematic of fabric-based sensor array, showing fabric/thread-based parallel plate capacitor (figure adapted from <sup>[20]</sup> ) (b) Sensor arrays, interconnects, and ADC PCB (c) Data collection PCB with four shielded sensor arrays (d) SLS sensor placed within the ISE beneath the sock with the ADC PCB attached. The ADC PCB of each sensor is connected to the exterior data collection system using flexible cables. The data collected PCB is mounted to the exterior socket to minimize encumbrance. Reprinted with permissions from <sup>[21]</sup> ©2021 IEEE. ....	99
Figure 23:	Artificial limb testing set-up and results (a) Artificial limb (b) Artificial limb on supporting frame at neutral, L5, and R3 positions (c) Diagram of artificial	

	limb prosthetic components (d) Positions of sensor placement (e) Placement of SLS on the PT and PD. Comparative results of pressure distribution from nine sensing points (3x3) of the Pliance <sup>®</sup> and SLS arrays placed at the (f) PT, and (g) PD. The baseline capacitance data for the SLS at the neutral position was removed from the capacitance recordings. The Pliance <sup>®</sup> sensor is unable to detect pressures <15kPa, and therefore some sensing points showed no response throughout the experiment. Reprinted with permissions from <sup>[21]</sup> ©2021 IEEE.....	105
Figure 24:	Able-bodied testing using a bent-knee adapter (a) Bent-knee adapter (b) Able-bodied participant wearing bent-knee adapter (c) Placement of SLS on the anterior location on top of the prosthetic liner (d) Weight shifting experiment - participant stances (e) Change in capacitance of the nine texels during bodyweight shifting experiments (f) Average capacitance change during bodyweight shifting experiments. For the weight shifting experiments, the neutral stance was considered as the baseline and was removed from the general capacitance profile. (g) Dynamic walking experiment (h) Change in capacitance and GRF during walking experiments. For the walking experiments, the minimum capacitance value during the walking trials (i.e., while the bent-knee adapter was unloaded) was taken as the baseline and removed from the response. Reprinted with permissions from <sup>[21]</sup> ©2021 IEEE.....	108
Figure 25:	Amputee testing (a) SLS placed at the PT and PD (b) Weight shifting - participant stances. Average capacitance change during bodyweight shifting experiments at the (c) PT and (d) PD. For the weight shifting experiments, the neutral stance was considered as the baseline and was removed from the general capacitance profile. Reprinted with permissions from <sup>[21]</sup> ©2021 IEEE.....	112
Figure 26:	Amputee testing results (a) Participant walking on a treadmill. The average change in capacitance and GRF at the (b) PT and (c) PD (d) Texel response at PT during walking. For the walking experiments, the minimum capacitance (i.e., while the prosthesis was unloaded) was taken as the baseline and removed from the capacitance response. Reprinted with permissions from <sup>[21]</sup> ©2021 IEEE.....	114
Figure 27:	TME fibers shape and sensor structure (a) TME fiber with sacrificial polymer (b) BiSoFT after removal of the sacrificial polymer and (c) BiSoFT woven into a fabric configuration with each individual texel formulating a capacitive sensor (d) Texel architecture compared to a parallel plate capacitor.....	121
Figure 28:	Results of thermal polymer characterization (a) DSC (b) MFR (c) TGA.....	125
Figure 29:	TME set-up (a) Schematic of melt extrusion line for extruder B/polymer B (b) Schematic representation of extrusion line with winding completed directly after air quenching (c) Schematic representation of extrusion line with winding completed after both air and water bath quenching.....	126
Figure 30:	Cross sectional images and dimensional analysis of the fibers (a) FR 60:25:15 (b) FR 60:25:15 with PLA removed (c) FR 60:25:15 dimensional analysis (d) FR 50:40:10 (e) FR 50:40:10 with PLA removed (f) FR 50:40:10	

	dimensional analysis (g) FR 50:40:10 with DR:1.6 (h) FR 50:40:10 with DR:2.2.....	132
Figure 31:	Tensile properties of TME fibers (a) FR 60:25:15, inset shows microscopic image of final fiber breakage (b) FR 50:40:10 undrawn (c) Microscopic image of FR 50:40:10 undrawn fiber breakage. Image demonstrates that PLA breaks prior to InPA6 and CoPA6 segments (d) FR 50:40:10 post-drawing with a DR of 1.6 (e) FR 50:40:10 post-drawing with a DR of 2.2 (f) Comparison of tensile properties of undrawn and drawn 50:40:10 fibers.....	134
Figure 32:	Electromechanical properties of BiSoFT (a) Mechanical behavior of a 60:25:15 texel when exposed to five compression cycles of ~20% strain (b) Electrical resistance fibers produced with different FRs and DRs (c) Capacitive response of texel to five compression cycles of ~20% strain (d) Comprehensive view of the texel's electrical and mechanical response to stain application (e) $C_m$ between the fibers within a texel (f) Electric field generated by texel (g) $C_p$ generated when object, such as finger, approaches the texel (h) Shunting of electric field when object approaches texel.....	138
Figure 33:	Tricomponent melt extruded fiber cross-sectional images. Extruder A: PP+orange PP, Extruder B: PP+blue PP, Extruder C: plain PP at FRs (a) 70:20:10 (b) 60:30:10 and (c) 60:25:15. Extruder A:In PA6 +red PA6, Extruder B: neat InPA6, Extruder C: PLA at FRs (d) 70:20:10 (e) 60:30:10 and (f) 60:25:15 .....	143
Figure 34:	Tricomponent melt extruded fiber cross-sectional images and dimensional analysis. Extruder A: CoPA6, Extruder B: InPA6, Extruder C: PLA. (a) FR 70:20:10 (b) FR 70:20:10 (with PLA removed) (c) FR 70:20:10 dimensional analysis (d) FR 60:30:10 (e) FR 60:30:10 (with PLA removed) (f) FR 60:30:10 dimensional analysis (g) 60:25:15 (h) FR 60:25:15 (with PLA removed) (i) FR 60:25:15 dimensional analysis (j) FR 50:40:10 (k) FR 50:40:10 with PLA removed (l) FR 50:40:10 dimensional analysis .....	144
Figure 35:	Schematics of winding/quenching set-ups (a) The normal extrusion set up with quench bath on floor, ~3m from spin-pack exit (b) Elevated bath set up to reduce spin-pack exit to bath distance to ~1m.....	145
Figure 36:	Schematic of drawing set-up .....	145
Figure 37:	Schematics of BiSoFT fiber electrical testing (a) Fiber resistance measurement set-up using multimeter (b) Pressure sensing set-up. PCB is connected to LCR via BNC cables .....	146
Figure 38:	TME fibers shape and sensor structure (a) TME fiber with sacrificial polymer (b) BiSoFT after removal of the sacrificial polymer and (c) BiSoFT woven into a fabric configuration with each individual texel formulating a capacitive sensor (d) sensing pixel formed at texel compared to a parallel plate capacitor (e) TME fiber cross sectional images with sacrificial polymer and (f) after removal of sacrificial polymer .....	151
Figure 39:	BiSoFT texels and their mechanical properties (a) (3x3) texel (b) schematic of (3x3) texel (c) schematic of texel connection to capacitance printed circuit board (PCB) (d) mechanical compressive behavior of a (1x1) texel when compressed to 20% strain .....	152
Figure 40:	Initial electromechanical results (a) electrical and mechanical behavior of a (1x1) fiber texel when compressed to 20% strain (b) a detailed view of the	

	fifth cycle of electrical and mechanical behavior of a (1x1) fiber texel when compressed to 20% strain (c) electrical and mechanical behavior of a (3x3) fiber texel when compressed to 20% strain (d) a detailed view of the fifth cycle of electrical and mechanical behavior of a (3x3) fiber texel when compressed to 20% strain (e) $C_m$ between fibers of texel (f) electric field generated by texel (g) image of $C_p$ generated when object, such as finger, approaches the texel (f) shunting of electric field when object approaches texel ..... 155	155
Figure 41:	(a) comparison of capacitive response of (1x1), (3x3), and (5x5) texels when compressed to 20% strain (b) a detailed view of the fifth cycle of the capacitive response of (1x1), (3x3), and (5x5) texels when compressed to 20% strain (c) expected versus measured response of (1x1), (3x3), and (5x5) texels (d) BiSoFT fiber dimensions determined via optical microscopy ..... 157	157
Figure 42:	Further electromechanical characterization of (3x3) BiSoFT texel (a) capacitive and mechanical response during 100 cycles of 20% strain cycling (b) first and (c) last five cycles of capacitive and mechanical response during 100 cycles of 20% strain cycling (d) five cycles of holding 20% strain for one minute, and then releasing the strain for one minute (e) a detailed view of a single cycle of holding 20% strain for one minute, and then releasing the strain for one minute 159	159
Figure 43:	BiSoFT pressure mat demonstration (a) woven BiSoFT mat and nomenclature (b) variation in the texels' response with 10 and 50 g weight application (c) $\Delta C$ scale for heat maps in pF. Capacitive response ( $\Delta C$ ) of R1C1 to (d) 10g and (e) 50g weight application. Capacitive response ( $\Delta C$ ) of R8C8 to (f) 10g and (g) 50g weight application. Capacitive response ( $\Delta C$ ) of texels when (h) square and (i) triangle shaped object applied to multiple texels. .... 161	161
Figure 44:	Initial results of SLSs integrated into compression sleeve (a) a 10x10 SLS array integrated into a compression sleeve. The response of the (b) upper right texel (c) upper left texel (d) the lower right texel (e) the lower left texel..... 167	167

## 1 Introduction

Many amputees depend on artificial devices, such as prosthetics, to restore function to their amputated limb. Unfortunately, the majority of amputees express moderate to severe pain when wearing their prosthetic devices.<sup>[7-9]</sup> To better understand sources of discomfort, researchers have primarily studied the ISE using commercially available, rigid sensors which are fabricated from semiconducting materials. While these sensors provide valuable information regarding the ISE, they are generally disadvantageous due to their bulkiness,<sup>[10]</sup> weight,<sup>[11, 12]</sup> inflexibility,<sup>[11, 12]</sup> low spatial resolution,<sup>[13]</sup> cost,<sup>[14, 15]</sup> and laborious integration methods.<sup>[16]</sup> Further, rigid sensors are uncomfortable for amputees during use<sup>[17]</sup> and irritate the user's skin.<sup>[18, 19]</sup> Many of the shortcomings associated with currently available ISE monitoring systems could be significantly improved using textile-based sensors which have yet to be explored for ISE monitoring. Here, I propose two approaches to creating textile-based sensing that could be utilized for ISE monitoring. Both approaches focus on maintaining the inherent properties of textiles, such as good flexibility and comfort, while also being produced using scalable techniques relevant to current textile manufacturing. Additionally, I propose two custom set-ups which can be used to evaluate the textile-based sensors in simulated prosthetic environments.

This dissertation consists of eight Sections. In Section 2, a literature review is provided which first introduces the common components of lower limb (LL) prosthetics, the sources of discomfort within the ISE, and how/why sensors are incorporated within the ISE. Subsequently, the literature review transitions into an overview of textile-based sensors including common materials, fabrication methods, sensing modes, and why textile-based sensors would be beneficial for ISE monitoring. In Sections 4-7, my research contributions are provided. These sections consist of four research articles: two have been published<sup>[20, 21]</sup> and two are in the publication process. It

is important to note that these research articles were written as stand-alone documents intended for separate publication, and therefore, some information and figures may be repeated.

Section 4, an article published in *Advanced Materials Technologies*, explores the seam-line sensing approach in which conductive yarns are sewn into fabrics to create capacitive sensors.<sup>[20]</sup> This publication provides an overview of the sensing architecture, material selection, fabrication method, and sensing performance. Section 5, an article published in *IEEE Sensors Journal*, demonstrates the ability of the seam-line sensors to sense pressure within the ISE.<sup>[21]</sup> This publication provides an overview of the sensing system specifically designed for ISE monitoring, custom test set-ups to prepare for human testing, as well as results of amputee participant testing.

Sections 6 and 7 introduce a different sensing approach in which uniquely-shaped fiber sensors, produced via melt extrusion, are organized into woven configurations to create capacitive sensors. Section 6 is an article which focuses on the process used to produce the uniquely-shaped fibers, tricomponent melt extrusion, including material selection/characterization, process development, as well as initial electrical, mechanical, and pressure-sensing capabilities of the fibers. Finally in Section 7, the sensing performance of the uniquely-shaped fibers is studied in detail. This dissertation concludes with Section 8 which provides a summary of my research contributions and suggestions for future work.

## **2 Review of Literature**

Amputation is one of the major causes of disability with approximately 1.7 million people living with limb loss in the U.S. alone. This number is expected to increase to 3.4 million by 2050 as the population ages and the occurrence of dysvascular disease increases.<sup>[1]</sup> Many amputees depend on artificial devices, such as prosthetics, to restore motor function to their amputated region.

Unfortunately, the majority of amputees express moderate to severe pain when wearing their prosthetic devices.<sup>[7-9]</sup>

While wearing a prosthesis, an amputee's residual limb is exposed to an uncomfortable environment of stress<sup>[8, 22]</sup>, increased moisture (entrapment of sweat)<sup>[2, 19, 23]</sup> and temperature.<sup>[3, 5, 24]</sup> Excessively high stress at the residual limb/prosthetic interface is not desired as it can cause pressure ulcers which can be debilitating,<sup>[25]</sup> require further amputation,<sup>[26]</sup> or result in life-threatening deep tissue injuries.<sup>[25]</sup> Skin irritation issues are amplified by elevated skin temperatures and excessive perspiration within the prosthetic socket<sup>[3, 19, 27]</sup> with evidence suggesting blisters form more quickly in hot, moist environment.<sup>[24]</sup> Skin irritation and pain can become so severe that amputees are no longer able to wear their prosthetics.<sup>[22, 28-31]</sup>

Despite recent advances in prosthetic technologies, many amputees express low satisfaction with their prosthetic devices mainly due to socket-related issues.<sup>[9, 22]</sup> Skin lesions occur in ~63% of LL amputees resulting ~25% of amputees reducing use of their prosthetic.<sup>[32]</sup> New prosthetic technologies are necessary to construct comfortable, well-fitted liners and sockets<sup>[2-5]</sup> but an established issue in the development of new prosthetic technology is the lack of practical, accurate, inner socket sensors to monitor the inner socket environment (ISE), or the region between the residual limb and the socket (see Section 2.2). Further, it is necessary to provide tools for care providers to help quantify parameters influencing prosthetic discomfort.<sup>[33, 34]</sup> Currently, care providers analyze the ISE utilizing subjective feedback from amputees, physical examinations, or by placing powder, lipstick or clay in sockets to assess socket contact.<sup>[35, 36]</sup> Quality of the prosthetic fit is heavily dependent on the clinician's intuition and experience.<sup>[37, 38]</sup> Such methods are inaccurate and subject to large variation.

Researchers have studied the ISE primarily using commercially available, rigid sensors such as strain gauges (SGs),<sup>[17, 39-45]</sup> thermistors,<sup>[5, 19, 24, 46, 47]</sup> and thermocouples<sup>[18]</sup> utilizing hard, semiconducting materials. While these sensors provide valuable information regarding the ISE, they are generally disadvantageous due to their bulkiness,<sup>[10]</sup> weight,<sup>[11, 12]</sup> inflexibility,<sup>[11, 12]</sup> low spatial resolution,<sup>[13]</sup> cost,<sup>[14, 15]</sup> and laborious integration methods.<sup>[16]</sup> Further, rigid sensors are uncomfortable for amputees during use<sup>[17]</sup> and irritate the user's skin.<sup>[18, 19]</sup> Many of the shortcomings associated with currently available ISE monitoring systems could be significantly improved using textile-based sensor for measuring stress,<sup>[48-68]</sup> temperature,<sup>[69-88]</sup> or moisture.<sup>[76, 79, 83-87, 89-93]</sup>

In subsequent sections, the prosthetic components commonly used in LL, specifically transtibial, prosthetics will be described. Issues related to the ISE and the sensors commonly employed to study the ISE will be discussed. Finally, fiber and textile based sensors which may be useful for monitoring the ISE will be reviewed including materials, fabrication, modes of sensing and commonly cited sensing parameters.

## **2.1 Prosthetic Components**

Transtibial prosthetic systems consist of the prosthetic device and suspension method. The prosthetic device consists of several components including the foot, pylon, socket and the products worn beneath the socket including the liner, liner-liner, and socks. These components are shown schematically in Figure 1. Prosthetic systems also consist of a suspension system, which is the method of maintaining a connection between the residual limb and the prosthetic device. The following sections provide a brief introduction into the most common components of a prosthetic device.

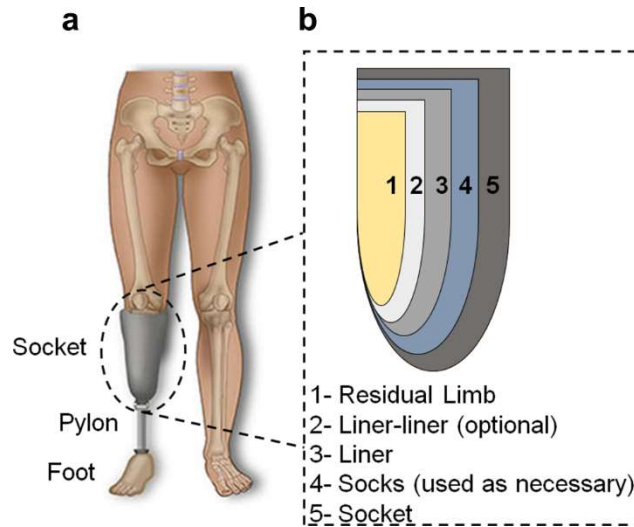


Figure 1: Prosthetic components (a) Socket, pylon and foot<sup>[94]</sup> (b) Cross-sectional view of layers worn beneath the socket

### 2.1.1 Liner-liner

A liner-liner is a thin knitted textile that may be worn beneath the prosthetic liner. The construction of the liner-liner is similar to a prosthetic sock; however, liner-liners are relatively thin compared to socks. Liner-liners are used to keep the limb cooler and drier by absorbing excess sweat. When saturated, the liner-liner may be removed and replaced to maintain comfort throughout the day. Liner-liners are made from materials including PET/spandex blends.

### 2.1.2 Liner

The prosthetic liner is a critical component of the prosthetic device. The liner serves as an interface between the delicate tissues of the residual limb and the rigid socket.<sup>[23, 95]</sup> Prosthetic liners serve two primary functions: protecting the residual limb and coupling the limb to the prosthetic.<sup>[95]</sup> Liners are often energy-absorbing, cushioning materials<sup>[23, 96]</sup> which interact directly with the skin and play a significant role in transferring load and distributing interface pressure over the residual limb.<sup>[23, 97, 98]</sup>

It is estimated that 85% of transtibial amputees use elastomeric liners.<sup>[99]</sup> Elastomeric liners are preferred as they provide improved suspension, cushioning,<sup>[23]</sup> pressure distribution, shock absorption compared to foam liners while also minimizing shear forces.<sup>[100]</sup> However, elastomeric liners are also relatively expensive and tend to increase the weight of the prosthetic system.<sup>[100]</sup> Many variations of elastomeric liners exist with more than sixty products on the market.<sup>[99]</sup> Elastomeric liners are primarily made from silicone, polyurethane (PU), or thermoplastic elastomer gel.<sup>[101]</sup> Liner materials are produced in various thicknesses typically in the range of 3-5mm. Liners produced by Ossur, Alps, Ottobock, and Willow Wood are most commonly used.<sup>[95]</sup> The proper liner for a patient is selected based on their limb shape, tissue quality, socket design, anticipated volume change, and activity level.<sup>[99]</sup> However, there is little scientific evidence that informs prosthetic liner prescription. Clinicians typically rely on personal intuition and experience to select the appropriate liner.<sup>[96]</sup> However, the liner selection process is critical with improper liner selection leading to issues such as pistoning, skin issues, misuse of the prosthetic, as well as reduced patient activity.<sup>[96]</sup>

### **2.1.3 Socks**

Prosthetic socks may be worn over prosthetic liners to accommodate residual limb volume changes which hard, plastic sockets are unable to adapt to.<sup>[100]</sup> Throughout the day, an amputee's residual limb may change dimensionally and cause the amputee discomfort. To maintain proper socket fit and compensate for volume changes, many amputees don/doff prosthetic socks throughout the day.<sup>[22]</sup> Socks are made in a variety of sizes and lengths to accommodate for differences in residual limb circumference and length. Socks are typically knit structures composed of a mixture of materials including cotton, polyamide (PA), wool, polyester (PET), and spandex.<sup>[36]</sup>

#### **2.1.4 Socket**

The socket is the most critical component of a transtibial prosthetic device. A socket serves as the connection or interface between an amputee's residual limb and their prosthetic foot.<sup>[102]</sup> Socket design significantly impacts quality of prosthetic fit<sup>[103]</sup> as well as amputees' comfort, mobility, and level of satisfaction with their prosthetic.<sup>[12, 23, 104, 105]</sup> The socket should provide an interface between the amputee and prosthesis without compromising comfort.<sup>[102, 106]</sup> If a prosthetic socket fits properly, effective transfer of forces from the socket to the residual limb should be achieved such that an amputee can complete daily activities without tissue damage or pain.<sup>[22]</sup> Similarly, forces from the limb, which are needed to control the motion of the prosthetic, should be transferred to the prosthetic via the socket.<sup>[36]</sup>

Evaluating the fit of prosthetic sockets is critical, particularly for transtibial amputees who often suffer from sensory impairment. Therefore, many amputees are not able to fully feel their residual limb making them prime candidates for abrasions, skin ulcers, and infection. Currently, evaluating the fit of prosthetic devices requires great attention, training, and practical experience<sup>[36]</sup> and evaluation techniques are subjective.

#### **2.2 The Inner Socket Environment**

The ISE, or the region between the residual limb and socket, is complex and making it comfortable for an amputee can be challenging. One inherent issue within the ISE is that the amputees' entire body weight must be tolerated by the interface of the residual limb tissues and the prosthetic socket. These tissues are not typically subjected to such intensive magnitudes of normal and shear stress.<sup>[12, 22]</sup> Excessively high stress at the residual limb/prosthetic interface is not desired as it can cause pressure ulcers which can be debilitating,<sup>[25]</sup> require further amputation,<sup>[26]</sup> or result in life-threatening deep tissue injuries.<sup>[25]</sup> Skin irritation and pain can become so severe that amputees are

no longer able to wear their prosthetics.<sup>[22, 28-31]</sup> Conversely, excessively low pressures are also undesirable as they can lead to instability and tissue damage from abrasion caused by excessive socket movement.<sup>[107]</sup>

Additionally, the length,<sup>[106]</sup> size and shape of each person's residual limb varies<sup>[22, 25, 106]</sup> which makes it difficult for prosthetists to optimize the socket fit and design.<sup>[108]</sup> Further, residual limbs are non-homogeneous consisting of bones, muscle, fat and skin thus leading to complex pressure distributions which cause formation of painful blisters and ulcers.<sup>[108]</sup> Prosthetists strive to regulate stump-socket interface stress distributions through liner and socket selection, as well as prosthetic alignment.<sup>[17]</sup> However, the prosthetic device selection process is heavily based on the judgement and experience of prosthetists.<sup>[17]</sup> Additional complications within the ISE arise due to short and long-term residual limb volume fluctuations which negatively impact socket fit.<sup>[22, 109]</sup> Day-to-day and long-term volume fluctuations can occur.<sup>[44]</sup> Thirty minutes of walking can reportedly result in an average limb volume gain of 3.7% or volume loss of 6.4% depending on the socket type.<sup>[109]</sup> As a result of limb volume fluctuations a socket design that is favorable at one time might not be favorable later that same day or weeks later.<sup>[44]</sup>

The treatment of amputee discomfort remains challenging. When amputees express discomfort to their care provider, the most common modes of clinical inspection are empirical, via visual and verbal assessments.<sup>[110]</sup> These methods of treatment are often time consuming and costly.<sup>[110]</sup> Overall, the ISE is complex, difficult to quantify, and not well understood. Subsequent sections will review the efforts completed to develop a better understanding of the ISE.

### **2.3 Sensors for the Inner Socket Environment Monitoring**

To better understand the ISE, researchers have primarily utilized commercial, semi-conductor based sensors. While as temperature<sup>[5, 18, 19, 24, 27, 46, 47]</sup> and relative humidity (RH)<sup>[27]</sup> have been

measured within the ISE, most efforts have been focused on measuring normal stresses within the socket.<sup>[11, 12, 22, 23, 26, 39-44, 106, 111-121]</sup> which will be the focus of this discussion. Monitoring prosthetic interfacial stresses is useful as it can provide valuable information regarding quality of socket fit/comfort<sup>[108, 117, 122]</sup> and can guide clinicians and researchers to improve socket design and fit.<sup>[122, 123]</sup>

### **2.3.1 Stress Sensing Mechanisms**

A sensor is a device that measures a certain stimulus and converts that stimulus to a measurable output.<sup>[124]</sup> A sensor therefore detects an input signal or energy and converts to the appropriate output or energy.<sup>[124]</sup> The input signal or measurand may be chemical, electrical, magnetic, mechanical, thermal, etc. while the output signal may again be chemical, electrical, magnetic, mechanical, thermal, etc. <sup>[124]</sup>

Stress sensing within prosthetics has been widely researched and several relevant reviews are available.<sup>[10, 13, 108, 125, 126]</sup> Various types of commercial sensors have been used to measure interfacial stresses including SGs,<sup>[17, 39-45]</sup> the F-Socket by Tekscan<sup>[23, 26, 113-118]</sup> and other types of force sensing resistors (FSR's)<sup>[22, 106]</sup> all of which are piezoresistive sensors, as well as the Pliance system by Novel<sup>[110, 112, 127]</sup> which operates via capacitive sensing. The working configurations and working principles of these sensors will be described in subsequent sections.

#### **2.3.1.1 Piezoresistive Stress Sensors**

Piezoresistive sensors undergo a change in electrical resistance when subjected to an external deformation.<sup>[66, 128]</sup> During the operation of piezoresistive sensor, voltage (or current) is fixed while resistance change is observed by a change in current (or voltage)<sup>[129]</sup> which is then calibrated into units of force or pressure.<sup>[107]</sup> The electrical resistance (R) of a prismatic bar can be expressed in terms of its bulk resistivity ( $\rho$ ), and dimensions,  $R = \frac{\rho x l}{A}$  where  $l$  is length, and  $A$  is the cross-

sectional area of the bar, see Figure 2a. Changes in resistance due to applied stresses may a result of geometrical changes in the resistors  $A$  or  $l$ . While the resistivity of a materials is its intrinsic property, for certain types of piezoresistive materials (e.g., conductive composites) changes in resistance due to applied stresses may be a result of changes in a material's  $\rho$ . When considering homogeneous materials,  $\rho$  is invariant therefore, the piezoresistive behavior for homogeneous materials is derived from the changes in resistor geometry ( $A$ , and  $l$ ) as shown in Figure 2a.

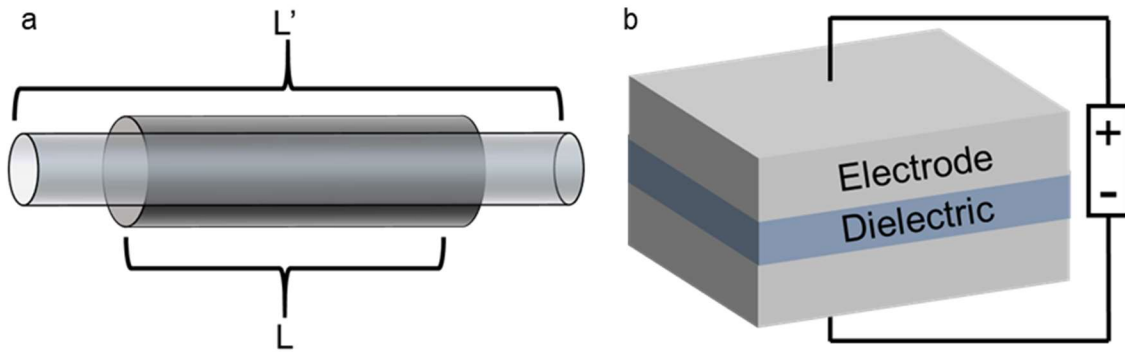


Figure 2: Sensor schematics (a) Resistive sensing modality (b) Parallel-plate capacitor

SGs are the most common form of piezoresistive sensors. The sensing component of SGs typically consists of small patches of silicon or metal<sup>[10]</sup> capable of measuring normal stresses with high accuracy and sensitivity.<sup>[130]</sup> There are two types of SGs which have been used to monitor the ISE: diaphragm deflection and piston-type transducers.<sup>[45, 131]</sup> While SGs are advantageous due to their high sensitivity and accuracy, they are generally bulky thus adding weight to prostheses and negatively affecting accuracy of interface pressure measurements.<sup>[10]</sup> When in use, areas between SG transducer sites are dismissed which results in poor spatial resolution.<sup>[13]</sup> Additionally, these devices have little use in clinical situations, as they require excessive power to operate.<sup>[132]</sup>

Another form of piezoresistive sensors used for monitoring the ISE are known commercially as FSRs. Compared to SGs, FSRs are generally considered more suitable for in-situ positioning within the prosthetic socket.<sup>[10]</sup> FSRs are preferred for inner socket monitoring, as they

are thin, possess small profiles, relatively good flexibility, desirable sensitivity, low cost, and relatively simple structures.<sup>[107, 133, 134]</sup> Additionally, FSRs can be produced in many different shapes and sizes. However, FSRs are known to be sensitive to many sources of error including drift and sensor-to-sensor variability.<sup>[107]</sup> FSR devices are made from a pressure sensitive material often in the form of an elastomer, conductive ink, conductive rubber, or carbon fiber.<sup>[129]</sup> These pressure sensitive materials are placed between two layers of flexible PET film and adhesively bonded to form the piezoresistive pressure sensor.<sup>[129]</sup> The resistivity of the pressure sensitive material changes when force is applied unlike SGs whose resistance changes solely due to shape deformation.<sup>[15]</sup>

The F-Socket by Tekscan is the most commonly used FSR for measuring LL prosthetic interface pressures.<sup>[23, 26, 113-118]</sup> This product contains an array of sensors formed with vertical and horizontal piezoresistive traces. The F-socket consists of sixteen rows and six columns to produce a total of ninety-six individual sensing points at<sup>[10]</sup> which can measure pressures between 0-517 kPa.<sup>[23]</sup> However, this product suffers from sensor drift, temperature sensitivity, hysteresis and provides a low frequency response.<sup>[10, 118]</sup> Additionally, while this system does not require socket modification, it is spatially limited, cannot be readily integrated into existing prosthetic components, and leaves room for improvement in flexibility and breathability desirable for long-term use.

### **2.3.1.2 Capacitive Stress Sensors**

Capacitive sensors consist of a dielectric layer sandwiched between conductive surfaces called electrodes, as shown in Figure 2b. Electrodes may be oriented in different configurations including parallel plate and interdigitated. Ideally, capacitive sensors should be designed with large-area conductive plates with a narrow distance between the plates.<sup>[124]</sup> This provides a highly sensitive

sensor without compromising accuracy and reproducibility of the sensor.<sup>[124]</sup> When a voltage is applied to a capacitor, charges accumulate on the two electrodes, while the dielectric layer prevents current flow.<sup>[128]</sup> Hence, a capacitive signal is generated, which is subsequently measured. The capacitance,  $C$ , of a parallel plate capacitor, with electrode area  $A$ , and electrode separation  $d$ , can be expressed as  $C = \frac{A\epsilon_0\epsilon_r}{d}$  where the constant  $\epsilon_0$  is the permittivity of free space ( $8.854 \cdot 10^{-12}$  F/m). Simply put, capacitive sensors are designed to undergo a change in any of the three parameters, distance ( $d$ ) between or area of the electrodes ( $A$ ), and the dielectric constant of the medium ( $\epsilon_r$ ) in the presence of a stimulant.<sup>[135]</sup> In general, capacitive sensors provide higher sensitivity, lower temperature dependency, more robust structure, lower power consumption, better frequency response, and a larger dynamic range than piezoresistive devices.<sup>[14, 15, 129]</sup> However, capacitive sensors are susceptible to crosstalk noise, so they may require more sophisticated electronics to filter out unwanted noise.<sup>[14, 15, 129]</sup>

The Pliance by Novel has been used by several researchers to measure normal stresses within the ISE.<sup>[110, 112, 127]</sup> This sensor system contains ninety-six capacitive sensors mounted in a silicon substrate. While this system does not require socket modification, it is spatially limited, cannot be readily integrated into existing prosthetic components, and leaves room for improvement in flexibility and breathability desirable for long-term use.

### **2.3.2 Monitoring Stress within the Inner Socket Environment**

Measuring interface stresses within prosthetics has been widely researched and several relevant reviews are available.<sup>[10, 13, 108, 125, 126]</sup> Some of the earliest work in this field was by Appoldt<sup>[136]</sup> and Pearson<sup>[41]</sup> in 1967 and 1973 who measured normal stresses within the ISE. Shear sensing within LL prosthetics was pioneered by Sanders<sup>[17, 43, 137]</sup> in the 1990's. Since these initial efforts, many have continued studying normal and shear stresses within the ISE.<sup>[22, 26, 39, 40, 42, 43, 106, 114-116,</sup>

<sup>118]</sup> Studies utilizing commercial pressure sensors for LL prosthetics were largely focused on providing a better understanding of the pressure distribution within prosthetic sockets. Researchers studied differences in pressure distributions when using different sockets,<sup>[22, 42, 106, 118, 120, 121]</sup> liners,<sup>[23, 26, 45]</sup> and suspension systems.<sup>[114]</sup> Alternatively, pressure measurements were utilized to validate FE modeling,<sup>[17]</sup> monitor changes in pressure and limb volume with time,<sup>[44]</sup> analyze the effect of prosthetic alignment on pressure distributions,<sup>[40]</sup> provide a better understanding of the factors that influence fit,<sup>[45]</sup> study how amputees navigate ramps or stairs,<sup>[112, 114]</sup> or for sensor validation.<sup>[11]</sup>

Normal pressure and shear stresses within the ISE have been studied utilizing various types of commercially available sensors including SGs<sup>[17, 39-45]</sup> or load cells<sup>[119]</sup> mounted to prosthetic sockets, see Figure 3a and b. Additionally, many efforts have been completed with the commercial F-Socket by Tekscan (shown in Figure 3c),<sup>[23, 26, 113-118]</sup> FSRs,<sup>[22, 106]</sup> and the Pliance system by Novel (shown in Figure 3d).<sup>[110, 112, 127]</sup>

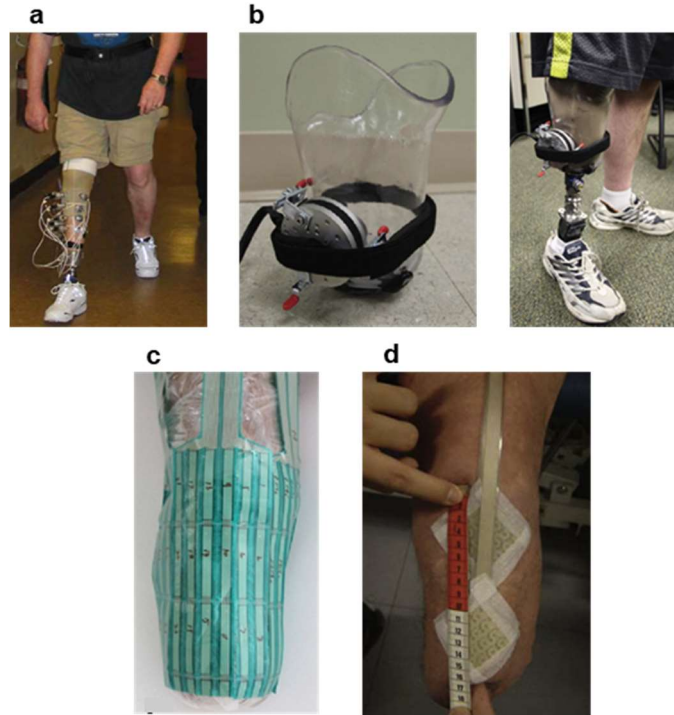


Figure 3: Commercial sensors used to measure LL prosthetic stress distributions (a) SGs mounted to prosthetic socket. Reprinted with permission from<sup>[44]</sup> © 2004 Elsevier Ltd. All rights reserved. (b) Load cell instrumented onto socket. Reprinted with permission from<sup>[119]</sup> © 2019 IPEM. Published by Elsevier Ltd. All rights reserved. (c) F-socket by Tekscan attached to residual limb. Reprinted with permission from<sup>[23]</sup> © 2012 Elsevier Ltd. All rights reserved. (d) Pliance by Novel attached to residual limb (Reprinted with permission from<sup>[127]</sup> © 2009 Elsevier Ltd. All rights reserved.)

Various approaches to incorporating pressure sensors into LL prosthetics have been explored. Researchers using SGs or load cells drilled holes in subjects' sockets and then mounted the sensor outside the socket, as shown in Figure 3a and b, such the sensing area was flush with the subjects' residual limb, sock, or liner.<sup>[11, 17, 39-44, 119-121]</sup> Therefore, this approach provided an understanding of pressure distributions at the limb/socket,<sup>[11, 41]</sup> liner/socket,<sup>[17, 43, 119]</sup> or sock/socket<sup>[39, 40, 42, 44, 120, 121]</sup> interface depending on whether a liner, sock, or neither is worn by the subject. FSR's were attached to liners to measure the liner/socket interface<sup>[22]</sup> or the socket to measure the liner/socket interface.<sup>[106]</sup> F-socket sensors were attached to the limb<sup>[23, 110, 116, 117, 127]</sup> using tape to measure the limb/liner interface<sup>[23, 110, 117, 127]</sup> or limb/socket interface.<sup>[116]</sup> Alternatively, the F-socket was attached to the internal portion of the socket using spray adhesive

to measure the limb/socket interface<sup>[115]</sup> or, researchers wrapped subjects' limbs in plastic wrap and then attached the F-socket using adhesive spray thus providing interfacial pressure measurements of the plastic/liner interface (see Figure 3c).<sup>[26, 113, 114]</sup> The Pliance Novel was taped to the residual limb, as shown in Figure 3d, to measure the limb/liner interface<sup>[110, 127]</sup> or placed between the liner and socket to measure the liner/socket interfacial pressure.<sup>[112]</sup>

Previous studies were primarily focused on measuring normal stresses<sup>[22, 23, 41, 42, 45, 106, 116-118, 120, 121]</sup> however some measured both normal and shear pressures utilizing SGs.<sup>[11, 40, 43, 44, 119]</sup> The normal pressures and shear stresses levels measured with commercial sensors are shown in Figure 4a and Figure 4b respectively. Normal pressure at patellar tendon can reach peak pressures of 300-400 kPa.<sup>[41, 122, 138]</sup> however, as shown in Figure 4a, most measured normal pressures range from ~0-150 kPa. This is supported by literature which claims peak pressures in well-designed sockets which properly distribute pressure are typically less than 200 kPa.<sup>[22, 43, 139]</sup> Alternatively, shear stresses within the prosthetic environment were typically reported in the range of ~0-50kPa. As shown in Figure 4a and Figure 4b, normal and shear stresses within the ISE can vary widely likely due to the fact that interface pressure is significantly affected by task, location on the residual limb, socket alignment, type of socket, liner type, suspension type, etc.<sup>[114, 140, 141]</sup>

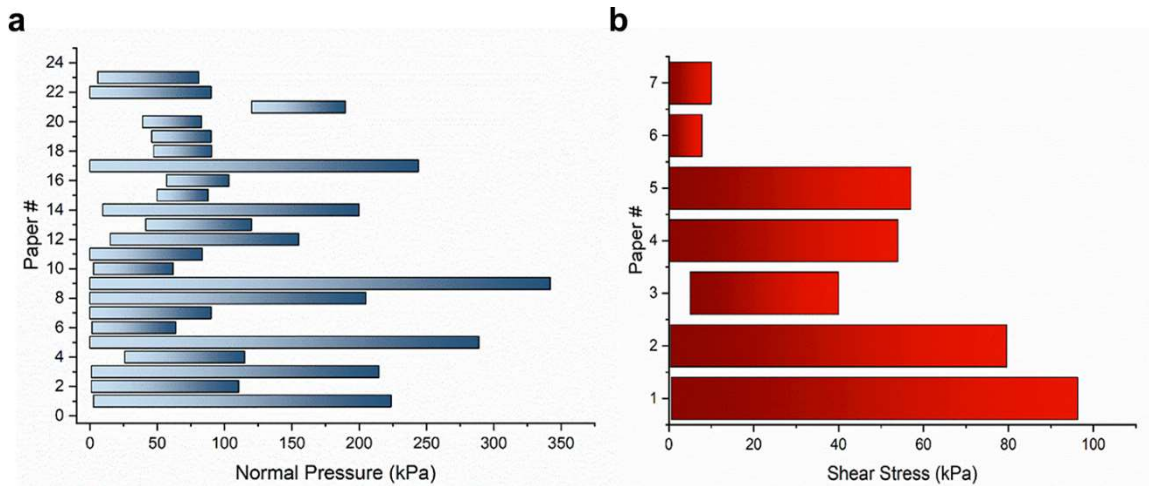


Figure 4: Normal and shear stresses reported within the ISE (a) Normal pressure ranges reported in literature (Paper 1,<sup>[39]</sup> Paper 2,<sup>[121]</sup> Paper 3,<sup>[40]</sup> Paper 4,<sup>[11]</sup> Paper 5,<sup>[41]</sup> Paper 6,<sup>[120]</sup> Paper 7,<sup>[42]</sup> Paper 8,<sup>[43]</sup> Paper 9,<sup>[44]</sup> Paper 10,<sup>[119]</sup> Paper 11,<sup>[22]</sup> Paper 12,<sup>[106]</sup> Paper 13,<sup>[118]</sup> Paper 14,<sup>[117]</sup> Paper 15,<sup>[23]</sup> Paper 16,<sup>[116]</sup> Paper 17,<sup>[115]</sup> Paper 18,<sup>[26]</sup> Paper 19,<sup>[114]</sup> Paper 20,<sup>[113]</sup> Paper 21,<sup>[112]</sup> Paper 22,<sup>[12]</sup> Paper 23<sup>[111]</sup>) (b) Shear stress ranges reported in literature (Paper 1,<sup>[39]</sup> Paper 2,<sup>[40]</sup> Paper 3,<sup>[17]</sup> Paper 4,<sup>[43]</sup> Paper 5,<sup>[44]</sup> Paper 6,<sup>[119]</sup> Paper 7<sup>[12]</sup>)

While these studies do provide valuable information regarding the pressures within the inner prosthetic environment, the sensors employed have several downfalls including stress concentrations at sensor edges due to sensor thickness, considerable additional weight and poor sensor design/integration which can cause loss of suspension thus distorting normal stump-socket interfaces.<sup>[17]</sup> Many of the sensors were made from semiconductors which can be heavy and inflexible<sup>[11, 12]</sup> and protrude into the skin causing discomfort.<sup>[17]</sup> Research involving SGs, or load cells requires socket modification which is laborious, costly,<sup>[16]</sup> and extra steps are necessary to preserve the subject's original socket.<sup>[119, 142]</sup> Further, this sensor placement method affects the accuracy of pressure measurements<sup>[108, 143]</sup> and may alter pressure distribution at the residual limb-socket interface.<sup>[13]</sup> Additionally, when sensors are mounted to the socket wall, only a small portion of the residual limb interface is studied.<sup>[118]</sup> Alternatively, research utilizing pressure mat products, such as the F-socket or Novel, provide greater spatial resolution and do not require modification of the socket because they are relatively thin and can be placed within the prosthetic.<sup>[143]</sup> While these systems do not require socket modification, they are still spatially limited, cannot be readily

integrated into existing prosthetic components, and leave room for improvement in flexibility and breathability desirable for long-term use

In the 1990's, researchers began proposing new sensors for prosthetic monitoring however, relatively few published efforts exist. While there has been work on optical sensors in this area<sup>[123, 143, 144]</sup> optical sensors will not be discussed here. Conventional optical sensors are often inconvenient for use outside lab settings, bulky, stiff, rigid, and brittle making them inappropriate for wearable applications.<sup>[145]</sup> Williams et al.<sup>[131]</sup> and Zhang et al.<sup>[122]</sup> were early contributors to this field developing and applying a specially designed transducer capable of sensing normal pressure and shear stresses within the socket. Williams et al.<sup>[131]</sup> developed a triaxial force transducer which was recessed into the walls of a prosthetic socket, as shown in Figure 5a. Similarly, Sanders et al.<sup>[137]</sup> developed a custom-designed transducer which measured stresses in three orthogonal directions. The transducer was mounted to the external socket surface, as described previously. While these sensors were novel and provided interesting information, the transducers were rigid raising concerns regarding comfort and weight. Additionally, these approaches require socket modification which as previously explained, is costly and laborious.<sup>[16]</sup>

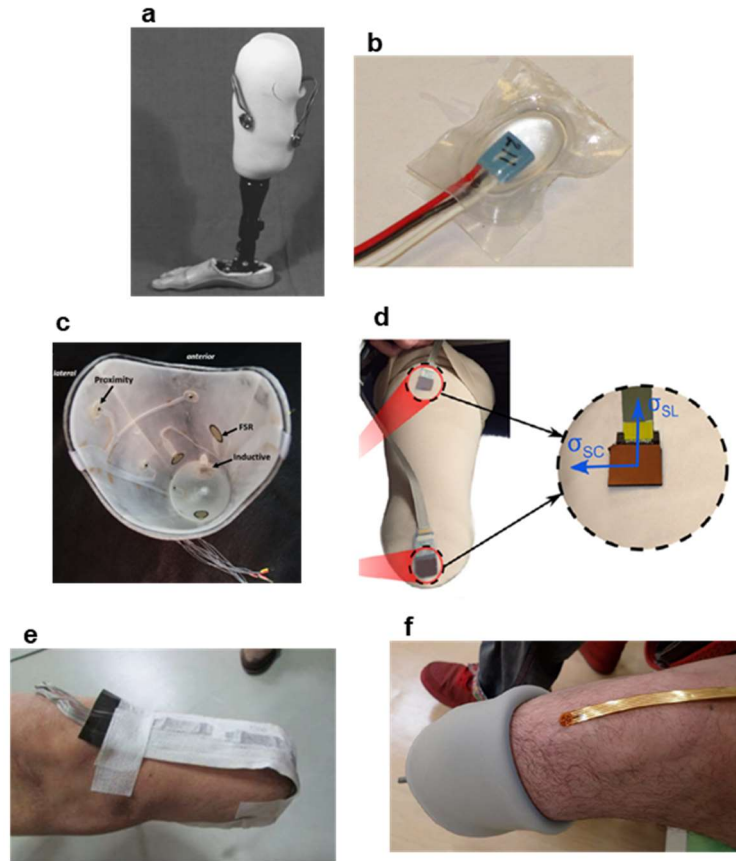


Figure 5: Sensors proposed for measuring stresses within the ISE (a) Transducers mounted to the socket. Reprinted with permission from<sup>[122]</sup> © 1998 IPPEM. Published by Elsevier Ltd. All rights reserved. (b) MEMS-based pressure sensor for ISE monitoring. Reprinted with permission from<sup>[146]</sup> © 2011, IEEE. (c) Custom-prosthetic socket insert with incorporated FSRs. Reprinted with permission from<sup>[142]</sup> © 2017 IPPEM. Published by Elsevier Ltd. All rights reserved. (d) Capacitive sensor structure created via 3D printing and lithography. Reprinted with permission from<sup>[6]</sup> © 2016 Published by Elsevier Ltd on behalf of IPPEM. (e) CNT/PVDF piezoresistive film sensor attached to residual limb. Reprinted with permission from<sup>[33]</sup> Copyright © 2017, IEEE. (f) Shear sensor for monitoring knee-bending. Reprinted with permission from<sup>[38]</sup> © 2017 MDPI.

In more recent research, flexible components have been incorporated into sensing devices used for ISE sensors.<sup>[6, 16, 25, 38, 146, 147]</sup> However, many approaches still rely on rigid, commercially available sensors for stress measurements.<sup>[16, 142, 146, 147]</sup> Wheeler et al. developed a microelectromechanical systems (MEMS)-based bubble sensor for monitoring normal pressure and shear stresses at the prosthetic socket interface.<sup>[146]</sup> A commercial MEMS sensor was mounted in a ceramic package and then embedded within a fluid-filled silicone bubble, as shown in Figure 5b. It is unclear why the MEMS sensor was surrounded by a fluid-filled silicone bubble and little

information is provided regarding the sensing mechanism. The sensor however was compared to commercial sensors and tests indicated that the MEMS-based bubble sensor exhibited substantial hysteresis but better performance in terms of drift. Mechanical properties of the sensor were not provided, and human testing was not completed. Swanson et al.<sup>[142]</sup> created a custom socket inserts with embedded commercial FSRs and proximity sensors into a socket, see Figure 5c. Sensors, wires and circuitry were placed within the inserts to reduce damage to electrical components and minimize irritation to residual limb tissue. Inserts were placed in the socket and tested on one amputee at five anatomical locations. The sensors were able to detect don/doff state, changes in limb mechanics and position, and sock thickness changes. However, the authors state that the insert design and fabrication process required significant time and therefore, this approach is currently only valuable in research settings.

Very few researches have proposed completely novel sensor designs for measuring pressure in the LL prosthetic environment.<sup>[6, 25, 33, 38]</sup> Laczczak et al.<sup>[6, 25]</sup> created an interfacial stress sensor, shown in Figure 5d, via 3D printing and lithography techniques. The basic structure of the sensor consisted of a flexible mechanical frame placed between two electrodes to create a capacitive sensor. Thus, normal and shear pressure could be monitored due to changes in electrode area and the distance between electrodes in the capacitive structure. The sensor was tested on one human subject at three locations at the liner/socket interface during walking. However, the sensor did exhibit hysteresis (15% for normal and 8% for shear). Additionally, the fabrication technique of this sensor required microfabrication techniques such as photolithography which are expensive and complex<sup>[148]</sup> requiring processes under vacuum and clean room environments.<sup>[84, 149]</sup> Ferreira et al.<sup>[33]</sup> developed a resistive normal pressure sensor for LL prosthetics by hot pressing carbon nanotube (CNT)/polyvinylidene difluoride (PVDF) films. The sensors were tested on four

amputees at two locations during standing and walking as shown in Figure 5e. Results were provided in terms of  $\Delta R$  and were not converted to pressure. Toyama et al.<sup>[38]</sup> created a shear sensor for the LL by placing two electrodes on an elastic rubber ring. The electrodes and interconnects were films patterned with copper via microfabrication techniques. Electrodes were attached to the rubber ring with an adhesive layer and the area between the electrodes was filled with a liquid electrolyte. When shear force was applied, the distance between the electrodes changed thus resulting in a change in capacitance. The sensors were attached to the residual limb, see Figure 5f, and tested on one human subject during a simple knee-bending experiment. Tests indicated that the sensor could detect changes in shear force however, the sensors were not tested during activity. Therefore, it is unclear if the sensors could withstand the forces experienced during regular use. Additionally, the fabrication of this sensor requires microfabrication techniques such as photolithography which are expensive and complex<sup>[148]</sup> requiring processes under vacuum and clean room environments.<sup>[84, 149]</sup>

In summary, research completed to measure interfacial normal and shear stresses has primarily been completed using commercial SGs mounted on the outer prosthetic socket wall.<sup>[11, 12, 17, 22, 23, 26, 39-44, 106, 111-121]</sup> However, these sensors are heavy,<sup>[11, 12, 17]</sup> inflexible,<sup>[11, 12]</sup> uncomfortable,<sup>[17]</sup> imprecise,<sup>[13]</sup> provide small sensing areas,<sup>[118]</sup> and require socket modification which is costly and laborious.<sup>[16]</sup> Other research efforts studied the ISE using the commercial Pliance system by Novel,<sup>[110, 112, 127]</sup> the F-Socket by Tekscan<sup>[23, 26, 113-118]</sup> and FSR's.<sup>[22, 106]</sup> While these approaches do not require socket modification and provide larger sensing areas, they suffer from non-linearity, hysteresis and drift<sup>[143]</sup> and leave room for improvement in terms of flexibility and breathability. Researchers have proposed using commercial stress sensors in novel configurations<sup>[16, 131, 137, 142, 146, 147]</sup> and completely novel sensors for monitoring the ISE.<sup>[6, 25, 33, 38]</sup>

However, these proposed sensors are problematic because some contain rigid components,<sup>[16, 122, 131, 142, 146, 147]</sup> require socket modification,<sup>[122, 131, 147]</sup> are fabricated through complicated methods,<sup>[6, 25, 38, 142]</sup> and in many cases have not been tested on human subjects.<sup>[146, 147]</sup>

## **2.4 Potential Application of Textile-based Sensing for Inner Socket Environment Monitoring**

Many of the shortcomings associated with currently available ISE monitoring systems could be significantly improved using textile-based sensors. However, their potential for monitoring the ISE has not yet been demonstrated. Textile-based sensors may be incorporated into fabric structures at one of the hierarchical levels of textiles: fiber, yarn, or fabric and have been explored for monitoring various stimuli, including chemical levels,<sup>[150]</sup> strain,<sup>[151, 152]</sup> stress,<sup>[48-68]</sup> temperature,<sup>[69-88]</sup> and RH.<sup>[76, 79, 83-87, 89-93]</sup> In this research, textile-based sensors for monitoring stress and moisture are explored and therefore, for the sake of brevity, efforts to develop fiber and textile based sensors to monitor stress,<sup>[48-68]</sup> and moisture<sup>[76, 79, 83-87, 89-93]</sup> will be the primary focus. Subsequent discussions will be focused on common materials, fabrication methods, sensing modalities, and performance parameters for textile-based stress and moisture sensing.

### **2.4.1 Materials**

One of the critical functional parameters of materials for textile-based sensors is electrical conductivity. Textile materials are mostly polymers which are inherently soft and electrically insulating. Therefore, it is necessary to impart electrical conductivity to textile structures to create sensors. There are a number of materials available for fabricating electrically conducting textiles including intrinsically conducting polymers (ICPs),<sup>[48, 77, 79, 80]</sup> conductive polymer composites (CPCs),<sup>[51, 56-59, 63, 64, 66, 68, 70, 72-76, 78, 81, 83-86, 88-90, 93, 153, 154]</sup> or all-metal or carbon based fibers/yarns.<sup>[155-171]</sup> Subsequent sections will provide advantages and shortcomings of each material and how they have been incorporated into fiber and textile-based sensors.

### 2.4.1.1 Intrinsically Conductive Polymers

Many researchers create fiber and textile based sensors using ICPs<sup>[48, 77, 79, 80]</sup> which can achieve conductivities up to 120-130 S/cm.<sup>[172]</sup> In particular, poly-(3,4-ethylenedioxythiophene) (PEDOT) has been commonly employed because of its high conductivity and solution processability.<sup>[172]</sup> ICPs are appealing as they ideally provide the electrical properties of a metal while maintaining the mechanical and processing properties of polymers.<sup>[173]</sup> The backbones of electrically conductive polymers are conjugated, that is, they possess alternating single and double bonds.<sup>[174]</sup> This chemical structure forms high-energy orbitals in which valence electrons are loosely bonded such that charge movement can be induced by the application of an electric or magnetic field.<sup>[175]</sup> When considering traditional polymers, like polyethylene, all valence electrons are bound and therefore immobile and unavailable for electrical transport.<sup>[175]</sup> The exact transport properties of ICPs will depend on the polymer chain packing, degree of order, the number of impurities present, and the presence of structural defects within the structure.<sup>[176]</sup>

In their natural state, ICPs are considered semi-conductive. The conductivity of these polymers may be enhanced through a process called doping.<sup>[173]</sup> During the doping process, a polymer's conjugated backbone reacts with an p- or n-type dopants (typically in the form of an oxidizing agent, a reducing agent, or a protic acid).<sup>[173]</sup> Doping agents add or remove electrons from the polymer backbone, thus creating delocalized polycations or polyanions, which improve the movement of electrons along the polymer chain.<sup>[173]</sup>

Many researchers strive to make conductive polymer systems by introducing conductive fillers to conventional polymers (see Section 2.4.1.2).<sup>[175]</sup> While this approach is cost efficient, it introduces issues such as surface corrosion, uneven mixing, reduced mechanical properties, and incompatibility between the polymer and filler.<sup>[175]</sup> These issues can be overcome with the use of

ICPs. However, ICPs also introduce several disadvantages. ICPs are generally environmentally unstable<sup>[172]</sup> and brittle due to their conjugated structure.<sup>[175]</sup> Their rigid backbone structure inhibits solubility and ICPs often decompose at temperatures lower than their melting temperature.<sup>[177]</sup> ICPs are mechanically too weak to withstand textile processes and therefore may only be incorporated into electronic textiles via coating processes.<sup>[178]</sup> Therefore, ICPs are currently restricted to lab-scale experimentation rather than large-scale manufacturing techniques.<sup>[175]</sup>

#### **2.4.1.2 Conductive Polymer Composites**

While the previous section discussed the use of ICPs for flexible electronics, many fiber and textile based sensors are produced with traditional polymeric materials, which are electrically insulating.<sup>[176]</sup> Therefore, conductive fillers, such as CNTs, graphene, carbon black (CB) and metal powders are added a polymer matrix to impart electrical conductivity and create CPCs.<sup>[175, 179]</sup> This method of fabrication is based on the percolation theory which correlates the resistivity of a composite based on the volume of a conductive filler.<sup>[176, 180]</sup> At a critical volume of filler, called the percolation threshold, conducting paths are formed such that an insulating material becomes conductive.<sup>[181]</sup> When adding conductive fillers to an insulating matrix, an initial decrease in electrical resistive is observed which is attributed to contact chains between conducting particles.<sup>[176]</sup> The volume fraction of particles when this initial decrease in electrical resistivity is observed is known as the percolation threshold.<sup>[176, 180]</sup> As the volume of conducting particles increases, the resistivity continually decreases until reaching a concentration at which the addition of further volume of particles does not cause a large decrease in electrical resistivity.<sup>[176, 180]</sup> Therefore, the percolation threshold is considered the lowest volume of conducting particles required within a particular polymer matrix to form electrically conductive pathways.<sup>[176, 182]</sup> The

conduction of electrons through a polymer matrix can be attributed to several phenomenon including the percolation theory, quantum mechanical tunneling, and thermal expansion<sup>[176, 182]</sup>

#### **2.4.1.2.1 Carbonaceous Particles**

Carbon based materials are commonly employed for functionalizing textile structures because they are generally regarded as flexible and lightweight.<sup>[58, 176]</sup> Therefore, carbon-based fillers, such as CNTs, graphene, and CB have been added to insulating matrices to impart electrical conductivity.<sup>[175, 179]</sup> Subsequent sections will provide advantages and shortcomings of each material.

##### **2.4.1.2.1.1 Carbon Nanotubes**

CNTs have been extensively explored for various applications including flexible electronics.<sup>[172]</sup> CNTs have shown promising potential for integration into fiber and textile based sensors<sup>[63, 68, 72-74, 76, 78, 81, 89, 90, 93]</sup> because of their structures provide superior physical, chemical, and mechanical performance.<sup>[183]</sup> Additionally, CNTs offer high carrier mobility, high current carrying capacities, ultrathin body for electrostatic control, and solution processability for low-cost production.<sup>[183, 184]</sup> CNTs are graphene sheets rolled into cylinders and may be considered single wall CNT (SWCNTs) or multi-wall CNTs (MWCNTs) based on their number of layers.<sup>[185]</sup> CNTs are produced with a range of diameters from 0.8-2 nm for SWCNTs and 5-20nm for MWCNT and lengths ranging from <100nm to several cm.<sup>[179]</sup> One particular advantage of CNTs is their low percolation threshold of ~0.1% wt<sup>[186]</sup> which makes them great candidates for flexible coatings as they do not require large filler amounts for conductivity.<sup>[187]</sup> Although, reported values of CNT conductivity vary widely from <10 to >5000 S/m with conductivity depending on electrical properties of individual CNTs, inter-tube contact resistance, and temperature.<sup>[172]</sup> Further, large-scale application of CNTs has been hindered by difficulty in controlling their structure.<sup>[172]</sup>

#### **2.4.1.2.1.2 Graphene**

Graphene was discovered in 2004<sup>[188]</sup> and has since served as a promising material for flexible electronics, such as textile-based sensors.<sup>[70, 83]</sup> Graphene is a single layer, or 2D material composed of carbon atoms bonded by a hexagonal lattice.<sup>[189]</sup> Graphene has garnished great attention for flexible electronics due to its excellent mechanical (tensile strength of ~130 GPa,<sup>[190]</sup> fracture strains of up to 25% and a Young's modulus of 1 TPa),<sup>[191]</sup> electrical (high mobility 5000–200000 cm<sup>2</sup>/(V•s), high electrical conduction)<sup>[189, 192]</sup> and optical properties (wide optical absorption spectrum (300–1400 nm), excellent transparency of ~97% in the visible wavelength range).<sup>[193, 194]</sup> Graphene also possesses a large surface area such that it adheres and conforms well to other materials.<sup>[190]</sup> In many wearable sensor applications, reduced graphene oxide (rGO) is utilized. GO is electrically insulating (conjugation is lost during oxidation process) therefore, it requires a reduction process to restore electrical conductivity.<sup>[195]</sup> The reduction of GO is usually done via exfoliation of GO sheets in hydrazine hydrate.<sup>[176]</sup>

Graphene may be prepared through different methods including chemical vapor deposition (CVD) growth on metal using a gaseous carbon source.<sup>[193]</sup> CVD methods of graphene growth are considered the most promising and feasible for large scale production<sup>[190]</sup> Graphene fabrication methods are more cost effective than current methods for producing CNTs.<sup>[176]</sup> However, it remains challenging to create high-quality, defect-free, large-area graphene which serves as a hurdle for scaling and commercialization.<sup>[190]</sup>

#### **2.4.1.2.1.3 Carbon Black**

While many research efforts employ CNTs and graphene to impart electrical conductivity, other carbonaceous materials such as CB have also been employed in fiber and textile based sensors.<sup>[51, 66, 154]</sup> CB is often utilized because it is relatively cost efficient.<sup>[196]</sup> CB is a primarily amorphous

carbon material with particles grown together to form aggregates of different sizes and shapes with high surface area to volume ratios.<sup>[197]</sup> Produced via thermal decomposition of hydrocarbons, CB is used primarily as reinforcement for products like tires and machinery belts.<sup>[197, 198]</sup> CB is employed in various applications to increase tensile strength, abrasion resistance, modulus, hardness, viscosity, UV resistance<sup>[198]</sup> (because is an almost perfectly absorbing material)<sup>[199]</sup>, etc. In terms of sensors, CB is added to impart electrical conductivity with CB providing electrical resistivity values between  $10^1$  to  $10^{-2} \Omega \cdot \text{cm}$ .<sup>[197]</sup> In applications in which CB is utilized to provide electrical conductivity, a moderately sized CB should be used with a low volatile content to ensure the CB filler has a moderate melt viscosity and high conductivity without requiring a high volume of CB loading.<sup>[186]</sup> However, the necessary loading of CB to achieve conductivity can be quite high with researchers using wt% of CB including 9%,<sup>[154]</sup> 14%<sup>[200]</sup> and 30%.<sup>[201]</sup> The precise amount of CB needed to make a polymer composite conductive will depend on the CB type, polymer type, and polymer properties like crystallinity, viscosity, and surface tension.<sup>[197]</sup>

#### **2.4.1.2.2 Metallic Particles**

Carbonaceous materials are advantageous as they provide flexibility, lightweightedness and can be applied to textile structures relatively easily. However, carbonaceous materials generally provide low electrical conductivity and structural stability.<sup>[58]</sup> Therefore, several research efforts explored metal particles for flexible sensors<sup>[56-59, 64, 66, 75, 84-86, 88, 153]</sup> to achieve high conductivities.<sup>[172]</sup> For example, researchers achieved conductivities of 470 S/cm to ~1800 S/cm when using Ag flakes.<sup>[172]</sup> Several metal materials have been incorporated into flexible sensors including Ag nanowires (AgNWs),<sup>[59, 64, 66, 153]</sup> Ag nanoparticles (AgNPs),<sup>[58]</sup> Pt,<sup>[57, 87, 88]</sup> Au,<sup>[56, 84-86]</sup> and zinc oxide nanowires (ZnO NWs).<sup>[75]</sup>

Electrodeposition<sup>[202]</sup> or electroless plating<sup>[203]</sup> are common methods for applying metals to textile materials. However, it is difficult to create uniform coatings with these techniques and the raw materials are quite expensive.<sup>[176]</sup> Further, materials made via electroless plating have low reported conductivity values.<sup>[204]</sup> Therefore other techniques for incorporating metals into fiber/textile based sensors have been explored such as dip-coating,<sup>[66, 153, 205]</sup> and application with brush pens.<sup>[59]</sup> While metal incorporation into fiber/textile based sensors presents many advantages there are also several challenges. Metal coatings are often insufficiently durable for wearable applications, they are challenging to produce at even thicknesses, and the raw materials are often expensive.<sup>[172, 204]</sup>

#### **2.4.1.2.3 Metallic and Carbonaceous Yarns**

Textile-based sensors can also be produced using metallic or carbonaceous yarns. Conductive yarns can be produced via coating (see Section 2.4.2.2) or spinning processes.<sup>[171]</sup> During coating processes yarns are functionalized using electrically conductive particles. Alternatively, conductive yarns can be produced directly from conductive materials such as carbon, copper, aluminum, titanium, or stainless steel (SS) with reported yarn conductivities ranging from 5  $\Omega$ /m to several k $\Omega$ /m.<sup>[170, 171, 206]</sup> Yarn-based sensing approaches are advantageous when compared to other methods, like fabric-coating, because conductive yarns can be directly integrated into textile structures<sup>[166]</sup> meaning they are minimally invasive.<sup>[169]</sup> Further yarn based sensors provide a convenient means of integrating several electronic components including sensors, antennas, and interconnects.<sup>[162, 164]</sup>

Conductive yarns are often produced from metals because they provide the best electrical properties.<sup>[170]</sup> Various metals can be used to create conductive yarns including copper, aluminum, titanium, or SS with SS being the most commonly used material likely due to its wide commercial

availability.<sup>[162-171]</sup> SS yarns are produced from SS fibers and are advantageous when compared to coated yarns because they may provide higher sensitivity, improved comfort/hand, and greater wash durability.<sup>[165]</sup> Further, SS yarns are flexible, deformable, cost effective, and can be used in high temperature/humidity environments.<sup>[166, 167, 169]</sup> SS yarns have been explored in various textile configurations, most often knitted<sup>[162, 165-169]</sup> but also woven,<sup>[163]</sup> braided,<sup>[164]</sup> and embroidered<sup>[164]</sup> for monitoring electrocardiograph signals<sup>[162, 164, 168, 169]</sup> strain<sup>[164-167]</sup> or moisture.<sup>[163]</sup>

Conductive yarns can also be produced directly from carbonaceous materials like CNTs and graphene. Such materials are appealing for yarn-structures because they provide a low-weight, high strength material for functionalizing textiles.<sup>[157]</sup> In particular, the production of CNT fibers and yarns has generated significant interest over the years due to CNTs desirable mechanical, electrical and thermal properties.<sup>[157]</sup> The production of CNT yarns has been explored via wet<sup>[155, 161]</sup> or dry-state spinning.<sup>[157-159]</sup> Alternatively, due to the one-dimensional nanostructure and high aspect ratio of CNTs, yarns can also be drawn directly from their arrays<sup>[81, 157-160]</sup> or high concentration suspensions.<sup>[155, 156]</sup> However, the production of these yarns requires significant financial investments<sup>[158, 159]</sup> and rigorous conditions ( $>1000^{\circ}\text{C}$ <sup>[207]</sup> and caustic conditions<sup>[155]</sup>). More recently, graphene yarns have garnered research interest. Several methods of fabricating graphene yarns have been proposed including one-step hydrothermal processes from GO suspensions<sup>[157]</sup> and wet-spinning from GO dispersions.<sup>[208, 209]</sup> However, many graphene yarn fabrication methods lack scalability which restricts wide-spread use.<sup>[157, 209]</sup>

## 2.4.2 Fabrication

To formulate textile-based electronics, several fabrication methods have been explored including microfabrication techniques,<sup>[84-88]</sup> coating,<sup>[48, 56, 57, 59, 63, 66, 74, 76-80, 89-91, 153, 205, 210, 211]</sup> extrusion,<sup>[49, 70, 72, 73, 93, 154]</sup> twisting/plying of yarns,<sup>[54, 66, 69, 81]</sup> as well as other textile approaches such as knitting

and weaving.<sup>[82, 84-88]</sup> Subsequent sections will discuss the advantages and shortcomings of each of these methods.

#### **2.4.2.1 Microfabrication**

Traditional microfabrication techniques have been explored to create textile-based sensors<sup>[84-88]</sup> specifically, temperature and humidity sensors. Researchers created what were called ‘electronic fibers’ by fabricating sensors via traditional microfabrication techniques (lithography, etching, plasma treatment) on polyimide (PI) slit films.<sup>[84-88]</sup> While this approach is appealing as it provides a linear response<sup>[84-88]</sup> and creates sensors sufficiently flexible and durable to withstand weaving on a commercial weaving machine<sup>[87]</sup> this fabrication method is disadvantageous because it requires processes under vacuum, clean room equipment, and batch processing.<sup>[84]</sup> Further, when the slit films were inserted into the fabric, the weaving machine was temporarily stopped such that the sensors could be manually inserted into the weaving machine<sup>[84]</sup> which is laborious and raises concerns regarding commercial viability.

#### **2.4.2.2 Coating**

The most common approach to creating fiber or textile-based sensors is coating. Coating techniques have been used to fabricate various sensor types including pressure,<sup>[48, 56, 57, 59, 63, 66, 153, 205]</sup> and humidity.<sup>[76, 79, 89-91, 210, 211]</sup> Coating is an advantageous method to create textile-based sensors as pre-made textile structures may be simply coated with electrically conductive material.<sup>[176]</sup> Coating eliminates the need to manufacture directly with electrically conductive materials which may not be compatible with current manufacturing processes.<sup>[212]</sup>

Several fiber and yarns types have been used for coating substrates to fabricate sensors including PU<sup>[59, 66, 75, 77, 153]</sup> PET,<sup>[77, 91, 153]</sup> cotton,<sup>[54, 57, 63, 89]</sup> PA,<sup>[48, 54]</sup> polydimethylsiloxane (PDMS),<sup>[49]</sup> and Kevlar.<sup>[58]</sup> Additionally, several fabric substrates have been explored for coating

including PA,<sup>[52, 55, 78, 79]</sup> PET,<sup>[78]</sup> and cotton/spandex fabric.<sup>[80, 90]</sup> The fiber, yarn or fabric substrate is generally selected to provide desired surface chemistry for coating adhesion or for specific mechanical properties. To functionalize the textile substrates, coatings containing ICPs,<sup>[48, 61, 79, 80]</sup> carbonaceous particles,<sup>[49, 51, 52, 60, 63, 66, 89, 90]</sup> and metallic particles<sup>[58, 59, 64, 66, 153, 205]</sup> have been explored. Each conductive particle type provides unique advantages and disadvantages in terms of electrical and mechanical properties as well as ease of processing (see Section 2.4.1.2).

Several coating techniques have been explored. Most commonly, dip-coating<sup>[63, 66, 74, 76, 78-80, 89, 91, 153, 205]</sup> approaches have been utilized however, other coating techniques such as nozzle/die coating,<sup>[48]</sup> sputtering,<sup>[56]</sup> low temp atomic layer deposition (ALD),<sup>[57]</sup> brush pens,<sup>[55, 59]</sup> electrophoretic deposition (EPD),<sup>[52]</sup> polymerization,<sup>[77]</sup> knife over roll,<sup>[90]</sup> spray coating,<sup>[211]</sup> and screen printing<sup>[51, 210]</sup> have been explored. While coating approaches are relatively simple, they do require extra steps during processing which may be excessively time consuming or expensive. Further, many of the coating techniques proposed in research are not inherent to the textile industry,<sup>[52, 56, 57, 62]</sup> and would require special equipment for incorporation which serves as a major barrier to integration and scale-up.

### **2.4.2.3 Extrusion**

Several extrusion methods have been explored for creating textile-based pressure<sup>[49, 154]</sup> and humidity<sup>[93]</sup> sensors. Approaches to fabrication include fiber extrusion<sup>[49, 93, 154]</sup> and direct fabric formation through nonwoven extrusion processes.<sup>[72, 73]</sup> Extrusion processes are advantageous because they are commonly utilized in the textile industry and can provide relatively few barriers to adaptation. Further, traditional extrusion methods are high volume processes thus providing desirable productivity.

Fiber-based sensors have been fabricated through melt-spinning of polylactic acid (PLA) and MWCNTs<sup>[93]</sup> as well as desktop extrusion printing of microstructured PDMS/CNT coated fibers and PDMS/CB biocomponent fibers.<sup>[49, 154]</sup> While the melt-spinning approach is promising due its relative simplicity<sup>[93]</sup> other extrusion approaches require secondary coating processing,<sup>[49]</sup> or custom, desktop set-ups that presumably produce fibers in relatively small batches.<sup>[49, 154]</sup>

Additionally, nonwoven fabrics sensors have been formulated through extrusion methods such as meltblowing of MWCNTs/poly( $\epsilon$ -caprolactone) PCL/polypropylene (PP)<sup>[73]</sup> and electrospinning of MWCNTs/polyamide,6 (PA6)/polypyrrole (Ppy).<sup>[72]</sup> These processes are advantageous due to their relatively high output however, electrospinning is a process of questionable commercial value. Further, connection of nonwoven fabrics to electrical components is a challenge for practical applications.

#### **2.4.2.4 Yarns**

As discussed in Section 2.4.1.2.3, yarns can be produced directly from conducting material like SS, CNTs, and graphene. Alternatively, sensory yarns can be formulated from a combination of insulating fibers or yarns and conducting material. Twisted yarn architectures are appealing for sensing applications because they provide improved load capacity,<sup>[81]</sup> elasticity,<sup>[69, 81]</sup> resiliency,<sup>[54]</sup> a stable and reversible signal even when the sensor is stretched<sup>[66]</sup> and allow sensors to endure severe bending without compromising electrical performance.<sup>[69]</sup> Yarn configuration sensors have been created using PET yarns/silkworm wrapper fibers and coated with (1-Ethyl-3-methylimidazolium bis(trifluoromethanesulfonyl)imide (EMIM Tf2N)/CNT)/PDMS,<sup>[69]</sup> PU fiber/wrapper fibers coated in AgNWs/PDMS/CB,<sup>[66]</sup> as well as PA fibers/conductive wrapper fibers coated in PU.<sup>[54]</sup> While yarn architectures are an appealing form factor for textile-based

sensors, many require custom wrapping set ups<sup>[69, 81]</sup> as well as additional coating processes to provide functionality or durability.<sup>[54, 66, 69]</sup>

#### **2.4.2.5 Knitting and Weaving**

In addition to yarn fabrication, researchers have explored creating textile-based sensors through other traditional textile methods such as knitting<sup>[82]</sup> and weaving.<sup>[48, 49, 57, 84-88]</sup> These approaches are advantageous because commercial textile equipment can be used to fabricate sensors directly into a textile structure. In one approach, commercial metal wires were knitted into a fabric structure.<sup>[82]</sup> While this fabric-based sensor provided a linear response and high sensitivity, fabrics containing metal wires and other rigid material are concerning with respect to biological compatibility, flexibility, durability, ease of manufacturing as well as user comfort.<sup>[89, 213]</sup> In another approach, previously discussed in 2.4.2.1, film slits were woven into fabrics using a commercial weaving machine for temperature and humidity sensing.<sup>[84-88]</sup> However, when the slit films were inserted into the fabric, the weaving machine was temporarily stopped such that the sensors could be manually inserted into the weaving machine<sup>[84]</sup> which is laborious and raises concerns regarding commercial viability. Other researchers have integrated fiber sensors into woven arrays by hand which while laborious, is a proof of concept.<sup>[48, 49, 57]</sup>

#### **2.4.3 Modes of Sensing**

With the discussion of materials and fabrication methods completed, it is now critical to discuss how fiber and textile sensors operate. Textile-based sensing can be achieved using various principles, including optical,<sup>[214-217]</sup> piezoelectric,<sup>[218]</sup> triboelectric,<sup>[219]</sup> resistive,<sup>[52, 59-64, 66]</sup> and capacitive sensing.<sup>[48-51, 53-58, 153, 205]</sup> However, most textile and fiber based sensors operate by monitoring changes in resistance or capacitance – these general modes of sensing were previously described in Section 2.3 and will be further described with specific focus on fiber and textile based

sensing. Fiber and textile sensors often employ resistive and capacitive sensing because these types of sensors are relatively easy to fabricate and use and require relatively simple electronics.<sup>[128, 220]</sup> Hence, the focus of the following sections will be on fiber and textile-based sensors which operate via resistive and capacitive sensing. These sensing modalities and how they detect changes in stress and moisture will be further described in subsequent sections.

#### **2.4.4 Performance Parameters**

To compare and contrast resistive and capacitive fiber and textile-based sensors, it is important to first understand the sensor performance parameters. There are various sensor performance parameters reported by researchers including sensitivity,<sup>[51, 64, 80, 84, 86, 92]</sup> durability,<sup>[54, 57, 91, 153, 205]</sup> stability,<sup>[69, 70, 77]</sup> hysteresis,<sup>[51, 53, 56, 84, 205]</sup> max elongation,<sup>[55, 56, 66, 89, 153]</sup> extensibility<sup>[75, 77, 81]</sup> response time,<sup>[54, 64, 69, 70, 76, 79, 90, 205]</sup> and relax times.<sup>[58, 64, 90]</sup>

Sensitivity is a critical and commonly cited sensor performance parameter. Sensitivity indicates the ratio of change in sensor output to the change in the measurand.<sup>[124]</sup> It is desirable to maximize sensitivity such that small changes in the given stimuli may be detected.

Additionally, sensors should be adequately durable to withstand cyclic testing and should ideally provide stable mechanical and electrical results throughout use. In terms of wearable technology, garments may be stretched repeatedly over their lifetime; therefore, it is important that such sensors are able to withstand cyclic testing. Researchers have tested sensors to a large range of cycle numbers, as high as 10,000,<sup>[57, 153, 205]</sup> to indicate mechanical durability and electrical stability. Electrical stability is often indicated by the drift or the amount that the electrical signal changes over the course of cyclic testing.

Another critical sensor parameter is hysteresis. Hysteresis indicates the difference in two output values during increases and decreases in the measurand.<sup>[124]</sup> For example, in the case of

pressure, sensing hysteresis may be defined as the difference in sensor output during loading (pressure application) versus unloading (pressure relaxation).<sup>[124]</sup>

Another commonly reported performance is stretchability and flexibility. Particularly in the field of wearable electronics, it is important that sensors can stretch and flex with the users. Conventional SGs provide a workable strain range of <5%,<sup>[221, 222]</sup> which is inadequate for wearable applications. During the basic movement of walking, the skin on the feet, the waist, and the joints are repeatedly stretched to as much as 55%.<sup>[223]</sup> However, it has proven challenging to produce sensors which simultaneously provide high conductivity, stretchability, and sensitivity.<sup>[59]</sup> Stretchability and flexibility of the fiber sensor relies on the concept that, when stretched or flexed, conductive networks are not destroyed.<sup>[59]</sup>

Furthermore, sensors should be capable of detecting stimuli at a range of frequencies, particularly when considering stress sensors. The exact frequency desired for measurement is dependent on the measurand of interest. For example, step frequency at low speeds of running is approximately 2.5 Hz and increases with increasing speed.<sup>[224, 225]</sup> Related sensor performance parameters include response time and relax time, which indicate how quickly a sensor responds to an applied stimulus and how quickly a sensor returns to its baseline electrical signal after the stimuli is removed. When considering fiber based sensors, the response and the relaxation behavior will be highly dependent on the viscoelastic properties of the polymeric material.<sup>[59]</sup> It is unclear what response and relax times are desirable; however, papers report response times of <100 ms<sup>[59, 65, 226]</sup> and relax times of 10–15 ms as desirably fast.<sup>[58, 59]</sup>

#### **2.4.5 Stress Sensing**

In Section 2.3.1, the structure and sensing modalities of commercial stress sensors were discussed. Here, the novel textile-based stress sensors will be reviewed. While the modes of sensing are like

those previously discussed, resistive or capacitive, the methods of fabrication and form factors vary quite significantly from commercial sensors. Textile-based stress sensors are designed to be soft and conformable to collect data in a non-invasive, and comfortable manner.

#### **2.4.5.1 Resistive Stress Sensors**

Resistive, textile-based stress sensors undergo a change in electrical resistance when subjected to an external deformation.<sup>[66, 128]</sup> As previously discussed in Section 2.3.1.1, changes in resistance due to applied stresses may be a result of geometrical changes in the resistors  $A$  or  $l$ . Alternatively, changes in resistance due to applied stresses may be a result of changes in a material's  $\rho$  which is an intrinsic material property. When considering homogeneous materials,  $\rho$  is invariant therefore, the piezoresistive behavior for homogeneous materials is derived from the changes in resistor geometry ( $A$ , and  $l$ ), as shown in Figure 2a. However, many fiber and textile-based resistive sensors are made by incorporating conductive particles into a polymer network to yield a conductive, bi-phasic system.<sup>[59, 62, 64, 66]</sup> For bi-phasic systems, such as CPCs, changes in resistance may also be attributed to composite materials' changes in bulk resistivity. Piezoresistive fiber and textile-based stress sensors may provide an increase or decrease in resistance with stress application. When a mechanical stimulus is applied to fiber or textile-based pressure sensors, an increase in resistance (positive piezoresistance.<sup>[63, 65, 66, 135, 227]</sup>) due to the disruption of conductive pathways may be observed. Alternatively, a decrease in resistance (negative piezoresistance<sup>[59, 64, 222, 228, 229]</sup>) may be observed due to the formation of new electrical pathways, which improves conductivity. Additionally, when fiber-based piezoresistive sensors are arranged in a fabric array, changes in electrical resistance may also be attributed to changes in contact area resistance between fibers arranged in a yarn configuration or fabric array.<sup>[59, 63, 66]</sup>

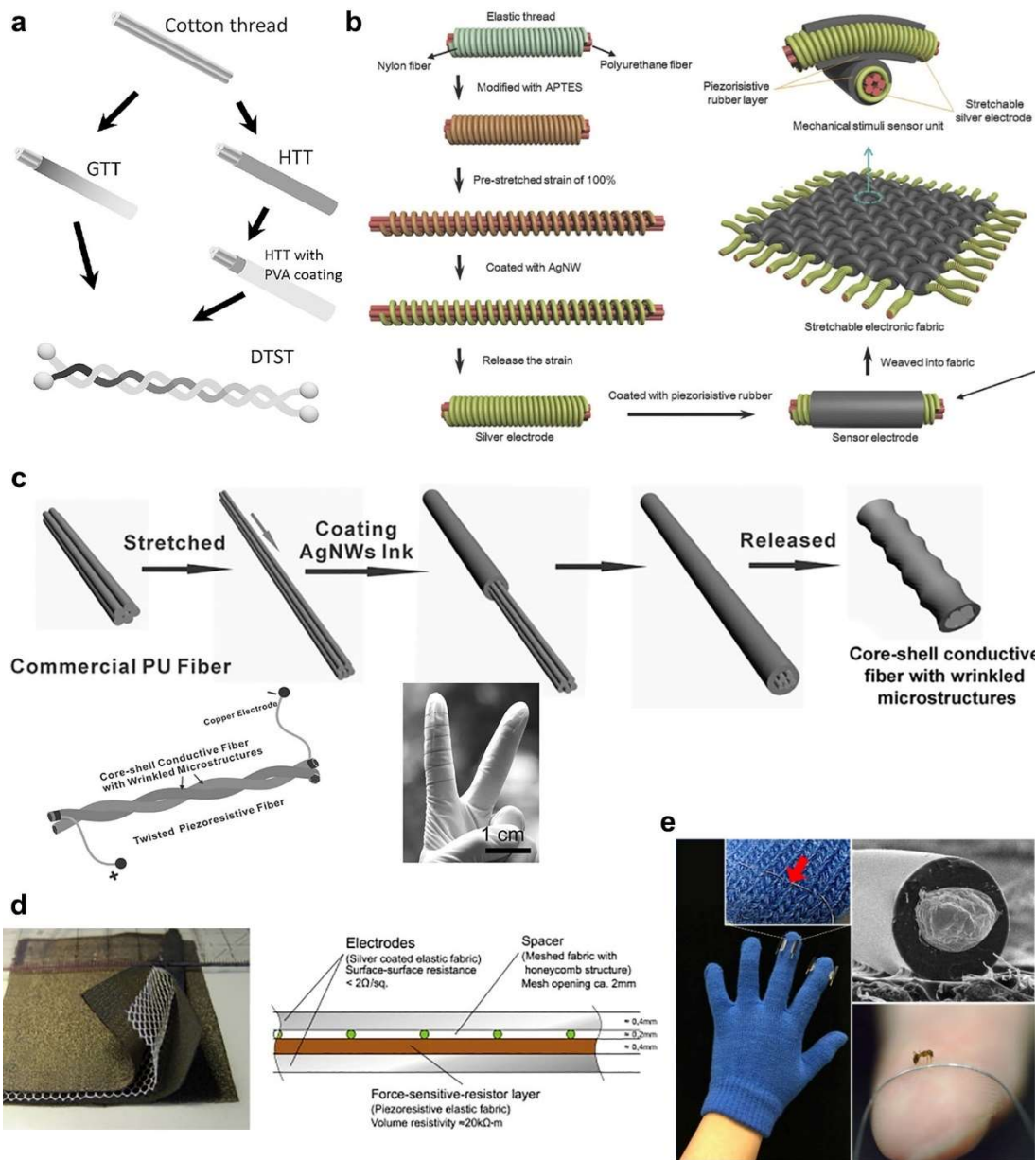


Figure 6: Textile-based resistive stress sensor fabrication and structure (a) Fabrication of a double-twisted conductive smart thread. Reprinted with permission from<sup>[63]</sup> © 2016 WILEY-VCH Verlag GmbH & Co. KGaA, Weinheim. (b) Fabrication of a stretchable electronic fabric capable of pressure sensing. Reprinted with permission from<sup>[66]</sup> © 2015 WILEY-VCH Verlag GmbH & Co. KGaA, Weinheim. (c) Fabrication of a stretchable conductive core-shell fiber with wrinkled microstructure including twisting of the fibers into a yarn-like structure and wrapping the yarn around a human figure to indicate flexibility. Reprinted with permission from<sup>[59]</sup> © 2016 WILEY-VCH Verlag GmbH & Co. KGaA, Weinheim. (d) Construction of sewn fabric sensor consisting of four fabric layers. Reprinted with permission from<sup>[61]</sup> © 2014 The Authors. Published by Elsevier B.V. (e) Elastomeric tubes injected with metallic alloy to create microfiber sensor which can be incorporated into a fabric gloves. Reprinted with permission from<sup>[230]</sup> © 2018, American Chemical Society.

Resistive stress sensors have primarily been fabricated via coating processes<sup>[48, 52, 59, 60, 63, 66]</sup> such as cotton fibers coated with SWCNTs,<sup>[63]</sup> PU/PA yarns coated with AgNWs/CB/PDMS,<sup>[66]</sup> PU yarns coated with AgNWs,<sup>[59]</sup> and aramid fabrics with CNTs.<sup>[52]</sup> Tai et al.<sup>[63]</sup> coated cotton fibers with SWCNTs through dip-coating and then twisted the fibers to create a double-twisted smart yarn, as shown in Figure 6a, which provided desirable resilience and fatigue properties. Pressure sensing capabilities, shown in Figure 7a, were attributed to the fact that, when yarns were loaded, the fiber-to-fiber contact increased, while the distance between nanoparticles also increased, thus leading to an overall increase in electrical resistance. These twisted yarn structures provided good sensitivity, and a fast response times however, the sensors were unable to measure pressures beyond 25 kPa.

Many researchers have coated elastomeric yarns, such as PU, to create resistive stress sensors<sup>[59, 66]</sup> because elastomers are able to stretch and flex, properties desirable for wearable applications. Ge et al. dip-coated PU/PA with AgNWs and PDMS-CB composite rubber using a process shown schematically in Figure 6b.<sup>[66]</sup> Fibers were then woven into an array for pressure sensing. When a mechanical stimulus was applied to the fibers, a change in contact area, thickness, or conductivity of the functionalized rubber layer was induced, which increased electrical resistance, as shown in Figure 7b. In the case of pressure sensing, the authors noted two regimes of sensing behavior. In the first pressure regime (0 to ~0.4 N), the authors attributed changes in resistance to changes in fiber contact area with pressure application. When larger loads were applied to the fiber array (0.4–2 N), the conductivity of the piezoresistive rubber layer increased due to CB particles moving closer with load application. These fiber sensors provided high conductivity, stretchability, and sensitivity in low pressure regimes. Additionally, the yarn could measure strain, bending, and twisting. Similarly, Wei et al. developed stretchable sensors using

PU fibers coated with AgNWs using a Chinese brush pen.<sup>[59]</sup> AgNWs were dispersed in a waterborne PU (WPU) to create a conductive ink. Intermolecular hydrogen bonding between the AgNWs and the WPU allowed them to immobilize more securely on the PU fiber such that AgNWs did not slip excessively during straining. Following coating, the pre-strained fibers were allowed to relax, and a unique microstructure on the surface of the fiber was formed, shown schematically in Figure 6c. For pressure sensing, two fibers were twisted together and when pressure was applied, the two fibers became more compressed thus increasing contact area and decreasing overall resistance, as shown in Figure 7c. The authors explained the fibers unique properties and sensing behavior with the fibers' surface texture.

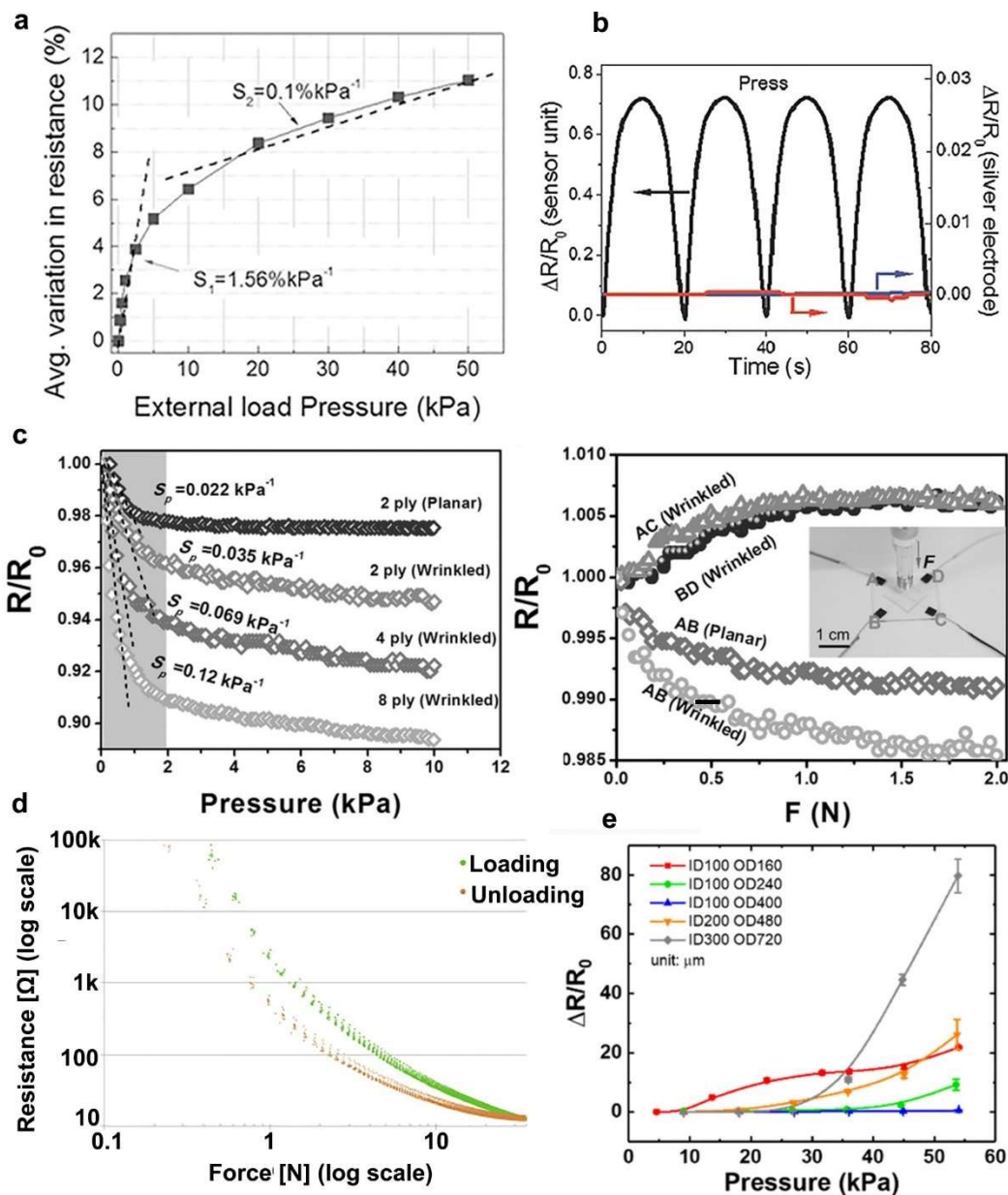


Figure 7: Responses of textile-based resistive sensors (a) Resistance versus applied load for a double-twisted conductive smart thread. Reprinted with permission from<sup>[63]</sup> © 2016 WILEY-VCH Verlag GmbH & Co. KGaA, Weinheim. (b) Relative resistance change with load of a stretchable electronic fabric. Reprinted with permission from<sup>[66]</sup> © 2015 WILEY-VCH Verlag GmbH & Co. KGaA, Weinheim. (c) Relative resistance change with pressure for stretchable conductive core-shell fiber with wrinkled microstructure and change of resistance with two stacked fibers (inlet image). Reprinted with permission from<sup>[59]</sup> © 2016 WILEY-VCH Verlag GmbH & Co. KGaA, Weinheim. (d) Layered fabric sensor performance when exposed to cyclic loads of 35N. Reprinted with permission from<sup>[61]</sup> © 2014 The Authors. Published by Elsevier B.V. (e) Pressure sensing and reliability performance of microfiber sensor consisting of elastomeric tubes injected with metallic alloy. Reprinted with permission from<sup>[230]</sup> © 2018, American Chemical Society.

Fabric-based, resistive stress sensors have also been fabricated by stacking and combining multiple fabric layers.<sup>[60, 61, 64]</sup> Buscher et al.<sup>[61]</sup> fabricated a four layer fabric structure, shown in in Figure 6d, consisting of two electrodes, a spacer fabric and a piezoresistive fabric layer. This fabrication approach is advantageous because it allows sensors to be fabricated in a wide range of shapes and sizes because fabrics can be cut and layered together in the desired configuration. The piezoresistive fabric layer, which was a knitted fabric coated in ICPs, was responsible for sensing – when loaded the resistance of the fabric decreased, as shown in Figure 7d, which was measured at the two outer electrode layers. This sensing approach provided a large pressure measurement range from 1-500 kPa and the ability to create a 54 pixel sensing array.

Other researchers have created fiber-based resistive pressure sensors by injecting a liquid metal alloy, eutectic gallium indium (eGaIn), into elastic microtubes.<sup>[230]</sup> Liquid metals are desirable for wearable sensing applications because they provide high conductivity as well as the ability to reconfigure after being deformed which provides robustness over a range of pressures. Researchers reported an electrical conductivity of  $3.27 \pm 0.08$  MS/m stretchability up to 120% strain using this approach. In addition, this sensing method provided minimal electrical drift even after repeated stretching and machine washing. PDMS microtubes were fabricated using a customized tip-coating technique in which a thin metal wire was dipped into uncured PDMS and then removed. eGaIn was injected using a syringe and the final fiber structure is shown in Figure 6e. Sensing capabilities were attributed to the eGaIn whose movement changes when compressed thus increasing resistance, as shown in Figure 7e.

In summary, a great deal of work has been completed in the area of resistive stress sensors. A few notable efforts with diverse materials and fabrication methods were discussed here. Most resistive stress sensors rely on coating methods for fabrication. While some coating approaches

are appealing due to their relatively simple fabrication techniques like dip-coating<sup>[63, 66]</sup> many require obscure coat formulations<sup>[230]</sup> and additional processing steps to protect the ink from fracturing when stretched.<sup>[230]</sup> Further, many fiber-based sensing approaches are limited in their sensing range<sup>[52]</sup> therefore fabric-based resistive sensors have been proposed.<sup>[60, 61, 64]</sup> While some of these approaches do provide larger sensing ranges<sup>[52, 60]</sup> others report high sensitivity in very small pressure regimes ( $<3\text{kPa}$ )<sup>[64]</sup> and many require laborious fabrication methods combining several fabrication techniques including film formation, sewing, and coating.<sup>[60, 61, 64]</sup> Liquid metal incorporation to form fiber-based sensors may be a promising route to creating highly conductive and flexible resistive stress sensors, however, this fabrication process is not transferrable to current textile processes which may serve as a barrier to wide spread application.

#### **2.4.5.2 Capacitive Stress Sensors**

Capacitive textile-based stress sensors are more common than resistive mode stress sensors. This is likely because capacitive stress sensors provide simple design, high sensitivity, good stability and low power consumption.<sup>[58]</sup> Capacitive stress sensors convert mechanical stimuli to an electrical signal via a change in their capacitance.<sup>[124]</sup> The relationship between  $C$ ,  $A$ ,  $d$ ,  $\epsilon_r$ , and  $\epsilon_0$ , was previously described in 2.3.1.2. The parallel plate capacitor configuration is most commonly employed for fiber and textile-based pressure sensors, however cylindrical configurations have also been explored for fiber-based stress sensors.<sup>[67, 231, 232]</sup>

The most common approach to create a fiber or yarn-based parallel plate capacitors is to utilize a conductive fiber or yarn coated in an insulating material which acts as the dielectric layer.<sup>[48, 49, 57, 58, 205]</sup> The fibers or yarns are then arranged perpendicularly to one another to form parallel plate capacitor configurations. For example, Lee et al. developed a cotton, fiber-based sensor consisting of Pt electrodes deposited via low temperature ALD.<sup>[57]</sup> After electrode

deposition, the fiber was coated in PDMS which served as the dielectric medium, as shown in Figure 8a. The fibers were sewn perpendicularly to one another to form cross-over points or sensing pixels. When a stress was applied, the distance between the electrodes decreased and the electrode overlap area increased, resulting in an increase in capacitance, as shown in Figure 9a. Similarly, Takamatsu et al. created a relatively large (16 cm × 16 cm) fabric sensor using PEDOT:PSS coated PA fibers for detecting pressures.<sup>[48]</sup> PA fibers were unwound from a package and passed through a nozzle that coated the fiber surface with PEDOT:PSS and then an insulating fluoropolymer (Cytop) layer. After fiber fabrication, the fiber-sensors were woven into an array and the ability of the array to map pressure was demonstrated. In a woven configuration, the PEDOT:PSS layers acted as electrodes separated by the Cytop dielectric layer, as seen in Figure 8b. When pressure was applied, the distance between the electrodes and overlapping electrode area increased, thereby increasing the capacitance, as shown in Figure 9b. The fibers provided a sensing range of 0.98–9.8 N/cm<sup>2</sup> which allowed for sensing human touch. In another similar approach, Zhang created a textile-only capacitive sensor with a core-spun yarn structure.<sup>[54]</sup> The yarn consisted of a core composed of Ag fibers and outer cotton wrapper fibers which were fixed with a PU coating, as shown in Figure 8c. The fibers were woven into a fabric configuration such that when pressure was applied at yarn intersections, distance between the yarns decreased thus capacitance increased, see Figure 9c. This approach provided sensitivity of 0.01922 kPa<sup>-1</sup>, response time of 110-230 ms, ability to withstand 500 pressure cycles as well as pressures of 200 kPa. However, this yarn structure had an elastic limit of 18.5% elongation. Other researchers focused on increasing the dielectric constant and sensitivity while also improving the flexibility of fiber or yarn-based sensors by utilizing dielectric layers with porous microstructures. For example, PDMS microstructured fibers were created via extrusion printing and then coated with CNT

electrodes via drop-coating.<sup>[49]</sup> In order to create a capacitive structure the PDMS/CNT fibers were attached to either side of a PDMS film which served as the dielectric, as shown in Figure 8d. When loaded, the distance between electrodes and overlapping area of the electrodes changed, as well as the dielectric permittivity of microstructured PDMS, resulting in an overall increase in capacitance, see Figure 9d. This sensing approach provided a sensitivity of  $0.17 \text{ kPa}^{-1}$ , a minimum detectable limit of  $0.02 \text{ kPa}$  and response time of  $25 \text{ ms}$ .

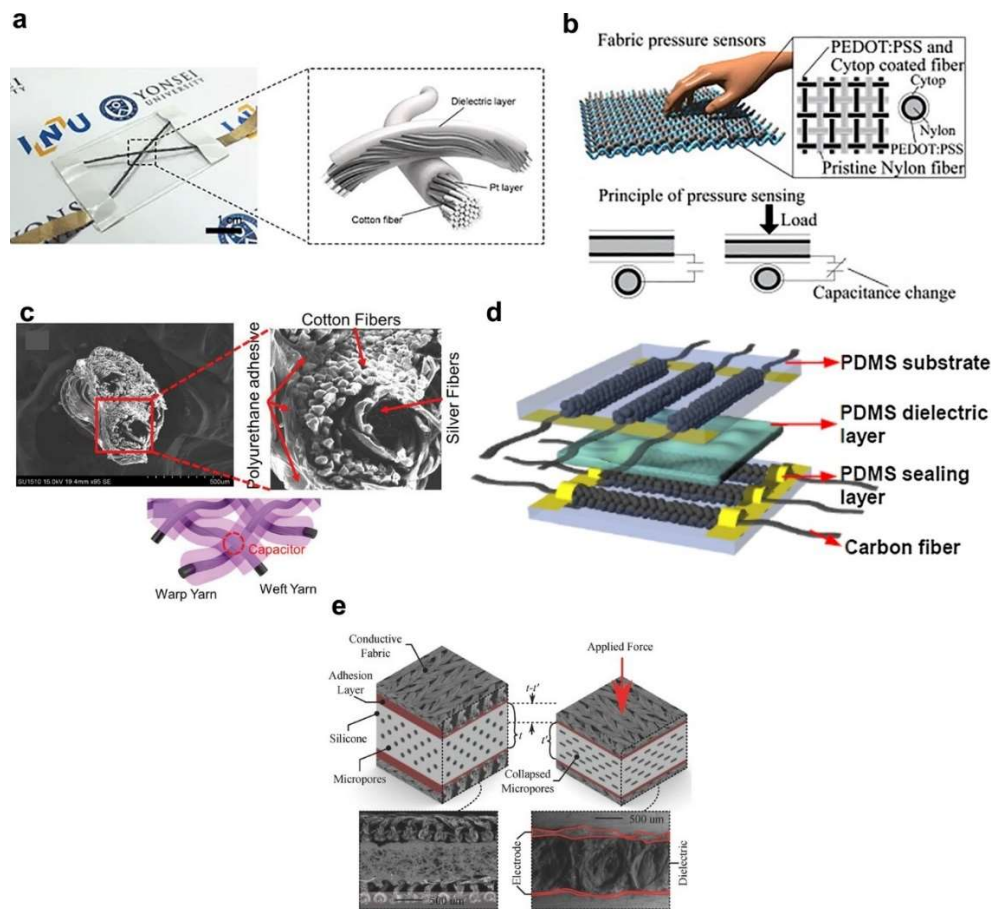


Figure 8: Capacitive textile-based stress sensors structure and sensing mechanisms (a) View of a fiber-based capacitive sensors. Reprinted with permission from<sup>[57]</sup> © 2016 Springer Nature. (b) PA/PEDOT:PSS/Cytop fiber-based sensor structure and schematic of sensing mechanism. Reprinted with permission from<sup>[48]</sup> © 2012 Elsevier B.V. All rights reserved. (c) Ag fibers/cotton wrapper fiber/PU yarn-based sensor structure and capacitor formation at crossover points in fabric structure. Reprinted with permission from<sup>[54]</sup> © 2019 WILEY-VCH Verlag GmbH & Co. KGaA, Weinheim. (d) Pressure sensing array consisting of microstructured PDMS/CNT fibers. Reprinted with permission from<sup>[49]</sup> © 2019 Elsevier B.V. All rights reserved. (e) Sensor structure and working mechanism of flexible sensor consisting of microstructured PDMS layer and fabric electrodes. Reprinted with permission from<sup>[50]</sup> © 2017 WILEY-VCH Verlag GmbH & Co. KGaA, Weinheim

Researchers have used various approaches to create pressure sensors at a fabric-level. Most approaches involve stacking insulating and conductive fabric layers<sup>[50, 53]</sup> or applying conductive coatings to insulating fabrics<sup>[51, 55]</sup> to create a parallel-plate configurations. For example, Guo et al.<sup>[51]</sup> screen printed CB/silicone electrodes on a textile substrate to create a fabric-based pressure sensor. When pressure was applied, the distance between the screen-printed electrodes changed as well as the dielectric permittivity of the dielectric leading to an overall increase in capacitance. This sensing approach however provided low sensitivity of  $0.0002536 \text{ kPa}^{-1}$ . In another approach, PEDOT:PSS electrodes were brush-coated onto a knitted fabric to create a wearable keyboard.<sup>[55]</sup> Subsequently, the electrode was coated in an insulating layer of PDMS. Unlike previous approaches, only one electrode was applied to the fabric substrate. The user's finger acted as the second or counter electrode which induced a change in capacitance when pressure was applied. This sensing approach provided a minimum detection limit of  $0.05 \text{ Ncm}^{-2}$  and the ability to withstand 1000 strain cycles with a 10% change in resistance. However, this sensor structure was restricted to a maximum elongation of 30%. In a different approach, Atalay et al. created a flexible sensor using conductive fabric electrodes and a porous silicone dielectric.<sup>[50]</sup> Woven or knit conductive fabrics were laminated to a porous silicone layer, as shown in Figure 8e. The porous silicone structure was formulated through integration and removal of sugar granules or salt crystals. When the sensor structure was loaded, the distance between the electrode decreased and the dielectric constant increased due to the removal of air which resulted in an overall increase in capacitance with pressure, as shown in Figure 9e. This sensing approach provided a sensitivity of  $121 \times 10^{-4} \text{ kPa}^{-1}$ , resolution of 0.86 kPa, and drift  $<0.15\%$ .

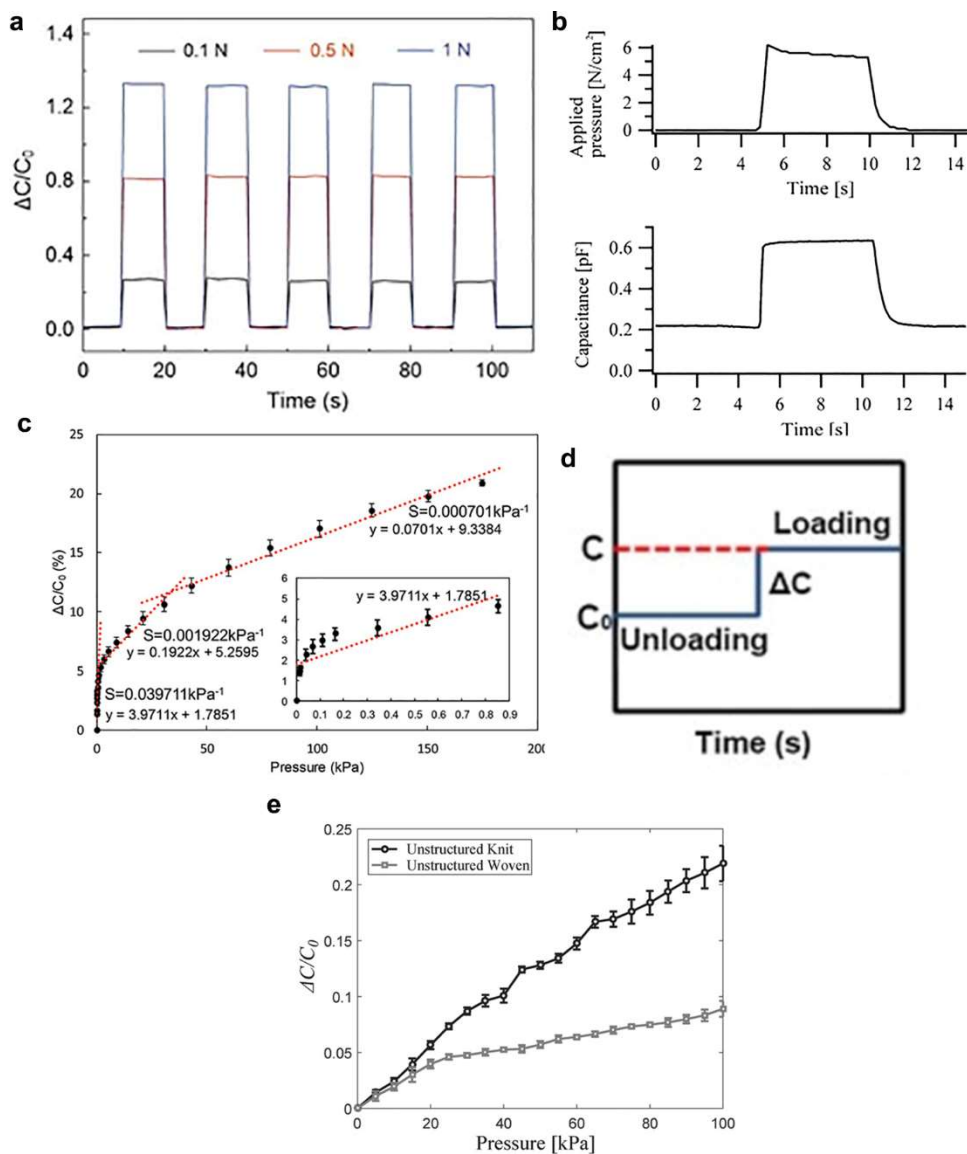


Figure 9: Capacitive textile-based stress sensor responses (a) Cotton/Pt fiber-based sensor response to loads of 0.1, 0.5 and 1 N. Reprinted with permission from<sup>[57]</sup> © 2016 Springer Nature. (b) PA/PEDOT:PSS/Cytop fiber-based sensor response to 4.9 N/cm<sup>2</sup> pressure. Reprinted with permission from<sup>[48]</sup> © 2012 Elsevier B.V. All rights reserved. (c) Relative change in capacitance and applied pressure of the array of Ag fibers/cotton wrapper fiber/PU yarn-based sensor. Reprinted with permission from<sup>[54]</sup> © 2019 WILEY-VCH Verlag GmbH & Co. KGaA, Weinheim. (d) Response of microstructured/CNT fibers to pressure. Reprinted with permission from<sup>[49]</sup> © 2019 Elsevier B.V. All rights reserved. (e) Relative change in capacitance of flexible sensor consisting of microstructured PDMS layer and knit or woven electrodes. Reprinted with permission from<sup>[50]</sup> © 2017 WILEY-VCH Verlag GmbH & Co. KGaA, Weinheim

In summary, a great deal of work has been completed in the area of capacitive, textile-based stress sensors. A few notable works with diverse materials and fabrication methods have been discussed here. While many textile-based stress sensors have been reported, there are still

several challenges to overcome in this field. Many textile-based sensors suffer from hysteresis,<sup>[53]</sup> drift<sup>[51]</sup> and cannot be greatly extended.<sup>[54, 56]</sup> Additionally, many of the fabrication methods proposed thus far are not transferrable to the textile industry which hinders scale-up and real world application.<sup>[49, 50, 52, 55, 57, 59, 62, 64]</sup> Therefore, traditional textile fabrication methods should be further explored for producing textile-based stress-sensor.

#### **2.4.6 Moisture Sensing**

Here novel textile and fiber-based moisture sensors will be reviewed. This text was reproduced with permission from<sup>[233]</sup> © 2020 WILEY-VCH Verlag GmbH & Co. KGaA, Weinheim. While fiber and textile-based sensors are like commercial moisture sensors in that they measure moisture according changes in resistance or capacitance, modes of fabrication and form factors vary quite significantly from commercial sensors. Wearable moisture sensors are designed to be soft and conformable to collect data in a non-invasive, and comfortable manner. In the field of fiber and textile based moisture sensors, most sensors are designed to measure RH, therefore RH sensors will be focus of subsequent discussion.

A number of concepts related to moisture and humidity are important for understanding the significance of wearable RH sensors.<sup>[234, 235]</sup> In the context of textiles, moisture is the amount of liquid water adsorbed or absorbed in the textiles. Humidity, on the other hand, is the amount of gaseous form of water present in the environment and can be measured in terms of either absolute humidity or RH. Needless to say, the amount moisture present in textiles is a function of the RH of the environment.<sup>[236]</sup>

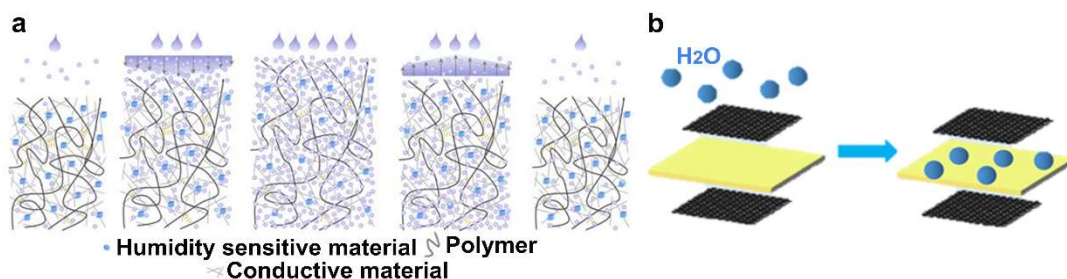


Figure 10: Schematics of common RH sensing mechanisms (a) Resistive RH sensing. Higher RH in environment results in more water captured by the hygroscopic material, increasing the distance between conductive particles and hence increasing the resistance. Reprinted with permission from<sup>[76]</sup> © 2017 Springer Nature. (b) Capacitive RH sensing. Higher RH in environment, more water captured by hygroscopic dielectric material (yellow layer), capacitance increases due to increase in dielectric constant. Reprinted with permission from<sup>[83]</sup> © 2017 American Chemical Society. Figure plate printed with permission from<sup>[233]</sup> © 2020 WILEY-VCH Verlag GmbH & Co. KGaA, Weinheim.

Some of the most common sensing mechanisms for textile-based moisture sensors include resistive,<sup>[76, 79, 86, 89-93]</sup> capacitive,<sup>[83-85, 87]</sup> and impeditive sensors.<sup>[237, 238]</sup> Other fiber-based sensing mechanisms also include optical fiber humidity sensors based on various principles of optical sensing such as optical absorption, gratings, interferometers, and resonators.<sup>[239-241]</sup> This section will focus on resistive and capacitive type RH sensors implemented in textile form factors, to limit the discussion. Resistive humidity sensors provide a change in resistance due to changes in conductivity while the capacitive sensors provide a change in capacitance due to the sensitivity of hygroscopic dielectric materials when in the presence of water.<sup>[234, 242]</sup> These sensing mechanisms are shown schematically in Figure 10. Subsequent sections will discuss the materials and fabrication methods employed to develop resistive and capacitive textile-based RH sensors.

#### 2.4.6.1 Resistive Relative Humidity Sensors

Most textile-based RH sensors operate via resistive sensing.<sup>[76, 79, 86, 89-93]</sup> Resistive textile-based humidity sensors typically consist of electrically conductive particles dispersed in a hygroscopic matrix material.<sup>[76, 89, 90, 92]</sup> When RH increases, the matrix material expands, thus increasing the distance between electrically conductive particles which results in an increase in electrical

resistance.<sup>[76, 89, 90, 92]</sup> Many resistive RH sensors utilize CNTs to impart electrical conductivity because CNTs provide stability, high conductivity, and relatively high RH sensitivity.<sup>[76, 89-93]</sup> Another popular material used for textile-based RH sensors is the ICP, poly(3,4-ethylenedioxythiophene–poly(4-styrenesulfonate) (PEDOT:PSS),<sup>[79, 86]</sup> which acts as both the conductive and moisture sensitive material.<sup>[79, 207]</sup> The PSS portion of PEDOT:PSS is hygroscopic and with increasing RH, water causes swelling and dissociation of PEDOT and PSS bond thus increasing bond energy between PEDOT chains and decreasing overall resistance.<sup>[243-245]</sup> PEDOT:PSS is a desirable material because it is solution processible, provides high conductivity and is environmentally stable.<sup>[79]</sup> However, PEDOT:PSS provides relatively low sensitivity at low RH levels.<sup>[243]</sup>

Primarily, polymeric materials have been utilized as the hygroscopic matrix component of resistive RH sensors. Polymers utilized include polyvinyl acetate (PVA),<sup>[90-92]</sup> Nafion,<sup>[89]</sup> and PLA.<sup>[93]</sup> PVA is a frequently used hygroscopic material for RH sensing because it contains a large number of hydroxyl groups making it a highly moisture swellable material, with the capability to undergo a tenfold increase in its volume in response to absorption of water.<sup>[90-92, 246, 247]</sup> PVA easily dissolves in hot water and can be applied to fiber or textile surfaces through coating processes.<sup>[92, 248]</sup> However, research employing PVA reports moderate to high RH sensing hysteresis as well as a greater swelling at high RHs meaning it provides lower sensitivity at low RHs.<sup>[92]</sup> RH sensors which rely on PVA for sensing report small sensing ranges typically above 60% RH.<sup>[90-92]</sup> Another matrix material employed for RH is  $C_7HF_{13}O_5S \cdot C_2F_4$ , otherwise known as Nafion. Nafion is a polyelectrolyte consisting primarily of hydrophobic (-CF<sub>2</sub>-CF<sub>2</sub>-) groups and relatively fewer ionic groups in the form of (-SO<sub>3</sub>-H<sup>+</sup>) which absorb moisture.<sup>[249, 250]</sup> Nafion is a desirable material for RH sensing because it exhibits high hydrophilicity,<sup>[251]</sup> chemical stability, small thermal

coefficient of expansion,<sup>[252]</sup> and good mechanical toughness.<sup>[253]</sup> Additionally, large sensing ranges and almost instantaneous response times have been reported when using Nafion.<sup>[89]</sup> However, when compared to PEDOT:PSS, PEDOT:PSS is more hydrophilic and hence better suited for sensing in excessively humid conditions while Nafion is more advantageous for dry-state sensing.<sup>[89]</sup> PLA has also been used as a matrix material due to its good water absorption properties and biodegradability, making it an environmentally conscious option.<sup>[254, 255]</sup> Additionally, PLA is advantageous for humidity sensing because it can be loaded with conductive particles and then processed via conventional textile processes such as melt-spinning.<sup>[93]</sup> However, sensors with PLA as a matrix can have a limited sensing range.<sup>[93]</sup>

Resistive textile-based humidity sensors have been fabricated through coating processes wherein the sensing material is applied on a pre-existing textile,<sup>[76, 79, 89-91, 210, 238]</sup> as well as in the structural form of fibers<sup>[93]</sup> and yarns.<sup>[92]</sup> Coating was one of the earliest methods of realizing RH sensors<sup>[79]</sup> and has remained a common method of fabricating fiber and fabric based RH sensors.<sup>[76, 89-91, 210, 238]</sup> Coating methods including dip-coating,<sup>[76, 79, 91]</sup> layer-by-layer,<sup>[89]</sup> knife-over-roll,<sup>[90]</sup> and screen printing<sup>[210]</sup> have been explored. In one of the early implementations, Daoud et al. dip-coated PA/spandex fabrics in PEDOT:PSS to create a fabric capable of sensing both temperature and humidity.<sup>[79]</sup> This sensing approach provided a large RH sensing range and linear sensing response.<sup>[79]</sup> Since this initial work, researchers have further explored dip-coating techniques for fabricating fiber and fabric based RH sensors.<sup>[76, 91]</sup> Ling et al. coated regenerated silk fibers (RSFs) with MWCNT/formic acid/Ca<sup>2+</sup> as shown in Figure 11a to create a sensor possessing a wide sensing range and a fast response time.<sup>[76]</sup> In another approach, Hee et al. dip-coated PET monofilament fibers in PVA and subsequently applied copper electrodes via RF magnetron sputtering, as shown in Figure 11b.<sup>[91]</sup> This sensor was only capable of monitoring RH

in a narrow range however, 50-500 cycles of bend testing was completed to indicate the fibers were sufficiently durable for wearable applications.<sup>[91]</sup> In another early effort, Shim et al. coated cotton yarns in a Nafion/CNT mixture<sup>[89]</sup> via a layer-by-layer dipping process. This sensor provided a wide sensing range and almost instantaneous response time.<sup>[89]</sup> However, the modulus of the yarn increased after coating which is not desirable for wearable applications which require flexibility and stretchability.<sup>[89]</sup> In more recent works, new coating methods have been explored including knife-over-roll techniques.<sup>[90]</sup> Cotton fabric substrates were coated with MWCNTs, PVA, 1,2,3,4-butanetetracarboxylic acid, and sodium hypophosphite monohydrate via a knife-over-roll approach.<sup>[90]</sup> However, this sensor only provided high sensitivity in a narrow RH range.<sup>[90]</sup>

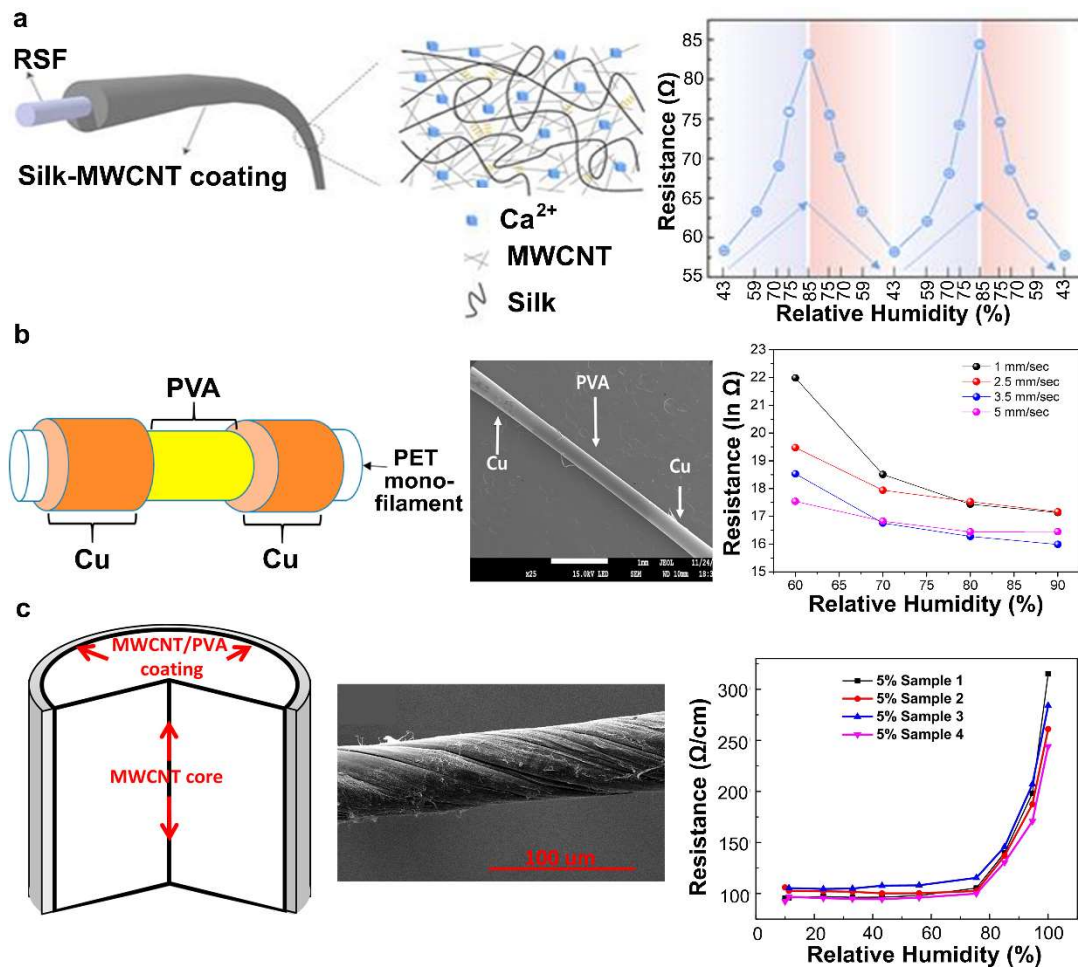


Figure 11: Fiber-based RH sensors and RH sensing results (a) RSF fiber coated in MWCNTs/Ca<sup>2+</sup>/silk coating to provide RH response. Reprinted with permission from<sup>[76]</sup> © 2017 Springer Nature. (b) PET fiber coated in PVA sensing layer and Cu sputtered electrodes and corresponding response to RH. Reprinted with permission from<sup>[91]</sup> © 2017 Elsevier B.V. All rights reserved. (c) MWCNT yarn and graphical representation of resistance change with RH. Reprinted with permission from<sup>[92]</sup> © 2016 Elsevier B.V. All rights reserved. Figure plate printed with permission from<sup>[233]</sup> © 2020 WILEY-VCH Verlag GmbH & Co. KGaA, Weinheim.

Fiber<sup>[93]</sup> and yarn<sup>[92]</sup> formation techniques have also been explored for resistive RH sensor fabrication. Devaux et al. developed a fiber-based RH sensors by dispersing MWCNTs into PLA with a twin-screw extruder.<sup>[93]</sup> Subsequently, the mixture was melt-extruded and drawn to form a fiber. The sensor provided repeatable results and a fast, reversible response. While this work is compelling due to its use of melt extrusion, a common process in the textile industry, the device only provided sensing capabilities in a narrow range. In other work, Wei et al. spun MWCNT yarns from a CVD and then coated the yarns in a PVA/MWCNT solution.<sup>[92]</sup> The yarn structure is

shown in Figure 11c. However, this approach is limited by its use of CVD which cannot be easily transferred to the textile industry. Additionally, sensors fabricated via this approach were only able to sense RH's above 75%.

Various performance parameters of resistive RH sensors have been reported including sensitivity<sup>[92]</sup> and response <sup>[76, 90]</sup> /relax times.<sup>[90]</sup> The only sensitivity value measured for textile-based resistive RH sensors was 1.89.<sup>[92]</sup> Response times ranging from 4s<sup>[90]</sup> to 30s have been reported.<sup>[90]</sup> Other sensor properties provided by researchers include modulus,<sup>[76, 89]</sup> breaking strain,<sup>[89]</sup> and durability.<sup>[91]</sup>

#### **2.4.6.2 Capacitive Relative Humidity Sensors**

Textile-based, capacitive RH sensors have been fabricated in parallel plate<sup>[83, 84]</sup> or interdigitated<sup>[210]</sup> configurations. Regardless of the sensor structure, capacitive RH sensors require a hygroscopic dielectric medium and conductive electrode materials. When the dielectric medium absorbs water, which possesses a dielectric constant of 80, the overall dielectric constant of the medium increases, which in turns increases overall capacitance.<sup>[83, 84]</sup> Textile-based, capacitive RH sensors have employed electrode materials Ag<sup>[84]</sup> and graphene.<sup>[83]</sup> Ag has been employed because it can be easily ink-jet printed onto fabric substrates<sup>[84]</sup> whereas graphene provides desirable electrical,<sup>[189, 192]</sup> mechanical,<sup>[190, 191]</sup> and optical properties.<sup>[193, 194]</sup> GO has also been used to fabricate flexible RH sensing devices due to its high sensitivity and response time,<sup>[256-258]</sup> however GO involves the use of toxic chemicals for fabrication and does not provide a linear change in capacitance with regards to changes in humidity, thereby making sensor calibration more complex.<sup>[83]</sup> The RH sensing techniques discussed here employ cellulose acetate butyrate (CAB) as the dielectric medium.<sup>[84, 85]</sup> CAB is an advantageous humidity sensing material because it easily

dissolves in many solvents, provides the best performance of cellulose derivatives, and is a well understood material that has been used for humidity sensing for many years.<sup>[84]</sup>

A commonly used method of fabricating capacitive textile-based RH sensors was previously discussed in 2.4.2.1, microfabrication techniques to create e-fibers.<sup>[84, 85]</sup> Conventional microfabrication techniques were utilized to create e-fibers using PI film strips. While this approach provided large RH sensing ranges, sensors fabricated with this approach reported excessively long response times as high as 16-17 minutes making them unsuitable for monitoring dynamic environments.<sup>[84]</sup> The long response time was attributed the fact that moisture absorption is dependent on the absorption properties of both the plastic PI substrate and the moisture sensing layer. Further, this fabrication technique is not scalable to textile manufacturing processes.

Recently, Zhao et al. created a parallel plate capacitor structure using mesh structure graphene woven fabrics (GWFs) electrodes and a CAB dielectric material.<sup>[83]</sup> Water molecules easily passed through the mesh-like structure of the GWFs and entered the CAB layer. Humidity sensing properties were demonstrated in a large sensing range with a sensitivity of 0.19 % / %. This work is particularly interesting because both humidity and temperature were monitored simultaneously. However, the GWFs were created in a CVD process requiring vacuum for fabrication.<sup>[259, 260]</sup>

While few researchers have explored capacitive, textile-based RH sensors, commercially, capacitive RH sensors make up more than 75% of the available humidity sensors<sup>[261]</sup> because capacitive RH sensors provide large sensing ranges,<sup>[262]</sup> low temperature dependence,<sup>[262, 263]</sup> and stability.<sup>[262]</sup> Therefore, there is great opportunity in further development of capacitive, textile based sensors.<sup>[83-85]</sup>

In conclusion, while many textile-based RH sensors have been proposed, many are disadvantageous due to limited production methods,<sup>[84, 85]</sup> and insufficient sensing ranges.<sup>[90-93]</sup> Most studies have been limited to coating processes.<sup>[76, 79, 89-91, 210, 238]</sup> While coating techniques are generally appealing due to their simplicity, they may reduce the breathability and comfort of a material. Additionally, coated materials typically possess a greater modulus compared to neat materials thus raising concerns regarding conformability. Further, current research is limited in durability testing including stretching, bending, washing, etc. therefore it is unknown if these sensors can withstand daily use. There is a need for improved textile-based humidity sensor research.

## **2.5 Summary and Outlook**

Amputees often experience discomfort when wearing their prosthetic devices. While wearing a prosthesis, an amputee's residual limb is exposed to an uncomfortable environment of stress<sup>[8, 22]</sup>, increased moisture (entrapment of sweat)<sup>[2, 19, 23]</sup> and temperature<sup>[3, 5, 24]</sup> which can lead to a range of issues including skin irritation,<sup>[3, 19, 27]</sup> pressure ulcers,<sup>[25]</sup> and life-threatening deep tissue injuries.<sup>[25]</sup> Currently, care providers address amputees' discomfort based on their intuition<sup>[100]</sup> and subjective patient feedback<sup>[35, 36]</sup> resulting in timely, costly, and generally inefficient fittings.<sup>[110]</sup>

Many of these issues could be potentially addressed using wearable sensors to continuously monitor the ISE. Currently, most sensors used for ISE monitoring are restricted to commercially available, rigid, semiconductor based sensors. While these sensors do provide some understanding of the ISE, they are generally disadvantageous due to their bulkiness,<sup>[10]</sup> weight,<sup>[11, 12]</sup> inflexibility,<sup>[6, 11, 12]</sup> low spatial resolution,<sup>[13]</sup> cost,<sup>[14, 15]</sup> and laborious integration methods.<sup>[16]</sup> Further, many sensors are uncomfortable for amputees during use<sup>[17]</sup> and irritate the user's skin.<sup>[18,</sup>

19]

Many of the shortcomings associated with rigid sensors used to monitor the ISE could be addressed using textile-based sensors. Rigid sensors do not possess required compliance for use at the residuum/socket interface<sup>[6]</sup> whereas textile-based sensors have the capability of being flexible and conforming to curved surfaces, such as the residual limb. Additionally, fiber or yarn based sensor configurations can be fabricated into high density, large-area arrays allowing for full mapping of the entire residual limb which is not possible with the relatively small area sensor mats currently on the market. Further, textiles are inherently comfortable and socially accepted in near-skin applications. Therefore, sensors could be placed within the socket environment rather than requiring mounting outside the socket which is a costly, laborious method which requires irreversible modification of the socket.<sup>[16, 119, 142]</sup> In summary, textile-based sensors offer great potential and many advantages for ISE monitoring applications but have yet to be explored for this application.

### **3 Textile-based Soft Sensors for Prosthetic Environment Monitoring Introduction**

As previously mentioned, there exists a great opportunity to explore textile-based sensors for ISE monitoring. Textile-based sensors present obvious advantages due to their compliant and breathable nature and as well as their relatively simple fabrication methods. Further, textile-based sensors provide opportunities for large-area sensing and unobtrusively mapping pressure of the entire residual limb by integrating sensors into existing textile prosthetic components like liners and socks. However, as previously discussed in Section 2.4.2, many of the methods proposed for developing textile-based sensors are limited due to their lack of scalability and applicability to textile processes which prevents widespread adaptation. Therefore, the objectives of this research are twofold:

1. Develop fully textile, scalable, and unobtrusive pressure sensors using conventional textile processes
  - Approach 1: Formulate textile sensors using sewn seam-lines
  - Approach 2: Fabricate uniquely shaped fiber sensors using tricomponent melt extrusion
2. Establish a systematic approach to integrating and evaluating textile-based sensors within the ISE
  - Approach 1: Evaluate sensors in simulated ISE utilizing an artificial limb
  - Approach 2: Evaluate sensors in simulated ISE utilizing bent-knee adapter and able-bodied subjects

To achieve these objectives, I propose two approaches to fabricating textile-based pressure sensors for ISE monitoring. The first is a capacitive sensor structure fabricated through a simple, and scalable sewing process using commercially available conductive yarns. In this architecture, the fabric serves as the dielectric medium and the conductive yarns serve as both capacitive “electrodes” for sensing as well as interconnect routes to external front-end circuits. The second sensor approach is a uniquely shaped fiber produced through a process commonly employed in the textile industry, melt extrusion. When woven into a fabric configuration, sensing pixels are formulated at each melt-extruded fiber crossover point. This fabrication provides a facile means of producing long-length fiber sensors with small diameters meaning large, highly dense sensor arrays can be easily configured. These sensing approaches will be further described in subsequent sections.

Additionally, I propose two preliminary experiments to work towards integrating the textile-based sensors within the ISE. To minimize the time required for validation of the proposed

sensors with an amputee participant, two preliminary evaluations are proposed: first, testing the sensors on an artificial limb followed by human testing with an able-bodied subject donning a bent-knee adapter to replicate the ISE. These preliminary evaluations will simulate the potential inner-socket pressures (artificial limb)<sup>[264]</sup> as well as gait patterns that could occur during amputee locomotion (able-bodied).<sup>[265, 266]</sup>

In the subsequent sections, I provide my research contributions towards creating flexible, textile-based sensors for ISE monitoring. These sections consist of four research articles: two have been published<sup>[20, 21]</sup> and two are in the publication process. The two published works explore the sewn, seam-line sensing approach including a comparison of sensing performance using different materials<sup>[20]</sup> and the integration of these sensors into prosthetics for pressure sensing.<sup>[21]</sup> The remaining articles, which are in the publication process, explore the creation of fiber-based sensors through melt extrusion. The first of these articles provides an overview of the material selection/characterization process and fiber manufacturing while the second provides an in-depth analysis of the fibers' sensing behavior. It is important to note that these research articles were written as stand-alone documents intended for separate publication, and therefore, some information and figures may be repeated.

#### **4 Fully-Textile Seam-Line Sensors for Facile Textile Integration and Tunable Multi-Modal Sensing of Pressure, Humidity, and Wetness**

In this section, textile-based sensors fabricated using ordered, sewn seam-lines is explored. This research was published in *Advanced Materials Technologies* and provides an overview of the sensing architecture, material selection, fabrication method, and sensing performance.<sup>[20]</sup>

Permission to reproduce this text was provided by<sup>[20]</sup> ©2020 WILEY-VCH Verlag GmbH & Co. KGaA, Weinhei.

## 4.1 Abstract

The unique potential of e-textiles for unobtrusive and ubiquitous monitoring and their innovative interfacing with electronic devices has garnished great attention. Sensors are one of the few essential devices or components necessary for most functional e-textile applications. Ideally, any e-textile based sensor should be soft, easily integrated in textile manufacturing processes, and tunable for the desired applications. Here, an easy-to-manufacture, tunable, fully-textile sensor system with capability of detecting pressure, humidity, or wetness is presented. Capacitive pressure sensors are formed via a traditional sewing process with two commercially available conductive sewing yarns (silver-plated polyamide (silver) and stainless steel (SS)) with cotton knit, polyethylene-terephthalate (PET) knit and elastomeric meltblown textile dielectrics. The relationship between the sensor's physical, mechanical, and electromechanical properties including hysteresis, sensitivity, response and relaxation time is evaluated. In addition, the same sensor configuration is assessed for its humidity and wetness sensing performance. Results indicate that pressure, relative humidity, and wetness sensing performance are easily tunable using different combinations of the conductive and dielectric textile materials. Finally, proof of concept deployment demonstrations as human-machine interfaces within a pressure sensing mat and a smart glove capable of remotely controlling a drone are provided.

## 4.2 Introduction

Textile based electronic technologies enable unique approaches for designing flexible, conformable, light weight sensors capable of detecting external stimuli including pressure,<sup>[48, 50, 53, 58, 68, 205]</sup> strain,<sup>[152, 232, 267-270]</sup> humidity,<sup>[92, 271, 272]</sup> and temperature.<sup>[70, 82, 273]</sup> Traditional sensors are made through relatively expensive and complex<sup>[148]</sup> microfabrication techniques requiring processes under vacuum and cleanroom environments.<sup>[84, 149]</sup> Whereas, e-textiles can be produced

via comparatively simple and lower-cost fabrication methods<sup>[234, 274]</sup> including coating,<sup>[58, 59, 176, 275]</sup> screen printing,<sup>[276, 277]</sup> fiber printing,<sup>[232]</sup> and atomic layer deposition processes.<sup>[57]</sup> While these production techniques are relatively straightforward, many require specially designed equipment<sup>[48, 232]</sup> or processes which makes accessibility, scalability or incorporation to conventional textile manufacturing processes more challenging;<sup>[48, 53, 57, 59, 68, 205, 275]</sup> thereby, limiting widespread adoption. While a few studies have utilized sewing and embroidery processes for textile-based sensing,<sup>[278-280]</sup> these studies did not explore the effect of textile material and physical parameters on capacitive sensing.

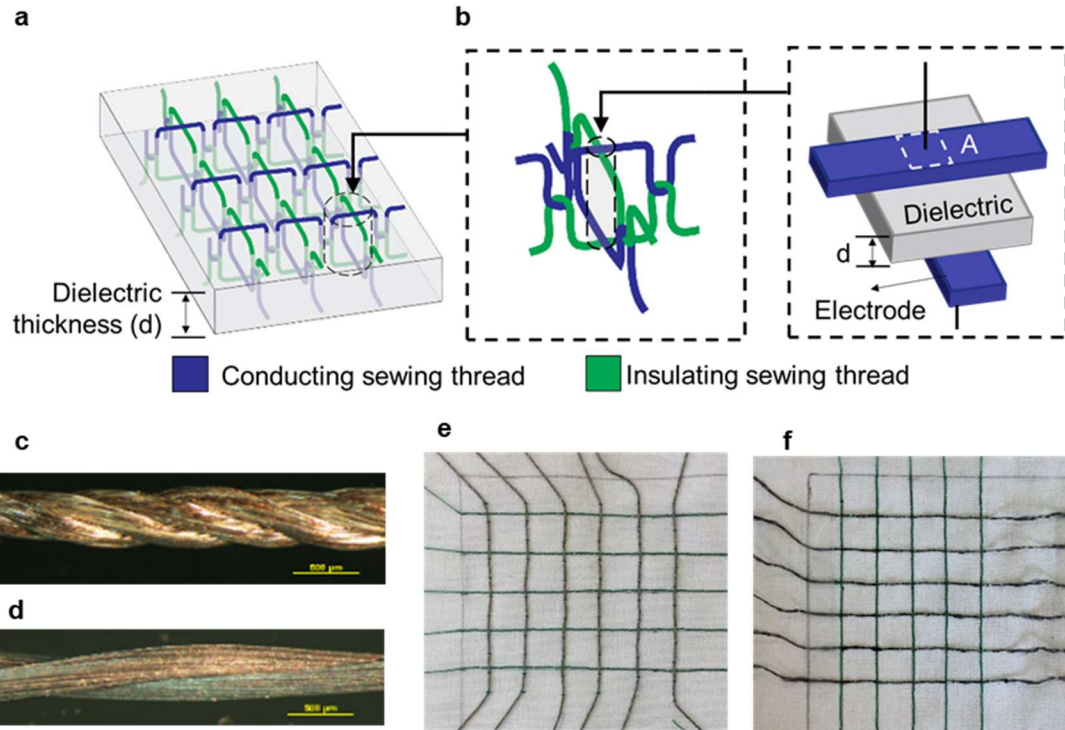


Figure 12: Sensor architecture and components (a) fabric-based distributed sensor network (b) schematic of fabric/thread-based parallel plate capacitor (c) silver threads at 40x magnification (d) SS threads at 40x magnification (e) SLS network produced with silver threads (f) SLS network produced with SS threads. Reprinted with permission from<sup>[20]</sup> ©2020 WILEY-VCH Verlag GmbH & Co. KGaA, Weinheim.

Here, we present a facile means of creating a textile-based sensor array capable of detecting pressure, humidity, or wetness. To achieve this, we fabricated a network of capacitive sensors consisting of sewn conductive threads, subsequently referred to as “seam-lines”, through a simple,

and scalable sewing process (see Figure 12). In this architecture, the fabric is the dielectric, and the conductive yarns serve both as capacitive “electrodes” for sensing as well as interconnect routes to external front-end circuits. In theory, this fabrication technique can be applied to any fabric substrate and sensor properties may be tuned by proper selection of the textile dielectric material and conductive yarn. Our previous publications introduced the general sensor structure and its ability to detect pressure, wetness and electrocardiograph signals.<sup>[281-283]</sup> These preliminary efforts lacked a standard manufacturing technique and analysis of the relationship between the sensing modalities and various fabric structures and conductive thread materials. In this new research, we focused on the use of a commercially viable and scalable process rather than more laborious hand-sewing. Additionally, we compared the performance of three textile dielectric materials (cotton knit, polyethylene-terephthalate (PET) knit, and Kraton meltblown) and two conducting yarns (silver-plated polyamide (silver) and stainless steel (SS)) on pressure, humidity and wetness sensing. A summary of the dielectric/electrode combinations studied is shown in Table 1. Cotton and PET textile dielectrics were selected because these polymers are commonly used in garments where the presented seam-line sensors (SLS) may be easily implemented for practical applications. Kraton (Kraton™ MD 1653, Kraton Corp.) is an elastomeric material consisting of a linear triblock copolymer based on styrene and ethylene/butylene. This material is expected to provide an elastic mechanical behavior particularly desirable for pressure sensing. The silver and SS yarns were selected because of their commercial availability, sufficient durability to withstand sewing processes, and relatively low electrical resistance.

Furthermore, we investigated the effect of material properties such as compressive modulus, mechanical hysteresis and moisture regain on sensor performance parameters such as pressure sensitivity, pressure hysteresis, humidity sensitivity and liquid absorption time. For proof

of concept demonstration of potential applications, we fabricated a 6×6 pressure sensing mat capable of detecting the location of pressure application. Additionally, we fabricated a touch-sensitive glove to provide a human-drone interface allowing the user to control a drone with sewn traces on a glove.

Table 1: Summary of samples and corresponding nomenclature Reprinted with permission from<sup>[20]</sup> ©2020 WILEY-VCH Verlag GmbH & Co. KGaA, Weinheim.

<b>Nomenclature (Dielectric-Electrode)</b>	<b>Dielectric Material (Fabric Type)</b>	<b>Electrode Material (Yarn Type)</b>
<b>Cotton-silver</b>	Cotton Knit	Silver
<b>Cotton-SS</b>	Cotton Knit	SS
<b>PET-silver</b>	PET Knit	Silver
<b>PET-SS</b>	PET Knit	SS
<b>Kraton-silver</b>	Kraton Meltblown Nonwoven	Silver
<b>Kraton-SS</b>	Kraton Meltblown Nonwoven	SS

### 4.3 Sensing Architecture

The sensor array was composed of multiple row and column conductors, or seam-lines, as illustrated in Figure 12. In this sensing architecture, spacing between the seam-lines is critical such that electrical shorting is avoided and should be selected based on the length of the sewn yarn stitches. At each crossover point in the array, a capacitive sensor was formed, subsequently referred to as a textile sensing element or “texel” similar to “pixel” referring to picture element in display technologies.<sup>[284]</sup> The texel’s response to applied mechanical deformations and humidity was measured from the changes in its capacitance.<sup>[282]</sup> A wetness texel is defined as the collection of four vertex texels formed using a pair of adjacent row and column conductors. The response to the presence of wetness was recorded using the resistance between the adjacent row and adjacent column conductors.<sup>[283]</sup> Since wetness uses adjacent threads for measurement, common mode rejection with pressure and humidity is possible - concurrent humidity and pressure applications do not change wetness measurements - but the reverse is not.

The simplified capacitive response of our sensor can be explained by the parallel plate capacitor model. A parallel-plate capacitive sensor consists of a dielectric layer sandwiched between two parallel conductive surfaces (electrodes), shown in gray and purple respectively in Figure 12 and b. The relationship between capacitance,  $C$ , vacuum permittivity  $\epsilon_0$ , dielectric constant  $\epsilon_r$ , area of the conductive electrodes,  $A$ , and the distance between the conductive electrodes,  $d$ , is described by  $C = \epsilon_0 \epsilon_r \frac{A}{d}$ . For textile-based capacitive pressure sensors, a mechanical deformation results in a change of  $\epsilon_r$ ,  $A$ , and  $d$ . This change defines the capacitance-pressure relationship. Humidity changes on the other hand, can be measured using capacitance due to the porous nature of textile materials and changing dielectric properties. With increasing relative humidity (RH), a greater amount of water enters the textile's pores thus increasing dielectric constant  $\epsilon_r$ . It should be noted that the total capacitance response of the sensor includes the baseline fringe capacitance formed by the row and column conductors outside of the sensing area.

It is noteworthy that, in the scope of this work, we considered the evaluation and deployment of these three sensing capabilities (pressure, humidity and wetness) individually and independently. The concurrent measurements, such as measurement of pressure while the humidity is changing or vice versa, would be possible by deploying the appropriate signal processing and statistical tools, which we kept beyond the scope of this paper.

#### **4.4 Results and Discussion**

In this section, we present the mechanical and electrical characterization results of the SLS assemblies and relate the sensor responses to the material properties. The results of mechanical and electromechanical experiments are summarized in Table 2 and Table 3.

#### 4.4.1 Characterization of Materials

Conductive yarns used in this research are displayed in Figure 1c and Figure 1d. The silver yarns were larger in diameter compared to the SS yarns ( $468.186 \pm 114.206$  versus  $387.847 \pm 28.961$   $\mu\text{m}$ ). This difference may cause some change in capacitive response due to the difference in electrode area. The electrical resistance values of the yarns were similar with the SS exhibiting greater resistance when compared to the silver yarn ( $0.29 \pm 0.033$  versus  $0.36 \pm 0.030$   $\Omega/\text{cm}$ ).

Differences in physical and electrical properties of the dielectric layers such as thickness, solidity, moisture regain, and dielectric constant were expected to alter the sensing behavior. Thickness of the fabric dielectric layer is critical as it affects the possible range of sensing. The cotton, PET and Kraton materials possessed thicknesses of  $1.10 \pm 0.02$ ,  $0.84 \pm 0.02$ ,  $1.82 \pm 0.05$  mm respectively. Solidity ( $\mu$ ) may be used to quantify the volume of fiber present in a textile structure relative to its air content.<sup>[285]</sup> It is calculated accordingly  $\mu = (M/V)/\rho_f = \rho_{fabric}/\rho_f$ , utilizing the mass of the fabric (M) and volume (V) of the fabric together with the density of the fiber ( $\rho_f$ ).<sup>[285]</sup> The  $\mu$  value of the Kraton meltblown fabric was the highest at  $19.97 \pm 0.46\%$  whereas the cotton and PET knit fabrics possessed  $\mu$  values of  $12.31 \pm 0.36$  and  $14.05 \pm 0.47\%$  respectively.

Moisture regain (%R) is defined as the amount of moisture present in a fiber under standard environmental conditions and is expressed as a percent of the bone dry weight of it. The value of %R and absorption/desorption behavior of the textile dielectric will vary depending on its constituents. Measured %R values confirm that cotton is a hydrophilic material with a %R of  $5.30 \pm 0.20\%$  whereas PET and Kraton are comparatively hydrophobic with %R values of  $0.79 \pm 0.07$  and  $0.72 \pm 0.01\%$  respectively.

The dielectric textile mediums possess three distinct dielectric constant values, thus altering the capacitive response of the sensors. As the porous structure of a textile fabric was compressed,

its air content decreased thereby changing its dielectric constant. For this reason, dielectric constant was measured under various levels of normal pressure. As expected, the dielectric constant of the textile samples increased with increasing compressive strain, as seen in **Figure 13a**. The dielectric constant of uncompressed cotton, PET, and Kraton fabrics were 3.35, 1.85, and 1.12 respectively. Dielectric constants of 6<sup>[286]</sup> 2.44<sup>[287]</sup> and 2-3<sup>[288]</sup> have been reported for raw cotton fibers, PET films and Kraton films respectively. The dielectric constant of the fabric structures is comparatively lower due to the porous nature of fabrics. At 50% strain, the dielectric constant of cotton increased by 30% followed by the PET and Kraton which increased by 18% and 9% respectively. Relative to Kraton, a much larger increase in dielectric constant is observed for cotton and PET fabrics. This can be due the larger air content within the cotton and PET fabric structures. Additionally, the changes in the dielectric constant of Kraton followed a linear trend while the increases in dielectric constant for cotton and PET were nonlinear. It is worth mentioning that the dissipation factor for cotton and PET increased for increasing strain but stayed at zero for Kraton as shown in Figure 19.

#### **4.4.2 Mechanical Properties of the Sensor Assembly**

Pressure sensing behavior of the seam-line sensors is mostly dominated by the compressive behavior of the constituent materials. Therefore, it is important to consider the mechanical properties of the samples, specifically the stress/strain behavior which is indicated by the force required to compress a sample. This is particularly important for a capacitive pressure sensor in which the capacitive response is greatly influenced by a change in the thickness of the dielectric medium, or the degree to which the sample is deformed with the applied force. The stress/strain relationship of a cotton-silver texel under cyclic compressive strain is shown in Figure 13b. While this graph presents the results of a single texel, it should be noted that all the tested textile dielectric

mediums and conductive yarn combinations exhibited similar trends in mechanical behavior as presented in Table 2. The samples displayed a bilinear stress/strain relationship which stabilized after the first strain cycle where the fifth and tenth cycles appeared essentially the same. The difference in behavior between first and subsequent cycles may be explained by the viscoelastic properties of the polymeric textile materials. In subsequent sections, we used results from the fifth strain cycle to compare the mechanical properties of each sample for consistency.

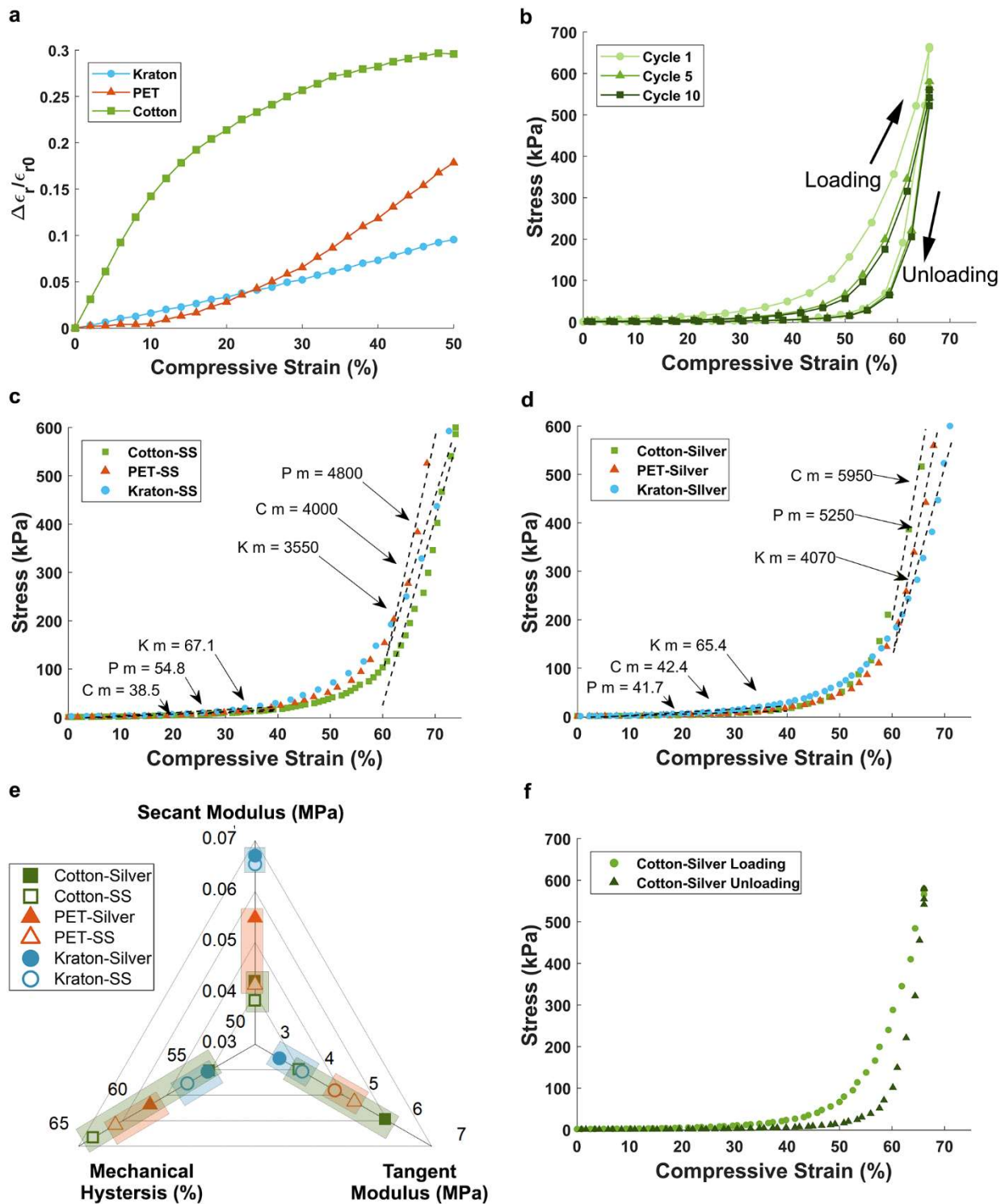


**Figure 13.** Dielectric properties of the textile mediums and mechanical properties of the seam-line sensors (a) change in dielectric constant of a textile dielectric layer under strain (b) stress/strain behavior of the cotton-silver sample (c) stress/strain behavior and moduli of samples produced with SS yarns (d) stress/strain behavior and moduli of samples produced with silver yarns (e) moduli and mechanical hysteresis values calculated for each sample (shaded regions group fabric dielectrics to aid in sample comparison) (f) mechanical hysteresis of a representative sensor. Reprinted with permission from<sup>[20]</sup> ©2020 WILEY-VCH Verlag GmbH & Co. KGaA, Weinheim.

The stress/strain relationships of a single texel of the SS yarn and silver yarn samples are provided in Figure 13c and Figure 13d, respectively. The stress/strain data obtained from three texels was used to calculate the average compression moduli of the materials. As illustrated by the stress/strain curves, there were two linear regions of mechanical behavior. The first was in compressive strain ranges of 0-40%, referred to as secant modulus, while the second was ranges of >60%, which is referred to as the tangent modulus. In the secant modulus region, the material was compressible thus, the modulus was much smaller than in the tangent modulus region when the fabric stiffened. When compressing the material within the secant modulus regime, it is likely that fibers were displaced and the pores within the textile structure were collapsing as air was removed. Rapid increase in tangent modulus was observed as the material essentially became solid with removal of air.

The calculated average secant and tangent moduli values are shown in Figure 13e . Moduli values of samples produced with SS versus silver yarns in secant modulus regimes were similar, however SS samples often provided higher moduli. This was expected, as SS is a higher modulus material when compared to polyamide used in the silver thread. The tangent modulus of samples produced with silver yarns was greater compared to sensors fabricated with SS. This could be due to the fiber constituents and yarn structure. The silver yarns contained a greater number of plies and filaments, as well as a greater level of twist (see Figure 12c,d) compared to SS yarns.

Another important parameter in the design of sensors is the mechanical hysteresis because these devices are expected to experience cyclic loading and unloading during practical use. Ideally, the seam-line sensor structure would be perfectly recoverable during cyclic testing such that the sensor output would be the same regardless of whether the sample is being loaded or unloaded. However, as textiles are viscoelastic, polymeric materials, their behavior during loading and

unloading is expected to vary because energy is expended during loading to overcome internal friction, whether at the polymer, fiber, yarn or fabric level, which cannot be fully recovered during unloading.<sup>[289]</sup> Therefore, it is important to quantify and understand this behavior such that it can be accounted for during signal processing and sensor calibration. One of the measures of mechanical hysteresis is the fractional energy that is lost or dissipated during the loading-unloading cycle. The lost energy may be dissipated as heat or in the form of other morphological changes in the material. Consequently, part of the deformation may not be recoverable. Hysteresis can be calculated from the unrecovered work, expressed as a percent of the work done in the loading cycle. In this research, hysteresis was calculated as,  $Hysteresis = \frac{\int Unloading - \int Loading}{\int Loading} \times 100\%$ , where  $\int Unloading$  is the area under the unloading curve and  $\int Loading$  is the area under the loading curve.

Mechanical hysteresis values provided in Figure 13e were calculated using loading/unloading curves such as those shown in Figure 13f. Hysteresis values were similar regardless of conductive yarn type when considering Kraton and PET samples. However, cotton-based samples demonstrated a different trend with yarn type influencing the degree of hysteresis apparently. It should be noted that the cotton-silver samples possessed the greatest degree of statistical variability so this apparent trend may be misleading. In general, samples with Kraton yielded the smallest hysteresis (with the lowest deviation) when disregarding the statistically variable cotton-silver sample. Kraton is an elastomeric material which means that its polymer chains readily and reliably respond to strain with little permanent deformation during cyclic exposure. Thus, Kraton polymer chains more readily return to their original position when compared to non-elastomeric materials like cotton and PET.<sup>[290]</sup> The low hysteretic behavior of Kraton samples may also be attributed to their fabric structure. Meltblown structures consist of micron-scale fibers which are extruded and collected on a screen while in a molten state. Once

cooled, the fabric consists of a large number of fiber-to-fiber contact points.<sup>[291]</sup> Fused fiber-to-fiber contact points may have provided the meltblown fabric with a more spring-like nature compared to PET and cotton knit structures. Within knit structures, yarns may easily slip past one another without recovery, thus providing greater hysteresis and greater material variability.

#### **4.4.3 Electromechanical Characterization of Seam-line Sensors**

The mechanical deformations applied on the seam-line sensors result in a change in capacitance formed at each texel. In this section, we evaluate this electromechanical relationship and relate the results to the mechanical characterization provided in the previous sections.

##### **4.4.3.1 Sensitivity**

The basic sensor response of the cotton-silver sample to cyclic pressure is shown in **Figure 14a**. Similar to the compressive strain-cycling curve given in the previous section, the sensor response to varying pressure was bilinear and stable after the first cycle for all the samples. We used the results from the 5<sup>th</sup> cycle to compare the sensor responses of each sample. The slope of the sensor response is generally defined as the sensitivity of a sensor. A sensor with a higher sensitivity is more desirable because it is less susceptible to environmental noise. The sensitivity is, therefore, formulated as  $\Delta C/\Delta P$ , where  $\Delta C$  is the change in capacitance and  $\Delta P$  is the change in pressure.<sup>[292]</sup> We selected this sensitivity equation without baseline normalization since the baseline capacitance is highly dependent on empirical parameters such as the textile dielectric layer thickness variation and tightness of the stitch which are difficult-to-control and would vary from sample to sample.

Figure 14b and Figure 14c respectively illustrate the sensor responses and average sensitivity values of representative texels from the SS yarn samples and the silver yarn samples to varying pressure. The bilinear trend of the sensor response shown in these figures indicated a major correlation between the mechanical stress/strain results and electromechanical sensor response. In

low-pressure regions (<50 kPa, <40% strain), the high sensitivity was likely due to the compressibility of the samples. In higher-pressure regions (>100 kPa, >60% strain), air was essentially removed from the sample which increased sample stiffness and reduced sensitivity. As an application note, the first linear region of the sensor response captures most of the low to medium pressures such as object manipulation<sup>[293]</sup> and the second region covers more rigorous pressures such as measuring the interfacial pressures in a prosthetic limb.<sup>[294]</sup>

Across all of the samples, the silver yarn samples provided higher sensitivity than the SS yarn samples in both linear regions. For the first linear region, this performance difference was likely related to the compressibility difference of the silver samples discussed in the previous section. In the second region, we expected a lower sensitivity from silver yarn samples because of higher modulus observed in the previous section. However, the sensitivity of the silver yarn samples were higher, which would indicate that another parameter affected the sensitivity performance other than the compressibility of the electrode material. We assume that this performance difference is related to the deformation of the yarn or the electrode area change under compression. The silver yarn possessed a higher diameter and more filaments than the SS yarn. Therefore, under compression, the silver yarn electrode area increased more significantly, which resulted in a greater change in capacitance and thus a higher sensitivity.

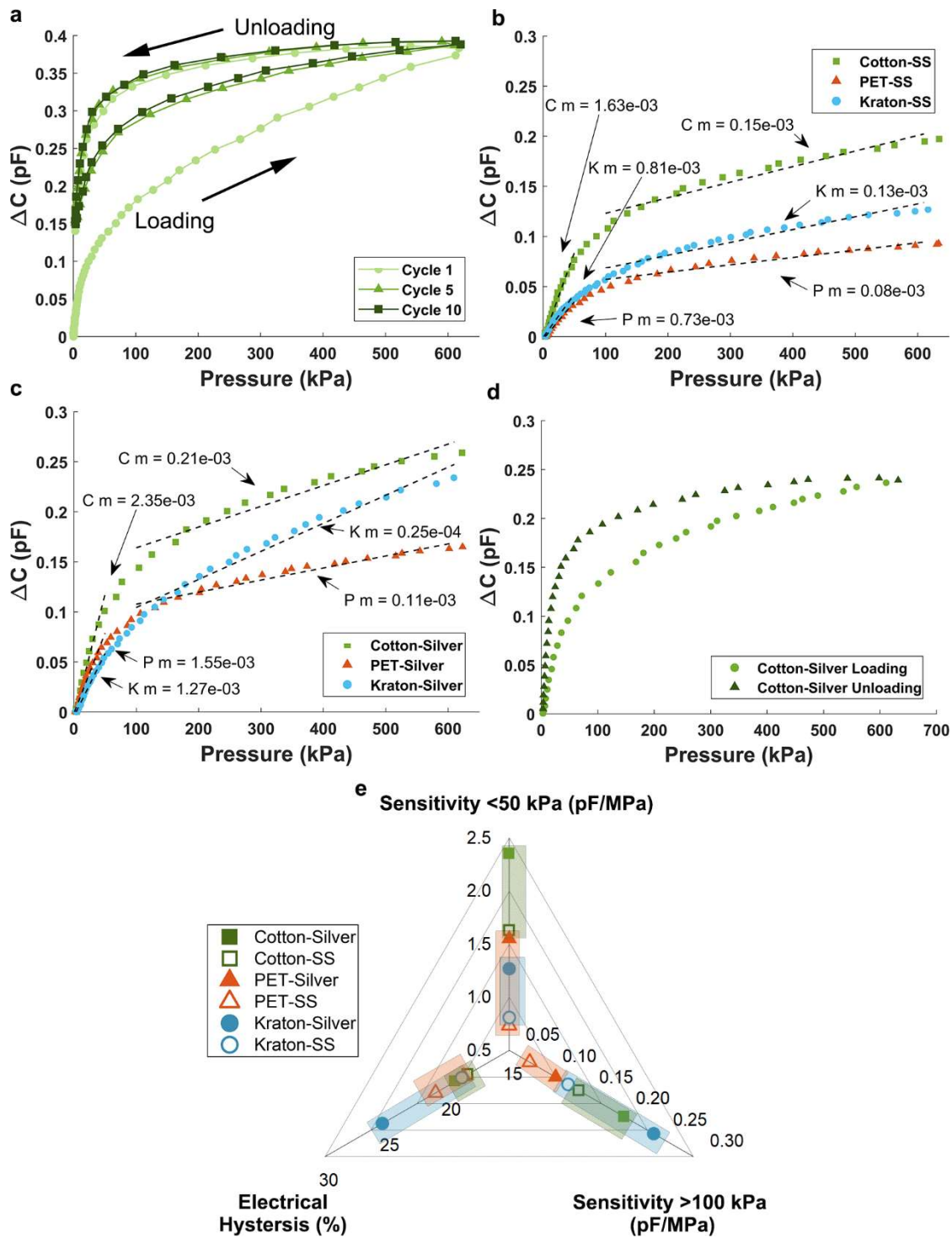


**Figure 14.** Sensor properties (a) electromechanical response of the cotton-silver sample (b) electromechanical responses and sensitivities of samples produced with SS yarns (c) electromechanical responses and sensitivities of samples produced with silver polyamide yarns (d) hysteresis of a single representative pixel (e) sensitivity and electrical hysteresis values calculated for each sample (shaded regions group fabric dielectrics to aid in sample comparison). Reprinted with permission from<sup>[20]</sup> ©2020 WILEY-VCH Verlag GmbH & Co. KGaA, Weinheim.

For the first linear region, samples consisting of a cotton dielectric layer demonstrated the best sensitivity performance. Some of this performance difference was likely due to the higher compressibility of cotton samples observed in the previous section. However, this compressibility difference was small; therefore, we assume that the main source of this performance difference is the dielectric constant increase observed in Figure 2a. The first linear sensitivity region contains strains less than 50% , which, according to Figure 2a, corresponds to a 30% increase in dielectric constant for the cotton dielectric layer. This increase in dielectric constant is the highest among the other textile dielectric mediums. The dielectric constant increase for cotton saturated after 50% strain which is when the performance of the cotton samples were similar to PET and Kraton dielectric samples. In higher pressure regions, Kraton samples performed better with Kraton-silver being the best performing sample. This response was caused by the Kraton's ability to remain relatively compressible with a lower tangent modulus as observed in the previous section, thereby, allowing this dielectric medium to perform better in high pressure regimes. The cotton and PET materials are highly compacted at the high pressure regimes, thus providing a lower sensitivity.

#### **4.4.3.2 Hysteresis**

Electromechanical hysteresis describes the difference in two sensor values during mechanical loading (pressure application) and unloading (pressure relaxation).<sup>[124]</sup> Lower hysteresis is always desirable for a sensor since it increases the accuracy of measurements. Here, electrical hysteresis was calculated using the same approach as mechanical hysteresis, as described in Section 4.4.2. Figure 14d shows the sensor response of the cotton-silver sample to consecutive loading and unloading cycles under normal pressure. The average hysteresis values are reported in Figure 14e. Overall, the electrical hysteresis values of all of the samples were similar to each other with only a 12% coefficient of variation. For the cotton and Kraton materials, samples produced with silver

yarn exhibited greater hysteresis than the SS yarn. This increase in hysteresis may be explained by the compressible nature of the silver yarn that adds to the time needed for the sample to come back to its original shape after a pressure cycle. For applications requiring high accuracy, the electromechanical relationship of the sensor can be modeled to predict and reduce the effects of hysteresis during use.<sup>[53]</sup>

#### **4.4.3.3 Dynamic and Cyclic Loading Response**

In order to visualize the transient sensor response and any possible sensor drift, we applied various loads on the silver thread samples in a dynamic load response experiment. The response of the cotton-silver, PET-silver, and Kraton-silver samples to dynamic loads are shown in Figure 15a-c respectively. A baseline capacitance increase was observed for all samples during the first pressure cycle. This was most likely due to the viscoelastic properties of the polymeric textile materials as mentioned previously. The cotton and PET samples demonstrated the highest baseline increase. This was likely due to polymer structure of cotton and PET samples. Cotton and PET samples were likely unable to recover from cyclic testing thus resulting in a baseline shift. This phenomenon was not observed for Kraton samples. Kraton is a crosslinked elastomeric material which provides desirable polymer chain recovery. This is reflected in Figure 15c which demonstrates minimal baseline movement over the course of testing.

In order to observe the stability and reliability of the sensors, all samples were subjected to extended cycling tests (1,000 cycles at 12 kPa to 50 kPa). All samples provided repeatable results and continued working without damage after experiments. The results indicate that the response range for all samples decreased and stabilized above cycle 300, see Figure 20. The response range decreased more dramatically for samples containing the silver-thread. This follows the general trend that silver-thread samples exhibited higher hysteresis and a higher response/relaxation time

(investigated in the next section). We believe this is due to the relatively elastic nature of the SS yarns in low strain regime. Another outcome of this study was that the baseline shifted for all samples and stabilized above cycle 600, see Figure 21. Changes in response range and baseline shifts can be explained by the viscoelastic properties of textiles that result in time-dependent recovery as well as non-recoverable deformation. This is also evident in the shorter cycle times as the number of cycles increased, as shown in Figure 20 and Figure 21. For applications requiring more accurate cyclic pressure measurements, the samples can be preconditioned, or the cyclic pressure response can be modeled. Without preconditioning, the sensors can still be used to detect the presence and location of certain levels of pressure as shown in the applications section of this paper. It is important to mention that this was a preliminary experiment to study the response range change and baseline drift under extended cycling. Further experiments are required to fully understand the stability and reliability under extended cycling, and this was kept beyond the scope of this work.

#### **4.4.3.4 Response and Relaxation Time**

Response and relaxation time parameters define how fast the sensor responds to mechanical loading and unloading respectively. Figure 15d and Figure 15e show the response and relaxation time results of the cotton-silver sample. The average response and relaxation times of the samples are reported in Figure 15f. In general, the relaxation times were higher than the response times. We believe that this is a direct result of the hysteresis observed in the previous section. Among the yarn types, the response and relaxation times for the samples made with SS yarn were in general lower than the samples made with silver yarn. We believe that this was because of the compressibility of the silver yarn which recovered to its original shape slower than the SS yarn.

We observed similar response and relaxation time performances among different dielectric textile mediums.

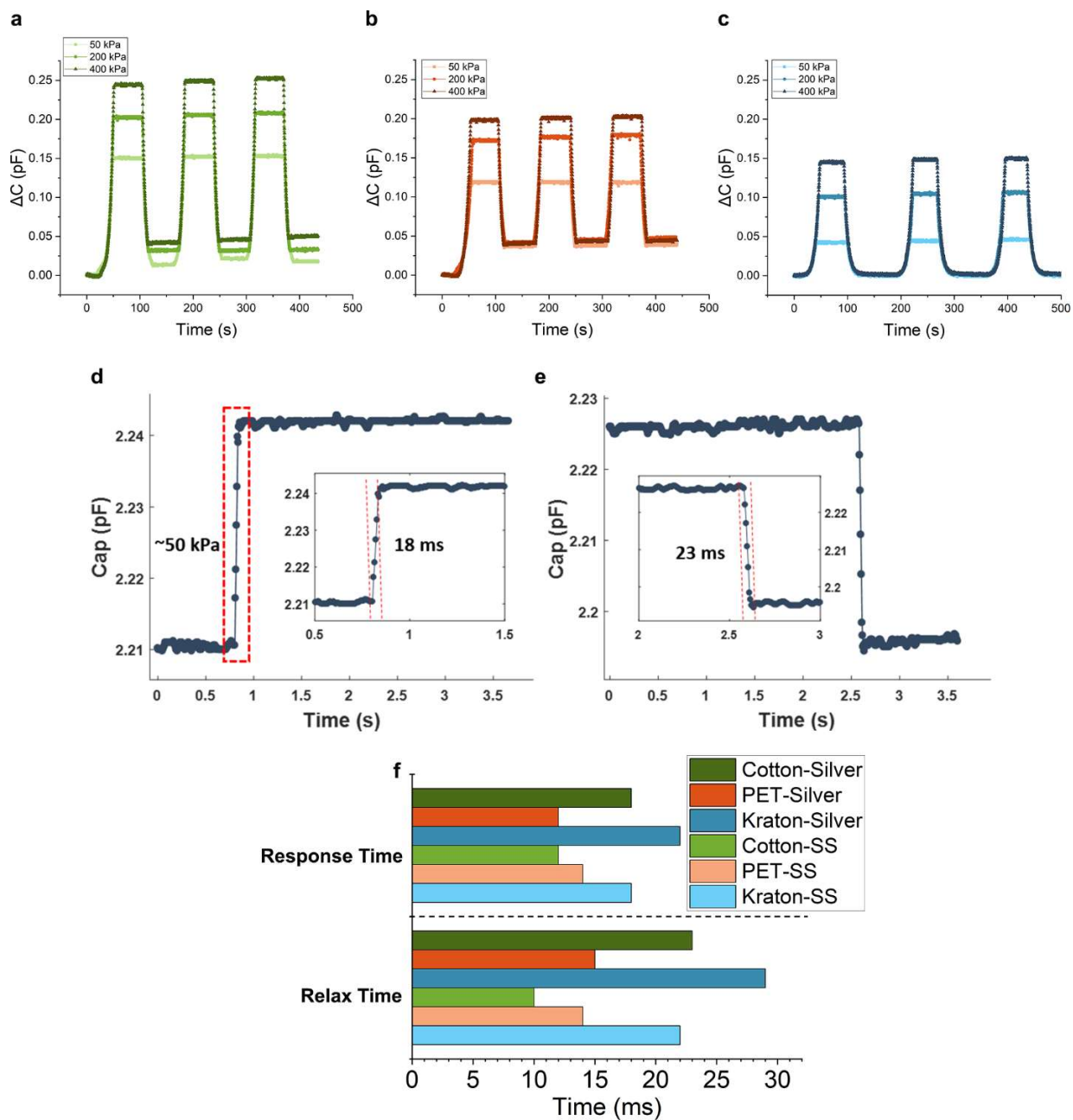


**Figure 15.** Dynamic response and response/relax time of seam-line sensors (a) dynamic response of cotton-silver samples (b) dynamic response of PET-silver samples (c) dynamic response of cotton Kraton-silver samples. (d) Response and (e) relaxation time of the cotton-silver sample for loading and unloading of ~50kPa (f) graphical representation of average response/relax times of each sample. Reprinted with permission from<sup>[20]</sup> ©2020 WILEY-VCH Verlag GmbH & Co. KGaA, Weinheim.

#### 4.4.4 Relative Humidity and Wetness Sensing

Textile based sensors have been explored for RH monitoring<sup>[92, 271, 272]</sup> and wetness detection, specifically sweat detection<sup>[163, 295]</sup> because such sensors can provide valuable information regarding an individual's thermal comfort.<sup>[296, 297]</sup> as well as health conditions, emotional states, and exercise levels.<sup>[298, 299]</sup> We evaluated the samples' abilities to sense RH and wetness since the seam-line sensors described here may be easily integrated into clothing and serve as promising candidates for wearable environment monitoring or wetness detection. Alternatively, moisture insensitive materials can be used or the sensor can be sealed completely in applications where the effects of RH and wetness need to be reduced. In the sensor configuration proposed here, a hydrophilic or hydrophobic textile dielectric layer could be chosen for the desired sensing application accordingly.

The experimental setup for humidity sensing and influence of humidity on samples' capacitive responses are shown in **Figure 16a** and Figures Figure 16b-d respectively. The results indicate that the capacitive response of cotton-based samples was far more influenced by elevated RH when compared to PET and Kraton samples. The cotton material, which possessed a larger %R value, was also more prone to retain moisture from its environment when compared to PET and Kraton. With increasing RH, a greater amount of water, which possesses a dielectric constant of ~80, entered the textile structure which in turn increased the overall dielectric constant and the resulting capacitance. The PET sample provided an intermediate response to humidity meaning it was less sensitive to humidity than cotton but more sensitive than Kraton. These results correspond to the fabrics' %R values with cotton possessing the largest %R, Kraton providing the least %R, and PET providing intermediate %R. Therefore, cotton was a better material for humidity sensing applications thanks to its higher sensitivity. Kraton, on the other hand, could be used for pressure

sensing applications where coupling to humidity needs to be minimized. For an intermediate response, PET could be employed.

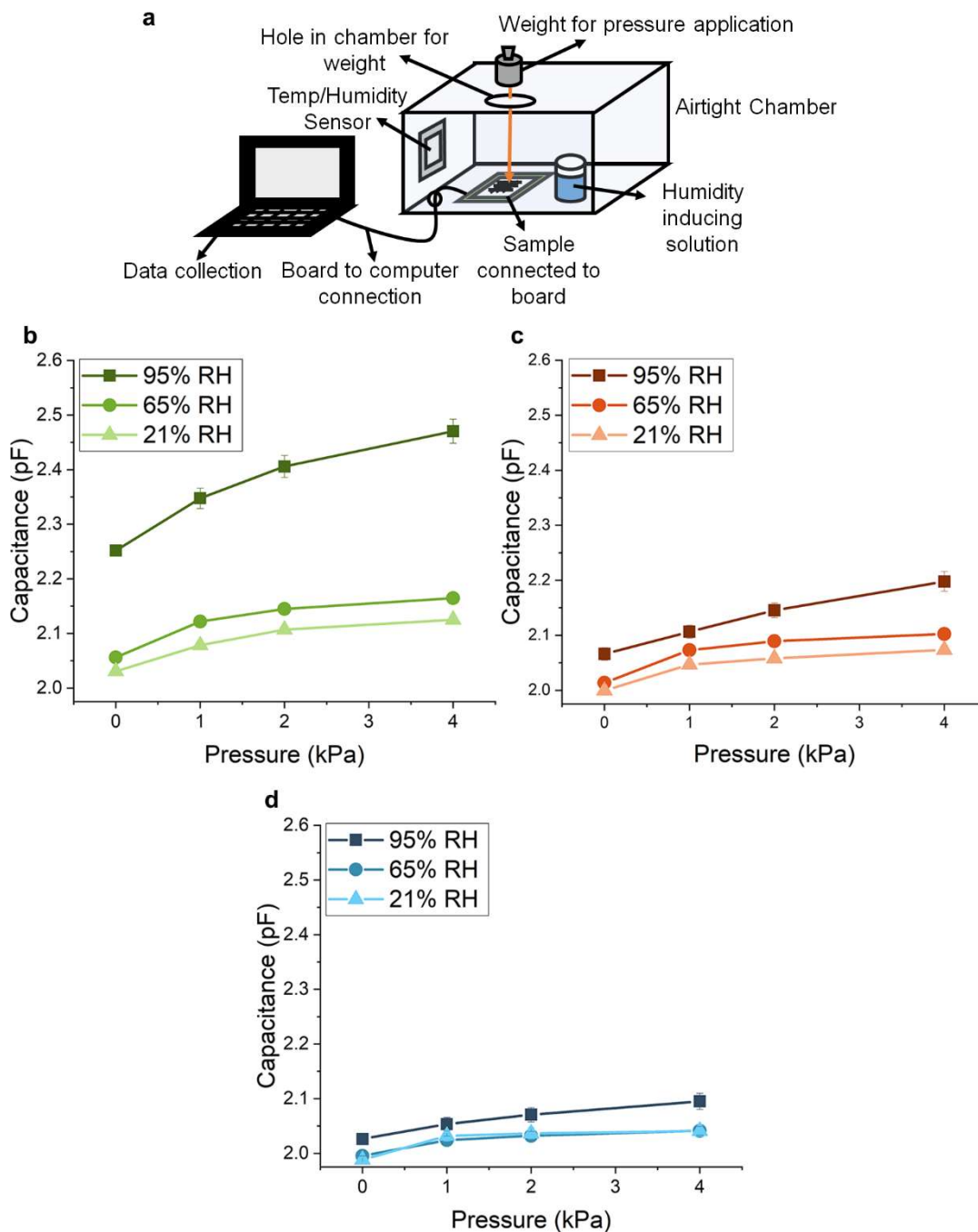


**Figure 16.** Relative humidity sensing (a) RH test set up (b) capacitive pressure responses of cotton-silver samples at various humidity levels (c) capacitive pressure responses of PET-silver samples at various humidity levels (d) capacitive pressure responses of Kraton-silver samples at various humidity levels. Reprinted with permission from<sup>[20]</sup> ©2020 WILEY-VCH Verlag GmbH & Co. KGaA, Weinheim.

**Figure 17** shows the wetness sensing evaluation for all the sensors. The impedance response of the row pairs (top side) are shown along with the impedance response of the column pairs (bottom side) in each sample. Figure 17 also contains inset pictures of each sample approximately one minute after the DI water application. The results indicate that the impedance of the top side for all samples started decreasing as soon as the DI water was applied on the sample. The bottom side impedance decreased slower as the DI water was absorbed through the fabric material. We defined full absorption time of DI water as the point at which the impedance of the top side and the bottom side were within 10% of their minimum value. The average absorption time for cotton-silver, cotton-SS, PET-silver, PET-SS, Kraton-silver and Kraton-SS samples were determined to be 5.7, 17.2, 0.5, 3.3, 15.9 and 19.7 m respectively (Figure 17). All of the samples dried within one hour of DI water application. The dry impedance readings contained more noise in the readings, however it was possible to distinguish wet regions and absorption times.

Even though absorption time varied, all of the samples exhibited potential to be used to detect the presence of wetness. Among the fabrics, the absorption time for PET was quickest based on the impedance readings and visual observations during the DI water application. It was anticipated that the cotton fabric would provide the fastest absorption due to its traditional hydrophilic nature. However, it was observed that the cotton samples provided relatively long absorption times. This may be explained by wax and grease applied on the surface of commercial cotton fibers/yarns which may increase the contact angle and hinder fabric wetting. Scouring, a common high temperature cleaning process used for cotton, is completed to remove waxes, greases and other debris. It has been determined that scouring reduces the contact angle of cotton thus improving fabric wettability.<sup>[300]</sup> Therefore, it is possible that the absorption of the cotton material could be improved with scouring or another high temperature cleaning process. Alternatively, the

high absorption time may be explained by residual stiffening product within the fabric structure which may have prevented water penetration (see Experimental Section). Similarly, Kraton-based samples displayed long absorption times. Depending on the desired wetness sensing properties, an appropriate textile material could be selected as the dielectric layer.

The results show a difference of absorption rate between the two yarns used. Samples constructed with silver polyamide yarns absorbed the liquid faster than the samples with the SS yarn. Polyamide absorbs water relatively easily when compared to a metallic material like SS. Therefore, it can be speculated that the yarns aided in the absorption process.

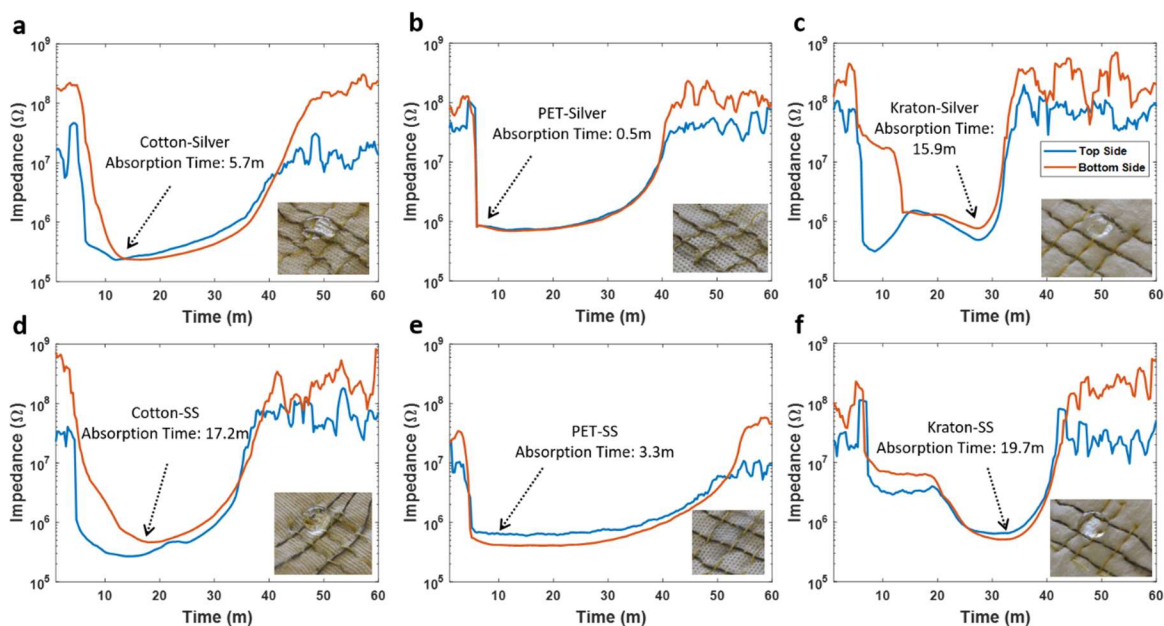


**Figure 17.** Wetness sensing performance of the various samples tested. Sample pictures ~1m after DI water application is given as insets. Average absorption time is found at the lowest impedance response of the top and bottom yarn in the sample (N=3). (a) cotton-Silver (b) PET-Silver (c) Kraton-Silver (d) cotton-SS (e) PET-SS (f) Kraton-SS. Reprinted with permission from<sup>[20]</sup> ©2020 WILEY-VCH Verlag GmbH & Co. KGaA, Weinheim.

#### 4.5 Proof of Concept Demonstration

To demonstrate some potential applications, we fabricated a pressure mat and a touch sensitive glove based remote controller. These are provided as proof of concept examples which would benefit from further optimization.

### 4.5.1 Pressure Mat

Here, we demonstrate the ability of the flexible, seam-line sensors to act as a pressure sensing mat. Such pressure mats may be useful in applications such as bedsores monitoring, gait analysis or building occupation management. We manufactured a fabric sensing mat containing 6 columns and 6 rows for a total of 36 texels (see **Figure 18**). We used cotton and silver yarns as this dielectric/electrode material combination displayed the greatest sensitivity in low pressure regimes and provided the best match for the anticipated pressures in this demonstration. A 100g weight (corresponding to 9.8 kPa) was placed on various sensing point locations on the pressure mat to demonstrate each sensor's ability to detect the corresponding pressure. We designed a custom data acquisition system (10 cm x 10 cm printed circuit board) to measure the individual capacitance values of the pressure mat. The data acquisition system included a Bluetooth enabled microcontroller module (Simpler RFD77001, Hermosa Valley CA), a capacitance to digital converter (Analog Devices AD7142, Boston MA), two quad analog switches for multiplexing (Analog Devices ADG788, Boston MA) and screw terminal blocks for PCB connection with row and column threads. We programmed the data acquisition system to continuously digitize and transfer the capacitive sensor readings to a computer. To remove possible interference and crosstalk between parallel threads, we programmed the data acquisition system to ground unused rows and columns during multiplexing. The sensor readings were logged at the computer.

Each sensing point was able to clearly reflect the location of the applied pressure, circled in red in Figure 18a-e. As shown in this Figure, the sensing point near the center of the placed weight showed the largest change in capacitance with pressure application. Surrounding texels in the same row or column experienced smaller increases in capacitance with the application of the weight. This can be explained by the dynamics of the sensor structure: because rows or columns

are made up of a single conductive sewing yarn, when a weight was applied to one texel it caused a slight movement in the conductive yarn in all the texels within the corresponding rows and columns, thus resulting in a relatively small capacitance increase. Also, the measurements conveyed a small variation in the read capacitance for the same applied weight. When the weight was applied to different texels, the average  $\Delta C$  was  $0.107 \pm 0.013$  pF at the center of pressure application. This small variation is likely due to the variable properties of textile materials. Variance in thickness, mechanical properties of the dielectric medium or electrode materials may lead to differences in the sensitivity of each texel. In our future design optimization studies, this will be accounted for in the sensor calibration process. During experimentation, we observed a small sensor response to bending deformations. This response requires additional experimentation to optimize the sensor structure for compliant applications. It is noteworthy that this simple integration of conductive seam-lines into a fabric-based, pressure sensing mat provides the advantage of scalability. A fabric mat of any size could easily be produced with tunable sensing properties based on the selected material as the dielectric layer. Additionally, the density of the sensing texels may be easily tailored by altering the stitch length and pitch between sewn conductive lines.

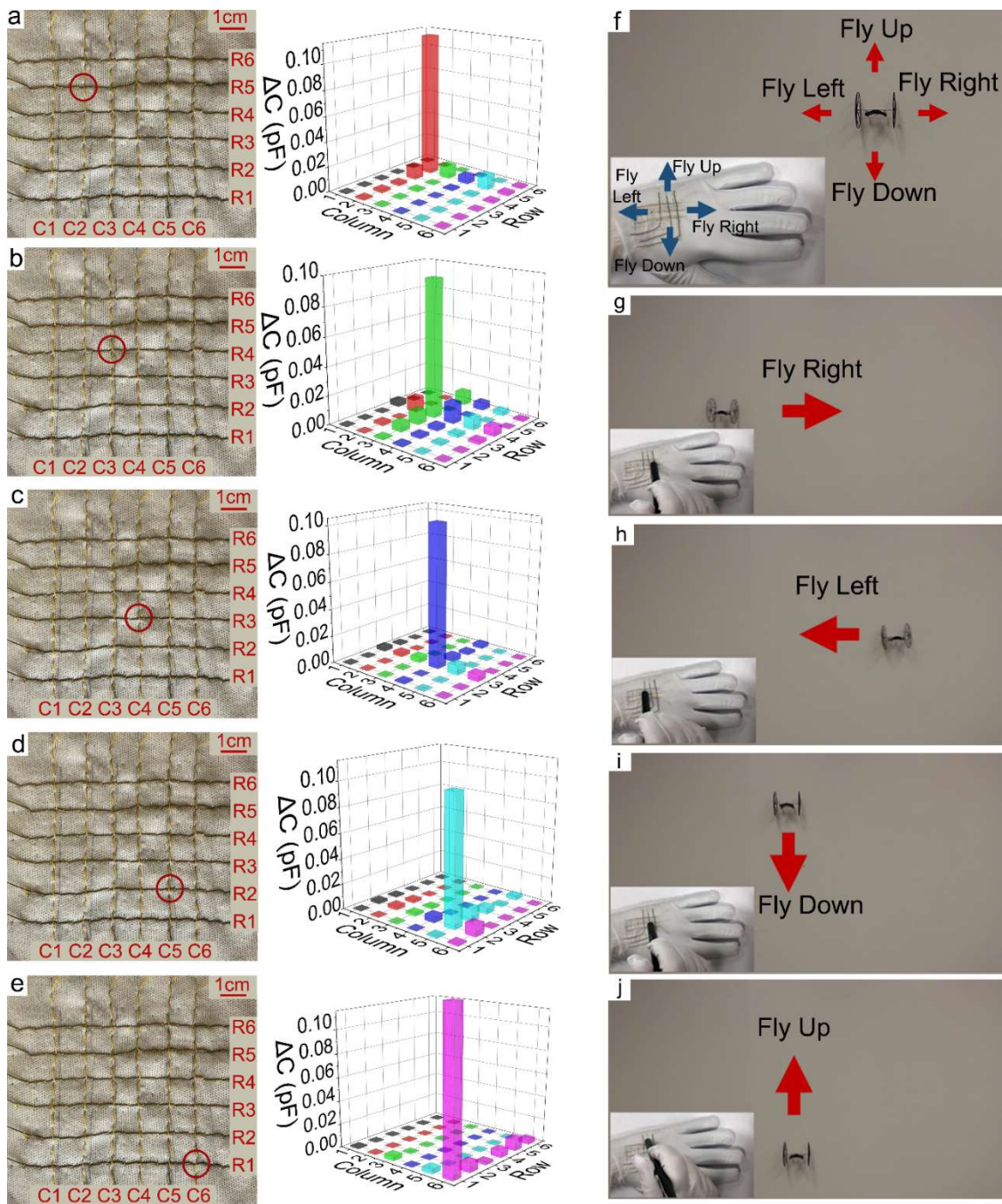


**Figure 18.** Proof of concept demonstrations (a) pressure application on pressure sensing mat - row 5, column 2 (b) pressure application on pressure sensing mat - row 4, column 3 (c) pressure application on pressure sensing mat - row 3, column 4 (d) pressure application on pressure sensing mat - row 2, column 5 (e) pressure application on pressure sensing mat - row 1, column 6 (f-j) demonstration of drone being operated by a wearable sensor interface. Reprinted with permission from<sup>[20]</sup> ©2020 WILEY-VCH Verlag GmbH & Co. KGaA, Weinheim.

#### 4.5.2 Wearable Human-Machine Interface

To demonstrate the use of this sensing principle for a remote-control application, a 3×3 pressure sensor array was sewn onto the dorsal side of a PET glove to act as a remote controller for a quadrotor drone (Rolling Spider, Parrot SA, Paris). To increase the performance of the sensor against any environmental electromagnetic noise, we used silver yarns as the conductive material which demonstrated higher sensitivity within lower pressure regimes corresponding to touch. After the sensor fabrication, we used the silver yarn as the interconnect for easy integration with our second custom data acquisition system (2.5 cm x 2.5 cm printed circuit board). The data acquisition system for this application included a Bluetooth enabled microcontroller module (Simpler RFD77001, Hermosa Valley CA), a capacitance to digital converter (Analog Devices AD7142, Boston MA), a quad analog switch for multiplexing (Analog Devices ADG788, Boston MA). Like the pressure mat application, the data acquisition system was programmed to continuously digitize and transfer the capacitive sensor readings to a computer. Unused threads were connected to ground during multiplexing to remove interference and crosstalk between parallel threads. At the computer, the sensor readings were mapped to Bluetooth control commands to wirelessly control the drone near a white colored wall where the protective wheel around the drone avoided wall collision. We used only four of the nine sensing points to move the drone in four directions (top sensing point to fly up, bottom sensing point to fly down, right sensing point to fly right and left sensing point to fly left). The successful remote control of the drone is shown in **Figure 18f-j**. In applications where a bare human hand will contact the sensor array, an electric field shielding layer is required for robust interaction. An additional concern for wearable applications is the effect of humidity changes on capacitance. Since humidity changes are experienced simultaneously by all texels in an array, for wearable applications, a differential measurement strategy can be used to

measure the change of capacitance between texels to find the pressure location. Another strategy is to apply a high-pass filter to remove the slow response of the humidity component. For further resilience to humidity changes, fabrics with lower humidity sensitivity can be used, such as Kraton. These proof-of-concept results indicate the potential of our sensor for human-machine interface applications.

#### **4.6 Conclusions**

In this study, we presented an easy-to-manufacture, tunable, fully-textile sensor system capable of detecting pressure, humidity, and wetness. The pressure and humidity sensing principle is based on conductive yarns orthogonally sewn into a dielectric fabric, thus forming a capacitive sensor at each texel. Additionally, wetness could be detected according to changes in the resistance between neighboring texels. To demonstrate the tunable nature of our sensing principle, we compared the use of various commercially available conductive yarns and fabrics on the sensor response. Extensive mechanical and electrical evaluation revealed unique advantages and disadvantages of various conductive yarn and textile dielectrics, as summarized in Table 4, which can be extended to other newly emerging materials. The pressure sensing results indicated that the use of silver yarn in the sensor increased the overall sensitivity and decreased the response/relaxation time. Sensors containing a dielectric layer consisting of cotton yielded a higher pressure sensitivity in the first linear range while the Kraton-silver combination performed the best in the second linear range. For humidity sensing, the cotton dielectric sample showed the highest sensitivity and the Kraton fabric showed the least sensitivity. The wetness sensing tests revealed that the sensors made with PET dielectric fabric and the sensors made with silver yarn had the fastest absorption time as compared to other fabrics and yarns used. Finally, we presented two proof of concept demonstrations where the presented pressure sensing mechanism was used for potential human-

machine interface applications including a pressure sensing mat array and a smart glove capable of controlling a wireless drone.

#### **4.7 Experimental Section**

*Fabric sensor fabrication:* We used a commercially available sewing machine (Durkopp E901/6, Duerkopp-Adler, Bielefeld, Germany) for sensor fabrication. Prior to sewing, we treated cotton and PET samples with a commercially available fabric stiffening product (Original Stiffen Quik, Aleene's®) for consistency during the sewing process. First, we loaded conductive yarns into the bobbin of the sewing machine to minimize stress on the yarn. A standard sewing yarn was used as the top component of the stitch and a 301stitch type was used with each stitch measuring ~7mm. Once the machine was appropriately set up, we inserted the fabric dielectric layer into the sewing machine and first sewed lines on one side of the fabric. Subsequently, we flipped the fabric dielectric layer and sewed conductive lines the opposite side of the fabric. The top and the bottom lines were sewn perpendicular to one another to make a sensor array. Spacing between the lines is critical such that electrical shorting is avoided and should be selected based on the length of the yarn stitches.

*Conductive Yarns (Electrodes):* We utilized two distinctive, conductive yarns types. The first was an electrolysis plated polyamide 6,6 yarn (Shieldex 235/36 4 ply, V Technical Textiles, Palmyra, USA) consisting of four plies, each ply containing 36 filaments with each filament measuring 235 deci-tex. The second was a stainless steel (SS) yarn (Bekinox® VN 14.2.9.175S, Bekaert, Waregem, Belgium ) made up of two plies, each ply containing nine filaments, with each filament measuring 14  $\mu\text{m}$  in diameter. We analyzed the structure and diameter of the yarns using a stereomicroscope (Nikon SMZ 1000) and measured the yarn diameter using ImageJ software. We measured yarn resistance values using a multimeter over a 10 cm length of the yarn.

*Fabric Dielectric Layer Materials:* We studied three distinct fabric materials for the dielectric layer: a cotton interlock knit, a PET interlock knit, and Kraton (triblock copolymer based on styrene and ethylene/butylene) meltblown nonwoven (MD1653 M). The knit materials were provided by North Carolina State University's Wilson College of Textiles. The nonwoven materials were provided by The Nonwovens Institute.

*Dielectric Constant Evaluation:* Prior to evaluation, we conditioned the textiles overnight in standard conditions of 70°F and 65% relative humidity (RH) per ASTM 1776. Testing was completed in standard conditions to eliminate effects of temperature and humidity. We measured the dielectric constant and dissipation factor using the Agilent dielectric test fixture (Agilent Technologies, 16451B) and a precision LCR meter (Keysights, E4980AL). Measurements were taken at a frequency of 1 kHz at 1V.

*Physical and Mechanical Characterization:* We completed the mechanical tests on standard tension/compression testing equipment (MTS 30/G) using a test speed of 3mm/min. Three texels in each sample were pressure cycled ten times from 0 kPa to 600 kPa. We calculated secant and tangent modulus values in two strain ranges corresponding to the two distinct regions of fabric mechanical behavior (0-40%, >60% strain). Average modulus values were calculated using the fifth pressure cycle of each texel. To calculate the mechanical hysteresis, we segmented the loading and unloading curves and found the corresponding exponential trend lines. Then, we calculated hysteresis by finding the area between the loading and unloading curves and dividing the result by the loading area. The modulus and hysteresis values were given as averages of three texel responses to show statistical evaluation and variability.

*Dielectric Material Moisture Regain:* We determined the %R of each material with the CEM Smart System 5 Microwave Moisture Analyzer. Testing was completed in standard testing

conditions of  $\sim 70^{\circ}\text{C}$  and 65% RH. Prior to testing, the textile dielectric materials were conditioned overnight in standard conditions of  $70^{\circ}\text{F}$  and 65% RH per ASTM 1776.

*Electromechanical Characterization:* We used a precision LCR meter (Keysights, E4980AL) applying a 1 kHz and 1V AC signal to measure capacitance for the sensitivity and hysteresis experiments. For all other experiments, we used a custom wireless data acquisition system with a capacitance to digital converter (Analog Devices, AD7142) which increased the sampling rate to  $>200$  Hz. Pressure cycles were applied to the sample, one texel at a time, using a custom built translational stage with a force sensor (ATI Gamma). More information about this custom electromechanical experiment setup and its validation can be found in our previous work.<sup>[301]</sup> We used LabVIEW to control the actuators while logging time synchronized pressure and capacitance data. For all the material testing, sensitivity and hysteresis experiments, the test speed was 3mm/min. For sensitivity and hysteresis experiments, five texels in each sample were pressure cycled ten times from 0 kPa to 600 kPa. We used the fifth pressure cycle from each texel for analysis. The sensitivity and hysteresis results were presented as averages of five texel performances for each sample to evaluate statistical variability. Like mechanical hysteresis, we calculated the electromechanical hysteresis by finding the area between the loading and unloading curves and dividing the result by the loading area. In dynamic loading experiments, each sample was loaded to 50, 200 and 400 kPa at the same experiment speed of 3mm/min. In the experiments, the stage head compressed the sample until the targeted pressure level was reached, and at that point the pressure was held for  $\sim 60$ s. The stage then decompressed the sample until the pressure level was 0 kPa and held the pressure for  $\sim 60$ s. This testing was done sequentially with 50 kPa cycles being applied first, followed by applications of 200 kPa and finally 400 kPa. For the extended loading experiment, the samples were subjected to 1,000 cycles between 12 kPa to 50

kPa of pressure. A single loading cycle was applied on all samples before the experiment to remove dramatic differences in the textile structure. The resulting cycles were segmented and centered before plotting for comparison. To examine the response and relaxation time of our samples, we increased the step size of the experimental setup to exert instantaneous pressures of ~50kPa and increased the sampling rate of the data acquisition to sample every ~5ms (200 Hz). To minimize any experimental error, each sample was tested five times and the results were averaged to find the response and relaxation times.

*Humidity Testing:* We determined the influence of humidity on capacitive response using a custom set up in a conditioned room located at North Carolina State University Wilson College of Textiles. In these experiments, temperature was held constant within the conditioned room at ~70°C. Sensing behavior was first characterized in standard conditions of ~70°C and 65% RH with samples connected to the previously described capacitance board. Using a saturated salt solution containing lithium chloride, an environment of 21% RH was induced. The saturated salt solution was placed in an airtight container with holes for weight application and electrical connection. The holes opened for connection were sealed using clay. Finally, deionized (DI) water was placed in the airtight container to create an environment of 95% RH. Samples were left in each distinct humid environment for at least four hours to allow the sample to come to equilibrium.<sup>[92]</sup> A commercial temperature/humidity sensor (Ecowitt DS102, Mount Laurel NJ, USA) was placed in the airtight container to monitor the temperature and RH of the environment within the chamber. Once equilibrated, samples were exposed to different weights (50g, 100g, and 200g) to study the effect of humidity on pressure responses. The weights applied during this experiment corresponded to pressures of 1, 2, and 4 kPa.

*Wetness Sensing:* We applied a 120  $\mu\text{L}$  droplet of DI water to evaluate the wetness sensing functionality of the samples while measuring the impedance changes. Impedance measurements were recorded from a wetness-sensing texel via electrochemical impedance spectroscopy using a Gamry Reference 600 Potentiostat system. To collect baseline dry impedance data from the samples, we applied DI water at the center of a wetness-sensing texel 5 minutes into the impedance data collection. More information about the wetness experiment setup and its evaluation can be found in our previous work.<sup>[283]</sup>

#### 4.8 Acknowledgment

T.A. and J.T. contributed equally to this work. The authors acknowledge support from the NCSU Chancellor’s Innovation Fund, NSF ECCS (Grant No. 1509043), NSF SCH (Grant No. 1622451), NSF Graduate Research Fellowship (DGE-1252376), and NCSU Provost Fellowship. The authors would also like to acknowledge Aydin Gokce for his assistance with the drone experiments. The authors also thank the Wilson College of Textiles and Nonwovens Institute for their fabrication and donation of the knit and meltblown materials respectively.

#### 4.9 Supplementary Information

Table 2: Mechanical properties of SLs. Reprinted with permission from<sup>[20]</sup> ©2020 WILEY-VCH Verlag GmbH & Co. KGaA, Weinheim.

Sample ID	Secant Modulus (MPa)	Standard Deviation	Tangent Modulus (MPa)	Standard Deviation	Mechanical Hysteresis (%)	Standard Deviation
Cotton-silver	0.042	0.011	5.950	0.870	53.87	11.42
Cotton-SS	0.039	0.002	4.000	0.300	63.77	1.66
PET-silver	0.042	0.013	5.250	0.270	61.88	7.42
PET-SS	0.055	0.012	4.800	0.090	58.92	1.87
Kraton-silver	0.065	0.001	4.070	0.500	55.75	2.65
Kraton-SS	0.067	0.004	3.550	0.150	54.05	0.7

Table 3: Electromechanical properties of SLS. Reprinted with permission from<sup>[20]</sup> ©2020 WILEY-VCH Verlag GmbH & Co. KGaA, Weinheim.

Sample ID	Sensitivity <50kPa (pF/MPa)	Standard Deviation	Sensitivity >100kPa (pF/MPa)	Standard Deviation	Electrical Hysteresis (%)	Standard Deviation	Response (n=5) (ms)	Standard Deviation	Relax (n=5) (ms)	Standard Deviation
Cotton-silver	2.35	0.32	0.21	0.03	19.39	1.79	18	4	23	5
Cotton-SS	1.63	0.25	0.15	0.05	18.39	1.91	12	6	10	5
PET-silver	1.55	0.23	0.11	0.01	18.69	1.89	12	6	15	5
PET-SS	0.73	0.14	0.08	0.02	21	1.86	14	3	14	3
Kraton-silver	1.27	0.18	0.25	0.03	25.32	2.53	22	4	29	4
Kraton-SS	0.81	0.12	0.13	0.02	18.86	1.74	18	4	22	5

Table 4: Summary of advantages/disadvantages and example applications of different materials used. Reprinted with permission from<sup>[20]</sup> ©2020 WILEY-VCH Verlag GmbH & Co. KGaA, Weinheim.

	Materials	Advantages	Disadvantages	Example Applications
<b>Dielectric Fabric</b>	Cotton Interlock Knit	<ul style="list-style-type: none"> <li>- Higher pressure sensitivity in the first linear region (&lt;50kPa)</li> <li>- Higher humidity sensitivity</li> </ul>		<ul style="list-style-type: none"> <li>- High sensitivity and extended precision for pressure sensing</li> <li>- Humidity sensing</li> <li>- Glove touch sensor</li> <li>- Object manipulation sensor</li> </ul>
	PET Interlock Knit	<ul style="list-style-type: none"> <li>- Faster liquid absorption</li> </ul>	<ul style="list-style-type: none"> <li>- Lower pressure sensitivity in the second linear region (&lt;100kPa)</li> <li>- Higher pressure dynamic range attenuation</li> </ul>	<ul style="list-style-type: none"> <li>- Wetness sensing</li> </ul>
	Kraton Meltblown Nonwoven	<ul style="list-style-type: none"> <li>- Higher pressure sensitivity in the second linear region when combined with Silver yarn (&lt;100kPa)</li> <li>- Lowest initial pressure baseline shift</li> </ul>	<ul style="list-style-type: none"> <li>- Lower pressure response/relaxation time</li> <li>- Slower liquid absorption</li> <li>- Lowest humidity sensitivity</li> </ul>	<ul style="list-style-type: none"> <li>- High pressure sensing</li> <li>- Insole/prosthetic pressure sensor</li> </ul>
<b>Electrode Yarn</b>	Silver Polyamide	<ul style="list-style-type: none"> <li>- Higher pressure sensitivity overall</li> <li>- Faster liquid absorption</li> </ul>	<ul style="list-style-type: none"> <li>- Lower pressure response/relaxation time</li> <li>- Higher pressure dynamic range attenuation</li> </ul>	<ul style="list-style-type: none"> <li>- Pressure and wetness sensing</li> </ul>
	SS	<ul style="list-style-type: none"> <li>- Higher pressure response/relaxation time</li> <li>- Lower pressure dynamic range attenuation</li> </ul>	<ul style="list-style-type: none"> <li>- Lower pressure sensitivity</li> <li>- Slower liquid absorption</li> </ul>	<ul style="list-style-type: none"> <li>- Higher precision in fast pressure change applications</li> <li>- Accuracy in extended pressure cycle applications</li> </ul>

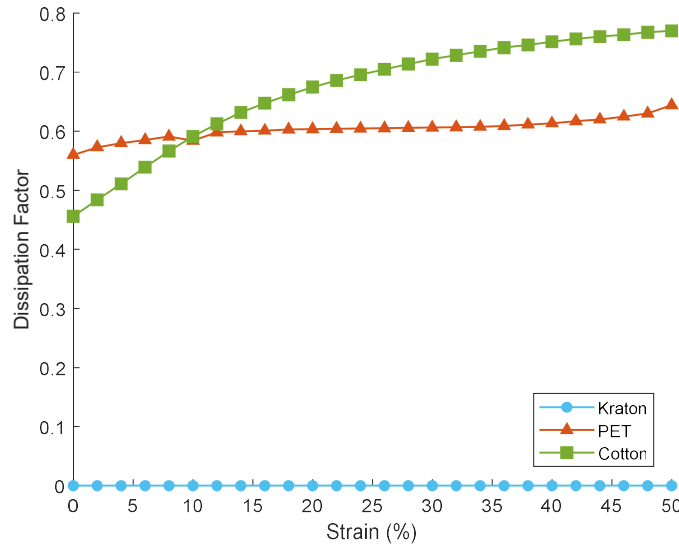


Figure 19: Dissipation factor of the textile dielectrics under compressive straining. Reprinted with permission from<sup>[20]</sup> ©2020 WILEY-VCH Verlag GmbH & Co. KGaA, Weinheim.

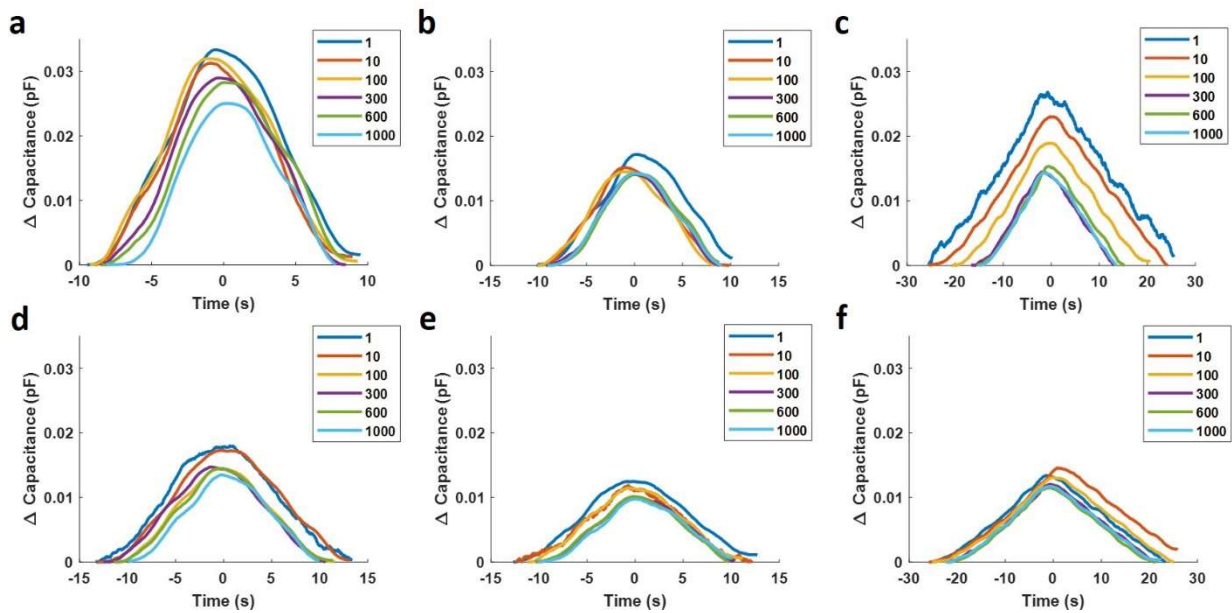


Figure 20: Stability of pressure sensing in 1,000-cycle tests. Silver thread samples with cotton (a) PET (b) and Kraton (c) dielectric materials. Stainless-steel thread samples with cotton (d) PET (e) and Kraton (f) dielectric materials. Capacitance differences are shown to highlight the response range changes. Reprinted with permission from<sup>[20]</sup> ©2020 WILEY-VCH Verlag GmbH & Co. KGaA, Weinheim.

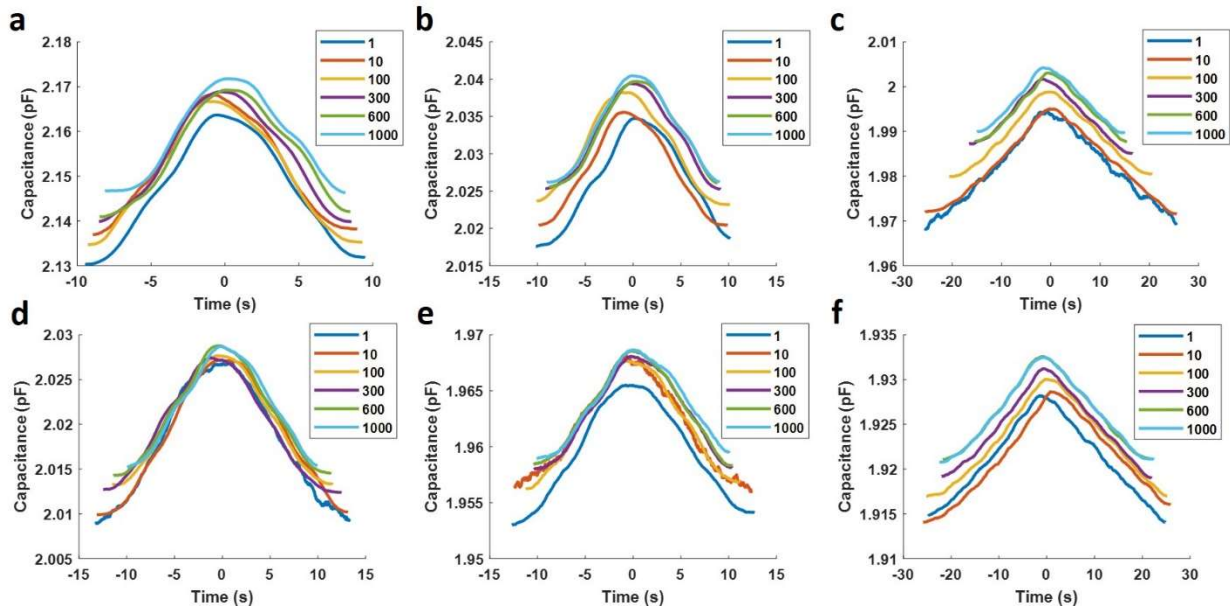


Figure 21: Stability of pressure sensing in 1,000-cycle tests. Silver thread samples with cotton (a) PET (b) and Kraton (c) dielectric materials. Stainless-steel thread samples with cotton (d) PET (e) and Kraton (f) dielectric materials. Capacitance is shown without baseline removal to highlight the baseline drift. Reprinted with permission from<sup>[20]</sup> ©2020 WILEY-VCH Verlag GmbH & Co. KGaA, Weinheim.

## 5 Textile-Based Pressure Sensors for Monitoring Prosthetic-Socket Interfaces

The initial characterization of the SLSs, discussed in Section 4, indicated that the seam-line sensing approach provides a simple means of creating flexible textile-based sensors useful in a range of applications. To further demonstrate the value and adaptability of the SLSs, we selected a specific application, pressure sensing within prosthetics, for further exploration. This research was published in IEEE Sensors Journal and provides an overview of the sensing system specially designed for ISE monitoring and demonstrates the ability of these sensors to detect pressure changes within the ISE.<sup>[21]</sup>

This work is ©2021 IEEE. Reprinted, with permission, from Jordan Tabor, Talha Agcayazi, Aaron Fleming, Brendan Thompson, Ashish Kapoor, Ming Liu, Michael Lee, He (Helen) Huang, Alper Bozkurt, and Tushar K. Ghosh, *Textile-Based Pressure Sensors for Monitoring Prosthetic-Socket Interfaces*, IEEE Sensors Journal, April 2021. In reference to IEEE copyrighted material

which is used with permission in this thesis, the IEEE does not endorse any of NC State University's products or services. Internal or personal use of this material is permitted. If interested in reprinting/republishing IEEE copyrighted material for advertising or promotional purposes or for creating new collective works for resale or redistribution, please go to [http://www.ieee.org/publications\\_standards/publications/rights/rights\\_link.html](http://www.ieee.org/publications_standards/publications/rights/rights_link.html) to learn how to obtain a License from RightsLink.

## **5.1 Abstract**

Amputees are prone to experiencing discomfort when wearing their prosthetic devices. As the amputee population grows this becomes a more prevalent and pressing concern. There is a need for new prosthetic technologies to construct more comfortable and well-fitted liners and sockets. One of the well-recognized impediments to the development of new prosthetic technology is the lack of practical inner socket sensors to monitor the inner socket environment (ISE), or the region between the residual limb and the socket. Here we present a capacitive pressure sensor fabricated through a simple, and scalable sewing process using commercially available conductive yarns and textile materials. This fully-textile sensor provides a soft, flexible, and comfortable sensing system for monitoring the ISE. We provide details of our low-power sensor system capable of high-speed data collection from up to four sensor arrays. Additionally, we demonstrate two custom set-ups to test and validate the textile-based sensors in a simulated prosthetic environment. Finally, we utilize the textile-based sensors to study the ISE of a bilateral transtibial amputee. Results indicate that the textile-based sensors provide a promising potential for seamlessly monitoring the ISE.

## **5.2 Introduction**

Amputation is one of the major causes of disability with approximately 1.7 million people living with limb loss in the U.S. alone.<sup>[1]</sup> The majority of amputees express low satisfaction with their

prosthetic devices,<sup>[9, 22]</sup> as well as moderate to severe pain when wearing their prosthetic devices.<sup>[7-9]</sup> While wearing a prosthesis, an amputee's residual limb is exposed to an uncomfortable environment within the socket, including high stress,<sup>[8, 22]</sup> which can cause debilitating pressure ulcers,<sup>[25]</sup> may require further amputation,<sup>[26]</sup> or result in life-threatening deep tissue injuries.<sup>[25]</sup> In fact, skin lesions occur in ~60% of lower limb (LL) amputees resulting ~25% of amputees reducing the use of their prosthetic.<sup>[32]</sup> One of the main hurdles in the development of new and improved prosthetic technologies is the lack of practical pressure sensors for monitoring the inner socket environment (ISE).<sup>[302]</sup>

Reported clinical studies on pressure distribution within the ISE primarily employed commercially available, rigid strain gauge sensors.<sup>[39, 41, 43, 45]</sup> While these sensors provide valuable information regarding the ISE, they are disadvantageous due to their bulkiness,<sup>[10]</sup> weight,<sup>[11, 12]</sup> inflexibility,<sup>[11, 12]</sup> low spatial resolution,<sup>[13]</sup> cost,<sup>[14, 15]</sup> and laborious integration methods outside of the socket.<sup>[16]</sup> Newly commercialized, semi-flexible pressure monitoring systems such as the Pliance<sup>®</sup> system (Novel<sup>®</sup> GMBH, Germany),<sup>[112, 127]</sup> or the F-Socket<sup>®</sup> (Tekscan, Inc. USA)<sup>[26, 114]</sup> have also been used to measure the pressure within the ISE. While these systems do not require socket modification, they are still spatially limited, cannot be readily integrated into existing prosthetic components, and leave room for improvement in flexibility and breathability desirable for long-term use. More recently, new research-grade sensors for monitoring pressure within the ISE have been proposed in the literature. These include a MEMS-based bubble sensor,<sup>[146]</sup> custom socket inserts with embedded commercial force-sensing resistors,<sup>[142]</sup> and sensors fabricated via 3D printing/lithography.<sup>[6, 25]</sup> However, these proposed sensors contain rigid components,<sup>[16, 122, 131, 142, 146, 147]</sup> require socket modification,<sup>[122, 131, 147]</sup> are fabricated through complex and costly methods,<sup>[6, 25, 38, 142]</sup> and have not been tested in-vivo.<sup>[146, 147]</sup>

Some of the shortcomings associated with currently available pressure monitoring systems could be significantly improved using textile-based sensors. These sensors present obvious advantages due to their compliant and breathable nature<sup>[303]</sup> as well as their potential manufacturing using relatively simple fabrication methods. Further, textile-based sensors provide opportunities for large-area sensing and unobtrusive pressure-mapping of the entire residual limb by integrating sensors into existing and conventional textile-based components of the prosthetic system such as liner-liners and socks worn under rigid prosthetic devices. Textile-based sensors have been explored for monitoring various stimuli, most commonly, pressure<sup>[50, 58, 68]</sup> or strain<sup>[152, 232, 267]</sup> in various applications; however, their potential for monitoring pressure within the ISE has not yet been demonstrated.

Here, we present the SLS approach and corresponding electronics for monitoring pressure within the ISE. The custom low-power electronic readout system attached to the textile sensing elements is capable of high-speed data collection from up to four sensor arrays. Previously, we demonstrated the seam-line pressure sensing approach for planar interfaces via benchtop experiments.<sup>[20, 281-283]</sup> In this work, we evaluate a set of new SLSs and corresponding custom-designed electronics for ISE pressure monitoring. The SLS evaluation is performed on curved surfaces during dynamic experiments to systematically work towards our final goal of monitoring the ISE. We report two preliminary experiments: first, evaluating the sensors on an artificial limb followed by human testing with an able-bodied subject donning a bent-knee adapter to replicate the ISE. Following the preliminary experimentation, we complete an in-vivo proof-of-concept study with a bilateral transtibial amputee. The SLSs successfully detected pressure changes within the ISE during weight-shifting and walking trials. Results indicate that the SLSs may provide a promising approach to monitoring the pressure distribution within the ISE.

### 5.3 System Design

The sensing system comprises three parts: a sensor array, a miniature printed circuit board (PCB) adjacent to the sensors for analog to digital conversion (ADC), and a data collection PCB. The prototype system allows for data collection from four sensor arrays each consisting of nine capacitive sensors, which we refer to as textile sensing elements, or “texels”. The system offers both wireless Bluetooth Low Energy or wired USB data transmission and an optional onboard data collection on a micro-SD card. Other features of this custom system include: (1) texel interconnects that reduce encumbrance and improve flexibility (see Figure 22b), (2) novel thread to PCB connections (see Figure 22b), (3) active electric field shielding around the sensor arrays and interconnects to diminish electric field noise(see Figure 22c), (4) the ADC PCB digitizing the analog sensor readouts before transmission to avoid interference noise (see Figure 22b), (5) parallel sensor array for increased spatial sampling rates, (6) low power consumption allowing up to twelve hours of data collection with a small lithium polymer battery, (7) trigger channel to synchronize the system time with external data collection systems, and (8) a real-time data visualization software for rapid sensor validation. Further details of these features will be provided subsequently.

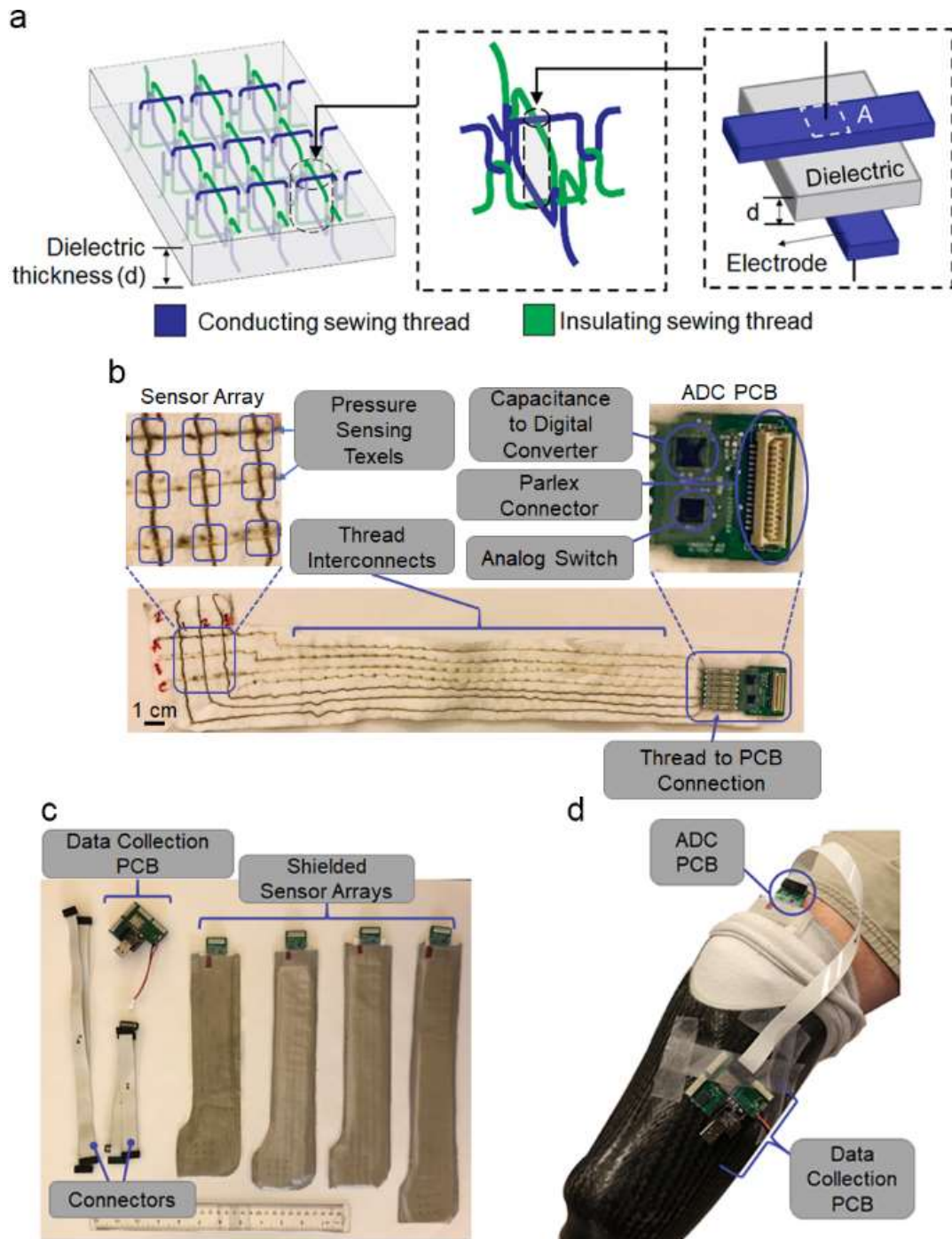


Figure 22: Sensor architecture, system design, and integration (a) Schematic of fabric-based sensor array, showing fabric/thread-based parallel plate capacitor (figure adapted from <sup>[20]</sup>) (b) Sensor arrays, interconnects, and ADC PCB (c) Data collection PCB with four shielded sensor arrays (d) SLS sensor placed within the ISE beneath the sock with the ADC PCB attached. The ADC PCB of each sensor is connected to the exterior data collection system using flexible cables. The data collected PCB is mounted to the exterior socket to minimize encumbrance.

Reprinted with permissions from<sup>[21]</sup> ©2021 IEEE.

### 5.3.1 Sensor Array

The sensor architecture used in this work consists of a network of texels formed through perpendicularly sewn seam-lines, using conductive and insulating yarns, on a commercial sewing machine (Durkopp E901/6, Duerkopp-Adler AG, Germany) to create 3×3 sensing arrays (see Figure 22a) <sup>[20]</sup>. The capacitive response of our sensor can be modeled by a parallel plate capacitor with conductive yarns serving as electrodes and the textile material as the dielectric, as shown in Figure 22a. The capacitance,  $C$ , is defined using vacuum permittivity  $\epsilon_0$ , dielectric constant  $\epsilon_r$ , area of the conductive electrodes  $A$ , and the distance between the conductive electrodes  $d$ , as  $C = \epsilon_0 \epsilon_r \left(\frac{A}{d}\right)$ . The sensed change in capacitance,  $\Delta C = C_p - C_0$ , results from a change in  $d$  and possibly in  $\epsilon_r$  and  $A$ , due to applied pressure. Here,  $C_0$  and  $C_p$  are the capacitance values before and after the application of pressure, respectively.

An advantage of the SLS fabrication method is the tunability of the sensor design. The spatial resolution, or the density of the sensing points, can be easily altered within a large range. Here, texels were placed 1 cm apart but, this could easily be changed by altering the stitch length and proximity of the seamlines for the application requirements. Additionally, the size of the array (number of texels) can be easily increased by adding additional seamlines but is limited by the electrical conductivity of the electrode materials. Further, the mechanical and sensing properties of the SLS can be tuned by proper selection of the textile dielectric. For example, the magnitude of the force that can be measured by the SLS primarily depends on the compressive properties of the dielectric thus providing desirable design flexibility.

The textile dielectric used in this research is a meltblown fabric having a thickness of  $1.82 \pm 0.05$  mm and comprised of a styrene-ethylene-butylene-styrene (SEBS) linear triblock copolymer material (Kraton™ MD 1653, Kraton Corp.).<sup>[20]</sup> SEBS was chosen for its mechanical

and dielectric behavior including low baseline shifts and low sensitivity to moisture (moisture regain of  $0.72 \pm 0.01\%$ ), necessary for pressure sensing within the ISE <sup>[20]</sup>. The conductive sewing thread used as electrodes is a commercially available silver-coated polyamide 6,6 yarn (Shieldex 235/36 4 ply, V Technical Textiles, Inc., USA) with a diameter of  $468.186 \pm 114.206 \mu\text{m}$  and having electrical resistance of  $0.29 \pm 0.033 \Omega/\text{cm}$ .<sup>[20]</sup>

The sensor arrays are designed to measure the pressure at specific lower-limb anatomical locations which could be up to 30 cm inside the socket. To place the sensors inside the socket while minimizing encumbrance, we used the same thread and dielectric material for sensor fabrication and sensor interconnect (see Figure 22b). Therefore, the interconnect possessed the same thickness and compliance as the sensor, without creating extra discomfort for the user. Additionally, a grounding thread was sewn between the row and column threads to reduce crosstalk and capacitance between the closest row/column threads.

To remove the effects of environmental electromagnetic noise on the sensor, we formed a Faraday cage around the entire sensor assembly, including the textile-PCB connections with a commercial conductive copper-nickel coated polyester fabric (Titan RF Faraday Fabric, MOS Equipment, Inc., USA) as seen in Figure 22c. The conductive fabric was attached to the sensor using double-sided adhesive tape (Scotch 34-8517-0998-9, 3M Ltd, USA).

### **5.3.2 Analog to Digital Conversion Printed Circuit Board**

As mentioned earlier, the ADC PCB is a custom-designed board for converting the capacitance of the sensor array to digital signals for a reliable RF interference-resilient transmission. The ADC PCB was placed outside the socket at the end of the thread interconnects, as close to the sensor as possible to reduce the effects of electromagnetic noise (see Figure 22d). The flexible thread to the rigid PCB connections was achieved using vias for alignment and connection pads covered with

Z-axis tape (9703, 3M Ltd, USA) for robust electrical connections. The main components of the PCB included a capacitance to digital converter with a built-in multiplexer (AD7142, Analog Devices Inc, USA) and a quad analog switch (ADG788, Analog Devices Inc, USA) for row selection. Aside from the address select resistors, the ADC PCB design was the same for each sensor array.

### **5.3.3 Data Collection Printed Circuit Board**

The data collection PCB is a custom-designed board for collecting the digitized capacitance values from four ADC PCBs and storing/transmitting the data. This PCB contains a Bluetooth enabled microcontroller module (RFD77001, Simblee, USA), micro-SD card socket, synchronization connector, and a UART connector. Another reason for having external ADC boards was to increase the sampling rate by parallelizing the data collection routine. This enabled us to achieve a 20 Hz sampling rate with four sensor arrays which were four times faster than a sequential data collection method. We selected the current sampling rate based on the optimal performance of our electronics. To our knowledge, no study has reported the sampling rate required to capture the dynamics of inner socket pressure changes during walking or other locomotive tasks. The most relevant publication reports that a 100 Hz frequency is required for measuring plantar pressure during walking.<sup>[304]</sup> However, our goal within this study was to determine whether the sensed pressure aligned with the expectation during each demonstration (e.g. higher pressure was expected in the stance than the swing phase of gait), rather than to capture the dynamics of pressure during activity. For this application, the used sampling rate was adequate. In the future, we plan to increase the sampling rate to at least 100 Hz and study the frequency components of the sensed inner socket pressure during various locomotor conditions (e.g., speed and terrain).

We performed a power consumption analysis of our system at the fastest sampling rate. The current draw breakdown was measured to be 1.2 mA for each sensor array and 6 mA for the rest of the system excluding the SD card. With four sensor arrays and an SD card, the current consumption was 40.8mA (including the typical 30mA power consumption of the SD card). This means that with a small-sized 500mAh Lithium Polymer battery, the entire system could collect data for approximately twelve hours before needing to be recharged. To limit packet loss, all experimental data reported in this paper was collected with a USB connection. The data collection board is shown in Figure 22c and d.

### **5.3.4 Real-time Data Visualization**

During our experiments, we found that real-time data visualization was a significant factor for rapidly verifying sensors before experiments. For this, we composed a MATLAB (MathWorks Inc, USA) code to receive and plot the transmitted capacitance values in real-time. Sensors were tested using this real-time data visualization routine before and after experimentation to double-check their successful operation. This validation step allowed us to visually inspect the sensor response to mechanical stimulus and identify any potential failure modes before lengthy experiments.

### **5.4 Seam-line Sensor Evaluation in Simulated Inner Socket Environment**

To adequately prepare for in-vivo assessment of the efficacy of our textile-based sensors to monitor the ISE, we conducted two preliminary evaluations. This included the use of an artificial limb simulating potential inner-socket pressure ranges<sup>[264]</sup> and an able-bodied subject walking with a bent-knee adapter for gait patterns that could occur during amputee locomotion.<sup>[265, 266]</sup> These setups allowed for an intermediate well-controlled environment for testing. All the presented human experimentation was performed with the approval of the Institutional Review Board at the

University of North Carolina at Chapel Hill where the study participants were provided informed, written consent to participate.

We would like to emphasize that the full calibration of the sensor response (conversion of capacitance to absolute pressure) is currently beyond the scope of this paper and reserved for a follow up future study involving a more detailed evaluation. Full calibration of the SLS requires quantitative measurement of the output of each group of texels (depending on the necessary spatial resolution) at the beginning of each use, because of the unique initial shape of the sensor array (curvature, etc.) and time-dependent change of its mechanical behavior. This will be the subject of continuing research and future publications in the development of the SLS. Therefore, here, we report relative capacitive changes to provide a valuable qualitative understanding of the ISE, such as relative pressure changes with activity and relative differences in pressure at various locations. For a more comprehensive understanding of individual texel's sensory behavior, we refer the interested reader to our previous publication.<sup>[20]</sup>

#### **5.4.1 Artificial Limb Testing**

In the first simulated ISE experiment, we used a custom artificial limb secured to a frame (see Figure 23a and b). The limb was tilted to predetermined angles and then screwed in place on the frame to induce different loading patterns on the SLS. The main objective of this experiment was to measure the sensor response ( $\Delta C$ ) at certain regions of the limb given a change in pressure due to different angles of tilt. Capacitance changes were measured at angles ranging from  $-15^\circ$  (Left-side position 5 (L5)) to  $+9^\circ$  (Right-side position 3 (R3)) as shown in Figure 23b. Measurements were taken at increments of  $3^\circ$  (i.e., L5 corresponded to  $-15^\circ$ , L4 to  $-12^\circ$ , L3 to  $-9^\circ$ , L0/R0 (Neutral) to  $0^\circ$ , R1 to  $+3^\circ$ , and so on).

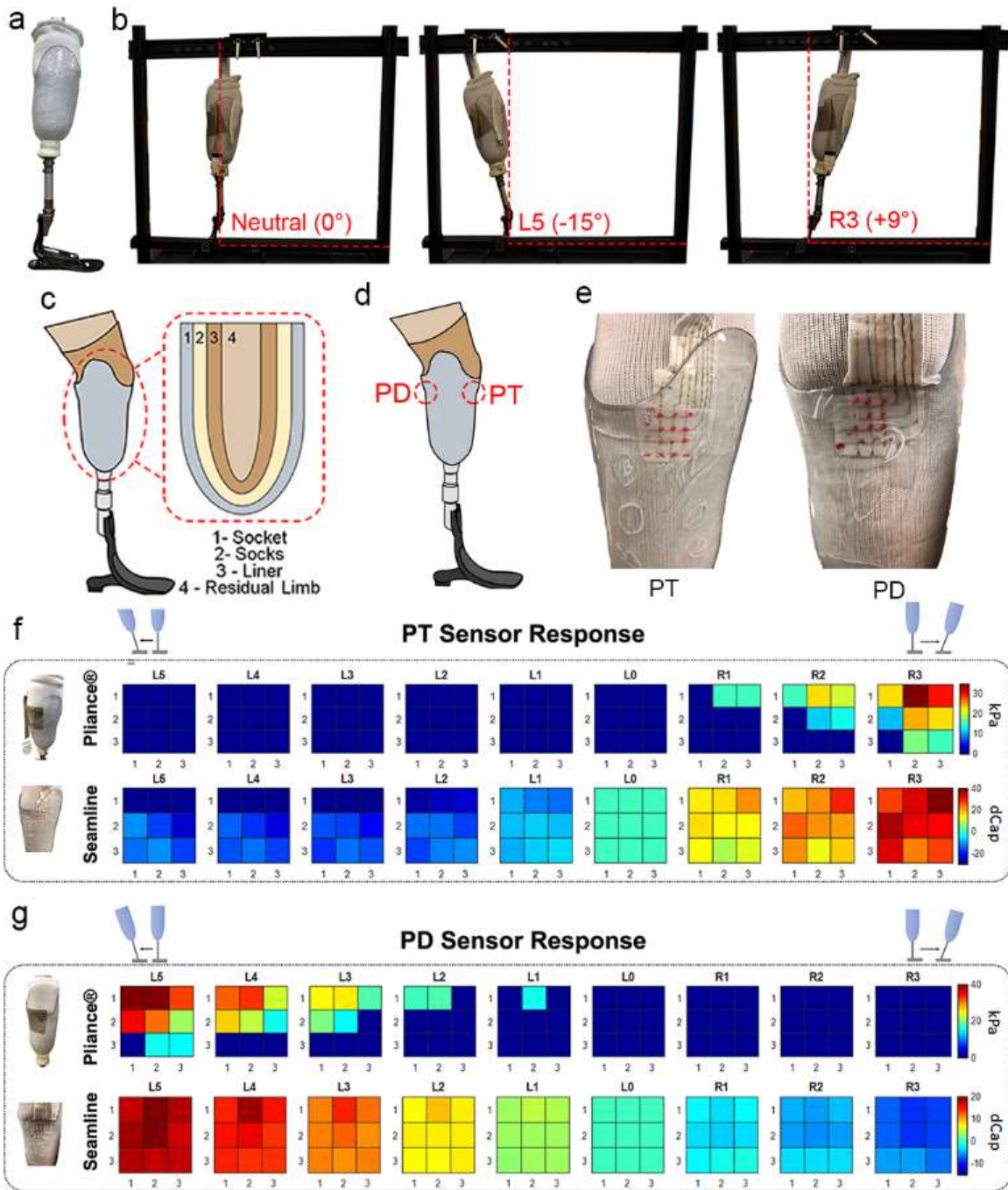


Figure 23: Artificial limb testing set-up and results (a) Artificial limb (b) Artificial limb on supporting frame at neutral, L5, and R3 positions (c) Diagram of artificial limb prosthetic components (d) Positions of sensor placement (e) Placement of SLS on the PT and PD. Comparative results of pressure distribution from nine sensing points (3x3) of the Pliance<sup>®</sup> and SLS arrays placed at the (f) PT, and (g) PD. The baseline capacitance data for the SLS at the neutral position was removed from the capacitance recordings. The Pliance<sup>®</sup> sensor is unable to detect pressures <15kPa, and therefore some sensing points showed no response throughout the experiment. Reprinted with permissions from<sup>[21]</sup> ©2021 IEEE.

The custom transtibial artificial limb and corresponding socket were fabricated by a prosthetist. The artificial residual limb was made using a commercial plaster (Gold Bond Brand Super White Moulding Plaster, National Gypsum LLC, USA) while the socket was fabricated using a transparent co-polyester material (Vivak®, Plaskolite LLC, USA) commonly used for test sockets. The socket was transparent which allowed us to easily align and monitor the sensors during the experiments. The plaster-socket interface contained a silicone liner and three textile socks which were removable to create more space inside the interface (see Figure 23c).

During these preliminary experiments, unshielded sensors were placed on two areas of clinical interest where prosthetic sockets typically apply higher levels of pressure: the patella tendon (PT) (i.e. anterior location) and popliteal depression (PD) (i.e. posterior location)<sup>[45, 112]</sup> (see Figure 23d). To find specific regions of interest within these areas (i.e., areas with a detectable change in pressure due to changes in the angle of tilt) we used a commercial pressure sensing array: the Pliance® system (Pliance® Hand/palm Elastic Sensor ES-FE-64-EL10, Novel® GmbH, Germany). The commercial sensor array was placed on several positions along with the PT and PD and the limb was tilted – regions of the PT and PD with distinct pressure changes were selected for the formal study. Specifically, nine of the sixty-four Pliance® sensing points were selected and marked on the transparent socket in red ink such that the nine texels of the SLS could be placed in the same location (see Figure 23e). The pressure measurements recorded using the Pliance® system were used to qualitatively compare with those from our sensor.

The resulting data from the Pliance® sensor and the SLS are plotted as heatmaps for comparison in Figure 23f and g. As expected, when the limb was tilted forward, toward position R3, the sensor output ( $\Delta C$ ) increased for the sensor located on the anterior of the artificial limb (i.e., PT location). Conversely, when considering the posterior sensor placement (i.e., PD location),

the output signal increased when the limb was tilted backward, or towards L5, and decreased when tilted forward. It is important to note that the Pliance<sup>®</sup> sensor is unable to detect pressures <15kPa, and therefore some sensing points showed no response throughout the experiment. In general, the pressure gradient across the Pliance<sup>®</sup> and SLS sensor arrays were similar across the tilt angles tested. This means that the SLS could be used as a pressure sensor to track the relative change in the distribution of forces. The SLS also seems to be more sensitive in the smaller pressure ranges, which might be desirable for sensitive anatomical regions in the socket-limb interface.

#### **5.4.2 Able-Bodied Testing with Bent-Knee Adapter**

Following the evaluation of the SLS using the artificial limb set-up, we tested the sensors using a custom-made bent-knee adapter as shown in Figure 24a and b. The bent-knee adapter provides a useful intermediate step between artificial limb testing and in-vivo amputee testing; it is a physical interface between human soft tissues and rigid material, which simulates the socket interface. Able-bodied studies also help determine if the sensors and the corresponding electronics are sufficiently durable to withstand in-vivo testing (weight shifting and walking) before recruiting an amputee participant. Further, using a healthy subject during this intermediate evaluation poses fewer risks and burdens to amputee subjects who may be suffering from comorbidities which can hinder extended periods of standing and walking during testing.

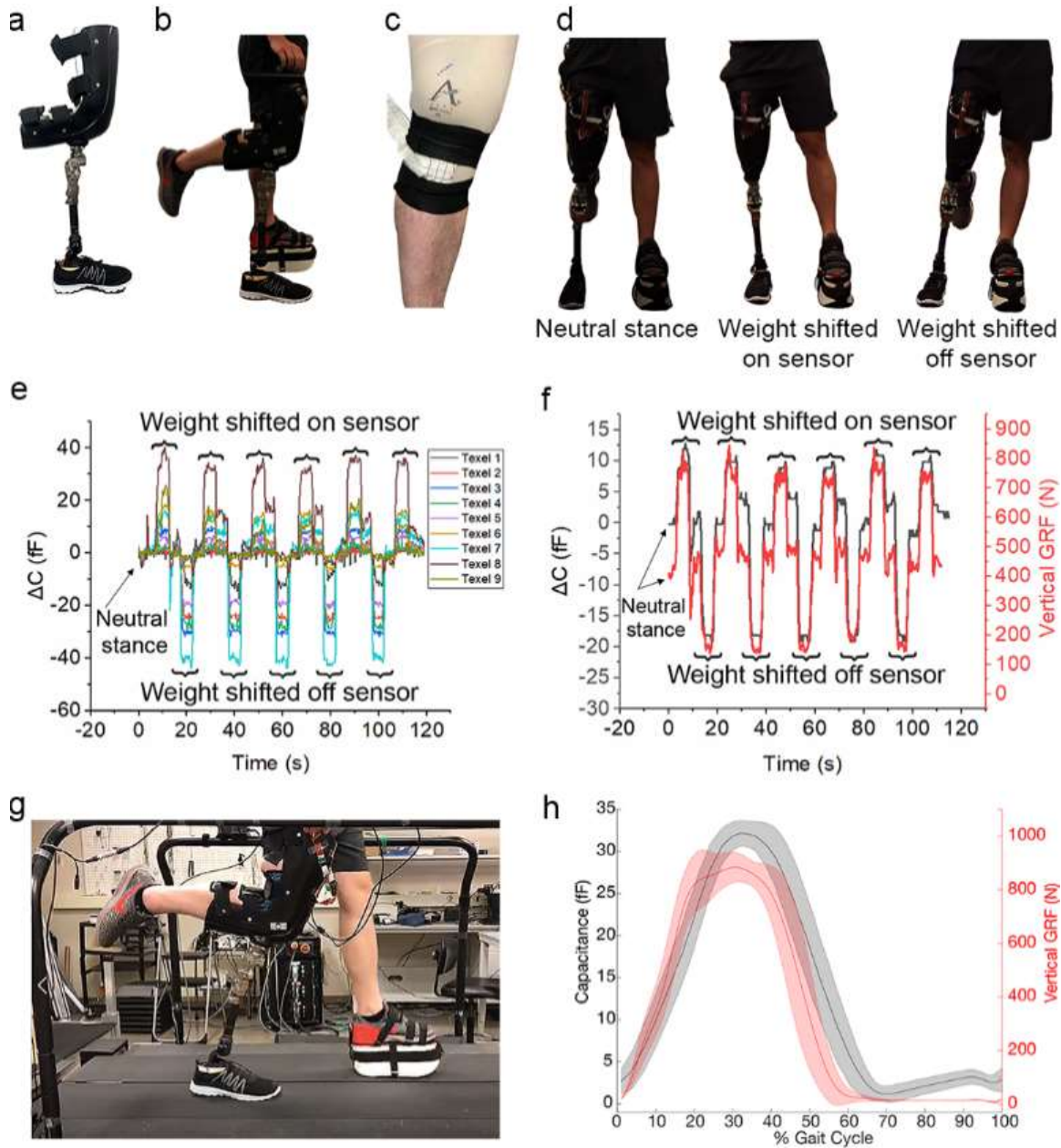


Figure 24: Able-bodied testing using a bent-knee adapter (a) Bent-knee adapter (b) Able-bodied participant wearing bent-knee adapter (c) Placement of SLS on the anterior location on top of the prosthetic liner (d) Weight shifting experiment - participant stances (e) Change in capacitance of the nine texels during bodyweight shifting experiments (f) Average capacitance change during bodyweight shifting experiments. For the weight shifting experiments, the neutral stance was considered as the baseline and was removed from the general capacitance profile. (g) Dynamic walking experiment (h) Change in capacitance and GRF during walking experiments. For the walking experiments, the minimum capacitance value during the walking trials (i.e., while the bent-knee adapter was unloaded) was taken as the baseline and removed from the response. Reprinted with permissions from<sup>[21]</sup> ©2021 IEEE.

The healthy participant wore a modified prosthetic liner such that the interface environment was more realistic and a single unshielded SLS was attached outside the liner during testing with medical wrap, as shown in Figure 24c. Similar to the artificial limb experiments, we used the commercial Pliance<sup>®</sup> pressure sensor to identify a general region of interest, specifically, a region where the pressure distribution among nine sensing points was notable while the pressure changes with the movement were significant. The region was found to be below the participant's knee-cap.

We performed two experiments with the able-bodied participant and the SLS. The first was a weight shifting experiment during which the participant was asked to shift their body weight from one leg to the other (see Figure 24d) while standing on a split-belt treadmill (1000Hz, Bertec Corp., USA) to measure the corresponding vertical ground reaction force (GRF). In the following dynamic walking experiment, the participant walked on the split-belt treadmill. During both experiments, a signal was used to synchronize the SLS output and the GRF recordings. The weight-shifting trials helped determine if the SLS sensor was capable of withstanding and detecting force changes induced by human body weight shifting. Walking trials allowed us to determine if the system and electronics were sufficiently durable to withstand dynamic activities while also applying repetitive force cycles to understand the repeatability of the sensors. Additionally, walking trials enabled the observation of whether the sensors were capable of detecting changes in force during transient activities. The participant's limb was in contact with a ground pad connected to the circuit to standardize the shunting of the limb and to provide external electric field shielding. The sensors were evaluated in-vitro on a benchtop after each experiment using the real-time data visualization to ensure no sensor damage occurred during the human experimentation.

The results from the weight shifting experiments for each texel are shown in Figure 24e. This demonstrates the ability of the SLS to collect individual capacitance values from each texel. The average response of the nine texels shown in Figure 24f provides a clear understanding of the change in capacitance when the participant shifted their body weight. GRF and  $\Delta C$  follow similar trends indicating that the SLS is capable of tracking changes in weight-shifting movements. During the weight shifting experiment, the participant was initially in a neutral stance and then shifted their body weight onto the SLS/bent-knee adapter which resulted in increased capacitance. The participant then returned to a neutral stance and subsequently shifted their body weight onto their other leg, resulting in a decrease in capacitance as pressure was removed from the sensor. We hypothesize that the observed variation in the sensor output at the neutral stance is due to the natural variation in human movement

In the subsequent walking trial, the able-bodied participant walked on the treadmill at a speed of 0.65 m/s (selected based on the subject's comfort level) for around one minute or approximately twenty walking cycles (see Figure 24g). Walking speeds vary for LL amputees with reported speeds including 0.60<sup>[305]</sup> and 0.78 m/s<sup>[306]</sup> therefore, the walking speed used here is within a typical range. In post-processing, the GRF and SLS data were time-synced using a square-wave pulse (5 V) that was sent to each system at the start of the trial. To compare behavior across gait cycles, we segmented the data into individual gait cycles starting at each heel strike (20 N threshold). We then averaged the GRF and SLS data across all cycles (see Figure 24h). Overall, the SLS provided consistent capacitive readings with little variation during the walking experiment. In general, the SLS response ( $\Delta C$ ) followed the GRF output, indicating that our sensor tracked the pressure variation at its location corresponding to the changes in GRF during walking.

During both the weight-shifting and walking experiments, the capacitance response was different for each texel, indicating a pressure distribution across the area.

The results of the able-bodied experiments show that the SLS is sufficiently robust to withstand its intended application. The SLS continued to function throughout the able-bodied experiments and provided consistent and meaningful data during multiple cycles of dynamic loading. Further, these results indicated that the sensors may be suitable for ISE pressure monitoring.

### **5.5 Amputee Testing**

In the final phase, the SLS was evaluated on a participant with bilateral transtibial amputations to determine if the sensors provide reliable qualitative data and are sufficiently durable to withstand the real dynamic ISE environment. Based on the able-body testing evaluation, we added additional conductive fabric layers to the SLS for electric field shielding before this experiment, to reduce electromagnetic interference and noise.

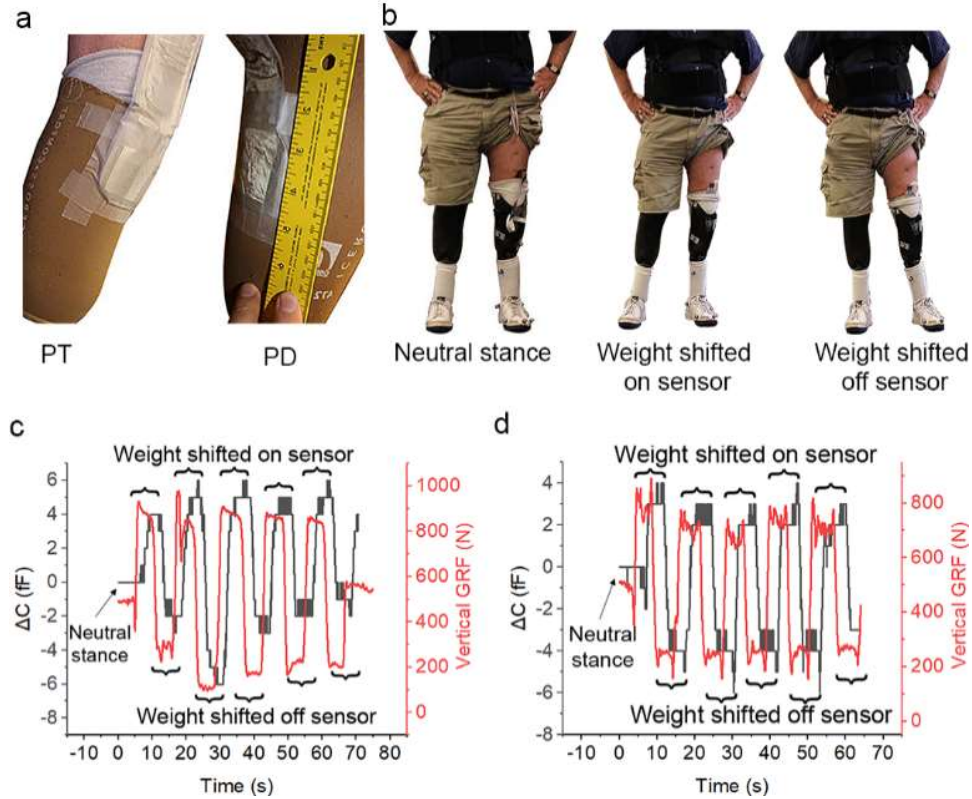


Figure 25: Amputee testing (a) SLS placed at the PT and PD (b) Weight shifting - participant stances. Average capacitance change during bodyweight shifting experiments at the (c) PT and (d) PD. For the weight shifting experiments, the neutral stance was considered as the baseline and was removed from the general capacitance profile. Reprinted with permissions from<sup>[21]</sup> ©2021 IEEE.

Two such shielded SLS arrays were placed on the participant's left residual limb in two anatomical regions of clinical interest<sup>[45, 112]</sup> where prosthetic sockets typically apply higher levels of pressure: the PT and PD (see Figure 23d and Figure 25a). We determined the pressure sensor placement based on the anatomical landmarks from the amputated limb.<sup>[112, 127]</sup> The SLSs were taped to the participant's liner before the participant donned their prosthetic socks. The participant reported that the SLS caused no additional discomfort during experimentation.

Similar to the able-bodied experiment, the amputee was asked to complete two experimental procedures. The first was a weight shifting experiment during which the participant shifted their body weight from one leg to the other, as shown in Figure 25b while standing on the split-belt treadmill to measure the corresponding GRF. In the second experiment, the participant

was asked to walk on the split-belt treadmill. During both experiments, a signal was used to synchronize the SLS output and GRF recordings. The experiments were designed to elucidate the same points made earlier in the case of the able-bodied experiment. The sensors were tested on the benchtop after each experiment using real-time data visualization to ensure no damage occurred by the amputee testing procedure.

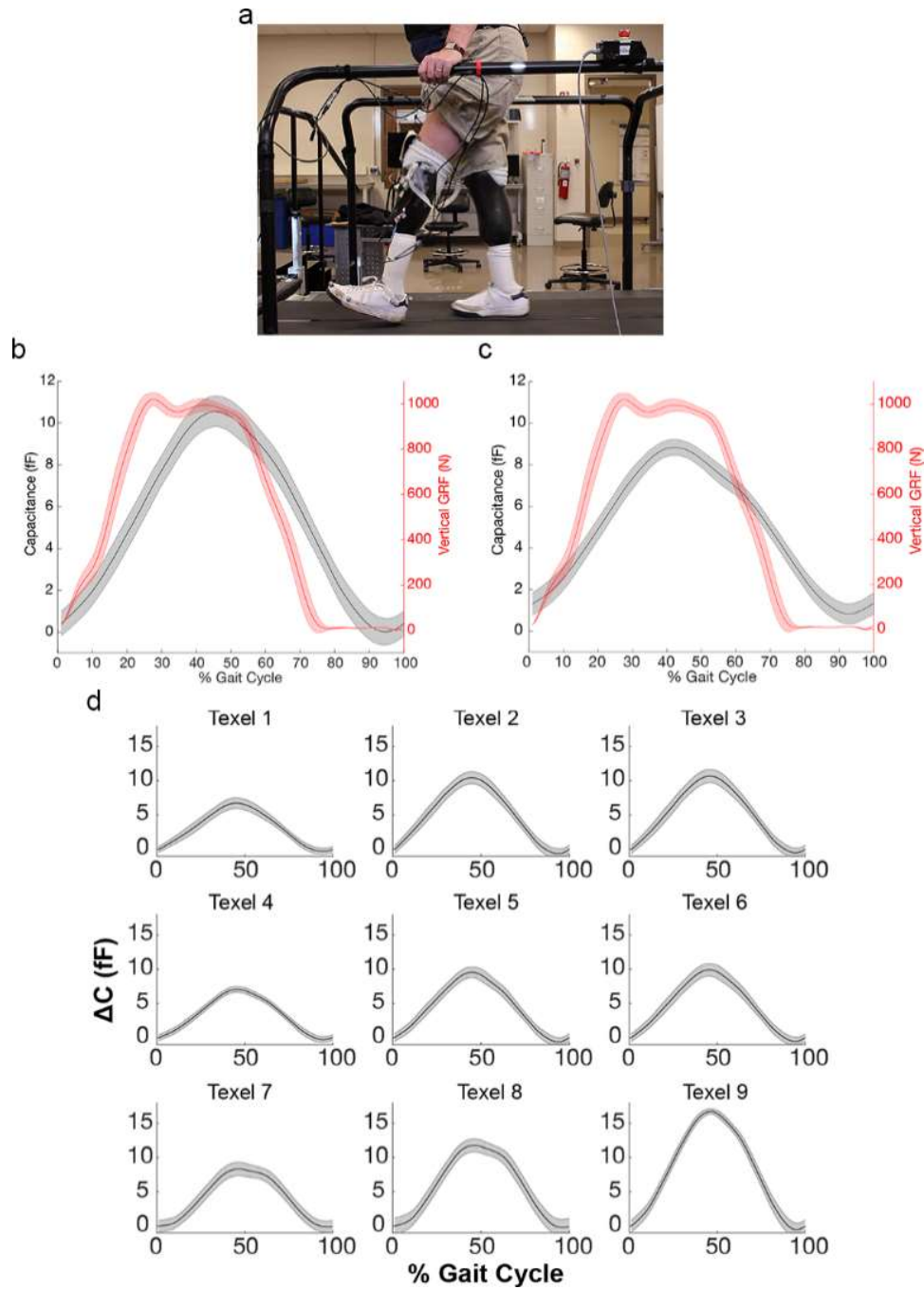


Figure 26: Amputee testing results (a) Participant walking on a treadmill. The average change in capacitance and GRF at the (b) PT and (c) PD (d) Texel response at PT during walking. For the walking experiments, the minimum capacitance (i.e., while the prosthesis was unloaded) was taken as the baseline and removed from the capacitance response. Reprinted with permissions from<sup>[21]</sup> ©2021 IEEE.

The average SLS responses recorded during weight shifting experiments at the PT and PD are shown in Figure 25c and d respectively. The capacitive response was smoothed using an

adjacent-averaging method. As we observed with the able-bodied testing, when the participant shifted body weight onto the leg with the SLS, the resulting capacitance increased. Alternatively, when the participant shifted body weight onto the other leg and off-loaded the sensor, the capacitance decreased. The peak  $\Delta C$  values were in similar ranges regardless of anatomical location however, slightly larger at the PT. Higher pressures are anticipated at this location with several studies in the literature reporting peak ISE pressures at the PT.<sup>[41, 122, 307]</sup> This can be attributed to common socket designs that aim to distribute the majority of an amputee's body weight on the PT.<sup>[307]</sup> During amputee testing, a time lag was observed between the GRF and  $\Delta C$  peaks at both anatomical locations which were not observed during able-bodied trials. This can be explained by the placement of the sensors and the fact that GRF was measured by the treadmill beneath the participant's foot. In able-bodied testing, the sensor was placed beneath the participant's bent-knee, parallel to the treadmill belt, therefore it experienced a similar load profile at a similar time as the bottom of the foot. In contrast, during amputee trials, the sensors were placed around the residual limb, not parallel to the treadmill belt. As a result, it experienced a load profile different than that measured by the treadmill, thereby experiencing peak loading at a different time.

During the subsequent walking trials shown in Figure 26a, the participant walked on the treadmill at a speed of 0.41 m/s (selected based on the subject's comfort level) for around one minute or approximately twenty walking cycles. While this walking speed is slightly lower than reported values for LL amputees (0.60<sup>[305]</sup> and 0.78 m/s<sup>[306]</sup>) this may be explained by the fact that the subject in this experiment was a bilateral amputee who may experience additional challenges during walking. We completed post-processing (alignment, segmentation, and averaging) for the GRF and capacitance data of this walking trial in a similar way to able-bodied experiments

described previously. The results of the walking trials, presented for the PT and PD in Figure 26b and c, provide expected trends with maximum GRFs/SLS values measured during the stance phase (initial 60% of the gait cycle)<sup>[308]</sup> and minimum GRF/SLS response measured during swing phase (final 40% of the gait cycle).<sup>[117, 119, 308, 309]</sup> Additionally, the SLS response provided little variation during the walking experiment. As noted earlier for the weight-shifting trials, the time lag between the peak GRF and  $\Delta C$  values can be attributed to the placement of the sensors relative to the location of the GRF measurement. Additionally, a larger value was observed at the PT than the PD. As previously mentioned, peak pressures are expected at the PT<sup>[41, 122, 307]</sup> and the PT is often the main site of weight-bearing during ambulation.<sup>[310]</sup> While verifying the source of these differences requires a further analysis which we reserve for a future study, the socket fit is likely to have contributed. During both the weight-shifting and walking experiments, the capacitance response was different for each texel, as shown in Figure 26d, indicating a pressure distribution across the area.

## 5.6 Conclusion

In this work, we presented a new method to seamlessly monitor pressure within the ISE utilizing a simple and inexpensive textile-based, soft sensor system. We described in detail the SLS system including textile interconnects, high-speed data recording, and transmission from four sensor arrays which require little power enabling up to twelve hours of data collection. Further, we presented two experimental approaches to systematically incorporate SLS within a simulated in-vitro and in-vivo ISE environment before evaluation with an amputee subject. In the first experiment, the SLS provided sound pressure tracking results for proof-of-concept when placed on the curved surface of the artificial limb. The sensor system continued to collect reliable information from the multiple sensor arrays simultaneously throughout the experiment. The results

of the subsequent able-bodied experiments show that the SLS was sufficiently robust to withstand human testing. The SLS continued to function throughout the able-bodied experiments and provided consistent data during cycles of dynamic loading which could be qualitatively explained by the general movement of the able-bodied participant. Results of the amputee participant experiment indicated that the SLS is robust and can monitor the ISE without causing discomfort to the subject. The results also correspond well to the general movement of the amputee participant. In summary, these preliminary results validate the concept of SLS as a promising approach for monitoring pressure distribution within the ISE that is amenable to full integration into prosthetic components. The future work will involve expansion to a larger clinical study with additional subjects, calibration of the sensors for the assessment of absolute pressure values, as well as a study of the effect of use, aging and washing on the material and sensor performance.

### **5.7 Acknowledgement**

The authors would like to acknowledge the Nonwovens Institute at NC State University for providing the nonwoven fabric for this research. The authors would also like to acknowledge and thank Derek Frankena, CPO for the fabrication of the artificial limb.

## **6 Tricomponent Melt Extrusion of Fiber Sensors for Electronic Textiles**

Here, a disparate sensing approach is explored in which sensing is achieved at a fiber-level rather than at a yarn-level. This article introduces a new fabrication method for fiber-based sensors as well as methods for material selection and characterization. Subsequently, the fibers' electrical, mechanical, and sensing behavior are analyzed. This work is not yet published but is intended for submission to Elsevier's Polymer journal.

## 6.1 Abstract

Tricomponent melt extrusion (TME), or the simultaneous extrusion of three distinct polymers, is a novel fiber formation process which provides exciting opportunities to produce specialty fibers. Here, we present a scalable means of producing uniquely shaped, fiber-based pressure sensors via TME. We discuss the TME process and our approach to selecting process settings based on selected polymers, machine restrictions and the desired fiber shape. Tricomponent melt extruded fiber sensors are successfully fabricated using various polymer flow ratios (FRs) based on simulations. Subsequently, the sensing fibers are characterized using optical microscopy, tensile testing, and electromechanical analysis which encompasses a pressure-sensing demonstration. Results indicate that the micron-scale sensing fibers can be produced at speeds of  $>100$  m/min thus providing a scalable method of producing fiber-based sensors for wearable technology.

## 6.2 Introduction

Man-made textile fibers are manufactured through polymer spinning methods, most commonly, wet, dry, and melt spinning.<sup>[311]</sup> Melt spinning is the most convenient and economic fiber formation technique because it is a relatively simple process that provides high spinning speeds and requires no auxiliary agents (like solvent, precipitation agents, etc.).<sup>[312]</sup> During melt spinning, solid, fiber-forming polymers are melted and extruded through an extrusion spin-pack. In a typical melt-extrusion process a single polymer, such as polyester or polyamide, is made into fibers. However, multi-component fibers containing two or more physically and/or chemically distinct polymer components, can also be processed via melt extrusion.<sup>[313]</sup> The bicomponent melt extrusion (BME) process, in which two polymers are extruded simultaneously to form a single fiber, is relatively common in both research<sup>[314-317]</sup> and commercial settings for applications such as thermal bonding and self-crimping fibers.<sup>[318]</sup> BME has been proposed for the fabrication of fiber-based sensors but

to our knowledge, these efforts have been restricted to core-sheath type fiber configurations.<sup>[314, 319-323]</sup> Bicomponent core-sheath fibers with material combinations of carbon black/high density polyethylene (core) and polyvinylidene difluoride (PVDF) (sheath) for piezoelectric force sensors,<sup>[314, 323]</sup> a cyclo-olefin (core) and a tetrafluoroethylene-hexafluoropropylene-vinylidene fluoride terpolymer (sheath)<sup>[322]</sup> for optical sensing of heart rate,<sup>[321]</sup> and PP/carbon nanotube (core) and PVDF (sheath) for piezoelectric fiber-based sensing<sup>[319, 320]</sup> have been proposed. The TME process, however, is rather uncommon.<sup>[324, 325]</sup> TME has been used to fabricate fibers with unique optical properties<sup>[324]</sup>, and for energy harvesting applications,<sup>[325]</sup> but has not yet been investigated for fabricating fiber-based sensors.

Fiber based sensors are considered essential for the emerging field of electronic textiles (e-textiles) or textiles with integrated electronic capabilities. In recent years, e-textiles have generated considerable research and commercial interest due their potential applications in healthcare, security, entertainment, and others.<sup>[176]</sup> Textile-based sensors have been proposed for monitoring various parameters including pressure,<sup>[48, 50, 53, 58, 68, 205]</sup> strain,<sup>[152, 232, 267-270]</sup> humidity,<sup>[92, 271, 272]</sup> and temperature.<sup>[70, 82, 273]</sup> These sensors may be incorporated into textile structures at one of the hierarchical levels of fiber, yarn, or fabric. Fiber-based sensors are advantageous because of their lightweightness, high aspect ratio, and flexibility thus allowing them to easily conform to the human body as wearable devices.<sup>[59, 226]</sup> Most experimental fiber-based sensors have been fabricated through batch processes like atomic layer deposition processes<sup>[57]</sup> using specially designed bench-top equipment<sup>[68, 232]</sup> or utilizing microfabrication techniques requiring processes under vacuum and cleanroom environments<sup>[84]</sup> which may not be scalable. Additionally, these methods present barriers to integration into traditional textile manufacturing processes; thereby, limiting widespread adoption. While few have proposed fiber spinning processes to create textile-

based sensors,<sup>[70, 93, 326-329]</sup> most of these efforts are limited to processes of questionable commercial value.

Here, we propose a TME process for manufacturing a Bicomponent Sensory Fiber for Textiles (BiSoFT) with unique cross-sectional shape that can be transformed into sensing arrays through the weaving process. We describe our approach in setting up the critical fiber formation process parameters for the TME as well our systematic experimental approach to introduce the TME polymers to successfully produce the BiSoFT. Prior to the melt extrusion process, the thermal and electrical properties of the selected polymers were characterized. The polymers were processed at various pump speeds selected based on simulations to determine the effect of polymer FR on the fiber shape. The flow ratio indicates the ratio of polymer mass extruded by each extruder per unit time and dictates the proportion of fiber cross-sectional area occupied by each polymer. Optical microscopy was used to analyze fiber shape and select optimal FRs for the desired BiSoFT application, i.e., pressure sensing. The tensile behavior of the fibers was determined and used to select the appropriate settings for post-extrusion drawing. Finally, the electromechanical properties of the fibers were determined including the electrical resistance of the fibers/unit length and the pressure-sensing capabilities of the BiSoFT. Results of this research indicate that the TME process is scalable and commercially relevant to produce fiber-based pressure sensors at speeds >100 m/min, for use in e-textiles.

### **6.3 Fiber Shape and Sensor Geometry**

The BiSoFT cross-section consists of two insulating side-lobes bridged by a conducting segment in the middle, see Figure 27a. The conducting polymer segment extends slightly into the insulating lobes to provide a strong interface between the insulating and conducting polymers. During the fiber formation process a sacrificial polymer, used as a third component, is required to envelope

the two other components for stable extrusion of the desired fiber shape. The sacrificial polymer can be removed post-production thus providing the unique BiSoFT shape, as shown in Figure 27b.

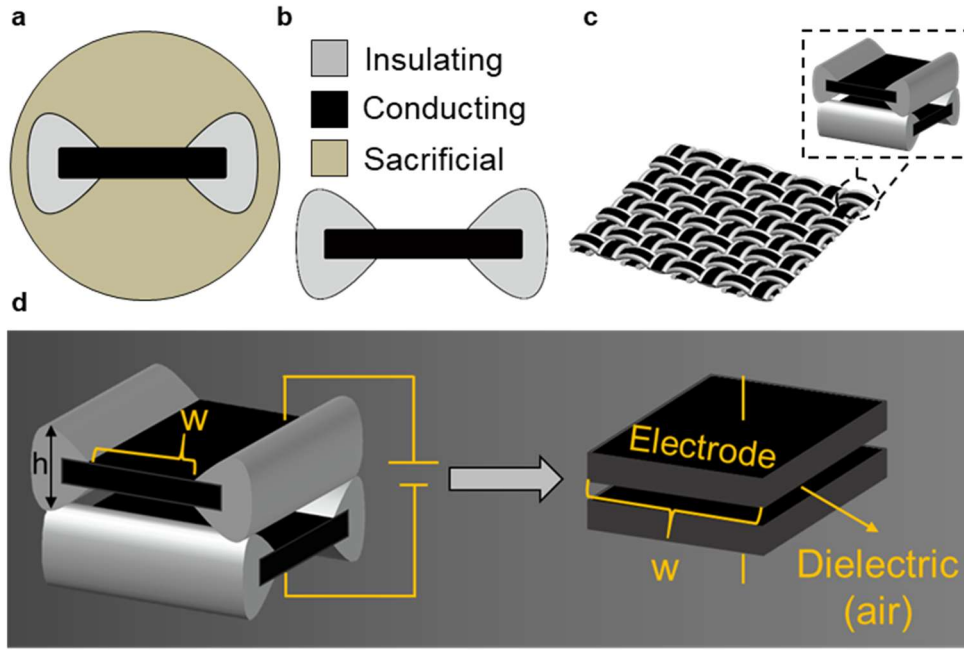


Figure 27: TME fibers shape and sensor structure (a) TME fiber with sacrificial polymer (b) BiSoFT after removal of the sacrificial polymer and (c) BiSoFT woven into a fabric configuration with each individual texel formulating a capacitive sensor (d) Texel architecture compared to a parallel plate capacitor

When the sensory fibers are woven into a fabric, each cross-over point forms a texel, see Figure 27c. In the texels, the conductive segments act as the parallel plate electrodes and the separation (or the cavity) created by the insulating lobes provides the space for the air to act as the dielectric, see Figure 27d. The sensory output or the change in capacitance ( $\Delta C$ ) of each texel upon the compression can be expressed in terms of its dimensional parameters as,

$$\Delta C = \varepsilon_0 \varepsilon_r w^2 \left( \frac{1}{h} - \frac{1}{h_0} \right) \quad \text{Equation 1}$$

Where,  $\varepsilon_0$ , and  $\varepsilon_r$ , are relative the permittivity of the free space and the dielectric, respectively,  $w$  is the width of the conductive segment,  $h$  and  $h_0$  are the thickness of the insulating segment of the BiSoFT, before and after deformation. Here, we assume that the change in the fiber dimension due to compression is limited to the parameter,  $h$ . In Section 6.6.3, the pressure sensing

capabilities of a single fiber cross-over point, or pixel, will be demonstrated to explain the influence of these parameters.

To produce this fiber shape, a custom extrusion spin-pack was designed in collaboration with and produced by Hills Inc. (Melbourne, FL) following the extrusion spin-pack design described in the relevant patents.<sup>[330-332]</sup> The spin-pack was designed with a final plate, known as the extrusion die, consisting of three exit spin hole diameters – 0.9, 1.2, and 1.5 mm. The spin-pack was designed based on simulations performed by Hills Inc using the properties of polypropylene (PP) with a melt density of 0.78 g/cc. Simulations were run at FRs anticipated to provide the desired fiber shape. FRs used during simulations (sacrificial polymer : insulating polymer : conducting polymer) were 70:20:10, 60:25:15, and 60:30:10.

## **6.4 Materials**

Three materials are required to produce the BiSoFT: a conducting polymer, an insulating polymer and a sacrificial polymer. One of the major challenges in the TME process is that all three polymers converge at the spin-pack that must be held at one, uniform temperature. Therefore, all three polymers must be stable and extrudable at similar temperatures. In order to ascertain the processibility at similar temperatures, thermal analysis was performed on all three of the polymers. Additionally, the electrical properties of the selected conducting polymer were measured to ensure that the material was sufficiently conductive for the BiSoFT.

### **6.4.1 Polymer Selection**

The most critical material in this fiber cross section is the conductive component. Most commercially available, melt-processible, conductive materials are polymer composites consisting of thermoplastic polymers and conducting nanoparticles, such as carbon nanotubes, carbon black (CB) or graphene to impart electrical conductivity.<sup>[333]</sup> Such materials are commonly used for static

dissipation, or electromagnetic interference/radio frequency interference shielding applications.<sup>[334]</sup> To produce these conductive composites, a bulk material is usually combined with electrically conductive nanoparticles through a compounding process.<sup>[333]</sup> During compounding processes, it can be quite challenging to achieve satisfactory filler dispersion.<sup>[333]</sup> Further, both electrical and mechanical properties can be negatively influenced by the degree of agglomeration and dispersion of the nanoparticles.<sup>[333]</sup> For this research a commercially available polymer compound made of CB fillers and conductive polyamide,6 (CoPA6) was used. The CoPA6 was chosen because it was readily available and PA6 is a commonly employed polymer in melt-extrusion processes. Once the conductive material was selected, the other fiber components were selected by closely matching the relative viscosity (RV) of the CoPA6. The RV is often an indication of melt flow index and intrinsic viscosity<sup>[335]</sup> of the polymer which are key parameters that determine fiber formation characteristics of a polymer.<sup>[291]</sup>

According to the data provided by the manufacturer, the RV of the CoPA6 is in the range of 2.62-2.83. Therefore, a commercially available insulating polyamide6 (InPA6, BASF, B27E) possessing a RV of 2.62-2.83 was selected for the research. For the sacrificial component of the tricomponent fiber, polylactic acid (PLA) (Natureworks, 6202D) with a manufacturer-reported RV of 3.1 was chosen. PLA was selected because it is commonly used in bicomponent fiber extrusion as a sacrificial component to create unique fiber shapes or micro-structures.<sup>[336, 337]</sup>

#### **6.4.2 Polymer Characterization**

Prior to the BiSoFT extrusion, the melt properties of the selected polymers were measured to ensure that the three selected materials could be simultaneously extruded. Thermal characterization of the polymers included differential scanning calorimetry (DSC), melt flow rate (MFR), and thermogravimetric analysis (TGA). DSC is a thermoanalytical technique used to

measure the occurrence of phase transitions such as glass transition and melting.<sup>[338, 339]</sup> In the TME process, the polymers are initially heated in three separate extruders however, the three materials converge at the extrusion spin-pack which must be held at one constant temperature. Therefore, it is necessary that all three polymers melt and can be extruded at similar temperatures. The results of DSC (TA Discovery DSC 250) shown in Figure 28a indicated that the polymers possessed sufficiently similar melt temperatures for co-extrusion with successful multicomponent extrusion processes utilizing polymers with similar or larger range in melting temperature.<sup>[314, 340]</sup> Analysis of the DSC peaks reveal that the onset melting temperatures were 156.76, 200.08, and 218.69°C whereas the peak melting temperatures were 165.93, 219.47, and 219.22 for the PLA, CoPA6, and InPA6 respectively. These results were used to select the appropriate temperature profiles for each extruder.

The MFR is one of the often-used polymer rheological properties for melt-extrusion of polymers and it is related to the more fundamental flow characteristics such as the zero-shear viscosity, molecular weight average, and its distribution.<sup>[291, 341-343]</sup> The MFR is measured as the mass of polymer that is extruded through an extrusion plastometer over 10 minutes under a prescribed temperature and mechanical loading conditions. The MFRs of the selected polymers were measured using a melt flow tester (Instron CEAST, 7026 Melt Flow Tester) according to a standard test method.<sup>[344]</sup> As shown in Figure 28b, the MFR values ranged from ~30-86 g/10 min. The MFR values were within similar ranges (<100 g/10min) utilized in previously reported bicomponent fiber extrusion processes.<sup>[314, 345, 346]</sup> While the MFR of the PLA is larger than the PA6 materials, it was hypothesized that the MFR values were sufficiently similar for co-extrusion since similar materials were previously utilized for bicomponent fiber extrusion.<sup>[347]</sup>

TGA is a technique in which the change in mass of a material is measured as a function of temperature.<sup>[198]</sup> In this instance the TGA (Perkin Elmer TGA 1) was performed in a standard furnace at temperatures up to 800°C at a heating rate of 20°C/min in N<sub>2</sub>, to determine the percentage of CB within the CoPA6. Two different batches of coPA6 were analyzed for consideration. As shown in Figure 28c, the first and second batch of CoPA6 contained ~26% and ~36% carbon respectively.

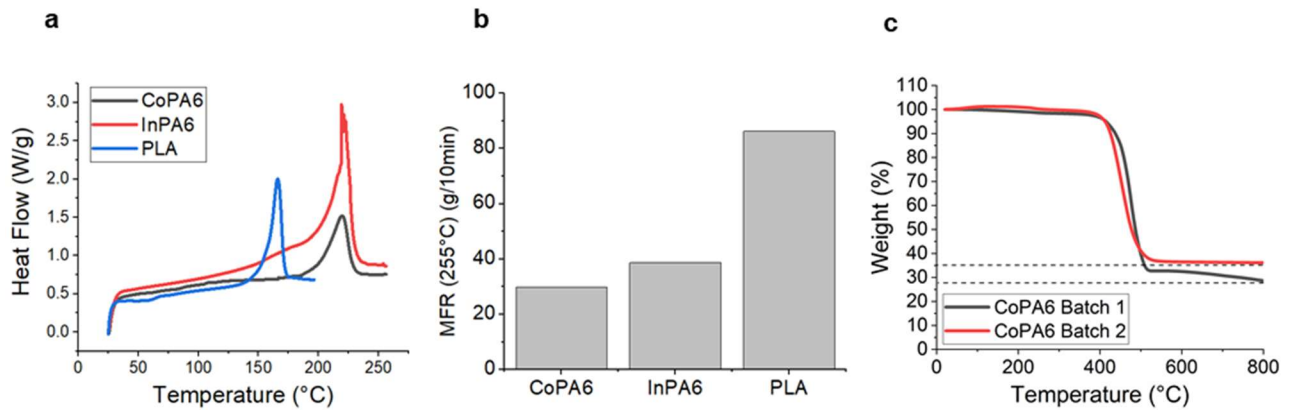


Figure 28: Results of thermal polymer characterization (a) DSC (b) MFR (c) TGA

To measure the electrical conductivity of the two batches of CoPA6 under consideration, films (thickness of ~1.5-1.7 mm) were produced using a heat press (Carver 3851-0) at a temperature of ~250°C and force of 2-3 metric tonnes. The conductivity of these films was measured using a custom-built 4-Probe measurement system with gold probes of 3 mm probe spacing, with the outer probes applying current and the inner probes measuring the voltage. The probes were attached to a Keithley 6221 alternating current and direct current source and a Keithley 2182a Nanovoltmeter. A correction term considering the dimensions and thicknesses of the films was applied. While the electrical resistance of the first batch of the CoPA6, containing ~26% of CB was too high to record using the current set up, the other batch of CoPA6 containing a higher concentration of carbon (~36%) was at an acceptable range of 2.8-6.58 Ω·cm. The high

electrical resistance of the first batch of CoPA6 is likely due to the poor dispersion and/or stability of the conducting networks leading to poor electron mobility.<sup>[348]</sup>

## 6.5 Fiber Formation: Tricomponent Extrusion and Drawing

The TME system consists of three separate melt extrusion lines (A, B, and C) which converge at the spin pack, see Figure 29. While this schematic shows details of one of the extruders (Extruder B), the other extruders, A and C are identical except for the extrusion screw diameters and metering pump capacities (see Table 5). Additionally, line C possesses a fourth heating zone.

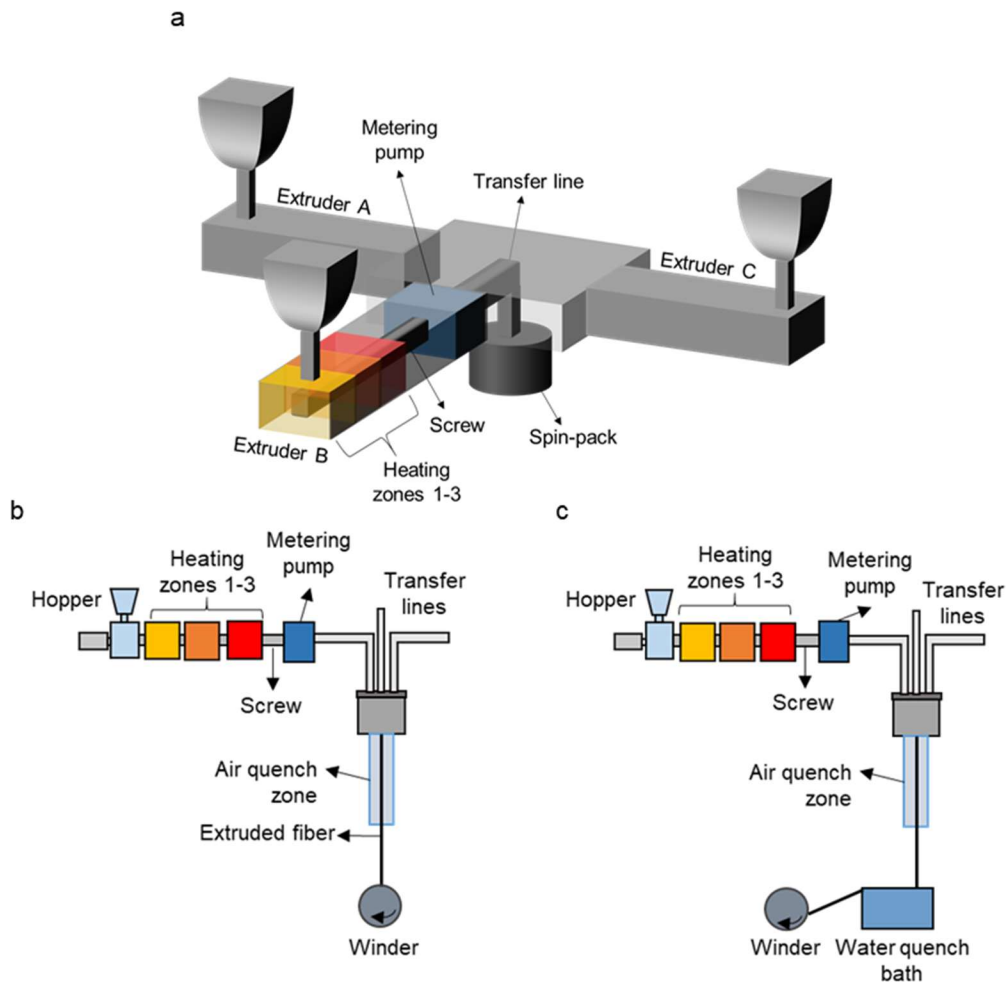


Figure 29: TME set-up (a) Schematic of melt extrusion line for extruder B/polymer B (b) Schematic representation of extrusion line with winding completed directly after air quenching (c) Schematic representation of extrusion line with winding completed after both air and water bath quenching

Each extrusion line includes a hopper, extrusion screw, metering pump, transfer line, and several heating zones. The molten polymer is extruded through the spin pack and can be quenched in air and/or in a water bath. Quenching of monofilament fibers can be particularly difficult when compared to multifilament fibers due to the relatively large fiber diameters. Monofilaments generally require more time and/or additional means of quenching in order to adequately cool the bulk of the fiber.

### 6.5.1 Optimization of the Extrusion Process Parameters

The most critical process parameters of the TME line are the pump speeds and temperature profiles of the extruders. The pump speeds determine the amount of material dispensed by the melt pumps per unit time and can be expressed in terms of other known parameters as, Pump speed (rpm) =  $\frac{1}{\text{Metering pump capacity } (\frac{\text{cm}^3}{\text{rev}})} * \frac{1}{\text{Melt density } (\frac{\text{g}}{\text{cm}^3})} * \text{Pump throughput } (\frac{\text{g}}{\text{min}})$ . The metering pump capacity is a constraint of each extruder and cannot be changed (see Table 5). A melt density of 1.0 g/cm<sup>3</sup> was utilized for both the CoPA6 and InPA6 based on available literature.<sup>[349,350]</sup> While the melt density of the CoPA6 may be slightly different due to the inclusion of CB particles, it was assumed to have the same melt density as neat PA6. The melt density of 1.08 g/cm<sup>3</sup> for the PLA was used as per the manufacturer's data sheet. Finally, the pump throughput was altered for each of the extruders, based on the selected FR, to achieve the material throughput required for the desired cross sectional shape. In addition to the FRs (70:20:10, 60:25:15, and 60:30:10) mentioned earlier in Section 6.3, we also utilized an additional FR of 50:40:10, to enhance the relative size of the insulating lobe to optimize the capacitive response of the sensing elements. To achieve the different FRs, the pump speeds were adjusted accordingly. The pump speeds used during the experimental portion of this research are provided in Table 6.

When selecting process settings, it is also important to consider mechanical and other specifications of the extrusion set up. On the TME line used here, pump pressures (pressure at the metering pump) and pump speeds up to 2000 PSI and 90 RPM respectively are acceptable. Another restrictive parameter is the extrusion pressure, or the pressure at the spin-pack, which was set at 750 PSI based on the spin-pack manufacturer's recommendations. The extrusion screw speeds up/slows down in order to maintain this pressure.

The temperature profile of the extruders is set based on the melting temperatures to slowly heat the polymers through the heating zones. The Zone 1 temperature is particularly critical, especially when running PAs. In Zone 1, it is important to keep the extruder near or slightly above the polymer's melting temperature. To build pressure in Zone 1, it is desirable that some polymer pellets are melted, while others remain in solid pellet form such that the melt is pushed through the machine. Moving to Zone 2, the temperature is increased to ensure full melting of the polymers. The peak temperature should be achieved in the melt pump and maintained through the transfer lines and spin-pack. The temperatures used during the TME extrusion trials are provided in Table 8.

### **6.5.2 Tricomponent Extrusion Trials**

The experimental trials performed in this research can be grouped into four phases: (1) initial trials run with only PP to validate spin-pack design and process parameters (2) phased introduction of the desired TME materials (PLA, InPA6, and CoPA6) (3) extrusion with all three selected materials and (4) fiber winding onto spools. Each trial was run with unique process parameters as discussed earlier in Section 6.5.1. These parameters are summarized in Table 7 and Table 8.

The objective of Phase 1 experiments was to validate the spin-pack design and the selected FRs. Initial trials were run with PP (ExxonMobil PP3155E3) in all three extruders because PP is

a robust material which is relatively easy to extrude. Small amounts of orange and blue stained PP pellets were added to Extruder A and B respectively to differentiate the fiber components microscopically to ascertain the cross-sectional shape. During initial trials, the smallest extrusion spinneret size (0.9 mm) was used to facilitate quenching. FRs of 70:20:10, 60:30:10, and 60:25:15 were utilized and fibers were collected in free fall to study via optical microscopy (see Figure 33). These images confirmed that the desired fiber shape was created with the spin pack and the selected FRs.

In phase 2 trials the selected TME polymers were systematically introduced into the process, one at a time, to aid trouble-shooting. The sacrificial polymer PLA was introduced first using extruder C. Extruders A and B were run with the same PP used in the previous phase. There was some initial flow discontinuity when running the PLA, but this was resolved by increasing the polymer throughput by raising the pump speed to >5 RPM. Next, stained InPA6 was introduced into extruders A and B. When extruding InPA6, excessive pressure build-up was observed in extruder B indicating formation of undesirable shear stresses, likely within the die. To reduce the amount of shear within the die, all subsequent trials were run using the largest spinneret orifice (1.5 mm) which mitigated the excessive pressure buildup. The FRs of 70:20:10, 60:30:10, and 60:25:15 were successfully processed and optical images of fibers resulting from these trials are shown in Figure 33.

After the successful extrusion of the InPA6 and PLA at all FRs, the final and most critical fiber component, CoPA6, was introduced in phase 3. It is important to note that even though the moisture regain of nylon is small, the absorbed moisture in the polymer could pose serious flow issues. After careful drying of CoPA6, the fibers were produced at FRs of 70:20:10, 60:30:10, 60:25:15, and 50:40:10 and optical images of fibers are shown in Figure 34. Winding of the fiber

on a spool, was a problem with the usual positioning of the water quenching bath at ~3m from the spin-pack exit. However, the fibers were successfully wound onto spools by lifting the quenching bath (see Figure 35) closer to the spin-pack exit (~1m). During winding trials, two FRs were prioritized, 50:40:10 and 60:25:15, based on their cross-sectional shape and dimensional consistency (see Figure 34.). The fibers collected on bobbins during the phase 4 trials were used for all subsequent experimentation. It is important to note that it is possible to remove the sacrificial PLA layer from the fibers using a NaOH solution or a scouring process,<sup>[336, 337]</sup> before or after fabric formation. In this research, the PLA was removed to expose the conductive material before the relevant characterizations.

### **6.5.3 Drawing**

Fiber drawing is a process in which fibers are uniaxially stretched to improve their fine structure through high degree of molecular alignment along the fiber axis which in turn improves their desirable textile properties such as tenacity, moduli, etc.<sup>[312]</sup> In this research, drawing was also of interest to reduce the size of the as-spun fibers closer to that of common textile fibers. Here, drawing was performed in a post-extrusion process, using a series of rolls (Stahle Air Texturing System), two of which were heated, and a winder (SSM), see schematic in Figure 36. The draw ratio (DR), or the degree to which the fiber was irreversibly elongated, was selected based on the results of tensile testing of the as-spun fibers (see Section 6.6.2). The choice of the DR in fiber manufacturing is often based on the polymer type and the intended end-use. In this instance, we decided to draw the TME fibers using DRs of 1.6 and 2.2. These draw ratios were selected based on their stress-strain behavior and will be discussed in Section 6.6.2. While the fibers extruded using a FR of 50:40:10 could be drawn (see process details in Table 8) drawing of the 60:25:15 fibers was unsuccessful because of the frequent breakage and delamination of the predominant and

excessively brittle PLA component. A likely remedy for this is to select polymer FRs with lower PLA content (<50%) or to utilize a PLA grade with lower crystallinity, and therefore, greater ductility for the drawing process.

## **6.6 Fiber Characterization**

The sensory fibers were first characterized using optical microscopy to ascertain their shapes as a function of the flow ratios used in the TME process. Subsequently, the fibers were evaluated for their axial tensile as well as transverse compressive stress-strain behavior. Additionally, the electrical and sensory behavior of the fibers were also evaluated.

### **6.6.1 Optical Microscopy and Dimensional Analysis**

Throughout the various phases of TME experiments, optical microscopy was performed to ascertain the desired cross-sectional shape of the fibers. The cross-sectional images were analyzed using an image processing software ImageJ (NIH) to measure the areal fraction of the various polymer components and to determine if the desired FRs were achieved. The cross-sectional shapes of the fibers produced using the two FRs (50:40:10 and 60:25:15) chosen for further investigation are shown in Figure 30a,b and Figure 30d,e respectively. Critical dimensions of interest of the fibers are shown in Figure 30c and f. The areas of the various fiber components were measured to compare the nominal and actual FRs. The nominal FRs of 50:40:10 and 60:25:15 were measured as ~53:36:11 and ~59:25:16, respectively. This indicates that the calculations used to adjust pump speed to achieve desired FRs were quite accurate.

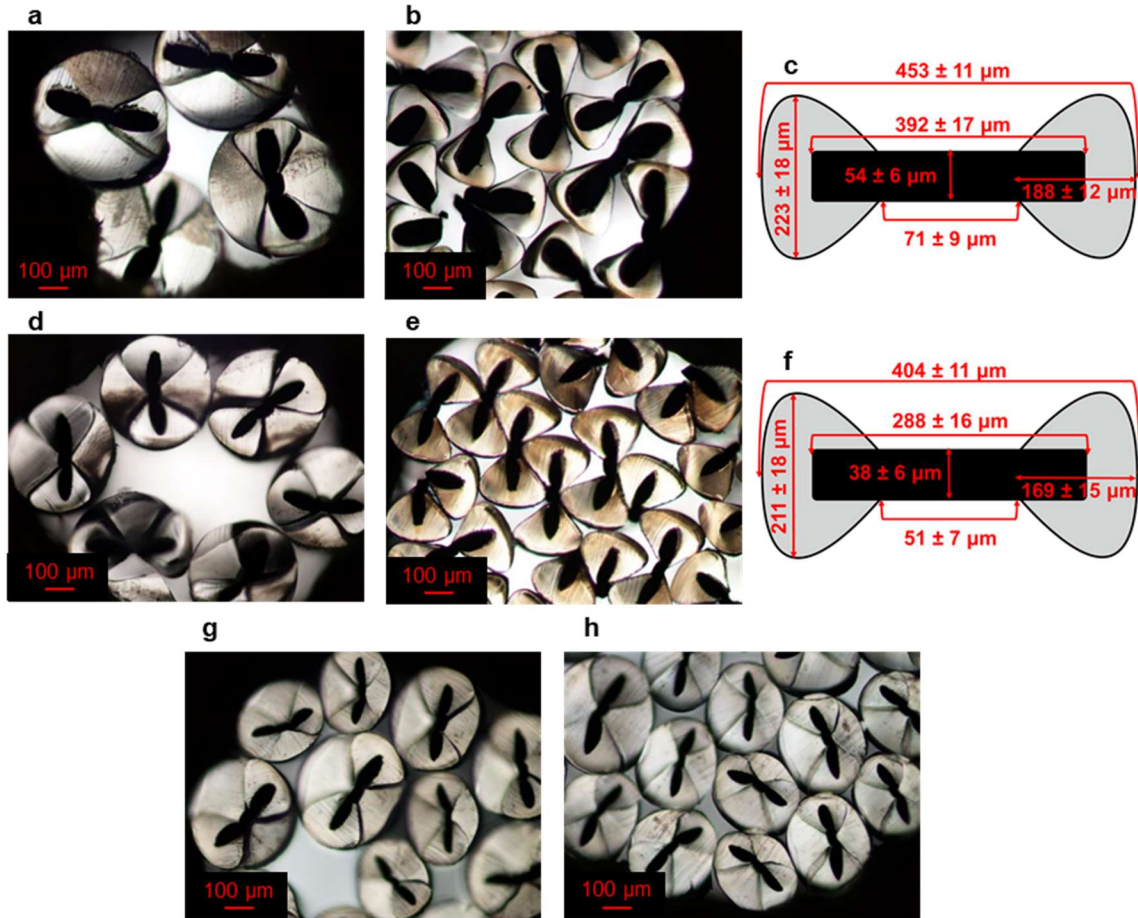


Figure 30: Cross sectional images and dimensional analysis of the fibers (a) FR 60:25:15 (b) FR 60:25:15 with PLA removed (c) FR 60:25:15 dimensional analysis (d) FR 50:40:10 (e) FR 50:40:10 with PLA removed (f) FR 50:40:10 dimensional analysis (g) FR 50:40:10 with DR:1.6 (h) FR 50:40:10 with DR:2.2

Optical microscopy was also performed to compare the fiber dimensions before and after drawing. As shown in Figure 30d, the diameter of the fiber produced using FR 50:40:10, changed from initial ~400 μm to 289, and 273 μm, respectively for the DRs of 1.6 and 2.2. For the applied DRs the diameters should have been reduced to 253 and 183 μm, respectively. The difference in measured and expected diameters may possibly be explained by incomplete drawing due to fiber slippage at the draw rolls. Overall, the difficulties of drawing of the TME fibers remains a subject of investigation.

## 6.6.2 Mechanical Behavior of Fibers

As previously mentioned, during drawing, fibers are heated and irreversibly extended to reduce the fiber size as well as improve their mechanical properties. Therefore, the mechanical behavior of the fibers was evaluated to select appropriate DRs as well as to compare the load-extension properties of the fibers before and after drawing. The tensile behavior of the fibers was measured on a tension/compression load frame (MTS 30/G) using a standard testing procedure<sup>[351]</sup> and a break sensitivity of 90%. Representative load-extension plots of all of the fibers at various stages of fabrication are shown in Figure 31.

As shown in Figure 31a, the undrawn FR 60:25:15 fibers, exhibited a yield point at ~5% strain, beyond which the fiber continued extending without requiring additional load. While the undrawn FR 60:25:15 fibers show fracture of all three fiber components simultaneously, as shown in the inset image of Figure 31a, at approximately 22% strain, the components of undrawn FR 50:40:10 fibers broke in a sequence, see Figure 31b. First, the FR 50:40:10 fiber reached its yield point at ~11% strain followed by the PLA breaking at around 25% strain. Subsequently, the remaining fiber components extended significantly more and then fractured at strains >400% strain. This is confirmed by the microscopic image of the FR 50:40:10 fiber breakage in Figure 31c which shows the relatively short PLA segments and longer InPA6 and CoPA6 component. The typical tensile behavior of the undrawn FR 50:40:10 fiber was seemingly more ductile than the undrawn FR 60:25:15 fiber, likely due to the lower PLA content. Thus, drawing of the 50:40:10 fibers was successful.

The expected improvement in tensile behavior of the drawn 50:40:10 fibers is apparent in Figure 31d, e, and f. After drawing, the PLA broke at higher strains (>150%), and in general the fiber breaking load was higher. Additionally, post-drawing, all three fiber components broke at

similar strains typically around 200-300%. Changes in tensile behavior post-drawing are expected because the drawing process alters polymer orientation and crystallinity.<sup>[312]</sup> With the focus of this investigation being different, we do not intend to further explore the exact changes in polymer orientation and crystallinity taking place within the TME fibers.

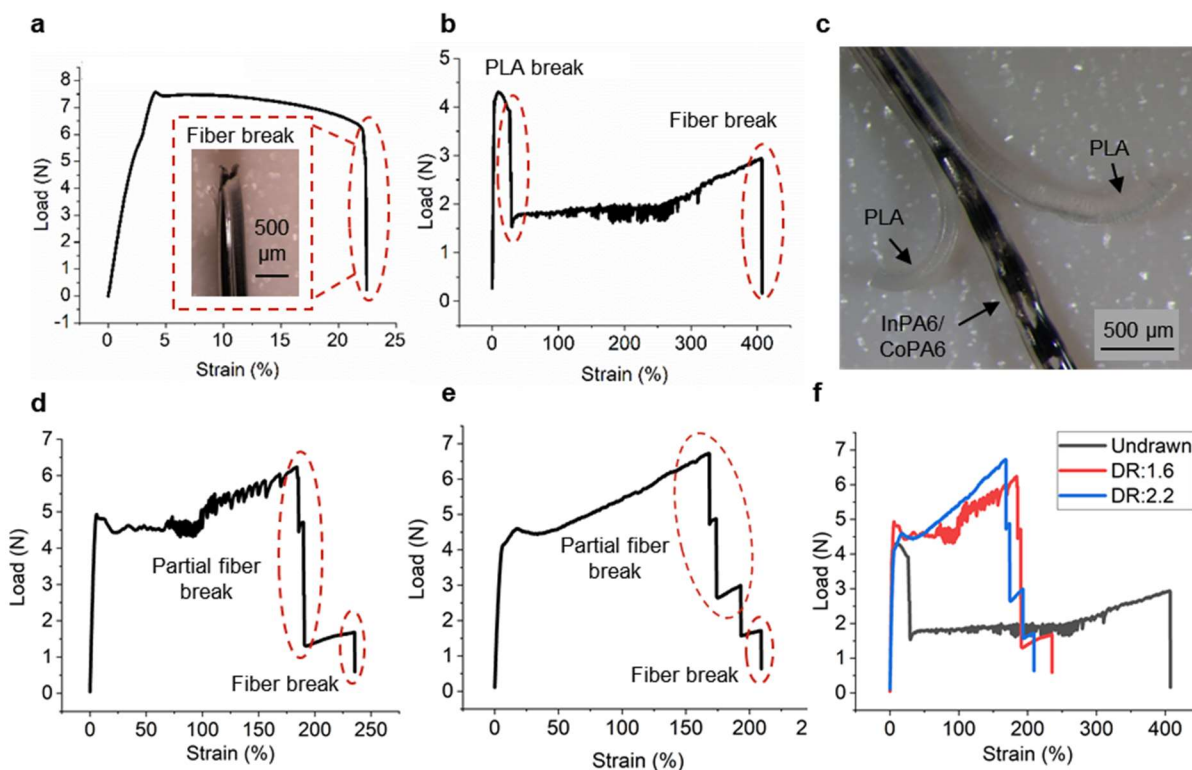


Figure 31: Tensile properties of TME fibers (a) FR 60:25:15, inset shows microscopic image of final fiber breakage (b) FR 50:40:10 undrawn (c) Microscopic image of FR 50:40:10 undrawn fiber breakage. Image demonstrates that PLA breaks prior to InPA6 and CoPA6 segments (d) FR 50:40:10 post-drawing with a DR of 1.6 (e) FR 50:40:10 post-drawing with a DR of 2.2 (f) Comparison of tensile properties of undrawn and drawn 50:40:10 fibers

Pressure or touch sensing behavior of the melt-extruded fiber-assembly in the form of woven fabrics is largely dictated by the transverse compressive behavior of the fibers. Based on the principle of sensing explained earlier in Section 6.3 and shown in Figure 27, it was important to also consider the compressive behavior of a texel under a normal load. This is particularly important for parallel plate capacitive pressure sensors in which the sensory response is influenced by a change in the capacitor geometry when a force is applied. Once again, the

tension/compression load frame (MTS 30/G) was used to compress the texel to approximately 20% strain for five cycles at a speed of 1 mm/min. The texel's capacitive response was simultaneously collected and will be discussed in Section 6.6.3. The load extension plot recorded during multiple compression cycles on an individual texel (produced with two perpendicularly oriented FR 60:25:15 fibers) is presented in Figure 32a. The plot shows that the texel's compressive behavior was repeatable throughout the cyclic testing. However, the plot does show the texel's lossy behavior including hysteresis, meaning the fractional energy that is lost or dissipated during the loading-unloading cycle, indicated by the difference in behavior during loading and unloading cycles. This hysteresis is expected because the texels are fabricated from polymeric materials which possess viscoelastic properties thus resulting in non-recoverable deformation.

### **6.6.3 Fiber Sensory Behavior**

The BiSoFT fibers are designed and intended for assembly into woven structures to perform as sensors. Accordingly, the electrical conductivity of the TME fibers (after PLA removal) was measured, using a set up shown in Figure 37. Direct and reliable measurement of electrical resistance of the fibers using a four or two probe set up was difficult because of the small dimension of conducting segment as well as the shape of the insulating lobes which restricts access to the conducting segment. Therefore, a predetermined length of fiber (5 cm) was attached to copper pads using conductive silver epoxy (MG Chemicals 8331) to create appropriate contacts and the electrical resistance was measured by using a multimeter (Keysight U1272A). As shown in Figure 32b, the electrical resistance per unit length of the FR 60:25:15 fibers was the lowest while the resistance of the FR 50:40:10 fibers increased with higher DR. This is obviously due to the dimensional difference of the CoPA6 cross-sectional area between fibers. The electrical

conductivity of fibers is deemed important in sensor applications because of the potential for lower signal-to-noise ratio for higher conductivity. Therefore, subsequent sensory behavior was studied with the FR 60:25:15 fibers which provided the lowest electrical resistance.

To demonstrate the pressure sensing capabilities of the BiSoFT, two FR 60:25:15 fibers were arranged into a texel and mechanically compressed (explained earlier in Section 6.6.3) while simultaneously measuring capacitance. The capacitance was measured using a LCR meter (Keysights, E4980AL) and the data was collected using commercially available software (BenchVue LCR Meter Control, Keysight). As shown in Figure 37, fibers were connected to copper pads via conductive silver epoxy (MG Chemicals 8331). Wires were soldered to the copper pads which were inserted to the screw terminals placed on a printed circuit board (PCB). A BNC port on the PCB provided a means of connection to the LCR.

The capacitive response of the texel during five compression cycles (of ~20% strain) is shown in Figure 32c while a more comprehensive view of a single cycle response is provided in Figure 32d. The capacitive response was smoothed using an adjacent-averaging method. As the compression probe approached the texel the measured capacitance, or the mutual capacitance ( $C_m$ ) between the two overlapping electrodes (see Figure 32e), decreased. This initial reduction in capacitance of the texel prior to application of load can be explained by the disruption of the electric field formed between the fibers, see Figure 32f, by an approaching object.<sup>[352, 353]</sup> As a conductive object, such as a finger or probe, approaches the texel, the parasitic capacitance ( $C_p$ ) formed between the object and sensor electrode, shown in Figure 32g, increases which disturbs and shunts the electric field between the electrodes of the sensor, see Figure 32h, thus resulting in a reduction of  $C_m$ .<sup>[353]</sup> Subsequently, when the probe contacts the texel and load is applied, the  $C_m$  increased due to a decrease in  $h$ , as described previously in Section 6.3 and Equation 1. As the

load is removed from the texel and the distance between the electrodes increases,  $C_m$  decreases until the load is completely removed. Finally, once the load is completely removed,  $C_m$  increases as the probe moves away from the texel resulting in lower  $C_p$ . In the future, signal processing techniques could be used to differentiate between the parasitic capacitance and the pressure induced response of the texel.

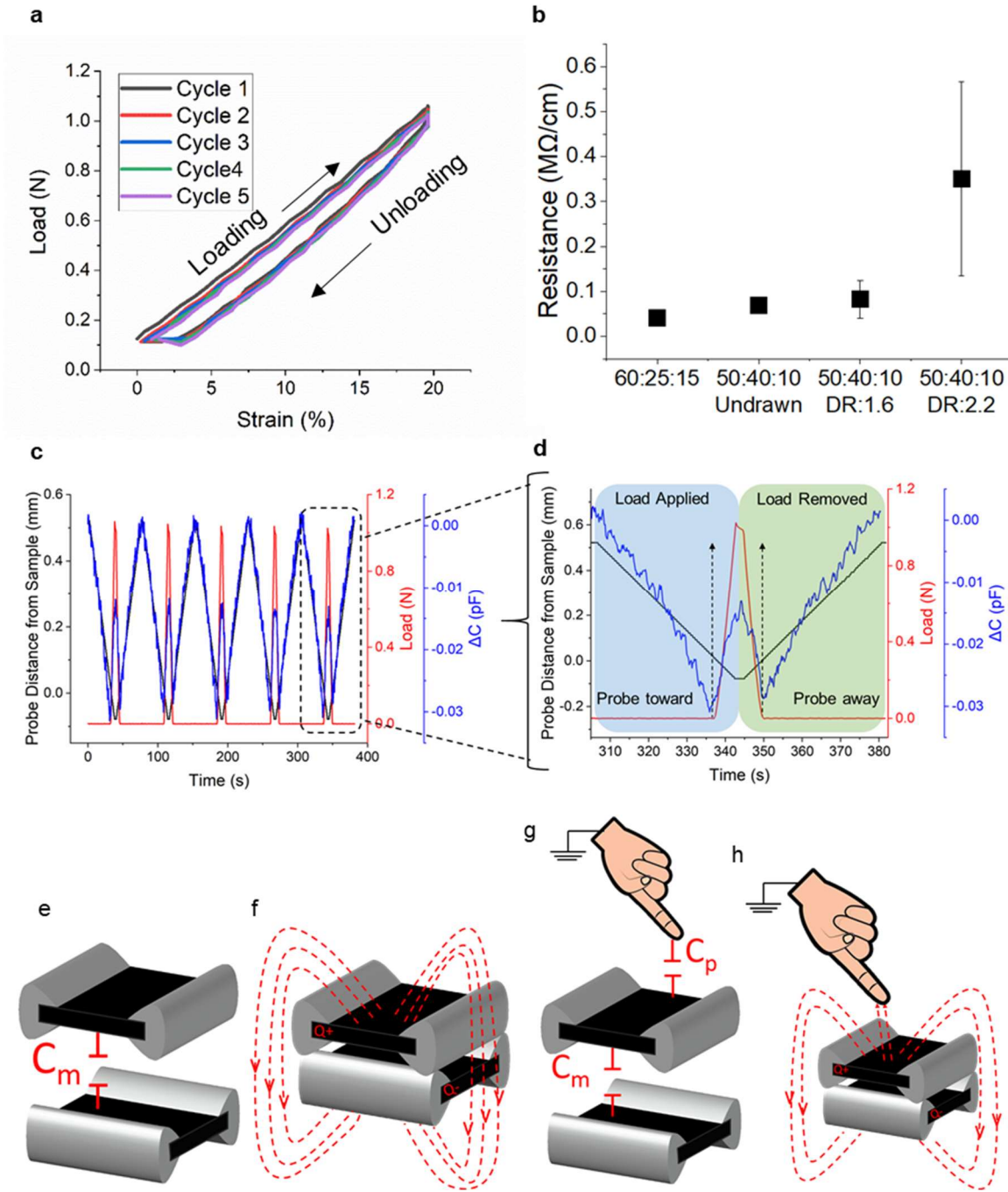


Figure 32: Electromechanical properties of BiSoFT (a) Mechanical behavior of a 60:25:15 texel when exposed to five compression cycles of ~20% strain (b) Electrical resistance fibers produced with different FRs and DRs (c) Capacitive response of texel to five compression cycles of ~20% strain (d) Comprehensive view of the texel's electrical and mechanical response to stain application (e)  $C_m$  between the fibers within a texel (f) Electric field generated by texel (g)  $C_p$  generated when object, such as finger, approaches the texel (h) Shunting of electric field when object approaches texel

## **6.7 Conclusion**

In this work, we proposed a scalable and commercially relevant method of producing uniquely shaped fiber sensors via TME. We described our approach to selecting compatible materials for TME fiber fabrication which included DSC, MFR, TGA and electrical analysis. We reviewed the TME process including challenges and key process parameters as well as methodology for selecting process parameters. Subsequently, we summarized our approach to successfully producing the TME fibers by first validating the spin pack and FRs, then systematically introducing the desired polymers, winding the fibers onto spools, and post-process drawing. Challenges faced during fabrication of the TME fibers and methods to overcome these obstacles were provided. Finally, the BiSoFT were characterized including optical microscopy and tensile testing. Optical microscopy indicated that desired FRs could be achieved using the pump speed equations employed in this research. Tensile testing indicated that some FRs are better suited to withstand the drawing process than others. Finally, the electromechanical properties of the fibers were determined including the resistance of the fibers/unit length and the pressure-sensing capabilities of a BiSoFT texel. Results of this research indicate that BiSoFT can be produced at speeds of  $>100$  m/min thus providing a scalable and commercially relevant method to producing fiber-based sensors for wearable technology.

## **6.8 Acknowledgement**

This work was supported by the NCSU Chancellor's Innovation Fund, NCSU Provost Fellowship, NSF ECCS under Grant 1509043, NSF SCH under Grant 1622451, NSF Graduate Research Fellowship under DGE-1252376, ASSIST ERC under EEC-1160483. The authors would like to acknowledge Eric Lawrence and Steve Sharp for their technical assistance with the tricomponent extrusion trials.

## 6.9 Supplementary Information

Table 5: Parameters of the tricomponent line's extruders

	<b>Extruder A</b>	<b>Extruder B</b>	<b>Extruder C</b>
Screw Diameter [mm (inch)] (constant)	18 (3/4)	18 (3/4)	25 (1)
Metering Pump Capacity (cm <sup>3</sup> /rev) (constant)	0.6	0.6	1.792

Table 6: Pump speeds used in the TME experiments

Phase 1 (Extruder A, B, and C: PP)					
Extruder A		Extruder B		Extruder C	
FR (%)	Pump Speed (RPM)	FR (%)	Pump Speed (RPM)	FR (%)	Pump Speed (RPM)
10	2.7	20	5.3	70	6.3
10	2.7	30	8.0	60	5.4
15	4.0	25	6.7	60	5.4
Winding speed:	N/A				
Phase 2 (Extruder A: PP, Extruder B: PP, Extruder C: PLA)					
Extruder A		Extruder B		Extruder C	
FR (%)	Pump Speed (RPM)	FR (%)	Pump Speed (RPM)	FR (%)	Pump Speed (RPM)
10	3.6	20	7.1	70	6.0
10	3.6	30	10.7	60	5.2
15	8.0	25	13.4	60	7.8
Winding speed:	N/A				
Phase 2 (Extruder A: InPA6, Extruder B: InPA6, Extruder C: PLA)					
Extruder A		Extruder B		Extruder C	
FR (%)	Pump Speed (RPM)	FR (%)	Pump Speed (RPM)	FR (%)	Pump Speed (RPM)
10	4.2	20	8.3	70	9.0
10	2.8	30	8.3	60	5.2
15	3.1	25	5.2	60	3.9
Winding speed:	N/A				
Phase 3 and 4 (Extruder A: CoPA6, Extruder B: InPA6, Extruder C: PLA)					
Extruder A		Extruder B		Extruder C	
FR (%)	Pump Speed (RPM)	FR (%)	Pump Speed (RPM)	FR (%)	Pump Speed (RPM)
10	4.2	20	8.3	70	9.0
10	4.2	30	12.5	60	7.8
15	6.3	25	10.4	60	7.8
10	3.0	40	12.1	50	4.7
Winding speed:	~105-120 m/min				

Table 7: Temperature profiles used in the TME experiments (please note that Extruder C has a fourth heating zone not present in Extruder A and B)

Extrusion Line Component	Zone 1 (°C)	Zone 2 (°C)	Zone 3 (°C)	Zone 4 (°C)	Pump Block (°C)	Transfer Line (°C)	Spin Head (°C)
Materials							
Phase 1 (Extruder A, B, and C: PP)							
PP	190	210	235	235	235	235	235
Phase 2 (Extruder A: PP, Extruder B: PP, Extruder C: PLA)							
PP	205	250	265	N/A	265	265	265
PLA	205	225	235	240	240	240	265
Phase 2 (Extruder A: InPA6, Extruder B: InPA6, Extruder C: PLA)							
InPA6	225	250	265	N/A	265	265	265
PLA	205	225	235	240	240	240	265
Phase 3 and 4 (Extruder A: CoPA6, Extruder B: InPA6, Extruder C: PLA)							
CoPA6	210	250	250	N/A	255	255	255
InPA6	220	250	255	N/A	255	255	255
PLA	205	225	235	240	240	240	255

Table 8: Process settings for drawing 50:40:10 fibers

DR	Master Speed (m/min)	Speed Roll 1 (m/min)	Speed Roll 2 (m/min)	Winding Speed (m/min)	Temp Roll 1 (°C)	Temp Roll 2 (°C)
1.6	20	20.4	12.750	20.869	75	65
2.2	20	20.4	9.273	20.869	75	65

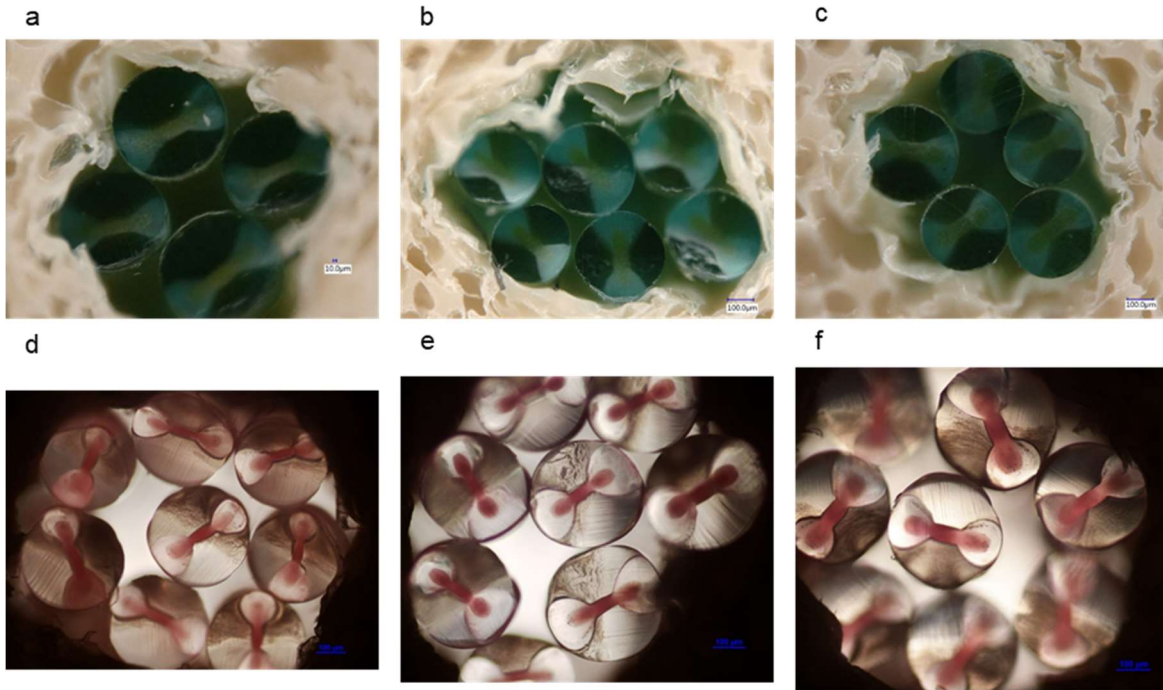


Figure 33: Tricomponent melt extruded fiber cross-sectional images. Extruder A: PP+orange PP, Extruder B: PP+blue PP, Extruder C: plain PP at FRs (a) 70:20:10 (b) 60:30:10 and (c) 60:25:15. Extruder A:In PA6 +red PA6, Extruder B: neat InPA6, Extruder C: PLA at FRs (d) 70:20:10 (e) 60:30:10 and (f) 60:25:15

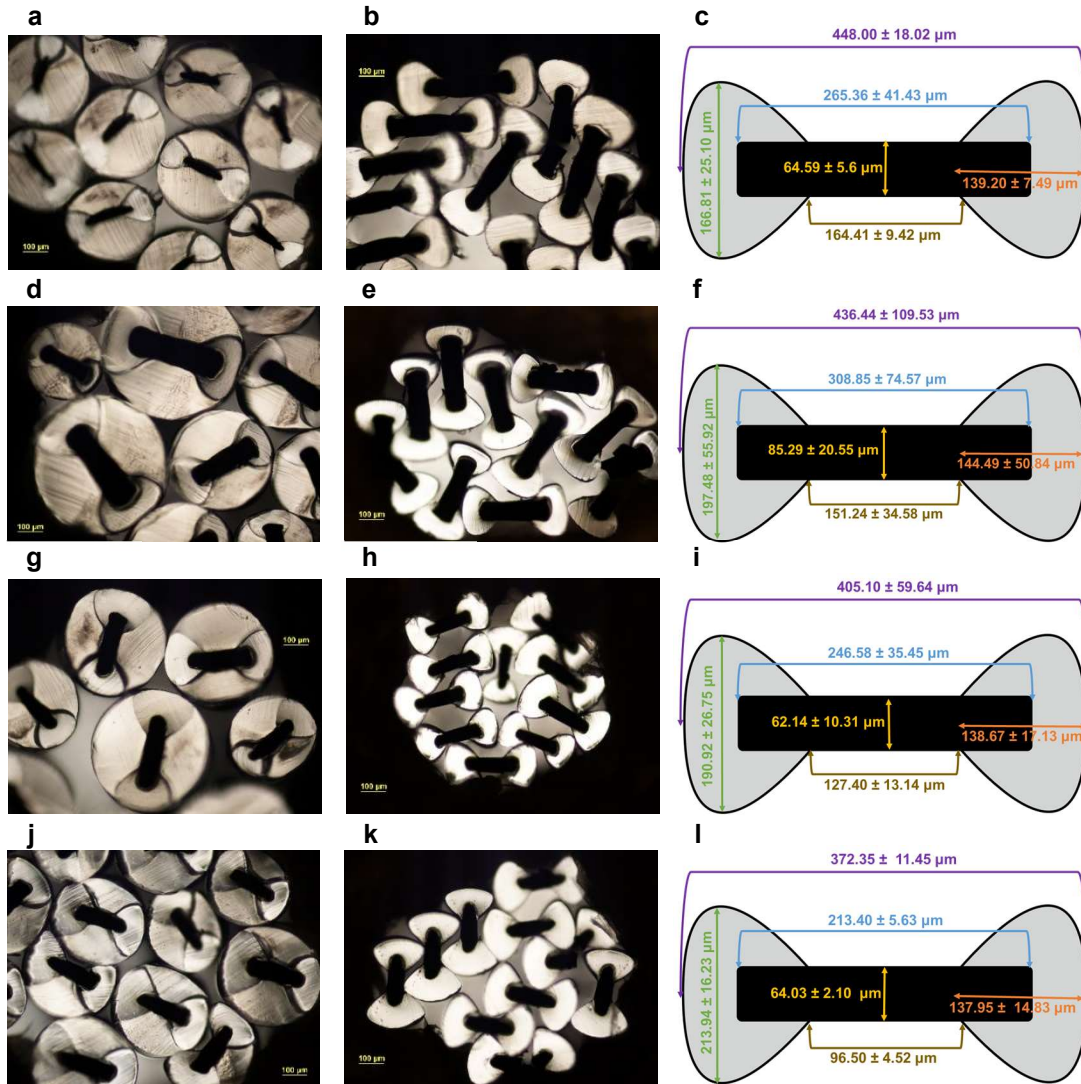


Figure 34: Tricomponent melt extruded fiber cross-sectional images and dimensional analysis. Extruder A: CoPA6, Extruder B: InPA6, Extruder C: PLA. (a) FR 70:20:10 (b) FR 70:20:10 (with PLA removed) (c) FR 70:20:10 dimensional analysis (d) FR 60:30:10 (e) FR 60:30:10 (with PLA removed) (f) FR 60:30:10 dimensional analysis (g) 60:25:15 (h) FR 60:25:15 (with PLA removed) (i) FR 60:25:15 dimensional analysis (j) FR 50:40:10 (k) FR 50:40:10 with PLA removed (l) FR 50:40:10 dimensional analysis

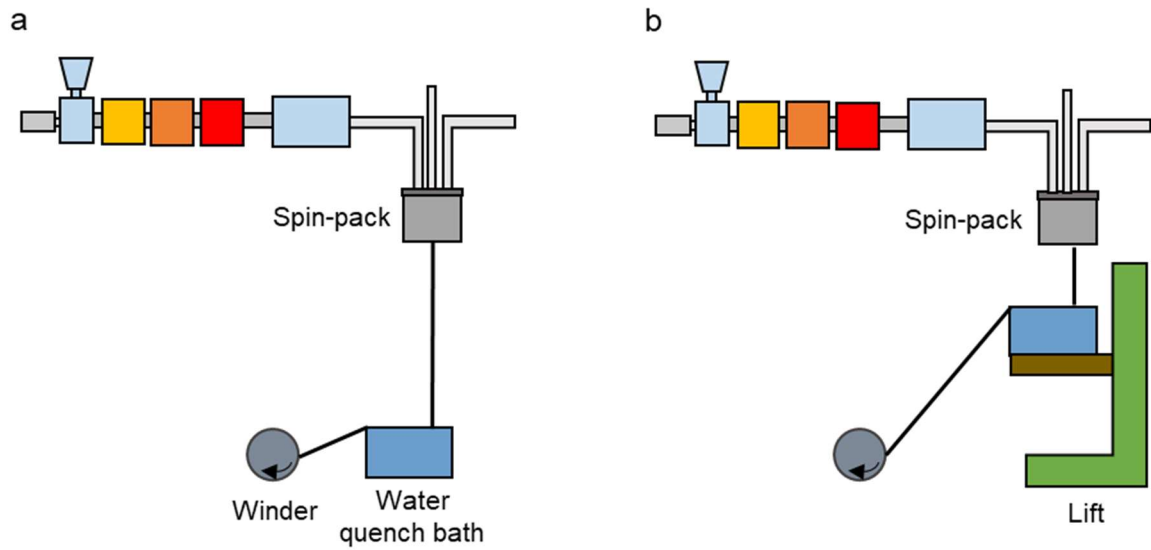


Figure 35: Schematics of winding/quenching set-ups (a) The normal extrusion set up with quench bath on floor, ~3m from spin-pack exit (b) Elevated bath set up to reduce spin-pack exit to bath distance to ~1m

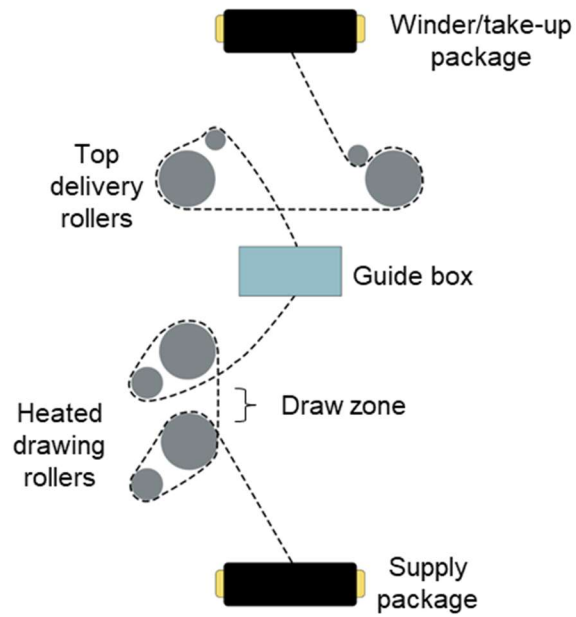


Figure 36: Schematic of drawing set-up

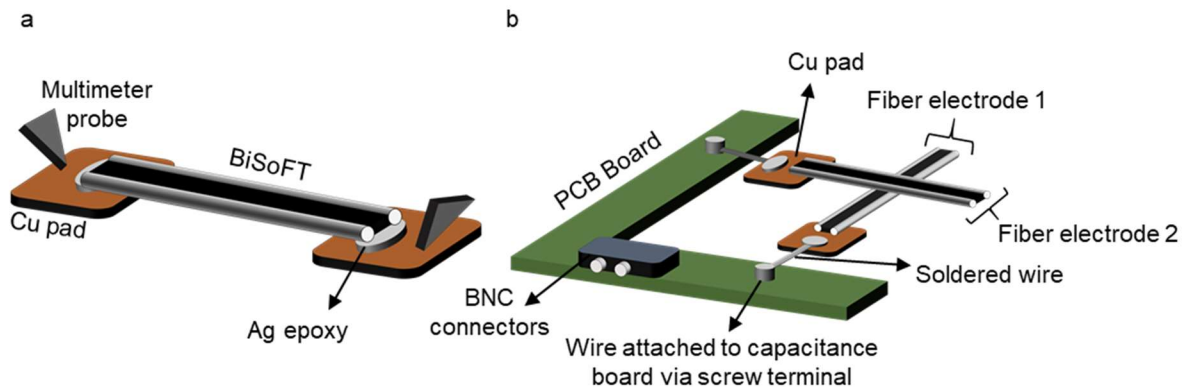


Figure 37: Schematics of BiSoFT fiber electrical testing (a) Fiber resistance measurement set-up using multimeter (b) Pressure sensing set-up. PCB is connected to LCR via BNC cables

## 7 Melt-Extruded Fibers Sensors for Electronic Textiles

The previous article provided an in depth overview of the BiSoFT fabrication method including material selection, characterization, and selection of process settings. In this section, the primary focus is further characterizing the sensory behavior of the BiSoFTs. This work is intended to be published in *Advanced Material Technologies*.

### 7.1 Abstract

Textile-based flexible sensors are key to the development of personal wearable electronic devices and systems for a wide range of applications including physiological monitoring, communication, comfort, etc. Textiles, for their many desirable characteristics and use, offer a natural interface between electronics and the human body. A wide range of fabrication techniques have been explored for textile-based sensors; however, most are not compatible or readily adaptable to the textile manufacturing processes. Here, a practical and scalable method of producing textile-based sensory fibers using a common manufacturing technique, melt extrusion, is proposed. An overview of the fabrication method as well as the mechanical and electrical properties of the fibers are presented. Subsequently, the fibers' ability to sense changes in pressure is studied in detail using fiber assemblies. Methods to improve the sensor performance by altering the geometry of

the fiber assembly are also presented. As a proof-of-concept demonstration, the fibers are woven into a pressure-sensing mat consisting of sixty-four sensing elements. The woven substrate can detect the location and level of pressure thus illustrating the fibers' potential for use as sensors in textile structures.

## 7.2 Introduction

Fiber-based sensors are considered essential for the emerging field of electronic textiles (e-textiles) or textiles with integrated electronic capabilities. In recent years, e-textiles have generated considerable research and commercial interest due their potential applications in healthcare, security, entertainment, and others.<sup>[176]</sup> Textile-based sensors have been proposed for monitoring various parameters including pressure,<sup>[48, 50, 53, 58, 68, 205]</sup> strain,<sup>[152, 232, 267-270]</sup> humidity,<sup>[92, 271, 272]</sup> and temperature.<sup>[70, 82, 233]</sup> These sensors may be incorporated into textile structures at one or more of the hierarchical levels: fiber, yarn, or fabric. Fiber-based sensors are advantageous because of their ease of integration, lightweight, high aspect ratio, and flexibility thus allowing them to easily conform to the human body as wearable devices.<sup>[59, 226]</sup> Most fiber-based sensors proposed in the literature have been fabricated through batch processes like layer by layer deposition,<sup>[57]</sup> using specially designed bench-top equipment<sup>[68, 232]</sup> or by utilizing microfabrication techniques requiring cleanroom environments.<sup>[84]</sup> Many of these either utilize processes that are not be scalable for commercial production or use materials that are not compatible with common textile structures and present barriers to integration into traditional textile manufacturing processes; thereby, limiting widespread adoption. While few have proposed fiber spinning processes to create textile-based sensors,<sup>[70, 93, 326-329]</sup> most of these efforts are limited to processes of questionable commercial value.

Conventional textile fibers are manufactured through wet, dry or melt spinning processes.<sup>[311]</sup> Melt spinning or extrusion is the most convenient and economic fiber formation technique because it is a relatively simple process that provides high spinning speeds and requires no auxiliary agents (like solvent, precipitation agents, etc.).<sup>[312]</sup> During melt spinning, solid, fiber-forming polymers are heated to melt and extrude through an extrusion spin-pack. In a typical melt-extrusion process a single polymer, such as polyester or polyamide, is used to produce fibers. However, multi-component fibers containing two or more physically and/or chemically distinct polymer components, can also be processed via melt extrusion.<sup>[313]</sup> The bicomponent melt extrusion (BME) process, in which two polymers are extruded simultaneously to form a single fiber, is relatively common in both research<sup>[314-317]</sup> and commercial settings for applications such as thermal bonding and self-crimping fibers.<sup>[318]</sup> BME has been proposed for the fabrication of fiber-based sensors but to our knowledge, these efforts have been restricted to core-sheath type fiber configurations.<sup>[314, 319-323]</sup> Bicomponent core-sheath fibers with material combinations of carbon black (CB)/high density polyethylene (core) and polyvinylidene difluoride (PVDF) (sheath) for piezoelectric force sensors,<sup>[314, 323]</sup> a cyclo-olefin (core) and a tetrafluoroethylene-hexafluoropropylene-vinylidene fluoride terpolymer (sheath)<sup>[322]</sup> for optical sensing of heart rate,<sup>[321]</sup> and polypropylene/carbon nanotube (core) and PVDF (sheath) for piezoelectric fiber-based sensing<sup>[319, 320]</sup> have been proposed. However, the tricomponent melt extrusion (TME) process, in which three polymers are extruded simultaneously to form a single fiber, is rather uncommon.<sup>[324, 325]</sup> TME has been used to fabricate fibers with unique optical properties,<sup>[324]</sup> and for energy harvesting applications,<sup>[325]</sup> but has not yet been investigated for fabricating fiber-based sensors.

Here, we propose a TME process for manufacturing a Bicomponent Sensory Fiber for Textiles (BiSoFT) with unique cross-sectional shape. When the BiSoFTs are woven into a fabric, parallel-plate capacitive sensors are formed at each cross-over point (henceforth called *texel*). First, we describe the sensor architecture and its modes of operation. Then, we present the capacitive response of the BiSoFTs under compression and explain the sensing phenomena in detail. We demonstrate the ability to combine multiple BiSoFTs to form a single texel to achieve greater sensitivity. The BiSoFT texel behavior is analyzed under cyclic and other loading conditions. Finally, the BiSoFTs are woven into a textile structure to create a pressure-sensing mat with sixty-four sensing locations for object detection. The results indicate that this approach has the potential to produce large area fiber-based sensors at commercially viable scales.

### **7.3 Fiber Shape and Sensor Architecture**

The BiSoFT cross-section consists of two insulating side-lobes bridged by a conducting segment in the middle, see **Figure 38a**. The conducting polymer segment in the middle extends slightly into the insulating side lobes to provide a strong interface between the insulating and conducting polymers. During the fiber formation process a sacrificial, third polymer component is required to envelope the two other components for stable extrusion of the desired fiber shape as shown in **Figure 38b**. The sacrificial polymer can be removed post-production thus providing the unique BiSoFT cross-sectional shape.

When the sensory fibers are woven into a fabric, each cross-over point in the fabric forms a sensor, we call a texel, see **Figure 38c**. In the texels, the conductive segments act as the parallel plate electrodes and the separation (or the cavity) created by the insulating lobes provides the space for the air to act as the dielectric, see **Figure 38d**. The sensory output or the change in capacitance

( $\Delta C$ ) of each texel upon the compression can be expressed in terms of its dimensional parameters as,

$$\Delta C = \varepsilon_0 \varepsilon_r w^2 \left( \frac{1}{h} - \frac{1}{h_0} \right) \quad \text{Equation 2}$$

Where,  $\varepsilon_0$ , and  $\varepsilon_r$ , are relative the permittivity of the free space and the dielectric, respectively,  $w$  is the width of the conductive segment,  $h$  and  $h_0$  are the thickness of the insulating segment of the BiSoFT, before and after deformation. Here, we assume that the change in the fiber dimension due to compression is limited to the parameter,  $h$ . Cross-sectional optical microscopy images of the produced fibers before and after PLA removal are shown in Figure 38e and Figure 38f, respectively.

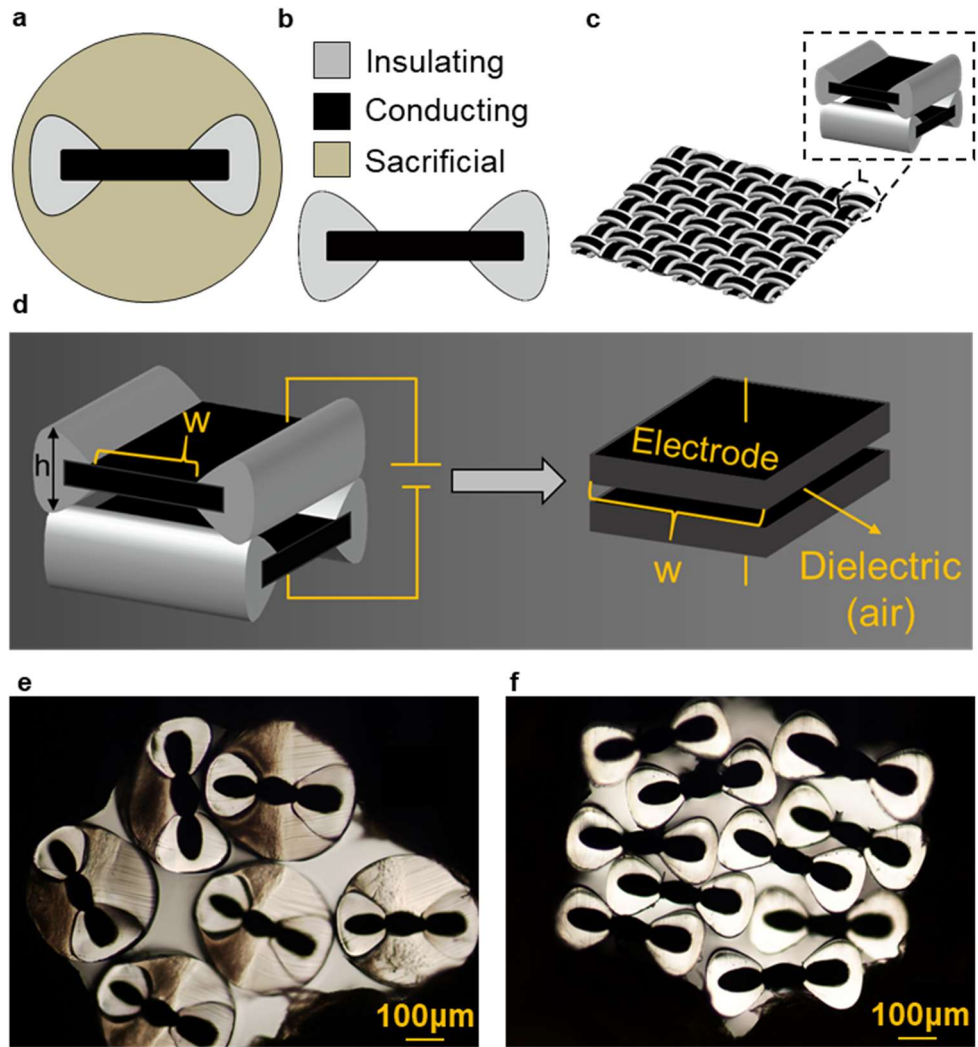


Figure 38: TME fibers shape and sensor structure (a) TME fiber with sacrificial polymer (b) BiSoFT after removal of the sacrificial polymer and (c) BiSoFT woven into a fabric configuration with each individual texel formulating a capacitive sensor (d) sensing pixel formed at texel compared to a parallel plate capacitor (e) TME fiber cross sectional images with sacrificial polymer and (f) after removal of sacrificial polymer

#### 7.4 Mechanical Characterization

Normal capacitive pressure or touch sensing behavior of the melt-extruded fiber sensor-array in the form of woven fabrics is largely dictated by the cross-plane (transverse) compressive behavior of the texel under a normal pressure. This is particularly important for parallel plate capacitive pressure sensors in which the sensory response is influenced by a change in the capacitor geometry when a force is applied. For the purpose of characterization of the texel behavior, the fiber cross-

over points were manually assembled on a rigid sheet of acrylic, as shown in **Figure 39a**. To study the effect of texel size on sensory properties, additional texels were fabricated with a varying number of fibers in each direction. For example, (1x1) texels were produced from two BiSoFTs - one in each direction, perpendicular to each other. Similarly, (3x3) samples were produced from a total of six BiSoFTs - three parallel fibers in each direction, as shown schematically in Figure 39b. These configurations represent potential woven structures of the sensory fabric.

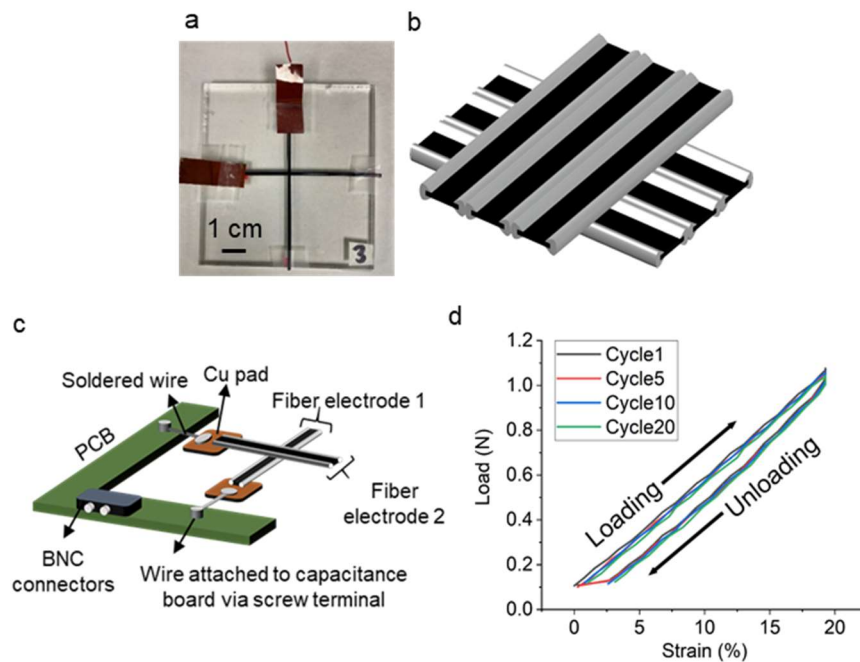


Figure 39: BiSoFT texels and their mechanical properties (a) (3x3) texel (b) schematic of (3x3) texel (c) schematic of texel connection to capacitance printed circuit board (PCB) (d) mechanical compressive behavior of a (1x1) texel when compressed to 20% strain

Multiple compression cycles were applied to the texel and the capacitive response of the texel was simultaneously collected by connecting the fibers to a measurement set-up shown in Figure 39c and discussed in more detail in the Experimental Section. The load versus compressive strain plots recorded during multiple compression cycles on an individual (1x1) texel is shown in Figure 39d. It is important to note that larger texel sizes, (3x3) and (5x5), exhibited similar compressive behavior. The cyclic load-extension behavior in compression indicates a moderate

level of lossy behavior in the form of hysteresis. Hysteresis results in non-recoverable deformation which is primarily due to the polymer behavior and can be minimized by the appropriate choice of the insulating polymer forming the side lobes.

## 7.5 Characterization of Sensory Behavior

The BiSoFT fibers are designed for assembly into woven structures to perform as electrodes in capacitive sensory elements described as texels. Before, embarking on the sensory characterization of the texels, the electrical conductivity of the BiSoFT fibers was measured. The measured resistance of the BiSoFTs was  $40.64 \pm 1.82 \text{ k}\Omega/\text{cm}$ . The corresponding calculated resistivity was  $13.97 \pm 3.61 \text{ M}\Omega\cdot\text{m}$ . There is, obviously, room for improvement of the BiSoFT conductivity by using a different material for the conductive segment.

To demonstrate the pressure sensing capabilities of the BiSoFTs, the fibers were arranged into texels and mechanically compressed (as discussed in Section 7.4) while simultaneously measuring capacitance. The capacitive response of a (1x1) texel during five compression cycles (of ~20% strain amplitude) is shown in **Figure 40a** while a more comprehensive view of a single cycle response is provided in Figure 40b. Similarly, the capacitive response of a (3x3) texel during five compression cycles (of ~20% strain) is shown in Figure 40c while a more comprehensive view of a single cycle response is provided in Figure 40d. Regardless of the texel size, as the compression probe approached the texel the measured capacitance, or the mutual capacitance ( $C_m$ ), between the two overlapping electrodes (see Figure 40e) decreased. This initial reduction in capacitance of the texel prior to application of load is well-known and due to the disruption of the electric field formed between the fibers, see Figure 40f, by an approaching conducting or dielectric object.<sup>[352, 353]</sup> As a conductive object, such as a finger or probe, approaches the texel, the parasitic or fringe capacitance ( $C_p$ ) formed between the object and sensor electrode, shown in Figure 40g,

increases which disturbs and shunts the electric field between the electrodes of the sensor, see Figure 40h, thus resulting in a reduction of  $C_m$ .<sup>[353]</sup> Subsequently, when the probe contacts the texel and load is applied, the  $C_m$  increases due to a decrease in electrode separation,  $h$ . As the load is removed from the texel the same response is observed, albeit in the reverse order. In the future, signal processing techniques could be used to differentiate between the parasitic capacitance and the pressure induced response of the texel.

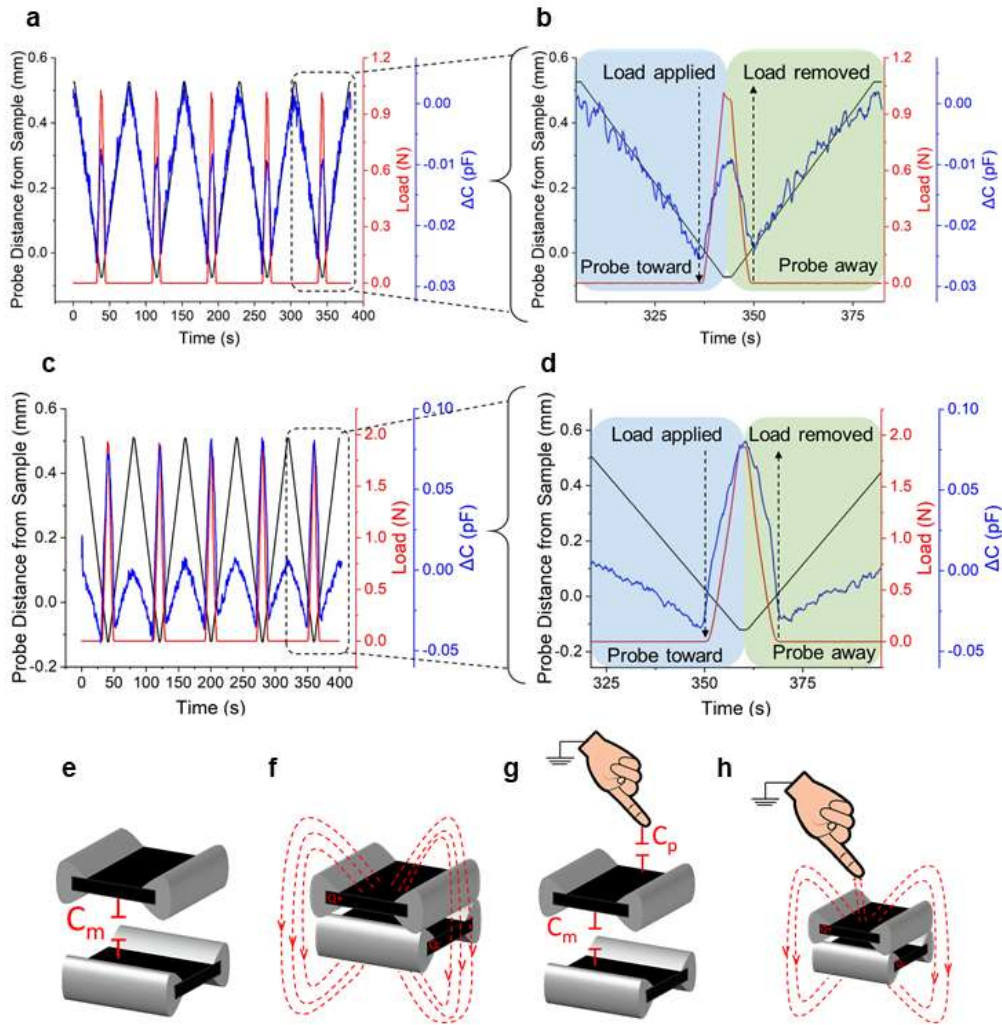


Figure 40: Initial electromechanical results (a) electrical and mechanical behavior of a (1x1) fiber texel when compressed to 20% strain (b) a detailed view of the fifth cycle of electrical and mechanical behavior of a (1x1) fiber texel when compressed to 20% strain (c) electrical and mechanical behavior of a (3x3) fiber texel when compressed to 20% strain (d) a detailed view of the fifth cycle of electrical and mechanical behavior of a (3x3) fiber texel when compressed to 20% strain (e)  $C_m$  between fibers of texel (f) electric field generated by texel (g) image of  $C_p$  generated when object, such as finger, approaches the texel (h) shunting of electric field when object approaches texel

The parasitic capacitance of the texels is similar regardless of the texel size however, interestingly the (3x3) texel elicits a larger response ( $\Delta C$ ) than the (1x1) texel when compressed to the same strain level. To further elucidate the change in response with texel size, three different texel sizes, (1x1), (3x3), and (5x5) were compared. The capacitive responses of the texels when compressed to five cycles of 20% strain amplitude are shown in **Figure 41a** while a more detailed

views of a single cycle in all three cases are shown in Figure 41b. As discussed earlier, the texels responded to both proximity and applied load. The measured  $\Delta C$  values after initial contact (i.e. excluding the proximity response) are shown in Figure 41c and indicate that the (1x1), (3x3) and (5x5) texels responded with a  $\Delta C$  amplitude of approximately 0.012, 0.075, and 0.225 pF, respectively, when compressed to 20% strain. The expected  $\Delta C$  values were calculated using Equation 2 and the relevant BiSoFT dimensions (see Figure 41d) determined via optical microscopy images (see Figure 38f). The calculated  $\Delta C$  values at 20% strain for the (1x1), (3x3), and (5x5) texels, shown in Figure 41c, are qualitatively close to the measured values mentioned earlier. As expected, the larger texel size provides better sensitivity, or a greater change in capacitance with applied strain. The sensitivity values calculated as  $\Delta C / \Delta \epsilon$ , where  $\Delta \epsilon$  is the change in strain, were approximately 0.060, 0.375, and 1.125 pF for the (1x1), (3x3), and (5x5) texels respectively. The increase in  $\Delta C$  and sensitivity with increasing texel size can be simply explained by the quadratic increase in the electrode area.

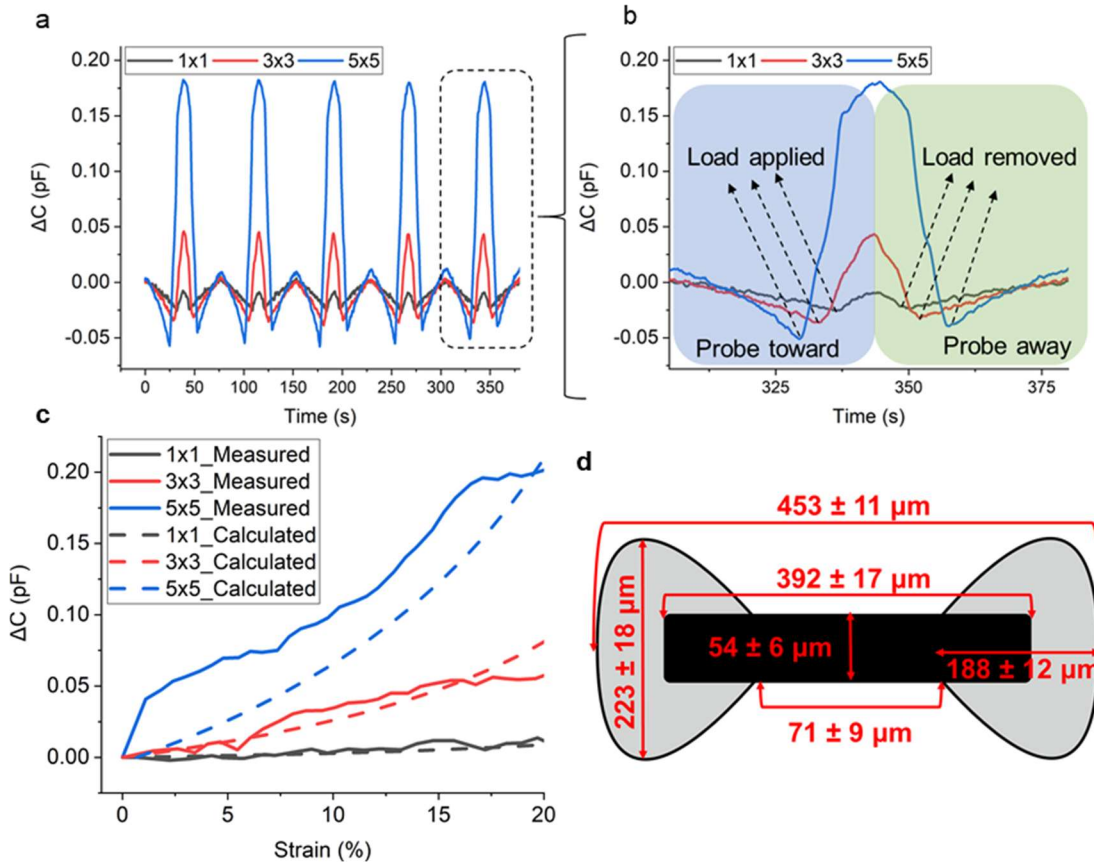


Figure 41: (a) comparison of capacitive response of (1x1), (3x3), and (5x5) texels when compressed to 20% strain (b) a detailed view of the fifth cycle of the capacitive response of (1x1), (3x3), and (5x5) texels when compressed to 20% strain (c) expected versus measured response of (1x1), (3x3), and (5x5) texels (d) BiSoFT fiber dimensions determined via optical microscopy

In most applications, the repeatability of the sensor output is critical. In order to determine the repeatability of the sensor response, a (3x3) texel was evaluated for 100 cycles at 20% strain amplitude. The electrical and mechanical responses of the texel are shown in **Figure 42a-c**. Figure 42a shows the response during all 100 cycles of measurement while Figure 42b and Figure 42c provide the results of the first and last five cycles respectively. The texel continued to function throughout the experiment, albeit there is a small but noticeable decrease in both load and capacitive response ( $\Delta C$ ) over time. The  $\Delta C$  decreased from approximately 0.078 pF during the first ten cycles to about 0.072 during the last ten cycles. Similarly, the load corresponding to the constant applied strain amplitude of 20% decreased with time from 1.4 N during the first ten cycles

to about 1.2 N during the last ten cycles. These changes in the mechanical response and consequently the electrical response of the sensor is obviously due to materials' viscoelastic response during the loading-unloading cycles. During repetitive compression cycles, the BiSoFT did not completely recover from the applied strain resulting in lower electrical response as well as mechanical resistance. The BiSoFT behavior could be improved by using more elastic materials having inherently better recovery behavior that are melt-extrudable, such as thermoplastic polyurethanes.

Another important characteristic of the sensor array is their ability to respond under constant load (or deformation) applied over a length of time. To characterize this behavior, the texel was evaluated for five cycles of repetitive loading for one minute at 20% strain followed by unloading for one minute, as shown in Figure 42d. The BiSoFT texel response to a single cycle of strain is shown more clearly in Figure 42e. When pressure was applied, the capacitance increased, and the electrical response remained stable throughout the one minute of loading. The noticeable decay in the load within the one minute is due to the stress relaxation of the material. Upon removal of the load, the capacitive response decreased and returned to approximately the initial baseline value (the  $\Delta C$  value observed after the first holding cycle). Once again, a proximity response due to the parasitic capacitance, discussed earlier, is noted. Again, a decay in the electrical and mechanical properties was observed over the five cycles due to the hysteretic loss of the viscoelastic polymers used in the fabrication of BiSoFT. As previously mentioned, this behavior could be improved using more elastic materials which offer improved recovery properties.

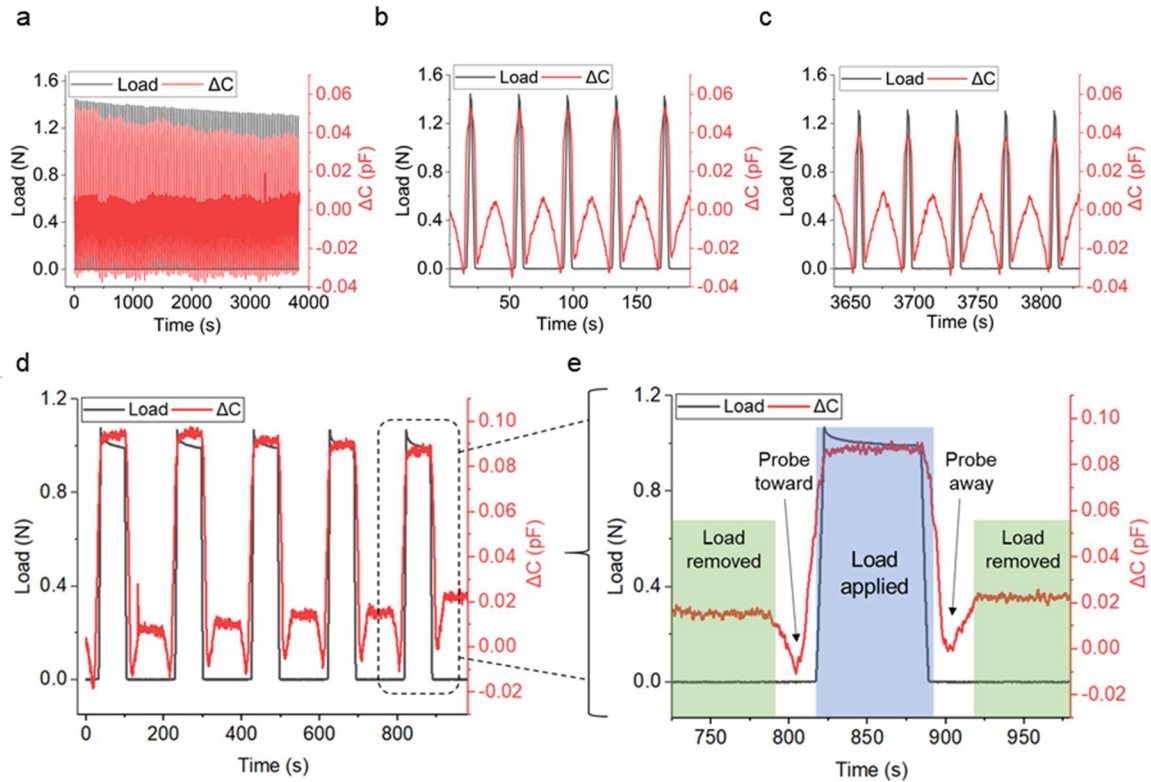


Figure 42: Further electromechanical characterization of (3x3) BiSoFT texel (a) capacitive and mechanical response during 100 cycles of 20% strain cycling (b) first and (c) last five cycles of capacitive and mechanical response during 100 cycles of 20% strain cycling (d) five cycles of holding 20% strain for one minute, and then releasing the strain for one minute (e) a detailed view of a single cycle of holding 20% strain for one minute, and then releasing the strain for one minute

## 7.6 Proof of Concept Demonstration – Pressure Sensing Fabric

The design and manufacture of the sensory fiber, BiSoFT, proposed here can be potentially used in a broad range of applications. Here, we demonstrate the ability the BiSoFT fibers to be integrated into a woven textile structure to create a pressure sensing mat. As shown in **Figure 43a**, the sensor array contains sixty-four, (3x3) texels with each texel being equidistant (approximately 1 cm) from each other. Such pressure mats may be useful in applications such as pressure sore (or bedsore) monitoring, gait analysis, or building occupation management.

To evaluate the sensor array for its potential, 10 and 50 g weights were placed on individual texels across the diagonal of the mat from the upper left to bottom right. Each pixel provided a

distinguishable capacitive response when the 10 and 50 g weights were applied, see Figure 43b. The variation in response ( $\Delta C$ ) between texels under the same loading condition weight is expected and may be attributed to variations in the fiber dimensions along its length and the fiber tension in the fabric. Heatmaps provided in Figure 43d-g, with the corresponding scale shown in Figure 43c, demonstrate the ability of texels R1C1 and R8C8 to detect the location and extent of normal pressure. The heatmaps also indicate that in some cases, when the load was applied to a specific texel, its surrounding texels also exhibited a small change in capacitance. This is also expected because of the boundary effect of the loaded texel; obviously the BiSoFT fibers forming a texel under load continues into other texels within the corresponding rows or columns. Therefore, continuity of the deformation or fiber movement manifests in a relatively small change in capacitance within relevant texels.

To further elucidate the fabric's potential application for object detection, square and triangle shapes were attached to the 50g weight to simultaneously apply pressure to multiple texels. The series of images and corresponding heatmaps shown underneath in Figure 43h and i, show that the sensor array successfully detected the location of the object. Once again, some surrounding texels also responded when weight was applied. These proof of concept demonstrations indicate the potential of the BiSoFT fibers for human-machine interface applications.

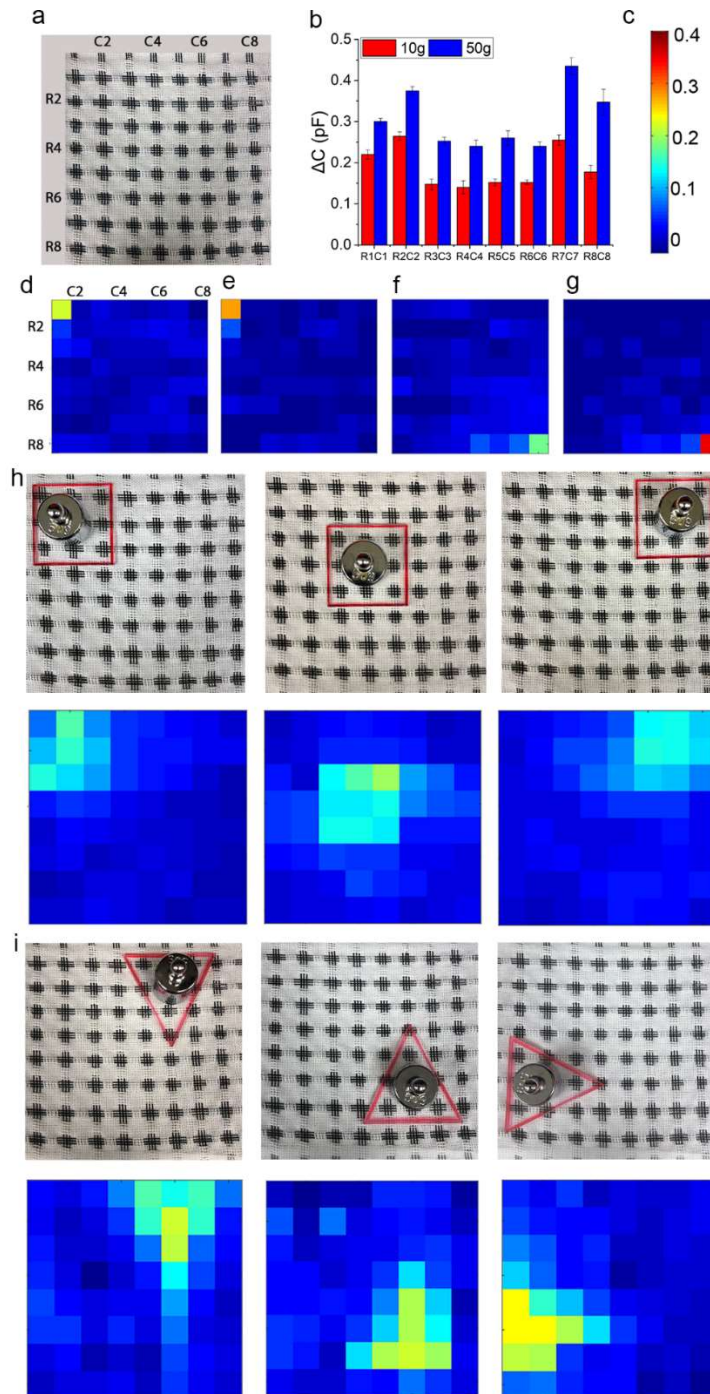


Figure 43: BiSoFT pressure mat demonstration (a) woven BiSoFT mat and nomenclature (b) variation in the texels' response with 10 and 50 g weight application (c)  $\Delta C$  scale for heat maps in pF. Capacitive response ( $\Delta C$ ) of R1C1 to (d) 10g and (e) 50g weight application. Capacitive response ( $\Delta C$ ) of R8C8 to (f) 10g and (g) 50g weight application. Capacitive response ( $\Delta C$ ) of texels when (h) square and (i) triangle shaped object applied to multiple texels.

## 7.7 Conclusion

We have developed a uniquely shaped, micron-scale sensory fiber, BiSoFT, that offers a novel fiber design for integration of sensors in textiles. The fibers have been produced using a commercial scale fiber extrusion system and assembled into textile structure to produce soft and conformable capacitive sensor arrays. The assembly of these fibers can be completed using commercially practiced processes such as weaving. The woven sensor arrays or texels are able to detect various levels of normal pressure including tactile. Using the BiSoFT fibers we have demonstrated the potential to form texels of various pressure sensitivity simply by changing the fabric design. The texel arrays can not only provide discernable sensory response to various levels of pressure but can also produce fringe capacitive response for the possible measurement of proximity before contact. The long term pressure sensing behavior of the texels is demonstrated via 100-cycles of compression. The texels continued respond during the prolonged loading-unloading cycles but a slight decay was observed in both the electrical and mechanical response. This could be improved using a polymer material possessing a lower degree of viscoelastic losses or better recovery properties. Finally, we present a sixty-four texel pressure sensing mat to demonstrate a potential application of the BiSoFT. The fibers were integrated into a woven structure and the resulting texel array could detect shaped objects at various locations and differentiate different loading levels. In summary, we have demonstrated that sensory fibers can be produced via melt-extrusion at high spinning speeds thus providing a means of manufacturing large-area fully-textile sensory arrays at commercial scale. The sensor fabrication approach presented here has the potential for application in a broad load-deformation range determined by the materials used for fabrication. The new generation of thermoplastic elastomers including various copolymers present tremendous opportunity for the proposed design of sensors in textiles.

## 7.8 Experimental Section

*Material Selection:* The three materials required to melt-extrude the BiSoFT are: a conducting polymer, an insulating polymer, and a sacrificial polymer. The most critical material in this fiber cross section is the conductive polymer. For this research, a commercially available (Hills Inc., Melbourne, FL) conductive polyamide 6 with CB fillers was used. The conductive polyamide 6 was chosen because it was readily available as a compounded composite and polyamide 6 is a commonly employed fiber-forming polymer in melt-extrusion. One of the requirements of the TME process is the thermal and flow compatibility of the polymers. Therefore, the other fiber components were selected by closely matching the relative viscosity of the conductive polyamide 6. Accordingly, a commercially available insulating polyamide 6 (BASF, B27E) and a fiber-grade polylactic acid (PLA, Natureworks, 6202D) were chosen as the insulating and sacrificial polymers, respectively. PLA was selected because it is commonly used in bicomponent fiber extrusion as a sacrificial component to create unique fiber shapes or micro-structures.<sup>[336, 337]</sup> The sacrificial component can be removed using a NaOH solution or a scouring process.<sup>[46, 47]</sup>

*Fiber Fabrication:* While the sensory fiber is a bicomponent fiber, a third sacrificial polymer is required for maintaining the fiber shape during melt extrusion. Therefore, the BiSoFT fiber is produced via a TME process. The TME set up used in the fabrication of the BiSoFT, located at NC State University, consisted of three separate melt extrusion lines that converge at the extrusion spin-pack. A custom extrusion spin-pack was designed and produced in collaboration with Hills Inc. (Melbourne, FL) following the extrusion spin-pack design described in the relevant patents.<sup>[330-332]</sup> The molten polymer was extruded through the spin pack, quenched in a water bath, and collected on a spool. The three polymers were extruded at specific polymer flow ratios,

indicating the ratio of polymer mass extruded by each extruder per unit time, to achieve the desired fiber shape.

*Mechanical Characterization:* The mechanical response of the texels were evaluated on a load frame (MTS 30/G) fitted with a tension/compression load cell. The texel was placed under an appropriately sized test probe mounted on the load frame. Texels were tested under approximately 20% strain amplitude for a selected number of cycles at a cross-head speed of 1 mm/min for all tests except the 100-cycle test which was completed at 2 mm/min. During the evaluation, the total distance traveled by the testing probe was kept constant (1.2 mm) to keep the cycle time consistent. Therefore, to achieve the desired strain level, the initial height of the probe was adjusted based on the thickness of the texel. It is important to note that the actual strain levels applied to the texels may vary from the desired levels due to small experimental errors when measuring texel thickness.

*Electrical Resistance:* Electrical resistance of the BiSoFTs was measured using a digital multimeter (Keysight U1272A). To ensure appropriate electrical contact with the multimeter leads, a predetermined length of fiber (5 cm) was attached to copper pads on either side using conductive silver epoxy (MG Chemicals 8331) to create appropriate contacts.

*Capacitance measurements:* A precision LCR meter (Keysights, E4980AL), set to apply a 1 kHz and 1V AC signal, was used to measure capacitance. To ensure electrical contact the fibers were connected to copper pads via conductive silver epoxy (MG Chemicals 8331) and the copper pads in turn were electrically connected to the screw terminals placed on a PCB, see Figure 39c. The PCB consisted of a total of 16 screw terminals (8 rows and 8 columns) as well as electrical switches (Analog Devices, ADG788) controlled by a microcontroller to select the desired texel within an array. The capacitance values from the texels were collected using an LCR meter connected to a computer.

*Pressure-sensing mat fabrication:* The experimental woven mat was produced using a commercially available woven fabric as a scaffold. Selected yarns were removed from the woven fabric and replaced with the BiSoFTs manually to produce the fabric.

## **7.9 Acknowledgement**

This work was supported by the NCSU Chancellor's Innovation Fund, NCSU Provost Fellowship, NSF ECCS under Grant 1509043, NSF SCH under Grant 1622451, NSF Graduate Research Fellowship under DGE-1252376, ASSIST ERC under EEC-1160483 and NIH under NIH NICHD F31HD101285. The authors would also like to acknowledge Eric Lawrence and Stephen Sharp for their assistance with the tricomponent melt extrusion process.

## **8 Summary and Future Work**

Amputees often experience discomfort when wearing their prosthetic devices and as the amputee population grows,<sup>[1]</sup> this becomes a more prevalent and pressing issue. Sensors are needed to monitor the ISE to improve the design of prosthetic components and reduce amputee discomfort. While rigid sensors do provide insight into the ISE, they do not possess required compliance for use at the residual limb/socket interface.<sup>[6]</sup> Textile-based sensors provide promising potential for sensing within the ISE because they are flexible and comfortable and also provide opportunities to create large, dense sensor arrays.

In this work, two scalable methods of creating textile-based sensors for ISE monitoring were proposed and explored. First, was the seam-line sensing approach in which conductive yarns were sewn into fabrics to create parallel-plate capacitive sensors. Various conductive yarns and fabrics were considered to serve as the electrodes and dielectric layer of the sensor structure. The relationship between the sensor's physical, mechanical, and electromechanical performance was evaluated. Additionally, the ability of the SLS to sense pressure, wetness, and humidity was

demonstrated. This work validated that the SLS approach provided a simple means of creating textile-based sensors and machine interfaces with tunable responses based on material selection.<sup>[20]</sup>

Based on these results, the best available textile-based electrode and dielectric materials were selected to create flexible sensors for monitoring pressure within the ISE. The sensor and electronics system were specifically designed for monitoring pressures within the ISE. Additionally, two custom set-ups, an artificial limb and bent-knee adapter, were designed to replicate the ISE and validate the SLS system prior to amputee subject testing. Preliminary testing indicated that the SLS reliably monitored pressure changes within the replicated ISE, and therefore, the system was tested on a bilateral amputee subject. The SLS was capable of monitoring pressure changes within a real ISE environment and thus demonstrated that the SLS approach is a promising means of seamlessly monitoring the ISE.<sup>[21]</sup>

As previously mentioned, one of the benefits of the SLS approach is that it provides a means of creating large arrays within existing textile structures. In the future, the SLS approach could be used to sew sensing lines directly into the garments worn by amputees, such as liner-liners. This is demonstrated in Figure 44a in which seam-lines have been sewn into a compression sleeve to create a 100-texel array. The pressure sensing response of the corner texels is demonstrated in Figure 44b-e. While this garment is intended for able-bodied individuals, the same approach could be used to create sensors within liner-liners. In future work, such garments could be produced for several amputees to complete a more extensive human study or for daily monitoring of the ISE.

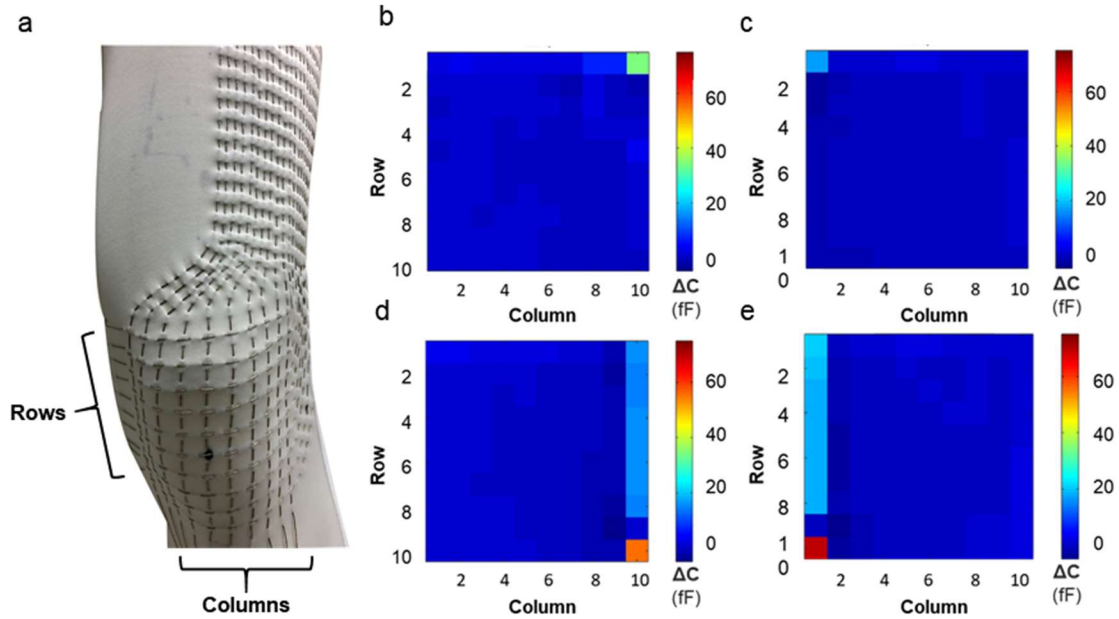


Figure 44: Initial results of SLSs integrated into compression sleeve (a) a 10x10 SLS array integrated into a compression sleeve. The response of the (b) upper right texel (c) upper left texel (d) the lower right texel (e) the lower left texel

The second sensing approach explored in this research was the uniquely-shaped fibers produced via TME. When the uniquely shaped fibers were woven into a fabric configuration, parallel-plate capacitors were formed at each fiber crossover point. In the first research article related to this work, the TME process and the approaches used to select process settings based on polymer properties, machine restrictions and the desired fiber shape were described. Additionally, the mechanical, electrical, and initial pressure sensing capabilities of the fibers were evaluated. The BiSoFT fibers were successfully produced indicating that the approaches to material selection and process development were appropriate. Further, the BiSoFT fibers successfully sensed changes in pressure thus indicating that this fabrication approach provides a means of creating micron-scale fiber sensors at high production speeds.

Subsequently, in the final research article, the sensing capabilities of the BiSoFTs were further explored. The fibers' pressure sensing capabilities were demonstrated, and the sensing

phenomenon was described. The BiSoFTs were arranged into texels of various sizes, (1x1), (3x3), and (5x5), and their pressure sensing response was compared. Additionally, the anticipated capacitive response was calculated according to the fiber dimensions and governing sensing equation. Results indicated that the sensitivity of the BiSoFT texel could easily be improved by increasing the number of fibers within the texel. Further, the calculated fiber responses closely matched those measured thus validating the sensor response. Finally, the BiSoFTs were woven into a fabric to create a pressure-sensing mat consisting of sixty-four texels. The mat could differentiate the location of pressure application as well as the level of pressure. Thus, this approach provides a novel method of fabricating fiber-based sensors using an industry relevant machinery. Such sensors can be seamlessly integrated into fabric structures to create textile-based sensors.

Future work for the BiSoFT fibers includes development of a wearable sensing system. To this point, the capabilities of the BiSoFT have only been demonstrated on benchtop. To further elucidate the benefits of this sensing approach, an appropriate wearable system for the BiSoFTs should be designed including the capacitance board and interconnection method. Subsequently, the BiSoFT sensing system could be utilized in the simulated ISE experiments (artificial limb and bent-knee adapter) or during trials with amputee subjects. Another useful application of the BiSoFTs would be large-area sensing. One of the benefits of the BiSoFT manufacturing method is that long fiber lengths may be produced at high speeds. Therefore, it would be compelling to use the BiSoFTs to produce a very large area sensing arrays that could for example, be integrated beneath carpets for occupancy sensing.

In addition, both the seam-line and BiSoFT sensing approaches should be considered for sensing moisture and humidity within the ISE. In Section 4, we demonstrated that the SLS

approach could be used to sense wetness and RH in benchtop experiments. This concept should be further explored for ISE monitoring since increased moisture within the ISE has been linked to amputee discomfort.<sup>[2, 19, 23]</sup> In theory, the BiSoFTs should also be capable of sensing changes in wetness and humidity due to changes in the dielectric constant. This concept however should be demonstrated through practical experimentation.

In the long-term, textile-based sensors, such as those proposed here, could be used in clinical settings such that prosthetists can optimize the fit and quality of prosthetic devices. Further, such sensors could be worn by amputees daily to analyze the long-term effects of wearing prosthetic devices and identify certain problematic components. Data from the sensors within the socket would allow clinicians to track changes within the ISE over long-term periods thus aiding in management of comfort and prosthetic fit. This would allow prosthetists to identify sources of discomfort more easily and accordingly address issues – thus providing improved medical care to amputees. Additionally, the data collected by these sensors could be used to design improved prosthetic devices. It is known that new prosthetic designs are necessary to confront issues regarding amputee discomfort.<sup>[2-5]</sup> Data collected by textile-based sensors could aid in efforts to identify certain problematic prosthetic components and analyze the effectiveness of new designs. Monitoring the residual limb using textile-based sensors, such as those proposed here, presents significant opportunity to improve amputees' quality of life.<sup>[354]</sup>

## 9 References

- [1] K. Ziegler-Graham, E. J. MacKenzie, P. L. Ephraim, T. G. Trivison, R. Brookmeyer, , *Arch. Phys. Med. Rehabil.* **2008**, *89*(3), 422-429.
- [2] K. Ghoseiri, M. R. Safari, , *Journal of Rehabilitation Research and Development.* **2014**, *51*(6), 855-68.
- [3] J. T. Peery, G. K. Klute, J. J. Blevins, W. R. Ledoux, , *TNSRE.* **2006**, *14*(3), 336-343.
- [4] L. Paterno, M. Ibrahimi, E. Gruppioni, A. Menciassi, L. Ricotti, , *TBME.* **2018**, *65*(9), 1996-2010.
- [5] G. Klute, E. Huff, W. Ledoux, , *Clin Orthop Relat Res.* **2014**, *472*(10), 3062-3067.
- [6] P. Laszczak, M. McGrath, J. Tang, J. Gao, L. Jiang, D. L. Bader, D. Moser, S. Zahedi, , *Med. Eng. Phys.* **2016**, *38*(7), 695-700.
- [7] C. C. Nielsen, , *JPO Journal of Prosthetics and Orthotics.* **1991**, *3*(3), 125-129.
- [8] D. M. Sengeh, H. Herr, , *JPO Journal of Prosthetics and Orthotics.* **2013**, *25*(3), 129-137.
- [9] T. R. Dillingham, L. E. Pezzin, E. J. MacKenzie, A. R. Burgess, , *American journal of physical medicine & rehabilitation.* **2001**, *80*(8), 563-571.
- [10] E. A. Al-Fakih, N. A. Abu Osman, F. R. Mahmad Adikan, , *Sensors (Basel, Switzerland).* **2016**, *16*(7), 1119.

- [11] N. A. Abu Osman, W. D. Spence, S. E. Solomonidis, J. P. Paul, A. M. Weir, , *Proceedings of the Institution of Mechanical Engineers, Part B: Journal of Engineering Manufacture*. **2010**, 224(8), 1239-1250.`
- [12] J. E. Sanders, C. H. Daly, , *Journal of rehabilitation research and development*. **1993**, 30(2), 191.
- [13] M. Silver-Thorn, J. W. Steege, D. S. Childress, , *Journal of Rehabilitation Research and Development*. **1996**, 33(3), 253-266.
- [14] C. H. Y. Lai, C. W. P. Li-Tsang, , *Burns*. **2009**, 35(6), 845-851.
- [15] P. Saccomandi, E. Schena, C. M. Oddo, L. Zollo, S. Silvestri, E. Guglielmelli, , *Biosensors*. **2014**, 4(4), 422-448.
- [16] C. Ko, S. Kim, Y. Cho, D. Lee, D. Kim, J. Ryu, D. Lim, H. Kim, , *Int. J. Precis. Eng. Manuf.* **2018**, 19(6), 899-905.
- [17] J. E. Sanders, C. H. Daly, , *T-RE*. **1993**, 1(2), 79-85.
- [18] N. Mathur, I. Glesk, A. Buis, , *JBHI*. **2016**, 20(1), 158-165.
- [19] E. A. Huff, W. R. Ledoux, J. S. Berge, G. K. Klute, , *JPO Journal of Prosthetics and Orthotics*. **2008**, 20(4), 170-173.
- [20] T. Agcayazi, J. Tabor, M. McKnight, I. Martin, T. K. Ghosh, A. Bozkurt, , *Advanced materials technologies*. **2020**, 2000155.

- [21] J. Tabor, T. Agcayazi, A. Fleming, B. Thompson, A. Kapoor, M. Liu, M. Y. Lee, H. Huang, A. Bozkurt, T. K. Ghosh, , *IEEE Sensors Journal*. **2021**, 21(7), 9413-9422.
- [22] T. L. Beil, G. M. Street, S. J. Covey, , *Journal of rehabilitation research and development*. **2002**, 39(6), 693.
- [23] S. Ali, N. A. A. Osman, N. Mortaza, A. Eshraghi, H. Gholizadeh, Wan Abas, W. A. B, **2012**.
- [24] Peery, J. T., Ledoux, W. R., Klute, G. K., , *Journal of Rehabilitation Research and Developmen*. **2005**, 42(2), 147-154.
- [25] Laszczak, P.|Jiang, L.|Bader, D.L.|Moser, D.|Zahedi, S, , *Medical Engineering and Physics*. **2014**, 37(1), 132-137.
- [26] S. Ali, N. A. Abu Osman, A. Eshraghi, H. Gholizadeh, Abd razak, Nasrul Anwar bin, Wan Abas, Wan Abu Bakar Bin, , *Clin. Biomech*. **2013**, 28(9–10), 994-999.
- [27] A. G. Cutti, P. Perego, M. C. Fusca, R. Sacchetti, G. Andreoni, , *Sensors (Basel, Switzerland)*. **2014**, 14(3), 5041-5055.
- [28] S. W. Levy, , *Cutis*. **1995**, 55(5), 297.
- [29] S. W. Levy, , *Prosthetics and Orthotics International*. **1980**, 4(1), 37-44.
- [30] F. T. Hoaglund, H. E. Jergesen, L. Wilson, L. W. Lamoreux, R. Roberts, , *Journal of rehabilitation R&D*. **1983**, 20(1), 57.

- [31] C. C. Lyon, J. Kulkarni, E. Van Ross, M. H. Beck, E. Zimerson, , *Journal of the American Academy of Dermatology*. **2000**, 42(3), 501-507.
- [32] H. E. Meulenbelt, J. H. Geertzen, M. F. Jonkman, P. U. Dijkstra, , *Arch. Phys. Med. Rehabil.* **2009**, 90(1), 74-81.
- [33] A. Ferreira, V. Correia, E. Mendes, C. Lopes, J. F. Vilela Vaz, S. Lanceros-Mendez, , *JSEN*. **2017**, 17(7), 2182-2190.
- [34] M. D. Geil, A. Lay, , *Prosthetics and Orthotics International*. **2004**, 28(2), 105-114.
- [35] M. Geil, , *Journal of Prosthetics & Orthotics*. **2002**, 14(4), 159-164.
- [36] M. M. Lusardi, M. Jorge, C. C. Nielsen, *Orthotics and Prosthetics in Rehabilitation*, 3rd edn., Saunders, Saint Louis **2012**.
- [37] L. Armitage, A. Buller, G. Rajan, G. Prusty, A. Simmons, L. Kark, , *Prosthetics and Orthotics International*. **2019**, 30936461986836-309364619868364.
- [38] S. Toyama, Y. Tanaka, S. Shirogane, T. Nakamura, T. Umino, R. Uehara, T. Okamoto, H. Igarashi, , *Sensors (Basel, Switzerland)*. **2017**, 17(8), 1752.
- [39] J. E. Sanders, D. Lam, A. J. Dralle, R. Okumura, , *Journal of rehabilitation research and development*. **1997**, 34(1), 19-43.
- [40] J. E. Sanders, D. M. Bell, R. M. Okumura, A. J. Dralle, , *T-RE*. **1998**, 6(1), 21-31.

- [41] J. R. Pearson, G. Holmgren, L. March, K. Oberg, , *Bulletin of prosthetics research*. **1973**, 10(19), 52.
- [42] J. C. H. Goh, P. V. S. Lee, S. Y. Chong, , *Journal of rehabilitation research and development*. **2004**, 41(3B), 491-501.
- [43] J. E. Sanders, C. H. Daly, E. M. Burgess, , *Journal of rehabilitation research and development*. **1992**, 29(4), 1.
- [44] J. E. Sanders, S. G. Zachariah, A. K. Jacobsen, J. R. Fergason, , *Journal of Biomechanics*. **2005**, 38(8), 1566-1573.
- [45] J. Rae, J. Cockrell, , *Bulletin of Prosthetics Research*. **1971**.
- [46] G. K. Klute, K. J. Bates, J. S. Berge, W. Biggs, C. King, , *Journal of rehabilitation research and development*. **2016**, 53(6), 721-728.
- [47] A. D. Segal, G. K. Klute, , *Journal of rehabilitation research and development*. **2016**, 53(5), 619-628.
- [48] S. Takamatsu, T. Kobayashi, N. Shibayama, K. Miyake, T. Itoh, , *Sensors & Actuators: A. Physical*. **2012**, 184, 57-63.
- [49] Y. Gao, M. Xu, G. Yu, J. Tan, F. Xuan, , *Sensors and Actuators: A. Physical*. **2019**, 299, 111625.
- [50] A. Ozgur, A. Asli, G. Joshua, W. Conor, , *Adv. Mater. Technol*. **2018**, 3(1), 1700237.

- [51] X. Guo, Y. Huang, X. Cai, C. Liu, P. Liu, , *Measurement Science and Technology*. **2016**, 27(4), 45105.
- [52] S. M. Doshi, E. T. Thostenson, , *ACS Sens*. **2018**.
- [53] J. Meyer, B. Arnrich, J. Schumm, G. Troster, , *JSEN*. **2010**, 10(8), 1391-1398.
- [54] Q. Zhang, Y. L. Wang, Y. Xia, P. F. Zhang, T. V. Kirk, X. D. Chen, , *Advanced Materials Technologies*. **2019**, 4(10), 1900485-n/a.
- [55] S. Takamatsu, T. Lonjaret, E. Ismailova, A. Masuda, T. Itoh, G. G. Malliaras, , *Advanced Materials*. **2016**, 28(22), 4485-4488.
- [56] Y. Hasegawa, M. Shikida, D. Ogura, Y. Suzuki, K. Sato, , *Journal of Micromechanics and Microengineering*. **2008**, 18(8).
- [57] J. Lee, J. Yoon, H. G. Kim, S. Kang, W. Oh, H. Algadi, S. Al-sayari, B. Shong, S. Kim, H. Kim, T. Lee, H. Lee, , *NPG Asia Materials*. **2016**, 8(11), 9.
- [58] L. Jaehong, K. Hyukho, S. Jungmok, S. Sera, K. J. Hoon, P. Changhyun, S. Seungbae, J. H. Kim, Y. H. Jang, D. E. Kim, L. Taeyoon, , *Adv Mater*. **2015**, 27(15), 2433-2439.
- [59] Y. Wei, S. Chen, X. Yuan, P. Wang, L. Liu, , *Advanced Functional Materials*. **2016**, 26(28), 5078-5085.
- [60] M. Liu, X. Pu, C. Jiang, T. Liu, X. Huang, L. Chen, C. Du, J. Sun, W. Hu, Z. L. Wang, , *Advanced Materials*. **2017**, 29(41), 1703700-n/a.

- [61] G. H. Büscher, R. Kõiva, C. Schürmann, R. Haschke, H. J. Ritter, , *Robotics and Autonomous Systems*. **2015**, 63, 244-252.
- [62] Y. Li, Y. A. Samad, K. Liao, , *Journal of Materials Chemistry A*. **2015**, 3(5), 2181-2187.
- [63] Y. Tai, G. Lubineau, , *Advanced Functional Materials*. **2016**, 26(23), 4078-4084.
- [64] Lai Ying-Chih, Ye Bo-Wei, Lu Chun-Fu, Chen Chien-Tung, Jao Meng-Huan, Su Wei-Fang, Hung Wen-Yi, Lin Tai-Yuan, Chen Yang-Fang, , *Adv. Funct. Mater.* **2016**, 26(8), 1286-1295.
- [65] Y. Cheng, R. Wang, J. Sun, L. Gao, , *Advanced Materials*. **2015**, 27(45), 7365-7371.
- [66] J. Ge, L. Sun, F. Zhang, Y. Zhang, L. Shi, H. Zhao, H. Zhu, H. Jiang, S. Yu, , *Advanced Materials*. **2016**, 28(4), 722-728.
- [67] W. Hongyan, L. Zunfeng, D. Jianning, Lepró Xavier, F. Shaoli, J. Nan, Y. Ninyi, W. Run, Y. Qu, L. Wei, L. Zhongsheng, Z. Mei, Ovalle-Robles Raquel, I. Kanzas, Y. Shougen, R. H. Baughman, , *Adv Mater.* **2016**, 28(25), 4998-5007.
- [68] C. Choi, J. M. Lee, S. H. Kim, S. J. Kim, J. Di, R. H. Baughman, , *Nano Lett.* **2016**, 16(12), 7677-7684.
- [69] R. Wu, L. Ma, C. Hou, Z. Meng, W. Guo, W. Yu, R. Yu, F. Hu, X. Y. Liu, , *Small*. **2019**, 15(31), e1901558-n/a.
- [70] T. Q. Trung, H. S. Le, M. L. Dang Thi, J. Sanghyun, S. Y. Park, Lee Nae-Eung, , *Adv. Healthcare Mater.* **2018**, 7(12), 1800074.

- [71] M. Bayindir, A. Abouraddy, J. Arnold, J. Joannopoulos, Y. Fink, , *Adv Mater.* **2006**, *18*(7), 845-849.
- [72] N. J. Blasdel, E. K. Wujcik, J. E. Carletta, K. S. Lee, C. N. Monty, , *IEEE Sensors Journal.* **2015**, *15*(1), 300-306.
- [73] I. Krucińska, B. Surma, M. Chrzanowski, E. Skrzetuska, M. Puchalski, , *Journal of Applied Polymer Science.* **2013**, *127*(2), 869-878.
- [74] M. Sibinski, M. Jakubowska, M. Sloma, , *Sensors (Basel, Switzerland).* **2010**, *10*(9), 7934-7946.
- [75] X. Liao, Q. Liao, Z. Zhang, X. Yan, Q. Liang, Q. Wang, M. Li, Y. Zhang, , *Advanced Functional Materials.* **2016**, *26*(18), 3074-3081.
- [76] S. Ling, Z. Qin, C. Li, W. Huang, D. L. Kaplan, M. J. Buehler, , *Nature Communications.* **2017**, *8*(1), 1387.
- [77] Y. He, Q. Gui, S. Liao, H. Jia, Y. Wang, , *Advanced Materials Technologies.* **2016**, *1*(8), 1600170-n/a.
- [78] L. Wang, K. J. Loh, , *Smart Materials and Structures.* **2017**, *26*(5), 55018.
- [79] W. A. Daoud, J. H. Xin, Y. S. Szeto, , *Sensors & Actuators: B. Chemical.* **2005**, *109*(2), 329-333.
- [80] Enzo Pasquale Scilingo, F. Lorussi, A. Mazzoldi, D. De Rossi, , *JSEN.* **2003**, *3*(4), 460-467.

- [81] Y. Shang, Y. Li, X. He, S. Du, L. Zhang, E. Shi, S. Wu, Z. Li, P. Li, J. Wei, K. Wang, H. Zhu, D. Wu, A. Cao, , *ACS Nano*. **2013**, 7(2), 1446-1453.
- [82] M. D. Husain, R. Kennon, T. Dias, , *Journal of Industrial Textiles*. **2014**, 44(3), 398-417.
- [83] X. Zhao, Y. Long, T. Yang, J. Li, H. Zhu, , *ACS applied materials & interfaces*. **2017**, 9(35), 30171-30176.
- [84] G. Mattana, T. Kinkeldei, D. Leuenberger, C. Ataman, J. J. Ruan, F. Molina-Lopez, A. Vasquez Quintero, G. Nisato, G. Troster, D. Briand, N. F. de Rooij, , *JSEN*. **2013**, 13(10), 3901-3909.
- [85] C. Ataman, T. Kinkeldei, A. Vasquez-Quintero, F. Molina-Lopez, J. Courbat, K. Cherenack, D. Briand, G. Tröster, N. F. de Rooij, , *Procedia Engineering*. **2011**, 25, 136-139.
- [86] T. Kinkeldei, C. Zysset, K. H. Cherenack, G. Troster, "A textile integrated sensor system for monitoring humidity and temperature", Jun 2011.
- [87] C. Kunigunde, Z. Christoph, K. Thomas, Münzenrieder Niko, Tröster Gerhard, , *Adv Mater*. **2010**, 22(45), 5178-5182.
- [88] T. Kinkeldei, C. Zysset, K. Cherenack, G. Troester, "Development and evaluation of temperature sensors for textile integration", Oct 2009.
- [89] B. S. Shim, W. Chen, C. Doty, C. Xu, N. A. Kotov, , *Nano Lett*. **2008**, 8(12), 4151-4157.

- [90] G. Rosace, V. Trovato, C. Colleoni, M. Caldara, V. Re, M. Brucale, E. Piperopoulos, E. Mastronardo, C. Milone, G. De Luca, M. R. Plutino, , *Sensors & Actuators: B. Chemical*. **2017**, 252, 428-439.
- [91] J. H. Jang, J. I. Han, , *Sensors & Actuators: A. Physical*. **2017**, 261, 268-273.
- [92] W. Li, F. Xu, L. Sun, W. Liu, Y. Qiu, , *Sensors and Actuators B: Chemical*. **2016**, 230, 528-535.
- [93] E. Devaux, C. Aubry, C. Campagne, M. Rochery, , *Journal of Engineered Fibers and Fabrics*. **2011**, 6(3), 155892501100600.
- [94] Anonymous .
- [95] B. J. Hafner, J. C. Cagle, K. J. Allyn, J. E. Sanders, , *Prosthet. Orthot. Int.* **2017**, 41(2), 149-156.
- [96] G. K. Klute, B. C. Glaister, J. S. Berge, , *Prosthet. Orthot. Int.* **2010**, 34(2), 146-153.
- [97] K. L. Coleman, D. A. Boone, L. S. Laing, D. E. Mathews, D. G. Smith, , *Journal of rehabilitation research and development*. **2004**, 41(4), 591.
- [98] C. Lin, C. Chang, C. Wu, K. Chung, I. Liao, , *Medical Engineering & Physics*. **2004**, 26(1), 1-9.
- [99] J. Cagle C., P. Reinhall G., B. Hafner J., J. Sanders E., , *Journal of Biomechanical Engineering*. **2017**, 139(4), 045001-12.

- [100] R. Seymour Ph.D., *Prosthetics and orthotics : lower limb and spinal*, Lippincott Williams & Wilkins, Philadelphia **2002**.
- [101] M. McGrath, J. McCarthy, A. Gallego, A. Kercher, S. Zahedi, D. Moser, , *Canadian Prosthetics & Orthotics Journal*. **2019**.
- [102] R. LeMoyné, in *Advances for Prosthetic Technology: From Historical Perspective to Current Status to Future Application* (Ed: Robert LeMoyné), Springer Japan, Tokyo **2016**, pp. 59-68.
- [103] X. Jia, M. Zhang, W. C. C. Lee, , *Journal of Biomechanics*. **2004**, 37(9), 1371-1377.
- [104] Ö Kristinsson, , *Prosthetics and Orthotics International*. **1993**, 17(1), 49-55.
- [105] I. McCurdie, R. Hanspal, R. Nieveen, , *Prosthetics and Orthotics International*. **1997**, 21(2), 124-128.
- [106] T. L. Beil, G. M. Street, , *Journal of rehabilitation research and development*. **2004**, 41(6A), 821.
- [107] E. Swanson, E. Weathersby, J. Cagle, J. E. Sanders, , *Journal of biomechanical engineering*. **2019**.
- [108] S. Laing, P. V. Lee, J. C. Goh, , *Annals of the Academy of Medicine, Singapore*. **2011**, 40(5), 252.
- [109] W. J. Board, G. M. Street, C. Caspers, , *Prosthetics and Orthotics International*. **2001**, 25(3), 202-209.

- [110] A. A. Polliack, D. D. Craig, R. C. Sieh, S. Landsberger, D. R. Mcneal, , *Prosthetics and orthotics international*. **2002**, 26(1), 23-34.
- [111] V. Rajtukova, R. Hudak, J. Zivcak, P. Halfarova, R. Kudrikova, , *Procedia Engineering*. **2014**, 96, 374-381.
- [112] P. Dou, X. Jia, S. Suo, R. Wang, M. Zhang, , *Clinical Biomechanics*. **2006**, 21(10), 1067-1073.
- [113] S. Ali, N. A. Osman, A. Razak, S. Hussain, W. A. Wan Abas, , *European journal of physical and rehabilitation medicine*. **2015**, 51(1), 31.
- [114] A. Eshraghi, N. Abu Osman, H. Gholizadeh, S. Ali, W. A. B. Abas, , *American Journal of Physical Medicine & Rehabilitation*. **2015**, 94(1), 1-10.
- [115] P. Convery, A. W. Buis, , *Prosthetics and orthotics international*. **1998**, 22(3), 193-198.
- [116] M. C. Faustini, R. H. Crawford, R. R. Neptune, W. E. Rogers, G. Bosker, , *Journal of biomechanical engineering*. **2005**, 127(6), 946.
- [117] A. Eshraghi, N. A. Abu Osman, H. Gholizadeh, S. Ali, S. K. SÃ|varsson, Wan Abas, W. A. B, **2013**.
- [118] T. Dumbleton, A. W. P. Buis, A. McFadyen, B. F. McHugh, G. McKay, K. D. Murray, S. Sexton, , *Journal of Rehabilitation Research and Development*. **2009**, 46(3), 405-415.
- [119] A. L. Lenz, T. R. Bush, , *Medical Engineering and Physics*. **2019**.

- [120] J. C. H. Goh, P. V. S. Lee, S. Y. Chong, , *Clinical Biomechanics*. **2003**, 18(3), 237-243.
- [121] J. C. H. Goh, P. V. S. Lee, S. Y. Chong, , *Proceedings of the Institution of Mechanical Engineers, Part H: Journal of Engineering in Medicine*. **2003**, 217(2), 121-126.
- [122] M. Zhang, A. R. Turner-Smith, A. Tanner, V. C. Roberts, , *Medical Engineering and Physics*. **1998**, 20(3), 188-198.
- [123] J. Wheeler, A. Mazumdar, L. Marron, K. Dullea, J. Sanders, K. Allyn, "A pressure and shear sensing liner for prosthetic sockets", Aug 2016.
- [124] S. M. Sze, *Semiconductor sensors*, 3. pr. edn., Wiley, New York [u.a.] **1994**.
- [125] J. Sanders, , *Medical and Biological Engineering and Computing*. **1995**, 33(4), 509-516.
- [126] G. Pirouzi, A. Osman, A. Eshraghi, S. Ali, H. Gholizadeh, Wan Abas, W A B, , *The Scientific World*. **2014**.
- [127] S. Wolf, M. Alimusaj, L. Fradet, J. Siegel, F. Braatz, , *Clinical Biomechanics*. **2009**, 24(10), 860-865.
- [128] S. Seyedin, P. Zhang, M. Naebe, S. Qin, J. Chen, X. Wang, J. M. Razal, , *Materials Horizons*. **2019**.
- [129] M. I. Tiwana, S. J. Redmond, N. H. Lovell, , *Sensors and Actuators A: Physical*. **2012**, 179, 17-31.

- [130] E. A. Al-Fakih, Noor Azuan Abu Osman, Faisal Rafiq Mahmad Adikan, , *Sensors*. **2016**, *16*(7), 1119.
- [131] R. B. Williams, D. Porter, V. C. Roberts, J. F. Regan, , *Medical & biological engineering & computing*. **1992**, *30*(1), 89-96.
- [132] B. Hafner, J. Sanders, , *Journal of Rehabilitation Research and Development*. **2014**, *1*(14), 509-516.
- [133] A. Almassri, W. Z. Wan Hasan, S. A. Ahmad, A. J. Ishak, A. M. Ghazali, D. N. Talib, C. Wada, , *Journal of Sensors*. **2015**.
- [134] J. S. Schofield, K. R. Evans, J. S. Hebert, P. D. Marasco, J. P. Carey, , *J. Biomech*. **2016**, *49*(5), 786-792.
- [135] Q. Fan, X. Zhang, Z. Qin, , *Journal of Macromolecular Science, Part B*. **2012**, *51*(4), 736-746.
- [136] F. A. Appoldt, L. M. Bennett, , *Bulletin of Prosthetics Research*. **1967**, 20-55.
- [137] J. E. Sanders, C. H. Daly, E. M. Burgess, , *Prosthetics and Orthotics International*. **1993**, *17*(1), 38-48.
- [138] P. Convery, A. W. P. Buis, , *Prosthetics and Orthotics International*. **1999**, *23*(2), 107-112.
- [139] S. G. Zachariah, J. E. Sanders, , *Prosthetics and Orthotics International*. **2001**, *25*(1), 34-40.

- [140] Mak, A. F. T., Zhang, M., Boone, D. A., **2001**, 38(2), 161-74.
- [141] M. P. McGrath, J. Gao, J. Tang, P. Laszczak, L. Jiang, D. Bader, D. Moser, S. Zahedi, ,  
*Proceedings of the Institution of Mechanical Engineers, Part H: Journal of Engineering in  
Medicine*. **2017**, 231(3), 235-242.
- [142] E. C. Swanson, J. B. McLean, K. J. Allyn, C. B. Redd, J. E. Sanders, , *Medical  
Engineering and Physics*. **2018**, 51, 111-118.
- [143] E. A. Al-Fakih, N. Azuan Abu Osman, F. Rafiq Mahamd Adikan, A. Eshraghi, P.  
Jahanshahi, , *JSEN*. **2016**, 16(4), 965-974.
- [144] E. Al-Fakih, N. Arifin, G. Pirouzi, F. R. Mahamd Adikan, H. N. Shasmin, N. A. Abu  
Osman, , *Journal of Biomedical Optics*. **2017**, 22(8), 087001.
- [145] Qiao Li, Li-Na Zhang, Xiao-Ming Tao, Xin Ding, , *Advanced Healthcare Materials*. **2017**,  
6(12), 1601371.
- [146] J. W. Wheeler, J. G. Dabling, D. Chinn, T. Turner, A. Filatov, L. Anderson, B. Rohrer,  
"MEMS-based bubble pressure sensor for prosthetic socket interface pressure  
measurement", presented at 2011 Annual International Conference of the IEEE  
Engineering in Medicine and Biology Society 2011.
- [147] G. Sordo, L. Lorenzelli, "Design of a novel tri-axial force sensor for optimized design of  
prosthetic socket for lower limb amputees", May 2016.

- [148] Y. Abdul Samad, K. Komatsu, D. Yamashita, Y. Li, L. Zheng, S. M. Alhassan, Y. Nakano, K. Liao, , *Sensors & Actuators: B. Chemical*. **2017**, *240*, 1083-1090.
- [149] D. Won, S. Baek, M. Huh, H. Kim, J. Kim, S. Lee, , *Sensors & Actuators: A. Physical*. **2017**, *259*, 105-111.
- [150] T. Seesaard, P. Lorwongtragool, T. Kerdcharoen, , *Sensors (Basel, Switzerland)*. **2015**, *15*(1), 1885-1902.
- [151] X. Liu, C. Tang, X. Du, S. Xiong, S. Xi, Y. Liu, X. Shen, Q. Zheng, Z. Wang, Y. Wu, A. Horner, J. Kim, , *Mater. Horiz*. **2017**, *4*(3), 477-486.
- [152] W. Chunya, L. Xiang, G. Enlai, J. Muqiang, X. Kailun, W. Qi, X. Zhiping, R. Tianling, Z. Yingying, , *Adv Mater*. **2016**, *28*(31), 6640-6648.
- [153] Y. Cheng, R. Wang, H. Zhai, J. Sun, , *Nanoscale*. **2017**, *9*(11), 3834-3842.
- [154] A. Kapoor, M. McKnight, K. Chatterjee, T. Agcayazi, H. Kausche, A. Bozkurt, T. K. Ghosh, , *Advanced Materials Technologies*. **2019**, *4*(1), 1800281-n/a.
- [155] L. M. Ericson, , *Science*. **2004**, *305*(5689), 1447-1450.
- [156] B. Vigolo, , *Science*. **2000**, *290*(5495), 1331-1334.
- [157] Z. Dong, C. Jiang, H. Cheng, Y. Zhao, G. Shi, L. Jiang, L. Qu, , *Advanced materials (Weinheim)*. **2012**, *24*(14), 1856-1861.
- [158] K. Jiang, Q. Li, S. Fan, , *Nature (London)*. **2002**, *419*(6909), 801.

- [159] M. Zhang, , *Science*. **2004**, 306(5700), 1358-1361.
- [160] M. Zhang, , *Science*. **2005**, 309(5738), 1215-1219.
- [161] A. B. Dalton, S. Collins, E. Muñoz, J. M. Razal, V. H. Ebron, J. P. Ferraris, J. N. Coleman, B. G. Kim, R. H. Baughman, , *Nature (London)*. **2003**, 423(6941), 703.
- [162] M. Catrysse, R. Puers, C. Hertleer, L. Van Langenhove, H. van Egmond, D. Matthys, , *Sensors and Actuators A: Physical*. **2004**, 114(2), 302-311.
- [163] T. Pereira, P. Silva, H. Carvalho, M. Carvalho, "Textile moisture sensor matrix for monitoring of disabled and bed-rest patients", Apr 2011.
- [164] G. Cho, K. Jeong, M. J. Paik, Y. Kwun, M. Sung, , *IEEE Sensors Journal*. **2011**, 11(12), 3183-3193.
- [165] J. Xie, H. Long, M. Miao, , *Smart materials and structures*. **2016**, 25(10), 105008.
- [166] H. Zhang, X. Tao, S. Wang, T. Yu, , *Textile Research Journal*. **2005**, 75(8), 598-606.
- [167] H. Zhang, X. Tao, T. Yu, S. Wang, , *Sensors & Actuators: A. Physical*. **2006**, 126(1), 129-140.
- [168] R. Paradiso, D. De Rossi, "Advances in textile technologies for unobtrusive monitoring of vital parameters and movements", Aug 2006.
- [169] R. Paradiso, G. Loriga, N. Taccini, , *TITB*. **2005**, 9(3), 337-344.

- [170] M. McKnight, T. Agcayazi, T. Ghosh, A. Bozkurt, in *Wearable Technology in Medicine and Health Care* (Ed: Raymond Kai-Yu Tong), Academic Press**2018**, pp. 153-171.
- [171] E. Ismar, S. Kurşun Bahadır, F. Kalaoglu, V. Koncar, , *Global challenges*. **2020**, 4(7), 1900092-n/a.
- [172] Z. Wei, S. Lin, L. Qiao, C. Song, W. Fei, Tao Xiao-Ming, , *Adv Mater*. **2014**, 26(31), 5310-5336.
- [173] M. S. Freund, *Self-doped conducting polymers*, Wiley, Chichester, England ; Hoboken, NJ **2007**.
- [174] G. A. Snook, P. Kao, A. S. Best, , *J. Power Sources*. **2011**, 196(1), 1-12.
- [175] D. Lu, C. P. Wong., Yi, *Electrical Conductive Adhesives with Nanotechnologies*, 1. Aufl. edn., Springer-Verlag, US **2010**.
- [176] K. Chatterjee, J. Tabor, T. K. Ghosh, , *Fibers*. **2019**, 7(6), 51.
- [177] Skotheim, Terje A.;reynolds, John, *Handbook of Conducting Polymers, 2 Volume Set*, 3<sup>a</sup> edn., CRC Press**2007**.
- [178] B. Kim, V. Koncar, C. Dufour, , *Journal of Applied Polymer Science*. **2006**, 101(3), 1252-1256.
- [179] Michael F. L. De Volder, Sameh H. Tawfick, Ray H. Baughman, A. John Hart, , *Science*. **2013**, 339(6119), 535-539.

- [180] S. M. Aharoni, , *Journal of Applied Physics*. **1972**, 43(5), 2463-2465.
- [181] Dang Zhi-Min, in *Dielectric Polymer Materials for High-Density Energy Storage*  
(Anonymous ), Elsevier**2018**, pp. 1.
- [182] J. Huang, , *Advances in Polymer Technology*. **2002**, 21(4), 299-313.
- [183] F. Alimohammadi, M. Parvinzadeh Gashti, A. Shamei, , *J Coat Technol Res*. **2013**, 10(1),  
123-132.
- [184] L. Xiang, H. Zhang, Y. Hu, L. Peng, , *Journal of Materials Chemistry C*. **2018**, 6(29),  
7714-7727.
- [185] T. Mirfakhrai, J. D. W. Madden, R. H. Baughman, , *Materials Today*. **2007**, 10(4), 30-38.
- [186] W. Bauhofer, J. Z. Kovacs, , *Composites Science and Technology*. **2009**, 69(10), 1486-  
1498.
- [187] R. Zhang, H. Deng, R. Valenca, J. Jin, Q. Fu, E. Bilotti, T. Peijs, , *Sensors & Actuators: A. Physical*. **2012**, 179, 83-91.
- [188] K. S. Novoselov, A. K. Geim, S. V. Morozov, D. Jiang, Y. Zhang, S. V. Dubonos, I. V. Grigorieva, A. A. Firsov, , *Science*. **2004**, 306(5696), 666-669.
- [189] G. Xin, T. Yao, H. Sun, S. M. Scott, D. Shao, G. Wang, J. Lian, , *Science (New York, N.Y.)*. **2015**, 349(6252), 1083-1087.

- [190] T. Das, B. K. Sharma, A. K. Katiyar, J. Ahn, , *Journal of Semiconductors*. **2018**, 39(1), 011007.
- [191] C. Lee, X. Wei, J. W. Kysar, J. Hone, , *Science*. **2008**, 321(5887), 385-388.
- [192] K. I. Bolotin, K. J. Sikes, Z. Jiang, M. Klima, G. Fudenberg, J. Hone, P. Kim, H. L. Stormer, , *Solid State Communications*. **2008**, 146(9), 351-355.
- [193] H. Jang, Y. J. Park, X. Chen, T. Das, M. Kim, J. Ahn, , *Advanced Materials*. **2016**, 28(22), 4184-4202.
- [194] R. R. Nair, P. Blake, A. N. Grigorenko, K. S. Novoselov, T. J. Booth, T. Stauber, N. M. R. Peres, A. K. Geim, , *Science*. **2008**, 320(5881), 1308.
- [195] S. Stankovich, D. A. Dikin, R. D. Piner, K. A. Kohlhaas, A. Kleinhammes, Y. Jia, Y. Wu, S. T. Nguyen, R. S. Ruoff, , *Carbon*. **2007**, 45(7), 1558-1565.
- [196] M. H. Al-Saleh, U. Sundararaj, , *Carbon*. **2009**, 47(1), 2-22.
- [197] M. E. Spahr, R. Rother, in *Fillers for Polymer Applications* (Ed: Roger Rother), Springer International Publishing, Cham **2017**, pp. 261-291.
- [198] K. H. J. Buschow, *Encyclopedia of materials science and technology*, Pergamon Press, Oxford [u.a.] **2001**.
- [199] R. M. Harris, in *Coloring Technology for Plastics* (Anonymous ), William Andrew Publishing/Plastics Design Library **1999**, pp. 1-6.

- [200] W. Zhang, R. Blackburn, A. Dehghani-Sanij, , *J Mater Sci.* **2007**, 42(18), 7861-7865.
- [201] I. Islam, S. Sultana, S. Kumer Ray, H. Parvin Nur, M. Hossain, W. Md. Ajmotgir, , *C.* **2018**, 4(1), 15.
- [202] B. K. Little, Y. Li, V. Cammarata, R. Broughton, G. Mills, , *ACS Applied Materials & Interfaces.* **2011**, 3(6), 1965-1973.
- [203] X. Liu, H. Chang, Y. Li, W. T. S. Huck, Z. Zheng, , *ACS Applied Materials & Interfaces.* **2010**, 2(2), 529-535.
- [204] H. M. Lee, S. Choi, A. Jung, S. H. Ko, , *Angewandte Chemie International Edition.* **2013**, 52(30), 7718-7723.
- [205] A. Chhetry, H. Yoon, J. Y. Park, , *Journal of Materials Chemistry C.* **2017**, 5(38), 10068-10076.
- [206] K. Cherenack, L. van Pieteron, , *Journal of applied physics.* **2012**, 112(9), 091301.
- [207] Y. Li, I. A. Kinloch, A. H. Windle, , *Science.* **2004**, 304(5668), 276-278.
- [208] R. Jalili, S. H. Aboutalebi, D. Esrafilzadeh, R. L. Shepherd, J. Chen, S. Aminorroaya-Yamini, K. Konstantinov, A. I. Minett, J. M. Razal, G. G. Wallace, , *Advanced functional materials.* **2013**, 23(43), 5345-5354.
- [209] S. H. Aboutalebi, R. Jalili, D. Esrafilzadeh, M. Salari, Z. Gholamvand, S. Aminorroaya Yamini, K. Konstantinov, R. L. Shepherd, J. Chen, S. E. Moulton, P. C. Innis, A. I. Minett, J. M. Razal, G. G. Wallace, , *ACS Nano.* **2014**, 8(3), 2456-2466.

- [210] C. Kutzner, R. Lucklum, R. Torah, S. Beeby, J. Tudor, "Novel screen printed humidity sensor on textiles for smart textile applications", Jun 2013.
- [211] P. Su, C. Chang, , *Journal of the Taiwan Institute of Chemical Engineers*. **2018**, 87, 36-43.
- [212] A. I. S. Neves, D. P. Rodrigues, A. De Sanctis, E. T. Alonso, M. S. Pereira, V. S. Amaral, L. V. Melo, S. Russo, I. de Schrijver, H. Alves, M. F. Craciun, , *Scientific reports*. **2017**, 7(1), 4250-10.
- [213] C. Winterhalter, J. Teverovsky, P. Wilson, J. Slade, B. Farell, W. Horowitz, E. Tierney, , *Journal of ASTM International*. **2005**, 2(7), 1-9.
- [214] M. Rothmaier, M. P. Luong, F. Clemens, , *Sensors (Basel, Switzerland)*. **2008**, 8(7), 4318-4329.
- [215] Ying Zhang, Dejun Feng, Zhiguo Liu, Zhuanyun Guo, Xiaoyi Dong, K. S. Chiang, B. C. B. Chu, , *LPT*. **2001**, 13(6), 618-619.
- [216] J. Guo, X. Liu, N. Jiang, A. K. Yetisen, H. Yuk, C. Yang, A. Khademhosseini, X. Zhao, S. Yun, , *Advanced Materials*. **2016**, 28(46), 10244-10249.
- [217] C. K. Harnett, H. Zhao, R. F. Shepherd, , *Advanced Materials Technologies*. **2017**, 2(9), 1700087-n/a.
- [218] Q. Liao, M. Mohr, X. Zhang, Z. Zhang, Y. Zhang, H. Fecht, , *Nanoscale*. **2013**, 5(24), 12350.

- [219] X. Li, Z. Lin, G. Cheng, X. Wen, Y. Liu, S. Niu, Z. L. Wang, , *ACS nano*. **2014**, 8(10), 10674-10681.
- [220] O. Atalay, W. R. Kennon, , *Sensors (Basel, Switzerland)*. **2014**, 14(3), 4712-4730.
- [221] A. A. Barlian, W. -. Park, J. R. Mallon, A. J. Rastegar, B. L. Pruitt, , *JPROC*. **2009**, 97(3), 513-552.
- [222] J. J. Park, W. J. Hyun, S. C. Mun, Y. T. Park, O. O. Park, , *ACS applied materials & interfaces*. **2015**, 7(11), 6317-6324.
- [223] T. Yamada, Y. Hayamizu, Y. Yamamoto, Y. Yomogida, A. Izadi-Najafabadi, D. N. Futaba, K. Hata, , *Nature nanotechnology*. **2011**, 6(5), 296-301.
- [224] C. J. Dillman, , *Exercise and sport sciences reviews*. **1975**, 3(1), 193-218.
- [225] A. V. Rowlands, M. R. Stone, R. G. Eston, , *Medicine and science in sports and exercise*. **2007**, 39(4), 716-727.
- [226] S. Chen, Z. Lou, D. Chen, K. Jiang, G. Shen, , *Advanced Materials Technologies*. **2016**, 1(7), 1600136-n/a.
- [227] H. Wu, Q. Liu, H. Chen, G. Shi, C. Li, , *Nanoscale*. **2018**, 10(37), 17512-17519.
- [228] T. J. Kang, A. Choi, D. Kim, K. Jin, D. K. Seo, D. H. Jeong, S. Hong, Y. W. Park, Y. H. Kim, , *Smart Materials and Structures*. **2011**, 20(1), 015004.

- [229] J. Eom, R. Jaisutti, H. Lee, W. Lee, J. Heo, J. Lee, S. K. Park, Y. Kim, , *ACS applied materials & interfaces*. **2017**, 9(11), 10190-10197.
- [230] L. Yu, J. C. Yeo, R. H. Soon, T. Yeo, H. H. Lee, C. T. Lim, , *ACS Applied Materials & Interfaces*. **2018**, 10(15), 12773-12780.
- [231] Z. Yang, J. Deng, X. Chen, J. Ren, H. Peng, , *Angewandte Chemie International Edition*. **2013**, 52(50), 13453-13457.
- [232] F. Andreas, J. T. Muth, D. M. Vogt, Mengüç Yiğit, C. Alexandre, A. D. Valentine, C. J. Walsh, J. A. Lewis, , *Adv Mater*. **2015**, 27(15), 2440-2446.
- [233] L. M. Castano, A. B. and Flatau, , *Smart Materials and Structures*. **2014**, 23(5).
- [234] V. Mečnika, A. Schwarz, I. Krieviņš, **2013**.
- [235] J. G. Wiegerink, , *Textile Research Journal*. **1940**, 10(9), 357-371.
- [236] J. Tabor, K. Chatterjee, T. K. Ghosh, , *Advanced Materials Technologies*. **2020**, 1901155.
- [237] D. McColl, B. Cartlidge, P. Connolly, , *International Journal of Surgery*. **2007**, 5(5), 316-322.
- [238] J. Weremczuk, G. Tarapata, R. Jachowicz, , *Procedia Engineering*. **2012**, 47, 1366-1369.
- [239] C. R. Zamarreño, M. Hernaez, I. Del Villar, I. R. Matias, F. J. Arregui, , *Sensors & Actuators: B. Chemical*. **2010**, 146(1), 414-417.

- [240] J. Ascorbe, J. M. Corres, F. J. Arregui, I. R. Matias, , *Sensors (Basel, Switzerland)*. **2017**, *17*(4), 893.
- [241] B. Du, D. Yang, X. She, Y. Yuan, D. Mao, Y. Jiang, F. Lu, , *Sensors & Actuators: B. Chemical*. **2017**, *251*, 180-184.
- [242] G. Zhao, X. Li, M. Huang, Z. Zhen, Y. Zhong, Q. Chen, X. Zhao, Y. He, R. Hu, T. Yang, R. Zhang, C. Li, J. Kong, J. Xu, R. S. Ruoff, H. Zhu, , *Chemical Society reviews*. **2017**, *46*(15), 4417-4449.
- [243] G. Hassan, M. Sajid, C. Choi, , *Scientific Reports*. **2019**, *9*(1), 1-10.
- [244] L. Bießmann, L. P. Kreuzer, T. Widmann, N. Hohn, J. Moulin, P. Müller-Buschbaum, , *ACS Applied Materials & Interfaces*. **2018**, *10*(11), 9865-9872.
- [245] X. Fan, W. Nie, H. Tsai, N. Wang, H. Huang, Y. Cheng, R. Wen, L. Ma, F. Yan, Y. Xia, , *Advanced Science*. **2019**, *6*(19), 1900813-n/a.
- [246] M. Liu, C. Wang, Z. Yao, N. Kim, , *RSC Advances*. **2016**, *6*(47), 41580-41586.
- [247] T. Li, L. Li, H. Sun, Y. Xu, X. Wang, H. Luo, Z. Liu, T. Zhang, , *Advanced Science*. **2017**, *4*(5), 1600404-n/a.
- [248] Y. Shao, Y. Wang, S. Cao, Y. Huang, L. Zhang, F. Zhang, C. Liao, Y. Wang, , *Sensors (Basel, Switzerland)*. **2018**, *18*(7), 2029.
- [249] F. Tailoka, D. J. Fray, R. V. Kumar, , *Ionics*. **2000**, *6*(5), 383-388.

- [250] C. Feng, S. Sun, H. Wang, C. U. Segre, J. R. Stetter, , *Sensors & Actuators: B. Chemical*. **1997**, *40*(2), 217-222.
- [251] S. Liu, Y. Ji, J. Yang, W. Sun, H. Li, , *Sensors & Actuators: A. Physical*. **2018**, *269*, 313-321.
- [252] S. YOSHIMOTO, H. HOSOMI, Y. TAKAI, K. ITO, , *KOBUNSHI RONBUNSHU*. **2017**, *74*(2), 85-90.
- [253] A. Saccà, R. Pedicini, A. Carbone, I. Gatto, P. Fracas, E. Passalacqua, , *Chemical Physics Letters*. **2014**, *591*, 149-155.
- [254] K. Madhavan Nampoothiri, N. R. Nair, R. P. John, , *Bioresource Technology*. **2010**, *101*(22), 8493-8501.
- [255] F. Ubaid, Z. Ahmad, R. A. Shakoor, A. M. A. Mohamed, , *Journal of Materials Science: Materials in Electronics*. **2018**, *29*(10), 8135-8141.
- [256] D. Zhang, J. Tong, B. Xia, Q. Xue, , *Sensors & Actuators: B. Chemical*. **2014**, *203*, 263-270.
- [257] H. Bi, K. Yin, X. Xie, J. Ji, S. Wan, L. Sun, M. Terrones, M. S. Dresselhaus, , *Scientific reports*. **2013**, *3*(1), 2714.
- [258] D. H. Ho, Q. Sun, S. Y. Kim, J. T. Han, D. H. Kim, J. H. Cho, , *Advanced Materials*. **2016**, *28*(13), 2601-2608.

- [259] X. Li, P. Sun, L. Fan, M. Zhu, K. Wang, M. Zhong, J. Wei, D. Wu, Y. Cheng, H. Zhu, , *Scientific reports*. **2012**, 2(1), 395.
- [260] X. Li, R. Zhang, W. Yu, K. Wang, J. Wei, D. Wu, A. Cao, Z. Li, Y. Cheng, Q. Zheng, R. S. Ruoff, H. Zhu, , *Scientific reports*. **2012**, 2(1), 870.
- [261] Z. M. Rittersma, , *Sensors & Actuators: A. Physical*. **2002**, 96(2), 196-210.
- [262] J. S. Wilson, *Sensor technology handbook*, Nachdr. edn., Elsevier, Amsterdam [u.a.] **2006**.
- [263] H. Farahani, R. Wagiran, M. N. Hamidon, , *Sensors (Basel, Switzerland)*. **2014**, 14(5), 7881-7939.
- [264] M. M. Wernke, R. M. Schroeder, M. L. Haynes, L. L. Nolt, A. W. Albury, J. M. Colvin, , *Advances in Wound Care*. **2017**, 6(7), 233-239.
- [265] D. Quintero, D. J. Villarreal, R. D. Gregg, "Preliminary experiments with a unified controller for a powered knee-ankle prosthetic leg across walking speeds", Oct 2016.
- [266] F. Sup, H. A. Varol, J. Mitchell, T. Withrow, M. Goldfarb, "Design and control of an active electrical knee and ankle prosthesis", Oct 2008.
- [267] J. Hong, Z. Pan, ZheWang, M. Yao, J. Chen, Y. Zhang, , *Sensors and Actuators A: Physical*. **2016**, 238, 307-316.
- [268] Z. Mingchao, W. Chunya, W. Huimin, J. Muqiang, H. Xiangyang, Z. Yingying, , *Adv. Funct. Mater.* **2017**, 27(2), 1604795.

- [269] J. Ren, C. Wang, X. Zhang, T. Carey, K. Chen, Y. Yin, F. Torrissi, , *Carbon*. **2017**, *111*, 622-630.
- [270] T. Yan, Z. Wang, Z. Pan, , *J. Mater. Sci.* **2018**, *53*(16), 11917-11931.
- [271] G. Zhou, J. Byun, Y. Oh, B. Jung, H. Cha, D. Seong, M. Um, S. Hyun, T. Chou, , *ACS Appl. Mater. Interfaces*. **2017**, *9*(5), 4788-4797.
- [272] Y. Guo, Z. Gao, X. Wang, L. Sun, X. Yan, S. Yan, Y. Long, W. Han, , *RSC Adv.* **2018**, *8*(2), 1078-1082.
- [273] S. Seyedin, J. M. Razal, P. C. Innis, A. Jeiranikhameneh, S. Beirne, G. G. Wallace, , *ACS Appl. Mater. Interfaces*. **2015**, *7*(38), 21150-21158.
- [274] M. Stoppa, A. Chiolerio, , *Sensors (Basel, Switzerland)*. **2014**, *14*(7), 11957-11992.
- [275] L. Lan, F. Zhao, Y. Yao, J. Ping, Y. Ying, , *ACS applied materials & interfaces*. **2020**, *12*(9), 10689-10696.
- [276] R. Cao, X. Pu, X. Du, W. Yang, J. Wang, H. Guo, S. Zhao, Z. Yuan, C. Zhang, C. Li, Z. L. Wang, , *ACS nano*. **2018**, *12*(6), 5190-5196.
- [277] M. A. Yokus, R. Foote, J. S. Jur, , *JSEN*. **2016**, *16*(22), 7967-7976.
- [278] J. F. Saenz-Cogollo, M. Pau, B. Fraboni, A. Bonfiglio, , *Sensors (Basel, Switzerland)*. **2016**, *16*(3), 365.

- [279] J. Meyer, P. Lukowicz, G. Troster, "Textile Pressure Sensor for Muscle Activity and Motion Detection", 2006.
- [280] E. R. Post, M. Orth, P. R. Russo, N. Gershenfeld, , *IBM Systems Journal*. **2000**, 39(3), 840-860.
- [281] T. Agcayazi, M. McKnight, H. Kausche, T. Ghosh, A. Bozkurt, "A finger touch force detection method for textile based capacitive tactile sensor arrays", 2016.
- [282] M. McKnight, T. Agcayazi, H. Kausche, T. Ghosh, A. Bozkurt, "Sensing textile seam-line for wearable multimodal physiological monitoring", 2016.
- [283] R. White, M. McKnight, J. Tabor, T. Ghosh, T. Agcayazi, A. Bozkurt, "A Wetness Detection Technique Towards Scalable, Array-Based, Fully-Textile Sensing", Oct 2018.
- [284] P. S. Girão, P. M. P. Ramos, O. Postolache, J. Miguel Dias Pereira, , *Measurement*. **2013**, 46(3), 1257-1271.
- [285] S. J. Russell, E. Textile Institute (Manchester, *Handbook of Nonwovens*, Woodhead Publishing, Boca Raton, Fla **2007**.
- [286] W. L. BALLS, , *Nature*. **1946**, 158(4001), 9-11.
- [287] J. C. Schug, A. C. Lilly, D. A. Lowitz, , *Physical Review B*. **1970**, 1(12), 4811-4818.
- [288] D. T. W. Toolan, K. Adlington, A. Isakova, A. Kalamiotis, P. Mokarian-Tabari, G. Dimitrakis, C. Dodds, T. Arnold, N. J. Terrill, W. Bras, D. Hermida Merino, P. D. Topham, D. J. Irvine, J. R. Howse, **2017**.

- [289] R. Houwink, *Elasticity, plasticity and structure of matter*, 3. ed. edn., Cambridge Univ. Press, Cambridge **1971**.
- [290] A. K. Bhowmick, *Handbook of elastomers*, Vol. 61, 2. ed., rev. and expanded edn., Dekker, New York [u.a.] **2001**.
- [291] S. K. Batra, B. Pourdeyhimi, *Introduction to nonwovens technology*, DEStech Publ, Lancaster, PA **2012**.
- [292] T. Agcayazi, M. Foster, H. Kausche, M. Gordon, A. Bozkurt, , *HardwareX*. **2019**, 5, e00048.
- [293] P. Maiolino, F. Galantini, F. Mastrogiovanni, G. Gallone, G. Cannata, F. Carpi, , *Sensors and Actuators A: Physical*. **2015**, 226, 37-47.
- [294] Y. Zang, F. Zhang, C. Di, D. Zhu, **2015**, 2(2), 14-156.
- [295] K. Sundara-Rajan, A. Bestick, G. I. Rowe, G. K. Klute, W. R. Ledoux, H. C. Wang, A. V. Mamishev, , *Measurement Science and Technology*. **2012**, 23(8), 85701.
- [296] J. Jia, C. Xu, S. Pan, S. Xia, P. Wei, H. Y. Noh, P. Zhang, X. Jiang, , *Sensors (Basel, Switzerland)*. **2018**, 18(11), 3775.
- [297] A. Aryal, B. Becerik-Gerber, , *Building and Environment*. **2019**, 160, 106223.
- [298] J. Kim, S. Schiavon, G. Brager, , *Building and Environment*. **2018**, 132, 114-124.

- [299] K. Kurosumi, S. Shibasaki, T. Ito, in *International Review of Cytology*, Vol. 87  
(Anonymous ), Elsevier Science & Technology, United States **1984**, pp. 253-329.
- [300] A. P. Gagge, J. A. J. Stolwijk, J. D. Hardy, , *Environmental Research*. **1967**, 1(1), 1-20.
- [301] Y. -. Hsieh, J. Thompson, A. Miller, , *Textile Research Journal*. **1996**, 66(7), 456-464.
- [302] P. Sewell, S. Noroozi, J. Vinney, S. Andrews, , *Prosthetics and Orthotics International*.  
**2000**, 24(2), 97-107.
- [303] Z. Zhao, Q. Huang, C. Yan, Y. Liu, X. Zeng, X. Wei, Y. Hu, Z. Zheng, , *Nano energy*.  
**2020**, 70, 104528.
- [304] M. N. Orlin, T. G. McPoil, , *Phys. Ther.* **2000**, 80(4), 399-409.
- [305] C. R. C. Walker, R. R. Ingram, M. G. Hullin, S. W. McCreath, , *Injury*. **1994**, 25(6), 387-  
392.
- [306] M. E. Jones, G. M. Bashford, J. M. Mann, , *Prosthetics and Orthotics International*. **1997**,  
21(3), 183-186.
- [307] N. A. Abu Osman, W. D. Spence, S. E. Solomonidis, J. P. Paul, A. M. Weir, , *Medical  
Engineering and Physics*. **2010**, 32(7), 760-765.
- [308] J. B. Webster, B. J. Darter, in *Atlas of Orthoses and Assistive Devices*, Fifth Edition edn.  
(Anonymous ), Elsevier Inc**2019**, pp. 49-62.e1.

- [309] D. H. K. Chow, A. D. Holmes, C. K. L. Lee, S. W. Sin, , *Prosthetics and Orthotics International*. **2016**, 30(2), 114-128.
- [310] H. Gholizadeh, N. A. Abu Osman, A. Eshraghi, N. Arifin, T. Y. Chung, , *Prosthetics and orthotics international*. **2015**, 40(4), 509-516.
- [311] S. J. Eichhorn, **2009**.
- [312] A. Ziabicki, *Fundamentals of fibre formation : the science of fibre spinning and drawing*, London; New York : Wiley, 1976], London;; New York **1976**.
- [313] S. Mukhopadhyay, in *Advances in Filament Yarn Spinning of Textiles and Polymers* (Ed: Dong Zhang), Woodhead Publishing**2014**, pp. 113-127.
- [314] A. Lund, C. Jonasson, C. Johansson, D. Haagensen, B. Hagström, , *Journal of Applied Polymer Science*. **2012**, 126(2), 490-500.
- [315] Y. Liu, B. Cheng, N. Wang, W. Kang, W. Zhang, K. Xing, W. Yang, , *Journal of Applied Polymer Science*. **2012**, 124(1), 296-301.
- [316] T. Kikutani, J. Radhakrishnan, S. Arikawa, A. Takaku, N. Okui, X. Jin, F. Niwa, Y. Kudo, , *Journal of Applied Polymer Science*. **1996**, 62(11), 1913-1924.
- [317] C. D. Han, , *Journal of Applied Polymer Science*. **1973**, 17(4), 1289-1303.
- [318] A. Karagiannis, A. N. Hrymak, J. Vlachopoulos, , *Rheologica Acta*. **1990**, 29(1), 71-87.

- [319] B. Glauß, W. Steinmann, S. Walter, M. Beckers, G. Seide, T. Gries, G. Roth, , *Materials*. **2013**, 6(7), 2642-2661.
- [320] M. Jux, T. Gries, G. Roth, S. Walter, M. Kubicka, G. Seide, B. Glauß, P. Wierach, , *Key Engineering Materials*. **2015**, 644, 110-114.
- [321] M. Krehel, M. Wolf, L. F. Boesel, R. M. Rossi, G. Bona, L. J. Scherer, , *Biomedical Optics Express*. **2014**, 5(8), 2537-2547.
- [322] F. A. Reifler, R. Hufenus, M. Krehel, E. Zraggen, R. M. Rossi, L. J. Scherer, , *Polymer*. **2014**, 55(22), 5695-5707.
- [323] E. Nilsson, A. Lund, C. Jonasson, C. Johansson, B. Hagström, , *Sensors & Actuators: A. Physical*. **2013**, 201, 477-486.
- [324] F. J. Aranda, J. Perry, D. Archambault, L. Belton, J. Carlson, D. Ziegler, B. Kimball, "Optical properties of a retro-reflection fiber cross section formed via tri-component fiber extrusion", Aug 17, 2010.
- [325] A. Talbourdet, F. Rault, A. Cayla, C. Cochrane, E. Devaux, A. Gonthier, G. Lemort, C. Campagne, , *IOP Conference Series: Materials Science and Engineering*. **2017**, 254, 72026.
- [326] B. Kim, V. Koncar, E. Devaux, C. Dufour, P. Viallier, , *Synthetic Metals*. **2004**, 146(2), 167-174.

- [327] Y. Li, B. Zhou, G. Zheng, X. Liu, T. Li, C. Yan, C. Cheng, K. Dai, C. Liu, C. Shen, Z. Guo, , *Journal of Materials Chemistry C*. **2018**, 6(9), 2258-2269.
- [328] B. Ding, M. Wang, J. Yu, G. Sun, , *Sensors (Basel, Switzerland)*. **2009**, 9(3), 1609-1624.
- [329] A. Chinnappan, C. Baskar, S. Baskar, G. Ratheesh, S. Ramakrishna, , *Journal of Materials Chemistry C*. **2017**, 5(48), 12657-12673.
- [330] W. Hills, **1996**.
- [331] W. Hills, **1996**.
- [332] J. Haggard, B. Norcott, **1998**.
- [333] Y. H. Choong Gabriel, De Focatiis Davide, S. A, J. Lidgett Mark, J. Thornton Matthew, J. Clifford Mike, , *AIP Conference Proceedings*. **2019**, 2055(1).
- [334] J. A. Heiser, J. A. King, J. P. Konell, L. L. Sutter, , *Advances in Polymer Technology*. **2004**, 23(2), 135-146.
- [335] J. R. Wagner, E. M. Mount, H. F. Giles, , *Extrusion (Second Edition)*. **2014**, 233-240.
- [336] B. Yeom, B. Pourdeyhimi, , *J Mater Sci*. **2011**, 46(10), 3252-3257.
- [337] S. Chung, M. P. Gamcsik, M. W. King, , *Biomedical Materials*. **2011**, 6(4), 045001.
- [338] A. Grumezescu, A. Holban, *Materials for Biomedical Engineering: Nanomaterials-based Drug Delivery*, Elsevier, US **2019**.

- [339] S. Mohapatra, S. Ranjan, N. Dasgupta, R. K. Mishra, S. Thomas, *Characterization and Biology of Nanomaterials for Drug Delivery*, Elsevier, US **2018**.
- [340] X. Q. Shi, H. Ito, T. Kikutani, , *Polymer (Guilford)*. **2006**, 47(2), 611-616.
- [341] A. V. Shenoy, S. Chattopadhyay, V. M. Nadkarni, , *Rheologica Acta*. **1983**, 22(1), 90-101.
- [342] A. Dutta, , *Rheologica Acta*. **1984**, 23(5), 565-569.
- [343] J. L. White, J. W. Crowder, , *J Appl Polym Sci*. **1974**, 18(4), 1013-1038.
- [344] ASTM International, **2010**.
- [345] R. Hufenus, C. Affolter, M. Camenzind, F. A. Reifler, , *Macromolecular materials and engineering*. **2013**, 298(6), 653-663.
- [346] M. Strååt, M. Rigdahl, B. Hagström, , *Journal of Applied Polymer Science*. **2012**, 123(2), 936-943.
- [347] N. Fedorova, B. Pourdeyhimi, , *Journal of applied polymer science*. **2007**, 104(5), 3434-3442.
- [348] M. E. Spahr, R. Gilardi, D. Bonacchi, in *Polymers and Polymeric Composites: A Reference Series* (Ed: Sanjay Palsule), Springer Berlin Heidelberg, Berlin, Heidelberg **2016**, pp. 1-26.
- [349] R. A. Kudva, H. Keskkula, D. R. Paul, , *Polymer*. **1999**, 40(22), 6003-6021.

- [350] C. R. López-Barrón, J. R. Robledo-Ortiz, D. Rodrigue, R. González-Núñez, , *Journal of Plastic Film & Sheeting*. **2007**, 23(2), 149-169.
- [351] Anonymous .
- [352] Zhenhai Chen, R. C. Luo, , *TIE*. **1998**, 45(6), 886-894.
- [353] S. Zhu, Y. Fang, B. Wang, J. Zhou, Q. Hu, B. Hu, B. Zhang, Z. Xiang, J. Zhong, Q. Zhong, Z. Wang, Y. Cao, , *Nano Res*. **2014**, 7(10), 1488-1496.
- [354] N. Mathur, I. Glesk, A. Davidson, G. Paul, J. Banford, J. Irvine, A. Buis, "Wearable mobile sensor and communication platform for the in-situ monitoring of lower limb health in amputees", May 2016.